ABSTRACT

MEDLIN, GRAHAM LUCAS. Characterization of the PULSTAR Ultracold Neutron Source. (Under the direction of Albert Young.)

Ultracold neutrons (UCN) are free neutrons with sufficiently low energy such that they may be confined for lengths of time approaching the neutron lifetime. They have great potential for a wide range of experimental studies, however almost all of these studies are limited by the available UCN density. A UCN source is being installed at the PULSTAR reactor at North Carolina State University (NCSU) that will efficiently provide a high UCN flux per available reactor power. The NCSU source is uniquely placed outside the reactor pool and features a system to transport neutrons from the reactor core. This transport is modeled and benchmarked against foil activation measurements. To produce UCN, a heavy water thermal moderator is coupled with a solid methane cold moderator, the temperature of which can be optimized for down-scattering in the solid deuterium UCN converter. This work will present the construction and testing of the NCSU source's cryostat, cryogenic helium system, and gas handling systems, including a deuterium spin-state converter and Raman spectrometer. Further, this work will characterize the growth of the solid deuterium crystal in our UCN source cryostat.

Characterization of the PULSTAR Ultracold Neutron Source

by
Graham Lucas Medlin

A dissertation submitted to the Graduate Faculty of
North Carolina State University
in partial fulfillment of the
requirements for the Degree of
Doctor of Philosophy

Physics

Raleigh, North Carolina

2017

APPROVED BY:

_____   _____
Daniel Dougerty   Ayman Hawari

_____   _____
Paul Huffman   Albert Young
                                                         Chair of Advisory Committee

DEDICATION

OKAY, HOLD STILL. AND REMEMBER, IF YOU *REALLY* BELIEVE IN THE LAWS OF PHYSICS, YOU WON'T FLINCH.

BIOGRAPHY

Graham was born on a Wednesday.

---

[1]This document was produced with LaTeX, which is an invaluable aid to the author [73, 115].

LIST OF TABLES

LIST OF FIGURES

Chapter 1

Introduction

Ultracold neutrons (UCN) are free neutrons with sufficiently low energy such that they may confined by a combination of material, gravitational, and magnetic traps for lengths of time approaching the unstable neutrons' mean decay lifetime. They have great potential for fundamental particle physics experiments and material surface studies. However, almost all of these experiments are limited by the available UCN density.

Currently, a state-of-the-art UCN source is being installed at the PULSTAR reactor at North Carolina State University (NCSU) that will efficiently provide a high UCN current per available reactor power. This Source[1] will serve both as a testbed for UCN source design and as a user facility for UCN-based research. This dissertation will describe the construction, continuing commissioning, and refinement of the theoretical understanding of the PULSTAR UCN Source. After providing background on ultracold neutron source research in this introduction, Chapter 2 will cover the transport of reactor neutrons to the Source, Chapter 3 will discuss UCN production in the Source, Chapter 4 will describe the necessary cryogenic and gas handling infrastructure, Chapter 5 will characterize the growth of solid deuterium crystals in the Source.

1.1 Neutrons and matter

Free neutrons find application in science and technology over an incredible energy range. To produce ultracold neutrons, the primary interest of this work, the kinetic energy of neutrons is brought down from order 10^6 electron-volts ($\sim$1 MeV) to of order 10^{-7} electron-volts ($\sim$100 neV) or less! The terminology used to characterize neutron energy varies by application, but the spectrum as used in this work is shown in Figure 1.1.

---

[1]The word "source" will be capitalized when it is referring to the PULSTAR UCN Source at NCSU. This is to distinguish it both from a generic source and other PULSTAR-based programs.

1

Figure 1.1 (Energy scales of the free neutron):

Temperature	Energy (eV)		Velocity (m/s)	Wavelength
10^{11} K	20 MeV		62 000 km/s	6 fm
		Fast		Nucleus
	10^6		0.05c	
10^9 K	0.1 MeV		4400 km/s	0.1 pm
		Slowing down	10^6	
	10^3			
			Voyager 1	
11 600 K	1 eV		14 km/s	30 pm
		Epi-Thermal	Low orbit	H atom
293 K	25.3 meV	Thermal	2200 m/s	0.18 nm
			10^3	U atom
	10^{-3}	Cold	Sound	
1 K	60 μeV		110 m/s	4 nm
		VCN		CPU node
	10^{-6}		Usain Bolt	
0.003 K	250 neV		7 m/s	60 nm
1st gravitational state 1.4 peV	10^{-8}	UCN	Walking 1	Violet light

Figure 1.1: Energy scales of the free neutron with some common references for length and velocity.

$$E = \frac{1}{2}mv^2 = \frac{\hbar^2 k^2}{2m} = \frac{h^2}{2m\lambda^2} \sim k_{\mathrm{B}}T \tag{1.1}$$

$$\phi(E) = v\,n(E)\,\mathrm{d}E \propto E \exp\left(\frac{-E}{k_{\mathrm{B}}T}\right)\mathrm{d}E \tag{1.2}$$

As a typical massive particle, the relationship between the neutron kinetic energy E, velocity v, wavenumber k, and de Broglie wavelength λ is given in Equation 1.1. It is also common to refer to the neutron temperature T, related to the most probable energy in a Maxwell-Boltzmann flux distribution by the Maxwell-Boltzmann constant k_{B}. This temperature is most physically meaningful when a collection of neutrons is in thermal equilibrium with a material. The flux density ϕ, or simply "flux," is the number of neutrons passing through a unit of area per unit time. The flux in an energy range $\mathrm{d}E$ can be written as in Equation 1.2.

The lack of electric charge makes acceleration of the neutron impractical. However large numbers of "fast" neutrons, with order MeV energy, are produced by fission in reactors and through spallation at accelerators. These two types of facilities are by far the most intense neutron sources, and the common choice even when low energy neutrons are desired in large number. The energy spectrum of these neutrons can then be tailored as desired through interactions with appropriately selected materials.

At higher energies, the wavelength of the neutron can be on the order of the size of the nucleus, and collisions are largely elastic and involve point-like *s*-wave scattering. The material will appear as a free gas of nuclei with a Maxwell-Boltzmann energy distribution, so at much higher neutron energies, these nuclei are effectively stationary. Neutrons in this higher "slowing down" energy range will predominately lose energy at each collision.

$$\xi = \ln\left(\frac{E_o}{E_f}\right)_{\text{avg}} \tag{1.3}$$

$$\ln(E) = \ln(E_o) - n\xi \tag{1.4}$$

A parameter ξ is defined as the average logarithm of the fractional energy loss with a initial neutron energy of E_o and an energy after collision of E_f as shown in Equation 1.3. A thermal neutron could lose all of its energy in a collision with hydrogen, the proton being of nearly identical mass to the neutron, and $\xi = 1$. This parameter is less for more massive atoms, 0.725 for deuterium and 0.158 for carbon-12. The average number of collisions n to reach a final energy E is given by Equation 1.4. From 2 MeV to 25 meV, n is 18 for hydrogen, 25 for deuterium, and 110 for carbon-12 [80].

As the neutron reaches a speed on the order of the speed of the thermal motion of nuclei, it could either lose or gain energy in each collision. After many more collisions, an ensemble of neutrons will statistically approach the Maxwellian thermal distribution of the atoms in the material. A material that does this effectively is called a moderator. It must be fairly opaque and able to create many collisions in a small volume without absorbing a large fraction of neutrons.

"Epithermal" neutrons are defined here as those slowing down neutrons that have reached realistic material temperatures but have not reached equilibrium with the moderator. At these energies and below, neutrons begin to scatter not just elastically from nuclei, but also inelastically through interations with molecular excitation modes and crystal lattice pseudoparticle phonons. This is covered in more detail in Chapter 3. "Thermal" neutrons are those that have approached equilibrium with a room-temperature moderator, and likewise "cold" neutrons have approached equilibrium with a moderator at colder temperatures, e.g. solid methane or liquid hydrogen.

Figure 1.2: A short section of UCN guide for the Source. The 16 cm inner-diameter quartz tube is coated with nickel-58.

"Very Cold Neutrons" (VCN) are significantly colder than typical moderator temperatures, less than 1 K. They are not the majority in any moderated flux, but they may still be found in the low energy tail of the Maxwellian distribution. "Ultracold neutrons" are VCN with sufficiently low energy that they may be stored in a contained volume. The upper-end of this definition then varies by the storage technology in use.

1.2 Ultracold neutrons and research

Ultracold neutrons are something of an oddity in particle physics; they have very human-sized time and length scales. They move at the speed of a brisk walk and have a half-life of about 10 minutes. With the gravitational potential $V_g = mgh$, they move in parabolic trajectories of at most a few meters in height, providing an upper limit to a storage volume. In particle physics terms, this makes for reasonably sized equipment. (Consider the Large Hadron Collider or Super-Kamiokande neutrino detector!) Their wavelength is similar to ultraviolet light, and surfaces that appear as mirrors to the human eye typically allow specular reflection of UCN.

Neutrons have a magnetic moment $\vec{\mu}$, and with a magnetic potential $V_B = \vec{\mu} \cdot \vec{\mathbf{B}}$, UCN can be completely trapped with a field strength of a few Tesla. This makes possible the production of very highly polarized UCN samples, and permits UCN interactions with atomic magnetism without the barrier of electric charge. While ignored entirely in this work, the polarization of ultracold neutrons is central to most UCN-based experiments. (And the magnetic moment allows production of UCN by magnons notably in oxygen.)

Lacking an electric charge, neutrons interact with nuclei through the strong nuclear force, which has a range of only a few femtometers (10^{-15} m). For low energy neutrons with longer wavelengths, the nuclear potential may be replaced with a point potential. For UCN with wavelengths of many atomic diameters, an effective step potential is formed at a surface. This potential is material-dependent and negative for some materials. For a positive material potential, UCN with lower energies are totally internally reflected, providing another means of storage. For example, the UCN guides at the PULSTAR Source are coated with nickel-58, which has one of the higher material potentials of 340 neV, see Figure 1.2. A straightforward treatment is given in *Ultracold Neutrons* by R. Golub et al. [43].

The properties of the neutron and its beta decay make it an interesting choice for fundamental physics study (for thorough recent reviews of neutron physics see [1, 27]). Free ultracold neutrons provide a very different environment for study that is complimentary to high-energy and atomic physics measurements in that it eliminates (or at least replaces) various systematic errors and corrections. A few areas of UCN research are given below.

The lifetime of the free neutron is an important parameter in many calculations and is surprisingly poorly known in particle physics terms. Cold neutron beams and UCN traps provide the most precise neutron lifetime measurements, and many such experiments have been made (see [172]).

The search for the so-far-undetermined neutron electric dipole moment (nEDM) is often identified as the leading experimental physics challenge since the discovery in the Higgs. UCN allow measurement times orders of magnitude longer than in typical beam experiments, enabling high precision spectroscopy of the precessing spins of a neutron population. Limits on the size of the EDM can place constraints on possible Beyond Standard Model physics, see [85, 121, 134].

Many of the arbitrary inputs to The Standard Model can be extracted from beta-decay product-correlation measurements. For an introduction and review of the recent work at the Los Alamos National Laboratory (LANL) UCN Source see A. Young, et al. [175].

UCN are such low energy that it is feasible to observe and even guide the first gravitationally-bound quantum states with micron wavelengths [110, 111]. This unique regime can be used to verify the mass equivalence principle probe for exotic interactions and other new physics. This technology also has potential surface studies applications [38, 67, 81].
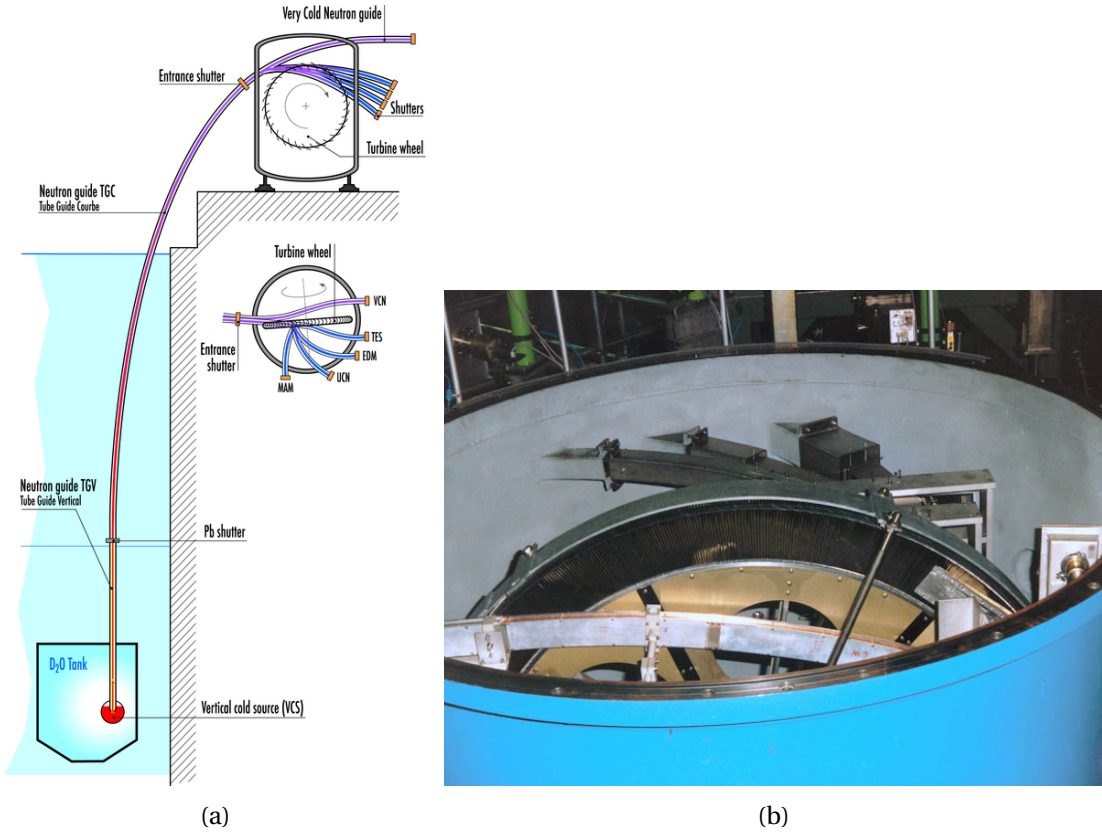
Figure 1.3: (a) The ILL UCN turbine (instrument PF2) connected to the liquid deuterium cold source by vertical guide and (b) a photograph of the turbine and extraction guides reproduced from [120].

1.3 A brief history of UCN sources

It is remarkable how quickly after Chadwick's discovery of the neutron in 1932 [21] the properties of low-energy free neutrons were measured [5]. By 1946, these "slow" neutrons were observed to coherently scatter from a material surface, behaving much like traditional optics [30, 31]. This observation would develop into neutron guides that can transport neutrons over considerable distances, maturing into today's cold neutron industry.

It is not a leap to imagine a free neutron of sufficiently low energy, an ultracold neutron, such that it may be totally reflected at any angle of incidence. These neutrons would be present in extremely small numbers in a reactor at the lowest end of the energy spectrum. Ya.B. Zeldovich, in 1952, was the first to put the idea into the literature, proposing a liquid helium moderator to increase the number of neutrons in the tail of the Maxwellian distribution. They could then be extracted and stored in a material bottle [178]. V.V. Vladimirskii defined the conditions necessary to confine neutrons magnetically [167]. Ultracold energy neutrons were successfully extracted independently by two
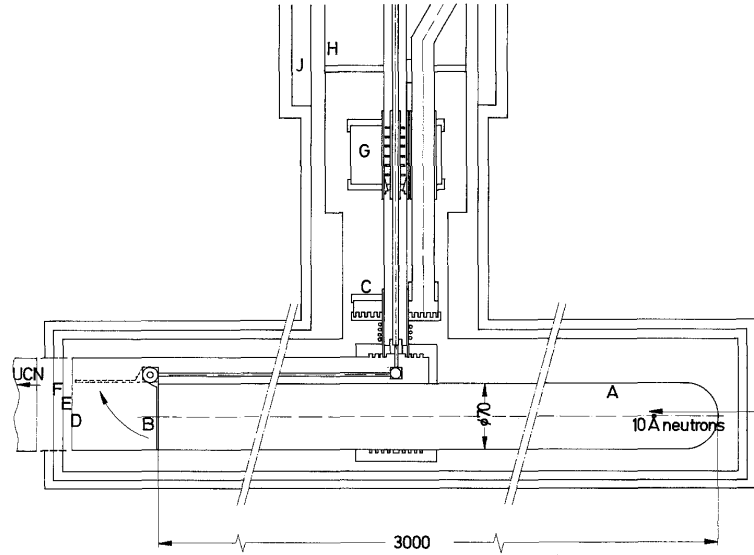
Figure 1.4: The first superfluid helium UCN source, reproduced from R. Golub et al. [42], with (A) UCN storage vessel, (B) UCN flapper valve, (D-F) windows, and (C,G-J) cryostat and refrigerator.

groups in 1969. V.I. Lushchikov, et al. used paraffin and polyethylene moderators with a curved horizontal guide for extraction and a thin foil-covered detector for detection [98]. A. Steyerl used a curved vertical guide to extract and gravitationally decelerate neutrons and used a rotating chopper with time-of-flight for detection [153].

The first practical sources resulted from coupling this vertical extraction with a strong cold neutron source, e.g. liquid hydrogen or deuterium. The source at the Petersburg Nuclear Physics Institute, PNPI (at the time, the Leningrad Nuclear Physics Institute, LNPI), used a liquid hydrogen source in the center of the reactor core to extract both cold and ultracold neutrons [3]. The source at the Institut Laue-Langevin (ILL) transports higher energy neutrons through a curved vertical guide to a mirrored turbine, Figure 1.3. The turbine Doppler shifts neutrons to lower energies through collisions with the rotating blades [154, 155].

However, the UCN density achieved by these sources, while sizable and reliable, is ultimately limited by the initial neutron flux. Liouville's theorem states that the phase space density, $\rho(r, p)\mathrm{d}^3 r\, \mathrm{d}^3 p$, of a collection of particles is constant, $\mathrm{d}\rho / \mathrm{d}t = 0$. Practically, conservative transformations such as a gravitational shift or reaching thermal equilibrium with a moderator cannot both slow neutrons and increase their density.

R. Golub and J.M. Pendlebury in 1975 proposed that this limitation could be circumvented by carefully choosing a material environment such that neutrons would preferentially surrender energy to material excitations, phonons, instead of reaching thermal equilibrium [40]. Liouville's theorem still applies to the total collection of neutrons and material phonons, but a portion of phase space has been donated to the phonons. They called this a "superthermal" source as the temperature of the source material was far greater than that of the resultant neutron flux. As thermal equilibrium is avoided, the material is not a moderator, and is instead referred to as a UCN "converter."

Golub and Pendlebury proposed superfluid helium-4 as one such material [41], and a working source was demonstrated shortly after at ILL [42]. Neutrons with energies around 1 meV (0.89 nm) can excite an equal energy phonon, inelastically scattering to UCN energies.

Maintaining a sufficiently low temperature limits the phonons available for upscatter, and suppresses the reverse process. The zero nuclear-absorption cross-section of helium-4 and along with its very low material potential allow for very long storage times, and thus very high UCN densities. As upscatter depends heavily on the converter's temperature, and the desired operating temperature is less than 1 K, heat removal is the primary challenge. As UCN storage technology improved, thus increasing the storage time, helium converters allowed measurements directly in the source volume, eliminating UCN transport. The magnetic trap for a neutron lifetime measurement at the National Institute of Standards and Technology (NIST) is an example [64].

Crystal monochromators can select out the 0.89 nm segment of a cold neutron beam, significantly reducing background, but also limiting overall intensity. See for examples the Japanese High Energy Accelerator Research Organization (KEK) efforts at the Japan Research Reactor (JRR)-3 [174], the development of a narrow-band 0.89 nm monochromator for UCN production at NIST [104], and source development work at ILL [14]. There is also an important down-scattering process involving multiple phonons [77]. This multi-phonon process was measured on earlier beam experiments [36, 37] and confirmed as part of UCN source development work by O. Zimmer et al. [180].

It was also realized that, although the storage time in other materials may be more limited, it would still be possible to extract a significant UCN current. Production in hydrogen and deuterium were first measured at LNPI in 1980 [4]. This process was conceptualized by R. Golub, et al. as a thin-film source [39, 177]. The prime example is solid deuterium, sD_2, which offsets a shorter residency lifetime with many more available phonon modes than helium. The converter can be operated at a higher temperature, 5 K, reducing the cryogenic requirement over a superfluid helium source. It is necessary to significantly reduce the para-deuterium content which allows an unacceptable mode of upscattering [93]. A.P. Serebrov, et al. successfully demonstrated a solid deuterium source at the continuous power WWR-M reactor at PNPI [140].
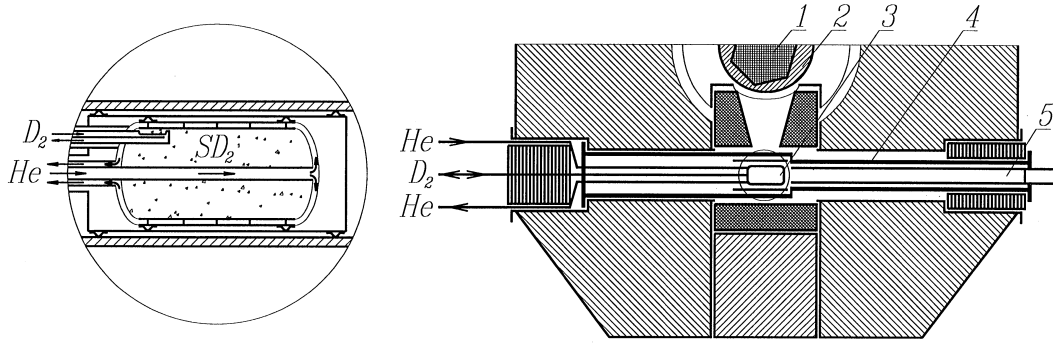
Figure 1.5:   The first PNPI solid deuterium UCN source in the WWR-M reactor, reproduced from A.P. Serebrov et al. [140]. From above is the (1) reactor core, (2) beryllium reflector, (3) source, (4) source containment, and (5) UCN guide.

For an application where high UCN current is preferred over UCN density, a sD_2 source based on a pulsed thermal neutron source is appealing. The total heat load is less in a low duty cycle pulsed source, and the large heat capacity of sD_2 limits temperature change. While most early sources were reactor-based, the heat per thermal neutron is less at a spallation source than at a reactor. This was realized by a demonstration source at the Los Alamos Neutron Science Center's (LANSCE) pulsed spallation neutron source [59, 107, 131]. In a pulsed neutron source, a UCN shutter may be used to further block visibility between the source and storage volume, allowing the stored UCN density to be determined by the peak flux [124]. This was realized by the next generation source at LANL [132].

1.4   Current and planned UCN sources

Today, there are a handful of operational UCN sources with many more planned. In addition, there are several planned experiments that generate UCN *in situ*, most notably the nEDM search at the Spallation Neutron Source (SNS) at Oak Ridge National Lab (ORNL) [163]. However, I focus on user-facility type sources here. (For a recent review of operational sources see Young et al. [175].)

The mechanical turbine source at ILL remains one of the most successful sources to this day, providing a steady-state current of 4×10^6 UCN/s and a density of >36 UCN/cm^3 in a storage volume [155]. Such traditional sources have not been entirely replaced by helium and deuterium, and a VCN-to-UCN turbine has recently come online at the Japan Proton Accelerator Complex (J-PARC) [66, 106]. A sD_2-based source is also planned at the facility.

More recently, two superfluid helium-based sources have been installed at ILL on a neutron beam from the cold source. The first, designated "SUN1," was originally tested on the FRM-II reactor at the Technical University of Munich (TUM) [182] before being moved to ILL. It provides a density of >55 UCN/cm^3 in a storage volume and is currently in operation as part of the GRANIT UCN gravitational
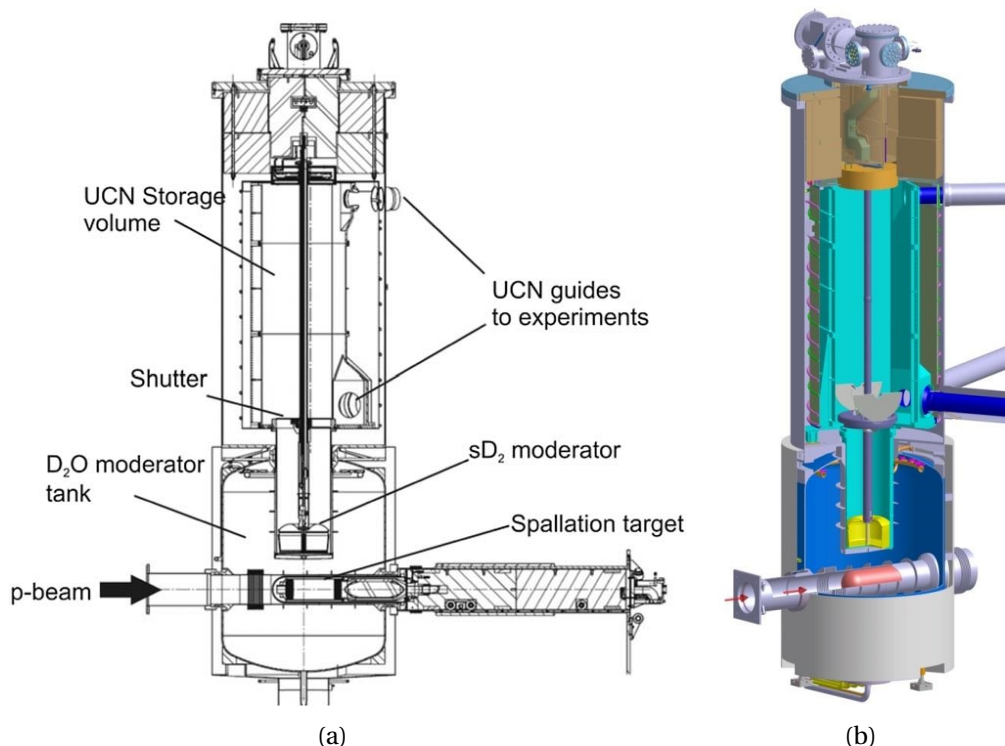
Figure 1.6: The PSI solid deuterium UCN source which uses a shutter to maintain UCN density between proton beam pulses, reproduced from A. Anghel et al. [7] and B. Lauss [87].

spectrometer [122, 135, 136, 182]. The second, designated "SUN2," has very recently accumulated well over 100 $^{UCN}/cm^3$ in the production volume [90, 181]. Both are considered prototypes for the next generation source, "SuperSUN," which is expected to provide a significant increase in UCN current. As planned, it will include a magnetic multi-pole reflector to polarize UCN inside the converter volume [179].

The Research Center for Nuclear Physics (RCNP) at Osaka University has demonstrated a helium source coupled to a spallation source, providing a current density of 40 $^{UCN}/cm^3 \cdot s$ [103]. The planned upgrade to this source will moved to TRIUMF[2] in Vancouver, notably switching the cold moderator from D_2O to ℓD_2 [121]. The PNPI group has planned a ℓHe source, the "supersource," to be installed on the WWR-M reactor [141, 143, 146]. It is notable to us in that it will also be installed in the thermal column of that reactor.

---

[2]The former "TRI-University Meson Facility" now includes many more than three universities.

While ℓHe sources can provide high UCN densities, sD_2-based sources have also seen considerable use as they can provide high UCN currents, especially on pulsed neutron sources. The source at LANL provides >52 UCN/cm³ in a storage volume, and is now host to many experiments [132]. Recent upgrades to the beam and UCN source appear to have significantly increased UCN production [118]. The solid deuterium source at the Paul Scherrer Institut (PSI) in Switzerland is likewise based off a spallation source, Figure 1.6. It utilizes a remarkable 5 kg of sD_2 converter. It can provide >34 UCN/cm³ in a storage volume [7, 16, 86]. There is also currently an operating sD_2 source at the TRIGA reactor at the Johannes Gutenberg University of Mainz. The reactor can be operated in both steady-state and pulsed modes, and has two beamtubes dedicated to UCN work. The installed source on beamtube D has provided >10 UCN/cm³ in a storage volume and 2.4×10^5 UCN total per pulse [69, 149]. Beamport C has been used to test several UCN source designs, in particular in support of a planned UCN source at the FRM-II reactor at TUM [162].

Although I have quoted available UCN densities, I caution that these are not directly comparable as each depends on details of the source and storage volume. I have also not quoted production values for upcoming sources. These predictions are often orders of magnitude greater than anything available today, and with existing sources having taken many years to reach their current output, some skepticism is healthy.

And of course there is a UCN Source at the NCSU PULSTAR reactor.

1.5   The PULSTAR UCN Source

The concept and design of UCN Source at the PULSTAR reactor has been described elsewhere [78, 92, 116, 169, 173]. A recent commissioning update is given by E. Korobokina et al. [79], and will be expanded upon in the following chapters. Briefly, the UCN Source utilizes a three-stage process that optimizes UCN production per the available reactor power, and operates in a steady-state mode.

Neutron sources are traditionally placed near the reactor core using existing beam ports. This comes at the cost of high heat loads, making a cryogenic solution difficult. The PULSTAR Source uniquely solves this by moderating neutrons outside the reactor pool. Both fast and thermal neutrons are efficiently transported from the core, through a specially designed port-structure, to the former thermal column facility.

In the former thermal column, a 677.6 L (179 gallons) heavy-water thermal moderator tank surrounds a vacuum-jacketed cryostat insert. This elbow-shaped insert contains the solid deuterium container and UCN guide. The disc of 200 g of solid deuterium is 17 cm in diameter by 5 cm in height (1 L), and is maintained at a temperature of 5 K. The solid deuterium container is surrounded by
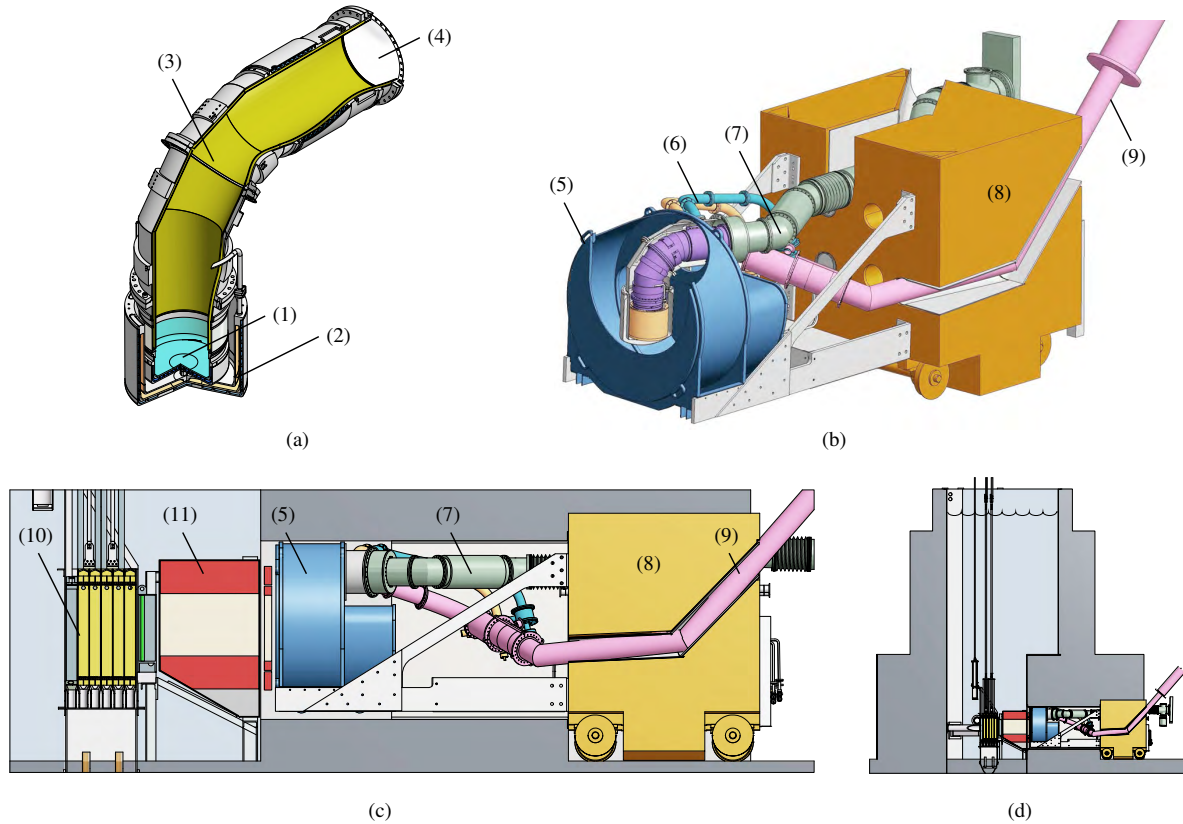
Figure 1.7: A cutaway engineering drawing of the UCN Source cryostat is shown in (a), including the (1) deuterium container, (2) methane container, (3) UCN guide, and (4) UCN window foil. The UCN Source assembly mounted on the shielding door is shown in (b), including the (5) heavy-water tank, (6) deuterium and methane gas lines, (7) UCN guide, (8) thermal column shield door, and (9) liquid helium transfer line. The heavy-water tank and cryostat vacuum jacket have been cut away to show the cryostat. A cross section of the reactor showing the Source assembly installed in the reactor thermal column, in the thermal column is shown in (c) and (d), where (10) is the reactor core and (11) is the neutron port. In all drawings, neutrons from the reactor core enter from the left and UCN exit to the right of the shielding door.

the 1 cm-thick bucket-shaped cold moderator containing 600 g of solid methane. The temperature of the solid methane can adjusted between 30 K and 60 K, optimizing the cold flux for downscattering in the solid deuterium UCN converter. The cryostat is cooled with liquid helium from an on-site liquefier.

It is a user facility; ultracold neutrons are generated in the Source and transported by a system guides to any number of different experiments. The entire assembly is attached to a movable shield door allowing it to be rolled in and out the biological shield for access. The area behind the shield door, shown in Figure 1.8, is available for UCN experiments, with the potential to extend the UCN guides some distance.

Figure 1.8: The UCN experimental area with the cryostat in its testing location to the left of the biological shield. The thermal column door is behind cinder blocks and rolls back along the tracks in the floor. The gas handling systems are just visible above the door

At present, all infrastructure components of the source, including the heavy-water system, gas handling systems, helium liquefier cooling system, graphite-lined assembly, and the source cryostat have been manufactured and assembled for commissioning tests.

Chapter 2

Neutron Transport

2.1 Introduction

The lower temperature required for operation of a UCN converter poses a challenge to the cryogenic engineering of UCN sources at reactor facilities. Increasing the distance from the core to reduce heating also decreases available thermal neutron flux, so the most common design of UCN facilities at reactors is to place the cold neutron moderator and often the UCN converter in either direct [69, 143] or tangential [33, 140, 162] beam ports. Neutrons are moderated to the thermal range as provided by the reactor design, but the source must tolerate a higher heat load.

The UCN Source at PULSTAR is unique in that it moderates fast neutrons outside the reactor pool, at a large distance from the core, by utilizing a specially designed structure which delivers fast and thermal neutrons through the reactor pool to the former thermal-column facility. Gamma heating from the core is reduced significantly, while thermal neutron flux is largely preserved. The total cryogenic heat load is about 20 W [78], in contrast to the kilowatts placed on cold neutron sources.

In this chapter, I characterize the neutron delivery system by benchmarking a model against previous gold foil activation measurements. Neutron transport was modeled using the Los Alamos MCNP6 Monte Carlo neutron transport code (MCNP) [44]. As similar recent examples, gold foil activation was compared with MCNP models in neutronics analysis of the Atominstitute's (ATI) TRIGA Mark II research reactor [71] and to benchmark the PSI UCN source [16]. Our model can then be used to calculate neutron flux across the UCN converter to estimate UCN production.
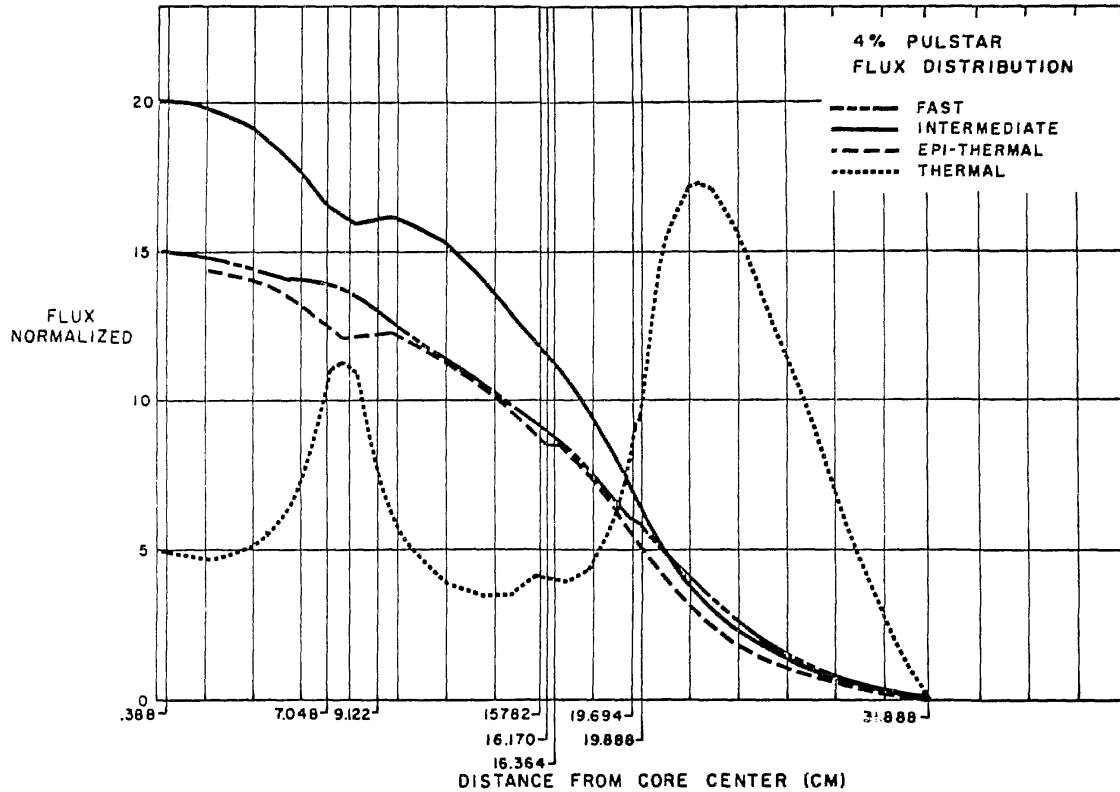
Figure 2.1: Core neutron flux spacial distribution of the NCSU PULSTAR reproduced from R. Carter and B. Leonard [20]. The thermal neutron peak is outside the core boundary at 20 cm.

2.1.1 The PULSTAR reactor

The NCSU PULSTAR [102, 161] is a heterogeneous pool-type university research reactor that has been in operation since 1972. It is fueled with 4% enriched uranium dioxide in a 5x5 grid of fuel assemblies, each assembly with a 5x5 grid of fuel pins. It currently operates in a steady-state mode at power levels up to 1 MW thermal. Recently its cooling system was upgraded and licensing is underway to allow up to 2 MWth, which would include refueling with 6% fuel [54, 55]. The reactor is typically powered during the day and shut down at night, but can be run continuously as required by experiments. As the name implies, the reactor can be pulsed with energy releases up to 35 MWth·s, although this has not been done since commissioning. The reactor has exposure ports, a pneumatic transfer system, six beamports, and a bulk thermal irradiation facility (graphite thermal column). Over the years it has been modified for several new facilities, including irradiation and isotope production, neutron power diffraction, neutron radiography, a positron source, and most recently, the UCN Source.
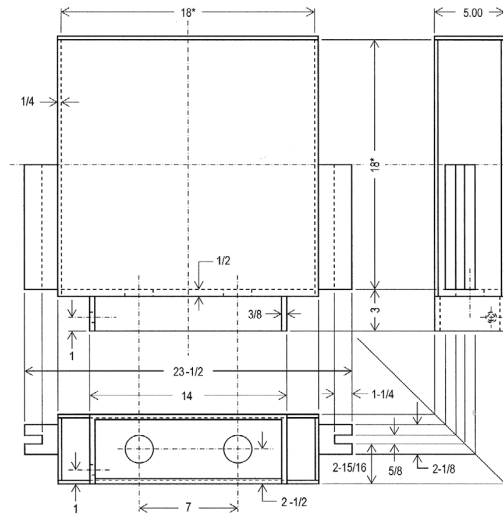
Figure 2.2: Dimensions of the shielding box.

The reactor is intentionally under-moderated, resulting in a high ratio of fast-to-thermal flux in the core, as well as high epithermal and thermal neutron leakage from the core face, Figure 2.1. This yields high thermal neutron fluxes outside the core at the beamports and at the thermal column. This allowed the thermal column to be modified to serve as a beamport for the UCN Source, somewhat analogous to the prototype PNPI solid deuterium UCN source [142] and their upcoming superfluid helium source [143].

2.1.2 Modification of thermal column

The original thermal column was intended to provide solely thermal neutrons through thermalization in the graphite of the nosepiece and thermal column graphite. The neutron delivery system that replaced it is designed to guide fast and thermal neutrons from the core to the Source cryostat with minimal losses.

Originally, this thermal column consisted of a 1.2 m (4 foot) square column of graphite running 1.5 m (5 feet) through the reactor biological shield from the outside of the pool liner. The chamber is lined with Boral, surrounded by Barytes type high density concrete, and has a large Barytes concrete door. A graphite "nosepiece" displaced the water between the pool liner and the Rotary Exposure Ports (REPs) at the reactor core faces.
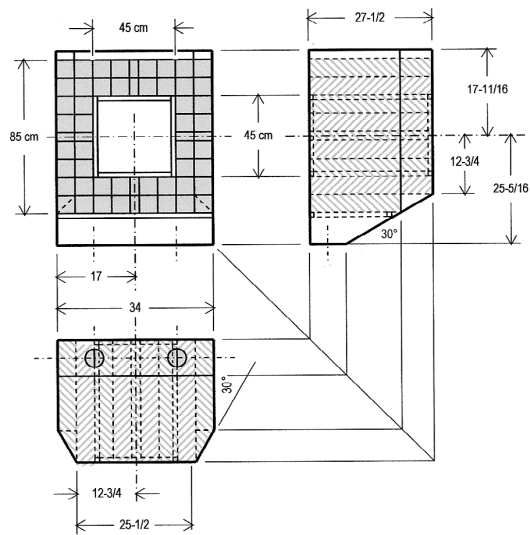
(a)

(b)

Figure 2.3:   (a) Dimensions and (b) photo of the nose port.

(a)
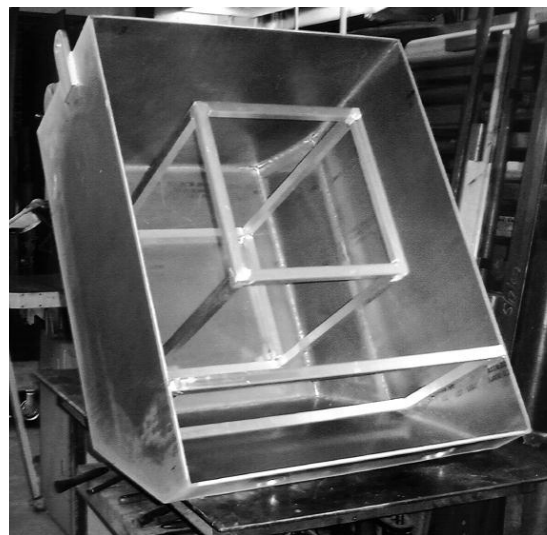
(b)

Figure 2.4:   Photos of the nose port before graphite was installed.
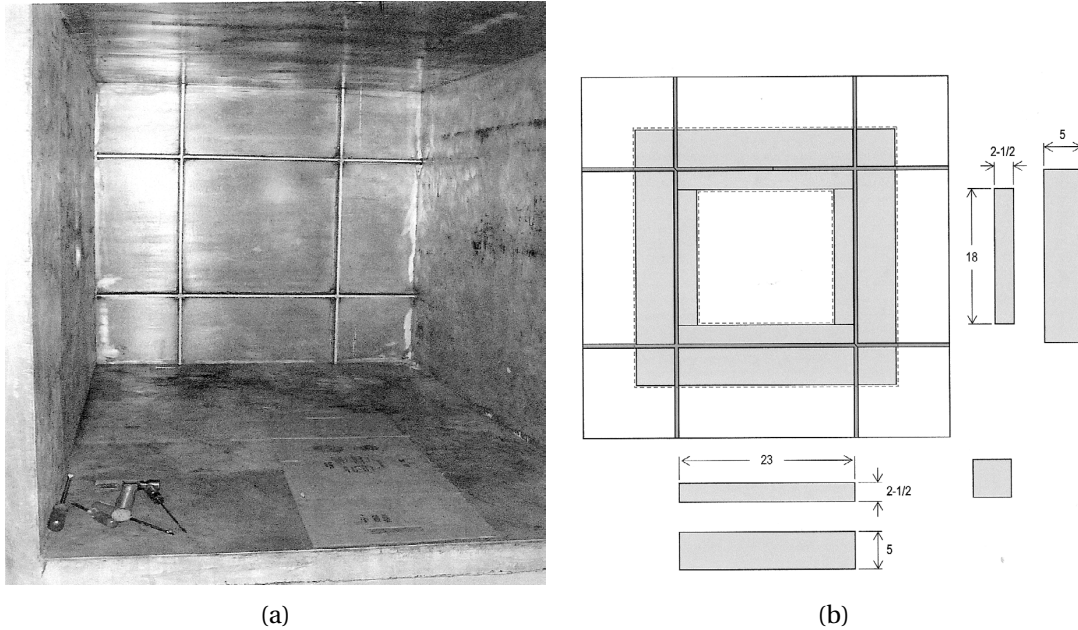
Figure 2.5: (a) Empty thermal column showing webbing before graphite was added and (b) dimensions of the graphite added to the webbing.

Several changes where made to accommodate the UCN Source. The graphite in the thermal column was removed. The UCN Source, mounted on the concrete door, can be rolled into this chamber, allowing easy access to the Source. The large size of the thermal column outside the reactor pool allows for a relatively large heavy water thermal moderator.

A "shielding box" that contains a 2.54 cm (1 inch) thick lead plate is placed between the core and the entrance of the nose port, replacing the REPs, to reduce heating of the UCN Source by core gammas. Although not necessary, the lead plate also serves as a reflector, helping maintain reactor reactivity. This box can be removed independent of the nose port to change the type or thickness of the shielding material, Figure 2.2.

The graphite nosepiece was replaced with a removable "nose port" between the wall of the reactor pool and the cryostat. It features a floodable 45 cm square central void, surrounded on the perimeter by 20 cm of graphite, and encased in a 6.35 mm (0.25 inch) thick walled aluminum box, see Figure 2.3. It allows the high neutron flux into the thermal column, acting as a collimator. It can also act as a neutron shutter; when neutrons are required for the Source, water can be forced out of the shielding box and the nose port with pressurized with helium gas. To minimize the pressure difference across the walls, a small vertical hole in the graphite and a tube, called the "bypass tube," allows air and water to flow between the empty spaces at the top and bottom of the nose port.

18

Lifting
Eyes

Assembly
Well

D$_2$O
Inlet / Outlet

Stringer
Hole

Wheels

(a)

(b)
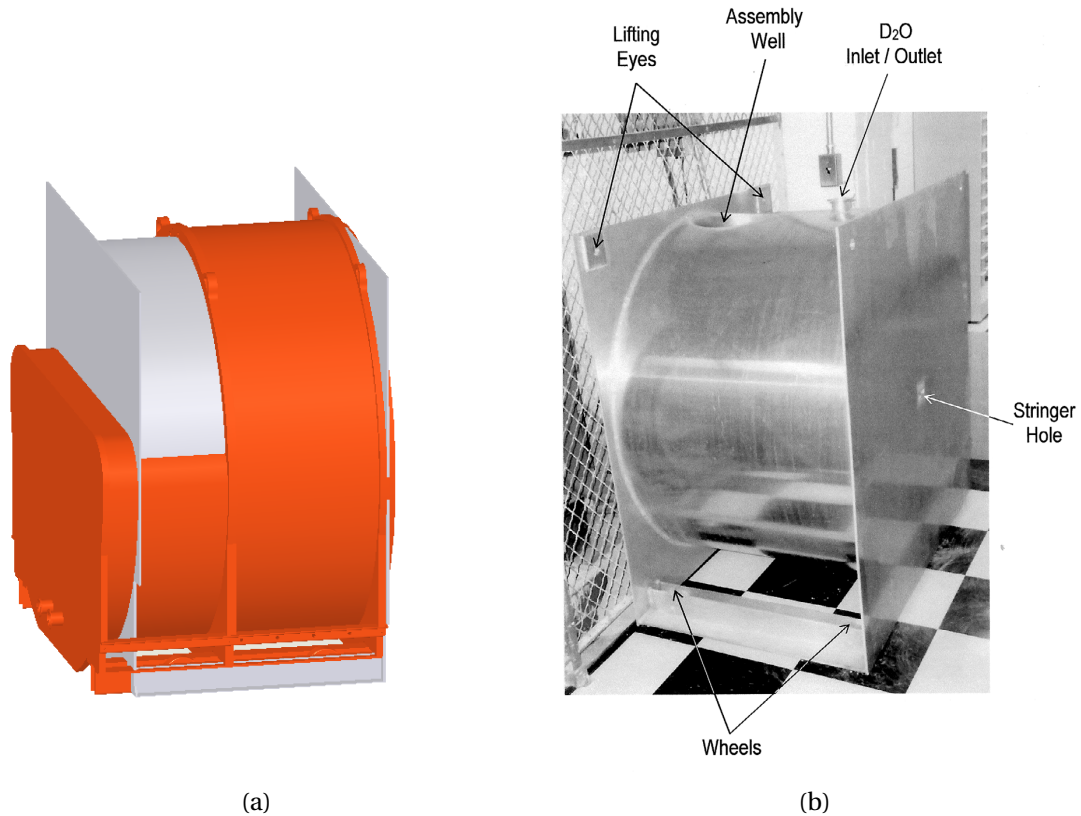
Figure 2.6: The heavy water test tank in gray compared to the UCN Source tank in orange, and (b) an image of the test tank with features labeled.

The graphite-lined void in the current setup avoids much of the neutron loss due to absorption in graphite, but delivers epithermal and fast neutrons to the Source in addition to thermal neutrons. The heavy water tank of the Source now serves to thermalize these neutrons.

A 2.54 cm (1 inch) thick aluminum plate was previously welded to the inside of the thermal column chamber to strengthen the pool liner. A 5.08 cm (2 inch) deep grid of aluminum bars was welded to this plate for further reinforcement. This "webbing" creates a gap at the front of the UCN Source, and to minimize neutron loss, a 45.7 cm (18 inch) square void was surrounded by 20.3 cm (8 inches) of graphite of the same thickness, overlapping this webbing, Figure 2.5. Penetrations through the door were made for the liquid helium cooling lines and UCN guide.

19

2.2 Neutron transport

2.2.1 Test tank measurements

To confirm the performance of the Source's heavy-water thermal-moderator tank, and verify the expected thermal neutron flux to the Source, a mockup of the heavy-water tank was constructed. This "test tank" was constructed out of 6061 aluminum and consists of a horizontal cylindrical tank, the same size as the Source tank, with a vertical well simulating the vacuum of the inner Source cryostat, Figure 2.6. It holds 662.4 L (175 gallons) of water, compared to the 677.6 L (179 gallons) of the UCN Source tank.

Neutron flux was estimated through the gold foil activation method. An acrylic "stringer" supporting the foils was inserted into a 1.27 cm–by–3.18 cm (0.5 inch–by–1.25 inch) rectangular tube running the length of the centerline of the test tank along the thermal column axis. The stringer was replaced with one made of aluminum after the first measurement, although MCNP calculations suggest the material had no impact on the measurements.

Typically a first measurement would be made with bare gold foils followed by a second measurement with cadmium-shielded foils, to block thermal neutrons, at the same positions. To limit the number of experimental runs required, bare foils and cadmium-shielded foils were alternated down the length of the stringer with the assumption that activities could be interpolated to each position. Four bare foils were placed at 2.54 cm, 12.70 cm, 22.86 cm, and 33.02 cm (1 inch, 5 inch, 9 inch, and 13 inch), and three shielded foils were placed at 7.62 cm, 17.78 cm, and 27.94 cm (3 inch, 7 inch, and 11 inch), from the front of the tank.

The test tank can be inserted into the thermal column chamber in either direction. Orienting the tank "backwards," with the well on the far side of the tank from the reactor core, approximates the thermal column filled with water to provide a good estimate of the neutron flux. Orienting the tank with the well on the core side then demonstrates the relative effect of the cryostat vacuum void.

Five measurements were conducted with the test tank between October 2009 and July 2010, Table 2.1. In each test, the reactor was run at 100 kW for 30 min. Calculated fluxes are scaled by a factor of 10 to the 1 MW reactor power. To verify the experimental procedure, the tank was first filled with deionized light water, and the tank was oriented with the well on the far side of the tank, away from the core. This was repeated with heavy water in the tank, both with and without the shielding box present. For the fourth and fifth measurements, the tank was oriented with the well on the side facing the core, mimicking the UCN Source void, with acrylic blocks around the inner perimeter of the well to mimic the cold moderator. The tank was only partially filled with heavy water, leaving a

Table 2.1:   Schedule of test tank foil activation measurements.

	Date	Tank moderator	Well direction	Stringer material	Shielding box
A	2009/10/23	H_2O	Away	Acrylic	Not present
B	2010/3/15	D_2O	Away	Aluminum	Present
C	2010/3/29	D_2O	Away	Aluminum	Not present
D	2010/6/2	D_2O*	Facing†	Aluminum	Present
E	2010/7/6	D_2O*	Facing†	Aluminum	Water-filled‡

* Moderator tank was partially filled; estimated to 3 cm to 26 cm below top of tank.
† Acrylic blocks were placed around the inner perimeter of well.
‡ Shielding box was present but filled with pool water.
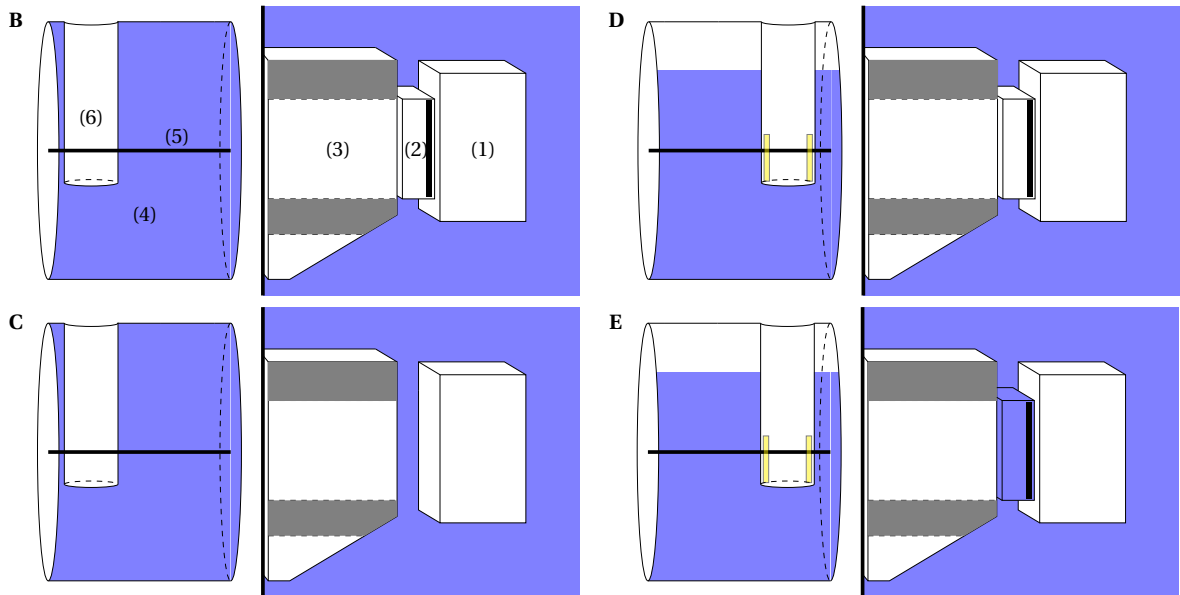
Figure 2.7:   Diagrams of test tank measurement configurations B, C, D, and E. Shown from right to left is the (1) reactor core, (2) shielding box, (3) nose port, and (4) test tank with (5) stringer shaft and (6) well.

gap at the top to mimic the UCN guide void. The water level in the tank was not well known because of uncertainty in the volume; it was estimated 16 cm to 30 cm from the top of the tank. The shielding box was present in both of these tests, but helium-filled (as normal) in the forth, and filled with reactor pool water in the fifth. Some analysis of the forth measurement is given in [116].

2.2.2 Gold foil activation method

The gold foil activation method for measuring thermal neutron fluxes is well known [6, 127]. Here I quickly cover the details important to this analysis. Gold is naturally a single isotope, is readily available chemically pure, and its neutron absorption cross-section is nearly the ideal $1/v$ dependence at low energy. These make it a logical choice for thermal neutron measurements. To exclude the influence of higher energy resonances, in particular the first resonance at 4.95 eV, typically measurements are made both with a bare gold foil and with a second foil shielded by cadmium. Cadmium-113 is a strong neutron absorber below the "cadmium cutoff" at 0.5 eV. The difference in activity of these two foils then indicates the thermal flux.

$$^{197}_{79}\text{Au} + \text{n} \rightarrow \ ^{198}_{79}\text{Au} \rightarrow \ ^{198}_{80}\text{Hg} + \text{e}^- + \gamma \tag{2.1}$$
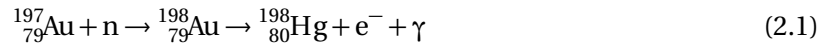
In a foil, ^{197}Au can capture a neutron to form ^{198}Au which then beta decays to ^{198}Hg with a half-life of 2.694 d, emitting primarily a 411.8 keV gamma (95.6%) in addition to 675.9 keV (0.81%) and 1087.7 keV (0.16%) gammas, Equation 2.1 [109]. After a period of irradiation, the foil is removed, and the products counted externally a few days later.

$$R = N_o \int \mathrm{d}E\, \sigma(E) \Phi(E) \tag{2.2}$$

The rate of neutron interaction in a target is given by Equation 2.2, where N_o is the initial number of target nuclei, $\sigma(E)$ is the reaction cross-section, and $\Phi(E)$ is the incident flux. Given a measurement of the rate, there can be many solutions for $\Phi(E)$. A single measurement is sufficient for a well understood flux, such as the thermalized flux from a reactor, but is not sufficient for unknown unique fluxes. The different cross-sections of multiple materials can be exploited to help define the shape of the spectrum, as has been done near the PULSTAR core [126]. Another approach is to assume an a priori solution, e.g. from MCNP, which is adjusted to be made consistent with the measured data. I begin by assuming the flux is thermalized to room temperature.

$$\frac{\mathrm{d}N}{\mathrm{d}t} = R - \lambda N \tag{2.3}$$

$$N(t_1) = \frac{R}{\lambda}\left(1 - \mathrm{e}^{-\lambda t_1}\right) \approx \frac{R}{\lambda}\lambda t_1 \tag{2.4}$$

Including the activity A (in disintegrations/s) of the product as $A = \lambda N$, the rate balance during irradiation is given in Equation 2.3, with the solution for an irradiation time of t_1 in Equation 2.4. N is the number of product nuclei and λ is the decay rate constant, related to the half-life by $t_{1/2} = \ln(2)/\lambda$. This can be approximated for $t_1 \ll t_{1/2}$.

$$C \approx A f f_E f_a t_3 e^{-\lambda t_2} \tag{2.5}$$

Some time after the end of irradiation t_2, the foils are moved to a detector and, in our case, the 411.8 keV gammas are counted for a period t_3. Given that the counting time is much less than the half life, $t_3 \ll t_{1/2}$, the total counts C is given in Equation 2.5. It is a fraction of the remaining activity A, the proportion of disintegrations giving 411.8 keV gammas (branching ratio) f, the detector efficiency including solid-angle f_E, and the self-shielding ratio f_a. Self-shielding is the decrease in neutron flux due to the finite size of the foil, roughly 0.94 for our gold foils. If the foil is embedded in a diffusive media, there can be a lowering of flux due to the neutron sink created by the foil. This is assumed to be a small effect in this geometry.

$$\Phi(E) \sim E \exp\left(-E/kT_o\right) \tag{2.6}$$

$$\frac{\sigma_a(E)}{\sigma_a^o} = \sqrt{\frac{kT_o}{E}} \tag{2.7}$$

$$\langle \sigma_a \rangle_\Phi = \frac{\int_0^\infty dE\, \sigma_a(E)\Phi(E)}{\int_0^\infty dE\, \Phi(E)} = \sigma_a^o \frac{\sqrt{\pi}}{2} \tag{2.8}$$

Assuming the neutron flux is well-thermalized, having a Maxwellian distribution at room temperature, Equation 2.6, and the capture cross-section is purely $1/v$, Equation 2.7, then the average neutron flux over the Maxwellian distribution, Equation 2.8, can be calculated in terms of the room-temperature cross-section, $\sigma_a^o = 98.70\,\mathrm{b}$ [109].

$$R_{\mathrm{th}} = \frac{m_{\mathrm{foil}} N_A}{M_{\mathrm{Au\text{-}197}}} \langle \sigma_a \rangle_\Phi \phi_{\mathrm{th}} \tag{2.9}$$

$$\phi_{\mathrm{th}} = \frac{C}{f f_E f_a t_3 e^{-\lambda t_2}} \ln(2) \frac{t_1}{t_{1/2}} \frac{2}{\sqrt{\pi}} \frac{M_{\mathrm{Au\text{-}197}}}{m_{\mathrm{foil}} N_A \sigma_a^o} \tag{2.10}$$

Then for the production of ^{198}Au by neutron capture in a well-thermalized room-temperature flux, Equation 2.2 gives Equation 2.9, where m_{foil} is the mass of the foil, $M_{\mathrm{Au\text{-}197}}$ is the atomic weight of ^{197}Au, $\langle \sigma_a \rangle$ is the neutron absorption cross-section of ^{197}Au averaged over a thermal Maxwellian distribution, and ϕ_{th} is the total thermal neutron flux. With Equation 2.5, we have an expression for the total thermal flux in terms of the detector count, Equation 2.10.
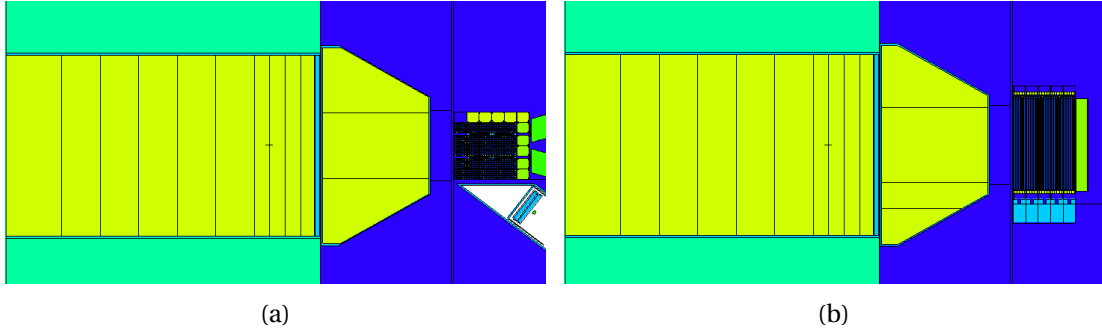
Figure 2.8: (a) Top and (b) side plots of MCNP geometry of the graphite thermal column.
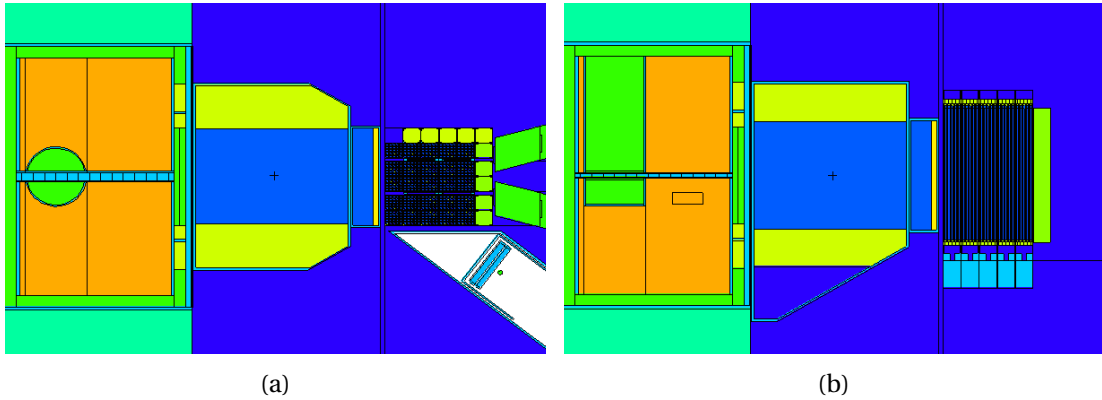
Figure 2.9: (a) Top and (b) side plots of MCNP geometry of the test tank. Here the well is orientated away from the reactor core.

2.2.3 MCNP model

As the geometry of the system, the UCN Source in particular, is too complex for a "paper" calculation, the neutron flux density in the thermal column was modeled using the Los Alamos MCNP6 Monte Carlo neutron transport code [44]. The NCSU Nuclear Reactor Program's detailed MCNP criticality calculation (KCODE) model of the PULSTAR reactor [168] was first used to repeat the analysis of the gold foil activation measurements done in the original graphite-filled thermal column. Details of those measurements are given in [173]. The geometry is shown in Figure 2.8

The model was then modified to include the geometry of the shielding box, nose port, and either the test geometry or UCN Source. The geometries are shown in Figure 2.9 and Figure 2.16. MCNP was run in simultaneous neutron and photon transport mode.

Except for solid methane as discussed in Chapter 3, the material cross-section data libraries used are all provided in the MCNP6 package, see Table 2.2. Thermal neutron interactions are described in the code by both a free gas model and an $S(\alpha, \beta)$ model where provided. A $S(\alpha, \beta)$ treatment was not used for aluminum; its use did not significantly change neutron tallies but did noticeably increase

24

Table 2.2:   MNCP material libraries used in the test geometry.

Material	Density (g/cm^3)	Thermal Library	Element	Library Identifier	Atomic Fraction
Lead	11.34	(NA)	Pb	82000.50c	1
Helium	0.000178	(NA)	^{5}He	2004.70c	1
Aluminum	2.699	(not used)	^{27}Al	13027.70c	1
Graphite	1.69	grph.20t	C	6000.70c	1
Air	0.00129	(NA)	C	6000.70c	0.02
			^{14}N	7014.70c	0.66
			^{16}O	8016.70c	0.32
Heavy Water	1.105	hwtr.20t	^{2}H	1002.70c	0.66667
			^{16}O	8016.70c	0.33333
Light Water	1	lwtr.20t	^{1}H	1001.70c	0.66667
			^{16}O	8016.70c	0.33333
Acrylic (PMMA, Lucite)	1.19	(NA)	^{1}H	1001.70c	0.534
			^{12}C	6012.70c	0.333
			^{16}O	8016.70c	0.133

run time. This structural aluminum was modeled as pure aluminum, although each component is certainly an alloy (e.g. 6061 which is as little as 95% aluminum). Graphite in the nose port is submerged in water, but this was assumed to have no effect. It was treated as pure graphite with typical reactor-grade density [105].

$$\frac{\Phi}{(\text{tally})} = P\frac{\bar{\nu}}{Q} = (1\,\text{MW})\left(\frac{2.46\,\text{n/fission}}{200\,\text{MeV/fission}}\right) = 7.68 \times 10^{16}\,\text{n/s} \tag{2.11}$$

MCNP tallies were converted to flux or current densities at a 1 MW steady-state reactor power level. The reactor power sets the rate of fissions, in terms of the energy released per fission, and the number of neutrons per fission is determined as part of the MCNP criticality calculation, roughly 2.46 neutrons per fission, Equation 2.11. The energy released per fission rises from 180 MeV at startup, to 200 MeV including delayed betas and gammas.

Surface detector tallies 1.27 cm–by–3.175 cm in size were placed down the length of the modeled stringer, following the existing geometry. Energy bin upper limits were 6.25×10^{-7} MeV, 5.53×10^{-3} MeV, 0.821 MeV, and 20 MeV. The model was run with 250 million neutron histories.
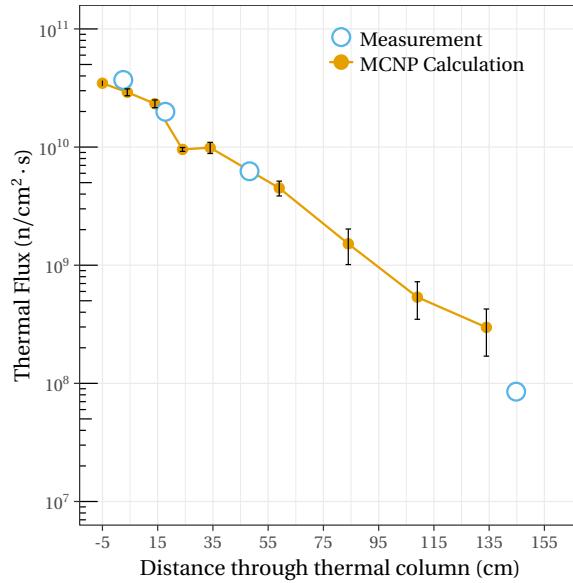
Figure 2.10:   Thermal fluxes through the graphite thermal column.

2.2.4   Results

The gold foil activation measurements of the original graphite-filled thermal column agree well with the MCNP model, Figure 2.10. This confirms the MCNP model of the reactor behaves as expected. Results from the test tank geometries are shown in Figure 2.11. While there was good agreement between the shapes of the test tank measurements and MCNP calculated fluxes, MCNP fluxes for geometries B and D are roughly 15% greater, and geometries C and E roughly 5% greater, than fluxes calculated from the measurements.

The neutron energy spectrum along the neutron transport system as calculated by MCNP both with and without the shielding box are shown in Figure 2.12 and Figure 2.13 respectively. Unlike the original thermal column measurements, neutron fluxes measured with the test tank have not completely reached thermal equilibrium. This affects our thermal flux as calculated from the gold foil activity in two ways. Both of these effects are greater in the geometries with the helium-filled shielding box than in the geometries with water.

There are a significant number of epithermal neutrons below the cadmium cutoff, and so our assumption of Maxwellian distribution used in calculating the average cross-section in Equation 2.8 is not true. Instead, the average cross-section can be calculated numerically using the MCNP neutron energy spectrum. Using the spectra from Figure 2.12, this lowers the average cross-section from 87.40 b to 77 b at the front of the tank and to 83 b at 50 cm inside the tank. The correction for geometry B is shown in Figure 2.11.
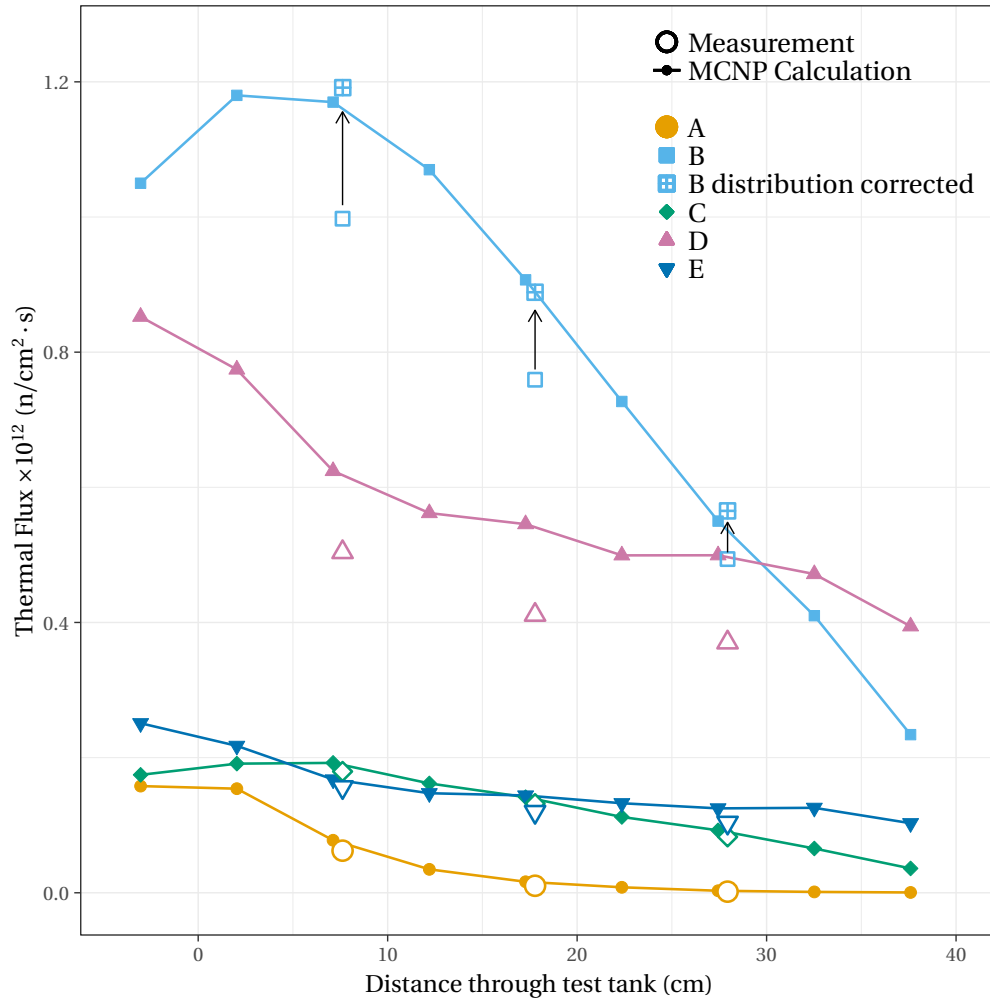
Figure 2.11: Thermal fluxes through the test tank. Fluxes calculated from the foil measurements assuming Maxwellian distribution are given by open symbols at the locations of the cadmium-shielded foils, 7.62 cm, 17.78 cm, and 27.94 cm. MCNP calculated fluxes binned from 0 to 0.625 eV are given by the solid symbols. For geometry B only, the foil measurement has been corrected using the MCNP-calculated flux energy distribution.

27
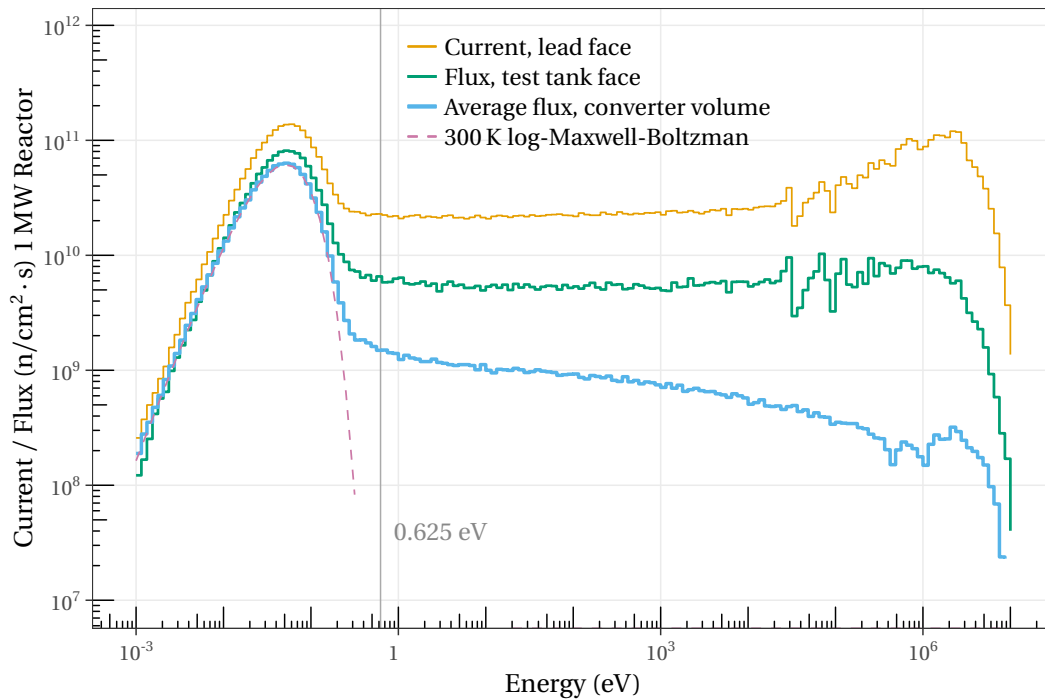
Figure 2.12:   Neutron energy spectra for geometry B, with shielding box, at three different locations along the neutron transport system. Neutron current is tallied at the shielding box lead plate facing the reactor core, representing flux streaming in the direction of the test tank. Neutron flux is tallied at the face of the test tank. Flux is averaged over the 1 L volume corresponding to the location of the UCN converter within the heavy water. There are sixteen logarithmic-width bins per decade, similar to flux per unit "lethargy," exaggerating higher energies over a linear axis plot. MCNP estimated statistical error is too small to be plotted.

Also, the ratio of fast and epithermal to thermal neutrons will decrease along the length of the tank. The activity of the shielded foils is subtracted from the interpolation of the activity of the unshielded foils to calculate the neutron flux less than the cadmium cutoff. This will tend to overestimate the number of fast neutrons, as the proportion of thermal neutrons is increasing as the total flux falls. MCNP suggests this effect is small when interpolating from the four positions of the bare foils to the three positions of the shielded foils, but not when extrapolating from the shielded foils to the bare foils. Practically this reduces the measurement points.
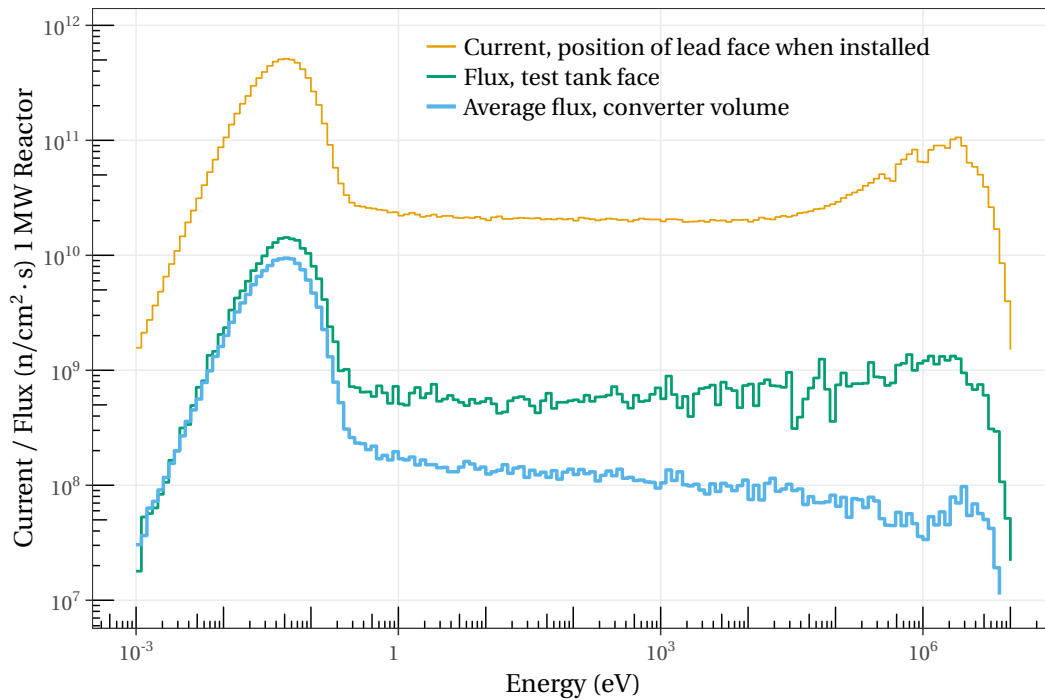
Figure 2.13: Neutron energy spectra for geometry C, without shielding box, at three locations along the neutron transport system. Plot details are the same as Figure 2.12.

2.2.5 Discussion

With the gold foil measurements adjusted for the non-thermal spectra, the MCNP calculations give the magnitude of the flux to within a percent. Experimentally, there is a water-filled gap between the shielding box and reactor core that is difficult to measure. This gap may be up to 2 cm thicker than designed, decreasing the real flux by up to 5%. The height of the heavy water in geometries D and E was uncertain, which can also affect the measured flux by a few percent. The calibration of reactor power, used to normalize MCNP tallies in Equation 2.11 may also not be sufficiently precise as used.

With the test tank filled with heavy water, and the well orientated away from the reactor core, we can judge the effectiveness of the neutron transport system in delivering neutrons to the UCN Source. The thermal neutron flux at the entrance to the heavy water was measured to be $1.1 \times 10^{12} \, \mathrm{n/cm^2 \cdot s}$, 30 times larger than the flux at entrance to the former graphite column with graphite nosepiece. The geometry with the heavy water-filled test tank oriented with the well facing the reactor core shows a 40% reduction of thermal neutron flux, which is expected due to the void of the Source cryostat.

29
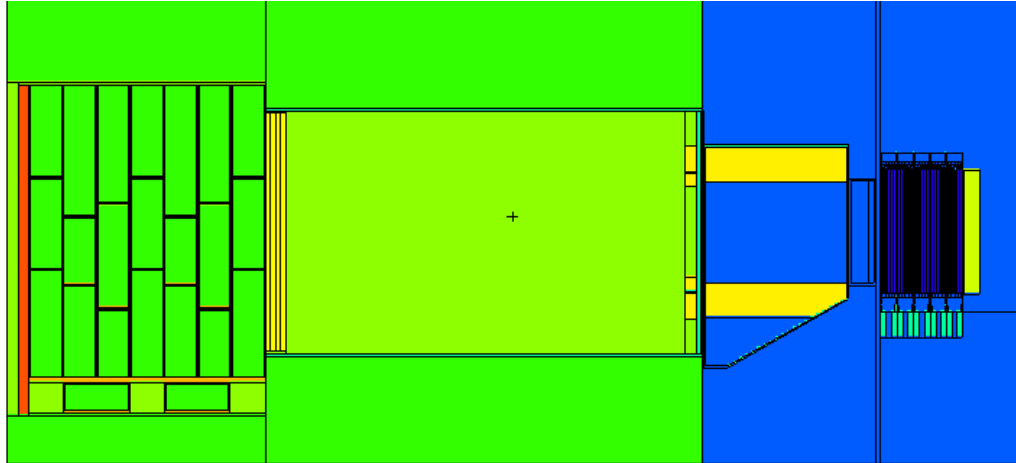
Figure 2.14: MCNP geometry of the shield cart, including borated polyethylene sheets in yellow, possibly present but water-filled nose port, and potentially necessary lead bricks in orange.

These tests also underscore the importance of the shielding box. Comparing geometry B to C, the 12.7 cm (5 inch) of water reduces the thermal flux by 80% and the epithermal flux by an order of magnitude. If it can be determined there is a water-filled gap between the shielding box and reactor core, it is worth eliminating.

To suggest an alternative approach to this analysis, the gold cross-section is well known at higher energies and MCNP could be used to calculate the activity of both shielded and bare gold foils directly at all seven positions. This would eliminate the errors in both interpolation between, and fluxes calculated from, the gold foil measurements, leaving only MCNP calculation and experimental errors.

2.3   Temporary shield door

Now that we have confidence in our MCNP model, it can be used to confirm the performance of radiation shielding. The UCN Source will be mounted to the thermal column shield door. We will continue to need access to the Source, however this door must remain closed for reactor operations. This limitation was not addressed in the original design. We designed and constructed a "shield cart" that can temporarily replace the shielding provided by the shield door. It will be lowered onto the shield door's tracks and rolled into the thermal column ahead of the Source.

MCNP was used to tally both neutrons and gammas along the thermal column. We assume the REPs will be installed instead of the shielding box, and these can be treated as water. This is the conservative choice; the lead plate in the water-filled shielding box could improve shielding. The nose port could potentially be removed if doing so lowered the shielding requirements.
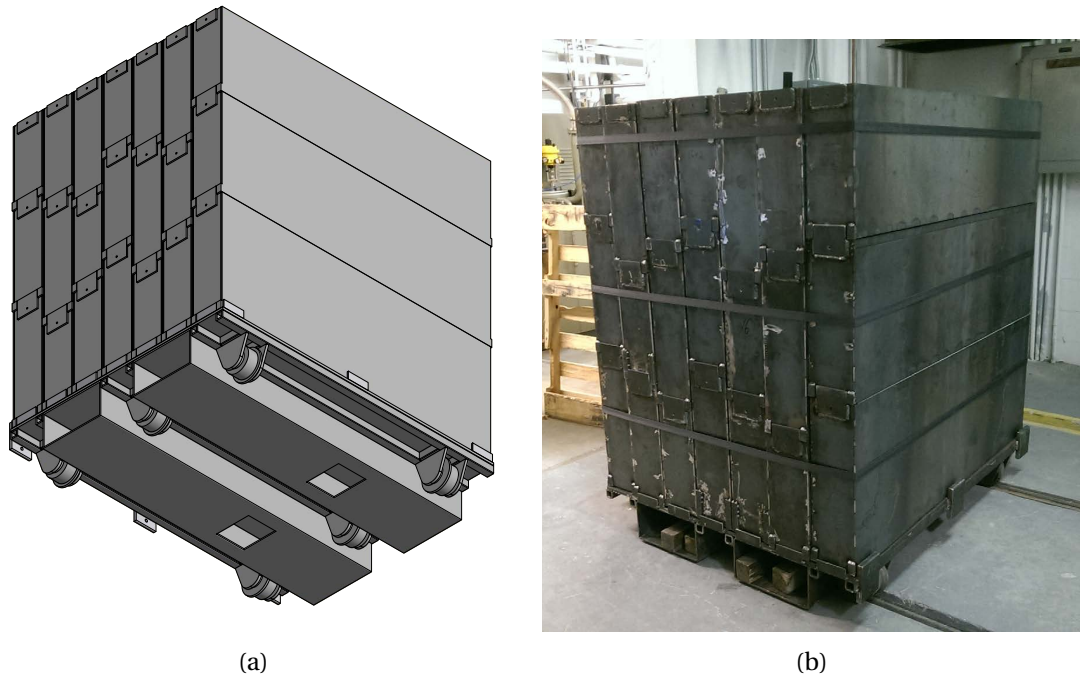
Figure 2.15:   (a) A CAD drawing of the temporary shield cart from below and (b) a photo during assembly, prior to adding concrete.

Without the nose port or shielding box, MCNP shows MeV-energy neutrons, streaming through water, are the main source of neutrons, tallied as 10^4 n/cm²·s at the graphite webbing. With the nose port, thermal neutrons dominate, 10^8 n/cm²·s at the graphite webbing. The graphite in the nose port provides slightly more gamma attenuation than the water, 10^{10} γ/cm²·s at the graphite webbing without the nose port, but it is preferable to remove the nose port for better neutron attenuation.

Shields were iteratively modeled in MCNP. The final design is shown in Figure 2.14. The shield reduces the equivalent dose immediately outside the shield from neutrons and gammas combined to <0.1 mSv (<10 mrem). Because the criticality calculation is computation intensive, and the fluxes relevant to safety are orders of magnitude lower than typical Source operation, the current model is insufficient. One potential solution is to use the surface-write functionality to record all tallies (SSW to RSSA file) which can then be repeatedly reproduced. However, this operation can not be easily multi-threaded, making it intractable on the available computer. Instead, the tallies were approx-
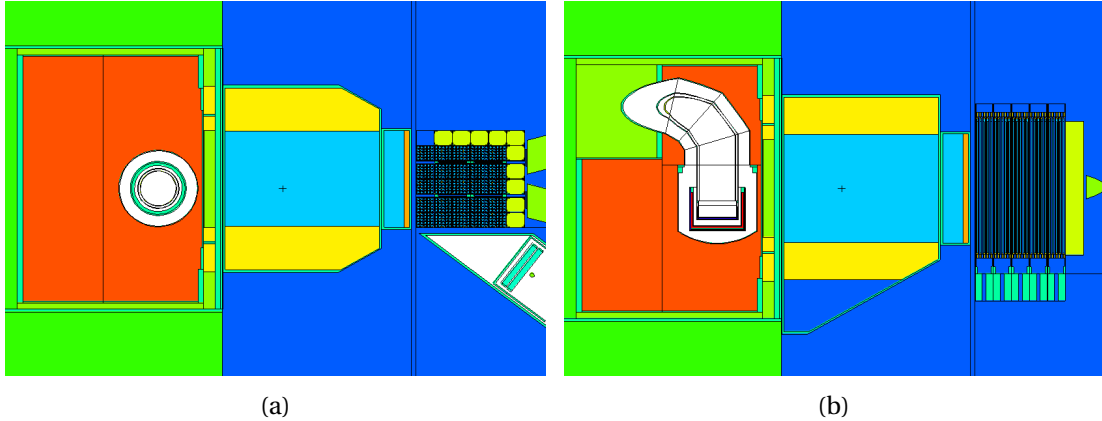
Figure 2.16: (a) Top and (b) side plots of the MCNP geometry of the UCN Source.

imated as fixed sources (SDEF). All high energy neutrons were defined conservatively at 10 MeV, moving parallel to the thermal column. Gammas were also defined conservatively at the maximum energy of several recorded bins, again emitted parallel to the thermal column. The shielding performance was verified with a paper calculation.

The limited distance to the mechanical room wall, with the Source helium transfer line installed, provides only approximately 8 inches clearance between the Source and the reactor biological shield. The supporting cart was designed to fit underneath the Source. Iron-filled concrete boxes 6.5 inches in width, interlocking by tongue-and-groove, can be stacked in this gap as the cart is rolled into the thermal column, Figure 2.15. Contingencies were made to add borated polyethylene sheets if further neutron reduction is required, and lead bricks if gamma shielding is insufficient. This shielding does not account for concrete blocks currently stacked inside thermal column as of this writing, which may not be present in the future.

2.4 Source model

With the MCNP model now benchmarked within an acceptable tolerance, the UCN Source geometry was included, and the reactor core was updated to its current configuration, Figure 2.16. In particular, core reflectors changed from one graphite reflector and one beryillium, to both beryillium.

The solid deuterium volume was left as vacuum. Although a solid deuterium scattering library is under development [45–47], it has not been as rigorously tested as the other thermal libraries. Liquid ortho-deuterium at 19 K is a better cold moderator than solid deuterium. While ℓD_2 showed further moderation of the neutron flux, it was not dramatic, so the effect of sD_2 was assumed to be small.
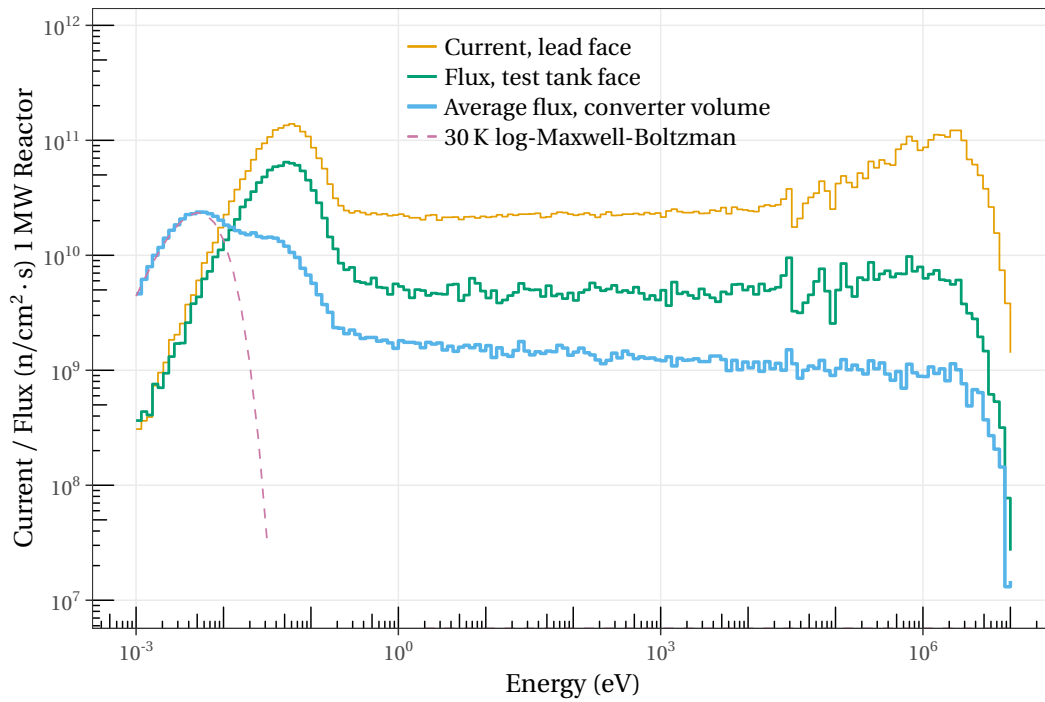
Figure 2.17: Neutron energy spectra for the Source geometry, with shielding box, at three different locations along the transport system. Plot details are the same as Figure 2.12.

The neutron energy spectrum is tallied inside the converter volume, Figure 2.17. The total thermal flux is 5.4×10^{11} n/cm²·s, and the total flux less than 24 meV is 4×10^{11} n/cm²·s, in line with the initial calculations [78]. This spectrum folded with the production cross section from A. Frei *et al.* [35] gives a production rate density in the solid deuterium of 6×10^3 UCN/cm³/s.

Chapter 3

Cold Neutrons and UCN Production

3.1 Introduction

In this chapter, I first quickly cover the formalism of thermal neutron scattering. Although this subject is well-covered in many textbooks [97, 117, 148, 152, 164], I discuss it in the context of multi-phonon incoherent scattering in solid methane and UCN production in solid deuterium.

In addition to the total neutron flux reaching the UCN converter, the UCN yield also depends on the energy-dependent UCN-production cross section of the converter material. By varying the temperature of the cold moderator, we have some freedom to match the incident neutron energy spectrum to the production cross-section. To model this temperature dependence in our MCNP model developed in Chapter 2, it was necessary to create scattering libraries in the Evaluated Nuclear Data Files (ENDF) format [22] over a range of temperatures using the "NJOY" Nuclear Data Processing System [101].

I then examine neutron scattering in solid deuterium, which is necessary to model both UCN production in deuterium (UCN creation by neutron downscattering) and the lifetime of UCN in deuterium (UCN loss by neutron upscattering). The cold neutron fluxes can then be folded with the the deuterium UCN-production cross section to model temperature-dependent UCN production in solid deuterium.

3.1.1 Neutron scattering

The strength of the following formalism is that it allows us to combine limited neutron scattering data with information about the target's molecular dynamics to extrapolate neutron scattering across the conditions of interest. We begin with a general rate equation and then simplify components based upon what we know or can approximate about the scattering system.

A neutron with initial momentum $\vec{\mathbf{k}}_o$, initial energy E_o, and wavefunction ψ_o at $\vec{\mathbf{r}}$ scatters off a target with initial state χ_o and initial energy E_{χ_o} at $\vec{\mathbf{R}}$, to a final momentum $\vec{\mathbf{k}}_f$, final energy E_f, and final wavefunction ψ_f, leaving the target in final state χ_f with energy E_{χ_f}. For convenience, $\vec{\mathbf{Q}} = \vec{\mathbf{k}}_o - \vec{\mathbf{k}}_f$ and $\epsilon = \hbar\omega = E_o - E_f$.

I follow the usual definitions. The total cross-section σ is the rate R of scatter per incident flux Φ per number of target particles N. From here forward, I assume the microscopic cross-section, given per target molecule, and drop the $1/N$. The differential cross-section is the rate into a solid angle $\mathrm{d}\Omega$, and the double-differential cross-section additionally into the final energy range E_f to $E_f + \mathrm{d}E_f$.

$$\sigma_{\text{total}} = \frac{R}{\Phi N} \tag{3.1}$$

$$\frac{\mathrm{d}\sigma}{\mathrm{d}\Omega} = \int_0^\infty \mathrm{d}E_f \left(\frac{\mathrm{d}^2\sigma}{\mathrm{d}\Omega\, \mathrm{d}E_f} \right) \tag{3.2}$$

$$V(\vec{\mathbf{r}}) = \left(\frac{2\pi\hbar^2}{m_n} \right) b\, \delta^3(\vec{\mathbf{r}}) \tag{3.3}$$

$$\psi = \mathrm{e}^{i\vec{\mathbf{k}}\cdot\vec{\mathbf{r}}} - \frac{b}{r}\mathrm{e}^{ikr} \tag{3.4}$$

$$\frac{\mathrm{d}\sigma}{\mathrm{d}\Omega} = \left(\frac{m_n}{2\pi\hbar^2} \right)^2 \left| \int \mathrm{d}\vec{\mathbf{r}}\, V(\vec{\mathbf{r}}) \mathrm{e}^{i\vec{\mathbf{Q}}\cdot\vec{\mathbf{r}}} \right|^2 = b^2 \tag{3.5}$$

$$\sigma_{\text{total}} = 4\pi b^2 \tag{3.6}$$

As the neutron interacts only through very short-range nuclear forces, at low energy it is a good approximation to treat only the spherically-symmetric S-wave scattering. Under this condition, the scattering potential may be replaced with a delta-function at the origin. For a plane wave, $\psi = \exp\left(i\vec{\mathbf{k}}\cdot\vec{\mathbf{r}} \right)$ scattering from a single fixed nucleus, that is $\chi_o = \chi_f$, $k_o = k_f$, with a delta-function potential, the outgoing wave is spherical and the total wavefunction is given in Equation 3.4. The amplitude b, called the total scattering length, is chosen such that the total cross section agrees with the cross-section of a hard sphere of radius b. The scattering length typically must be measured in lieu of a full nuclear theory.

$$V(\vec{\mathbf{r}} - \vec{\mathbf{R}}_\ell) = \left(\frac{2\pi\hbar^2}{m_n} \right) b_\ell\, \delta^3(\vec{\mathbf{r}} - \vec{\mathbf{R}}_\ell) \tag{3.7}$$

This delta-fuction potential is called the "Fermi pseudopotential," and it can be extended to a system of scatterers, Equation 3.7, where $\vec{\mathbf{R}}_\ell$ is the vector to the nucleus at the ℓth location. The scattering length, b_ℓ, is the "bound" scattering length corresponding to a fixed nucleus. To account for recoil, we treat the center-of-mass of the scattering system and the bound scattering length is related to the scattering length of a nucleus "free" to recoil by replacing the mass with the reduced mass.

$$\text{(transition rate)} = \frac{2\pi}{\hbar} \left| \left\langle \text{final} \left| \widehat{\mathbf{H}}' \right| \text{initial} \right\rangle \right|^2 \times \text{(phase space)} \tag{3.8}$$

$$\left(\frac{\mathrm{d}\sigma}{\mathrm{d}\Omega} \right)_{\chi_o \to \chi_f} = \frac{1}{\Phi} \frac{1}{\mathrm{d}\Omega} \frac{2\pi}{\hbar} \left| \left\langle \psi_f \chi_f \left| \widehat{\mathbf{H}}' \right| \psi_o \chi_o \right\rangle \right|^2 \rho_{\vec{\mathbf{k}}_f}$$

$$\left(\frac{\mathrm{d}^2\sigma}{\mathrm{d}\Omega\,\mathrm{d}E_f} \right)_{\chi_o \to \chi_f} = \frac{k_f}{k_o} \left(\frac{m_n}{2\pi\hbar^2} \right)^2 \left| \left\langle \psi_f \chi_f \left| \widehat{\mathbf{V}} \right| \psi_o \chi_o \right\rangle \right|^2 \delta(E_{\chi_o} - E_{\chi_f} + \hbar\omega) \tag{3.9}$$

"Fermi's Golden Rule," which is a first-order perturbation approximation derived in quantum mechanics [130], gives the transition probability between states as the interaction amplitude and density of states $\rho_{\vec{\mathbf{k}}_f}$, Equation 3.8. A statement of this rule is made for the scattering cross-section, Equation 3.9, with the delta-function given by the conservation of energy.

$$\left(\frac{\mathrm{d}^2\sigma}{\mathrm{d}\Omega\,\mathrm{d}E_f} \right)_{\chi_o \to \chi_f} = \frac{k_f}{k_o} \left| \sum_\ell b_\ell \left\langle \chi_f \left| \mathrm{e}^{\mathrm{i}\vec{\mathbf{Q}} \cdot \vec{\mathbf{R}}_\ell} \right| \chi_o \right\rangle \right|^2 \delta(E_{\chi_o} - E_{\chi_f} + \hbar\omega) \tag{3.10}$$

$$= \frac{k_f}{k_o} \sum_{\ell_1 \ell_2} b_j b_q \left\langle \chi_o \left| \mathrm{e}^{\mathrm{i}\vec{\mathbf{Q}} \cdot \vec{\mathbf{R}}_{\ell_1}} \right| \chi_f \right\rangle \left\langle \chi_f \left| \mathrm{e}^{\mathrm{i}\vec{\mathbf{Q}} \cdot \vec{\mathbf{R}}_{\ell_2}} \right| \chi_o \right\rangle$$

$$\times \left(\frac{1}{2\pi\hbar} \right) \int_{-\infty}^{\infty} \mathrm{d}t \, \mathrm{e}^{-\mathrm{i}\omega t} \mathrm{e}^{\mathrm{i}\left(E_{\chi_f} - E_{\chi_o} \right) t / \hbar} \tag{3.11}$$

The usual formulation is to begin integrating the matrix element in Equation 3.9, using this pseudopotential, with respect to the neutron's coordinates $\vec{\mathbf{r}}$, Equation 3.10. Assuming the initial and final neutrons are unpolarized, and their wave functions are plane waves, the matrix element's dependence on ψ_o and ψ_f drops out. The energy delta-function is expressed as an integral over time. The square of the matrix element is expanded as a double-sum and given in Equation 3.11.

$$p_\chi = \left(\frac{1}{\sum_{\chi_i} \mathrm{e}^{E_{\chi_i}/k_{\mathrm{B}}T}} \right) \mathrm{e}^{E_\chi/k_{\mathrm{B}}T} \tag{3.12}$$

$$\langle A \rangle_T = \sum_{\chi_o} p_{\chi_o} \langle \chi_o | A(x) | \chi_o \rangle = \int_{-\infty}^{\infty} \mathrm{d}x\, A(x) f(x) \tag{3.13}$$

Finally, we do not measure the cross-section for a specific $\chi_o \to \chi_f$ transition, we measure a sum of the final states for each initial state. The collection of target particles are initially in a mixture of accessible states, each state with a weight of p_χ. This probability distribution is typically Maxwell-Boltzman, Equation 3.12, for a scattering system at temperature T. This thermal averaging is often abbreviated in notation (or ignored entirely). When I do, I will abbreviate as $\langle A \rangle_T$ for an arbitrary function $A(x)$. This average can be also be expressed as the integral of a probability function, Equation 3.13.

$$\frac{\mathrm{d}^2\sigma}{\mathrm{d}\Omega\,\mathrm{d}E_f} = \frac{k_f}{k_o} \left(\frac{1}{2\pi\hbar} \right) \sum_{\ell_1 \ell_2} b_{\ell_1} b_{\ell_2}$$

$$\times \int_{-\infty}^{\infty} \mathrm{d}t\, \mathrm{e}^{-\mathrm{i}\omega t} \sum_{\chi_o} p_{\chi_o} \sum_{\chi_f} \left\langle \chi_o \left| \mathrm{e}^{\mathrm{i}\vec{\mathbf{Q}} \cdot \vec{\mathbf{R}}_{\ell_1}(0)} \right| \chi_f \right\rangle \left\langle \chi_f \left| \mathrm{e}^{i\widehat{\mathbf{H}} t/\hbar} \mathrm{e}^{\mathrm{i}\vec{\mathbf{Q}} \cdot \vec{\mathbf{R}}_{\ell_2}(0)} \mathrm{e}^{-i\widehat{\mathbf{H}} t/\hbar} \right| \chi_o \right\rangle$$

$$\tag{3.14}$$

$$\frac{\mathrm{d}^2\sigma}{\mathrm{d}\Omega\,\mathrm{d}E_f} = \frac{k_f}{k_o} \left(\frac{1}{2\pi\hbar} \right) \sum_{\ell_1 \ell_2} b_{\ell_1} b_{\ell_2} \int_{-\infty}^{\infty} \mathrm{d}t\, \mathrm{e}^{-\mathrm{i}\omega t} \sum_{\chi_o} p_{\chi_o} \left\langle \chi_o \left| \mathrm{e}^{-\mathrm{i}\vec{\mathbf{Q}} \cdot \vec{\mathbf{R}}_{\ell_1}(0)} \mathrm{e}^{\mathrm{i}\vec{\mathbf{Q}} \cdot \vec{\mathbf{R}}_{\ell_2}(t)} \right| \chi_o \right\rangle \tag{3.15}$$

Bringing the matrix element inside the time integral and expressing the energy-dependence as the Hamiltonian gives Equation 3.14. This is referred to as the "Van Hove" formalism, having first been presented by L. Van Hove [166]. Using the completeness of states on the sum over χ_f, $\left| \chi_f \right\rangle\!\left\langle \chi_f \right| = 1$, and applying the Hamiltonian to $\vec{\mathbf{R}}_j$ gives Equation 3.15. This is an expression of the scattering in terms of the position of nucleus ℓ_1 at $t = 0$ and of the position of nucleus ℓ_2 at time t.

3.1.2 Coherent and incoherent scattering

Given a system with multiple scattering lengths b_i, each occurring with a probability of f_i, the scattering lengths in Equation 3.15 can be replaced with the average $\overline{b}$. Assuming there's no correlation between the scattering lengths of different nuclei, we can use the identities in Equation 3.16 and Equation 3.17 to split the differential cross-section into two components, coherent and incoherent as in Equation 3.18. Integrated, the total coherent and incoherent cross-sections are given in Equation 3.19. The incoherent part gives scattering due to correlations between only the same nuclei to themselves over time (sum over ℓ), while the coherent part includes correlations between

different nuclei over time (sum over ℓ_1 and ℓ_2) which can give rise to interference effects.

$$\sum_i f_i = 1 \quad \text{and} \quad \overline{b} = \sum_i b_i f_i \quad \text{and} \quad \overline{b^2} = \sum_i b_i^2 f_i \tag{3.16}$$

$$\overline{b_{\ell_1} b_{\ell_2}} = \begin{cases} (\overline{b})^2 & \text{for} \quad \ell_1 \neq \ell_2 \\ \overline{b^2} & \text{for} \quad \ell_1 = \ell_2 \end{cases} \tag{3.17}$$

$$\frac{d^2\sigma}{d\Omega\, dE_f} = \frac{k_f}{k_o}\left(\frac{1}{2\pi\hbar}\right)(\overline{b})^2 \sum_{\ell_1\ell_2} \int_{-\infty}^{\infty} dt\, e^{-i\omega t} \sum_{\chi_o} p_{\chi_o} \left\langle \chi_o \left| e^{-i\vec{\mathbf{Q}}\cdot\vec{\mathbf{R}}_{\ell_1}(0)} e^{i\vec{\mathbf{Q}}\cdot\vec{\mathbf{R}}_{\ell_2}(t)} \right| \chi_o \right\rangle$$

$$+ \frac{k_f}{k_o}\left(\frac{1}{2\pi\hbar}\right)\left(\overline{b^2}-(\overline{b})^2\right) \sum_{\ell} \int_{-\infty}^{\infty} dt\, e^{-i\omega t} \sum_{\chi_o} p_{\chi_o} \left\langle \chi_o \left| e^{-i\vec{\mathbf{Q}}\cdot\vec{\mathbf{R}}_{\ell}(0)} e^{i\vec{\mathbf{Q}}\cdot\vec{\mathbf{R}}_{\ell}(t)} \right| \chi_o \right\rangle \tag{3.18}$$

$$= \left(\frac{d^2\sigma}{d\Omega\, dE_f}\right)_{\text{coh}} + \left(\frac{d^2\sigma}{d\Omega\, dE_f}\right)_{\text{inc}}$$

$$\sigma_{\text{coh}} = 4\pi(\overline{b})^2$$
$$\sigma_{\text{inc}} = 4\pi\left(\overline{b^2}-(\overline{b})^2\right) \tag{3.19}$$

$$\left(\frac{d^2\sigma}{d\Omega\, dE_f}\right)_{\text{coh/inc}} = \frac{\sigma_{\text{coh/inc}}}{4\pi} \frac{k_f}{k_o} S_{\text{coh/inc}}(\vec{\mathbf{Q}},\omega) \tag{3.20}$$

It is common to define correlation functions describing parts of this interaction with identified physical meaning. The time-dependent thermal average under the integral is called the intermediate function, $I(\vec{\mathbf{Q}},t)$. The pair-correlation function $G(\vec{\mathbf{r}},t)$ is its Fourier transform in space and the scattering function $S(\vec{\mathbf{Q}},\omega)$ its Fourier transform in time. The coherent scattering function and the incoherent scattering function will be used here often. They are defined in Equation 3.20 in terms of Equation 3.18 and Equation 3.19. (It is also referred to as the dynamic structure function and dynamical response function).

3.1.3 Scattering in solids

Having now developed a description of scattering, we need to relate it to the molecular dynamics. For atoms in a solid, a good approximation is to assume each atom has a well-defined equilibrium position during the measurement. (This notably excludes solids like hydrogen and deuterium where atoms have significant quantum motion.) For a crystal with high periodicity, an additional simplification can be made. The position of the atom in a Bravis crystal is given in Equation 3.21, where $\vec{\ell}$ is the position of the ℓth unit cell and $\vec{\mathbf{u}}_\ell$ is the time-dependent displacement of the atom from its equilibrium position. In normal crystallography notation, $\vec{\ell}$ is a vector were each direction is indexed over integer values, e.g. $\vec{\ell} = h\hat{\mathbf{a}}_1 + k\hat{\mathbf{a}}_2 + \ell\hat{\mathbf{a}}_3$, but $\vec{\ell}$ has been given an index here to emphasize this sum and remain consistent with the other indexed sums. (This can be extended to non-Bravis crystals by defining $\vec{\mathbf{R}}_{\ell d}(t) = \vec{\ell}_\ell + \vec{\mathbf{d}}_d + \vec{\mathbf{u}}_{\ell d}(t)$ where $\vec{\mathbf{d}}$ is the equilibrium position of the dth atom within the unit cell.) In Equation 3.22, each term in the ℓ_1 sum is the same, and in Equation 3.23, each term in the ℓ sum is the same, so these may be replaced with the total number of atoms in the unit crystal N_u.

$$\vec{\mathbf{R}}_\ell(t) = \vec{\ell}_\ell + \vec{\mathbf{u}}_\ell(t) \tag{3.21}$$

$$S_{\text{coh}}(\vec{\mathbf{Q}}, \omega) = \frac{1}{2\pi\hbar} \sum_{\ell_1 \ell_2} e^{-i\vec{\mathbf{Q}}\cdot(\vec{\ell}_{\ell_1} - \vec{\ell}_{\ell_2})} \int_{-\infty}^{\infty} dt\, e^{-i\omega t} \sum_{\chi_o} p_{\chi_o} \left\langle \chi_o \left| e^{-i\vec{\mathbf{Q}}\cdot\vec{\mathbf{u}}_{\ell_1}(0)} e^{i\vec{\mathbf{Q}}\cdot\vec{\mathbf{u}}_{\ell_2}(t)} \right| \chi_o \right\rangle$$

$$= N_u \frac{1}{2\pi\hbar} \sum_\ell e^{i\vec{\mathbf{Q}}\cdot\vec{\ell}} \int_{-\infty}^{\infty} dt\, e^{-i\omega t} \sum_{\chi_o} p_{\chi_o} \left\langle \chi_o \left| e^{-i\vec{\mathbf{Q}}\cdot\vec{\mathbf{u}}_0(0)} e^{i\vec{\mathbf{Q}}\cdot\vec{\mathbf{u}}_\ell(t)} \right| \chi_o \right\rangle \tag{3.22}$$

$$S_{\text{inc}}(\vec{\mathbf{Q}}, \omega) = \frac{1}{2\pi\hbar} \sum_\ell e^{-i\vec{\mathbf{Q}}\cdot(\vec{\ell}_\ell - \vec{\ell}_\ell)} \int_{-\infty}^{\infty} dt\, e^{-i\omega t} \sum_{\chi_o} p_{\chi_o} \left\langle \chi_o \left| e^{-i\vec{\mathbf{Q}}\cdot\vec{\mathbf{u}}_\ell(0)} e^{i\vec{\mathbf{Q}}\cdot\vec{\mathbf{u}}_\ell(t)} \right| \chi_o \right\rangle$$

$$= N_u \frac{1}{2\pi\hbar} \int_{-\infty}^{\infty} dt\, e^{-i\omega t} \sum_{\chi_o} p_{\chi_o} \left\langle \chi_o \left| e^{-i\vec{\mathbf{Q}}\cdot\vec{\mathbf{u}}_0(0)} e^{i\vec{\mathbf{Q}}\cdot\vec{\mathbf{u}}_0(t)} \right| \chi_o \right\rangle \tag{3.23}$$

$$\vec{\mathbf{u}}_\ell(t) = \sqrt{\frac{\hbar}{2M_\ell N_u}} \sum_{j,q} \frac{\vec{\mathbf{e}}_{jq}}{\sqrt{\omega_{jq}}} \left(\hat{\mathbf{a}}_j e^{-i\vec{\mathbf{q}}_q \cdot \vec{\ell}_\ell} + \hat{\mathbf{a}}_j^\dagger e^{i\vec{\mathbf{q}}_q \cdot \vec{\ell}_\ell} \right) \tag{3.24}$$

We can assume the restoring force is a linear, that is, that the atoms are harmonic oscillators with frequencies ω_n. The well-known properties of the harmonic oscillator greatly simplifies evaluation. The displacements $\vec{\mathbf{u}}_\ell$ are a superposition of the displacements of the $3N_u$ oscillator modes, and can be written in terms of each modes' creation and annihilation operators, $\hat{\mathbf{a}}_j^\dagger$ and $\hat{\mathbf{a}}_j$, as Equation 3.24 where $\vec{\mathbf{e}}_j$ is the polarization of the jth oscillator mode, j=1,2,3. $\vec{\mathbf{q}}$ is the wavevector for each normal

mode, $q = 1 \ldots N_u$. (A more consistent but awkward notation might be $\vec{\mathbf{q}} = \vec{\mathbf{k}}_\chi$.)

$$f(x) \propto \exp\left[-x^2\left(\frac{\hbar}{M\omega}\coth\left(\frac{\hbar\omega}{2k_\mathrm{B}T}\right)\right)^{-1}\right] \quad \text{where} \quad \int_{-\infty}^{\infty}\mathrm{d}x\, f(x) = 1 \tag{3.25}$$

$$\left\langle \mathrm{e}^A \right\rangle_T = \exp\left(\frac{1}{2}\left\langle A^2 \right\rangle_T\right) \tag{3.26}$$

$$\left\langle \mathrm{e}^{-\mathrm{i}\vec{\mathbf{Q}}\cdot\vec{\mathbf{u}}_0(0)}\mathrm{e}^{\mathrm{i}\vec{\mathbf{Q}}\cdot\vec{\mathbf{u}}_\ell(t)} \right\rangle_T = \exp\left[\left\langle -\left(\vec{\mathbf{Q}}\cdot\vec{\mathbf{u}}_0(0)\right)^2 \right\rangle_T\right]\exp\left[\left\langle \left(\vec{\mathbf{Q}}\cdot\vec{\mathbf{u}}_0(0)\right)\left(\vec{\mathbf{Q}}\cdot\vec{\mathbf{u}}_\ell(t)\right) \right\rangle_T\right] \tag{3.27}$$

Assuming the probability of states is a Maxwellian distribution, the thermal average probability function is Gaussian for a harmonic oscillator, Equation 3.25. This allows the identity given in Equation 3.26, allowing the thermal average in Equation 3.22 to be rewritten as a product of exponentials, Equation 3.27.

$$2W(\vec{\mathbf{Q}}) = \left\langle \left(\vec{\mathbf{Q}}\cdot\vec{\mathbf{u}}_0(0)\right)^2 \right\rangle_T \tag{3.28}$$

$$\mathrm{S}_{\mathrm{coh}}(\vec{\mathbf{Q}},\omega) = \frac{N_u}{2\pi\hbar}\mathrm{e}^{-2W(\vec{\mathbf{Q}})}\sum_\ell \mathrm{e}^{\mathrm{i}\vec{\mathbf{Q}}\cdot\vec{\ell}}\int_{-\infty}^{\infty}\mathrm{d}t\,\mathrm{e}^{-\mathrm{i}\omega t}\sum_{\chi_o}p_{\chi_o}\left\langle \chi_o\left|\mathrm{e}^{\left(\vec{\mathbf{Q}}\cdot\vec{\mathbf{u}}_0(0)\right)\left(\vec{\mathbf{Q}}\cdot\vec{\mathbf{u}}_\ell(t)\right)}\right|\chi_o\right\rangle \tag{3.29}$$

$$\mathrm{S}_{\mathrm{inc}}(\vec{\mathbf{Q}},\omega) = \frac{N_u}{2\pi\hbar}\mathrm{e}^{-2W(\vec{\mathbf{Q}})}\int_{-\infty}^{\infty}\mathrm{d}t\,\mathrm{e}^{-\mathrm{i}\omega t}\sum_{\chi_o}p_{\chi_o}\left\langle \chi_o\left|\mathrm{e}^{\left(\vec{\mathbf{Q}}\cdot\vec{\mathbf{u}}_0(0)\right)\left(\vec{\mathbf{Q}}\cdot\vec{\mathbf{u}}_0(t)\right)}\right|\chi_o\right\rangle \tag{3.30}$$

The first exponential is independent of time. This is the Debye-Waller factor, $W(\vec{\mathbf{Q}})$, as Equation 3.28. It describes an attenuation neutron scattering caused by initial thermal motion of the material. Equation 3.22 and Equation 3.23 then become Equation 3.29 and Equation 3.30.

$$\left\langle \mathrm{e}^{\left(\vec{\mathbf{Q}}\cdot\vec{\mathbf{u}}_0(0)\right)\left(\vec{\mathbf{Q}}\cdot\vec{\mathbf{u}}_\ell(t)\right)} \right\rangle_T = 1 + \sum_{p=1}^{\infty}\frac{1}{p!}\left\langle \left(\vec{\mathbf{Q}}\cdot\vec{\mathbf{u}}_0(0)\right)\left(\vec{\mathbf{Q}}\cdot\vec{\mathbf{u}}_\ell(t)\right) \right\rangle_T^p \tag{3.31}$$

$$\mathrm{S}_{\mathrm{coh}}^{\mathrm{el.}}(\vec{\mathbf{Q}},\omega) = \frac{1}{2\pi\hbar}\mathrm{e}^{-2W(\vec{\mathbf{Q}})}\sum_\ell \mathrm{e}^{\mathrm{i}\vec{\mathbf{Q}}\cdot\vec{\ell}}\int_{-\infty}^{\infty}\mathrm{d}t\,\mathrm{e}^{-\mathrm{i}\omega t}$$

$$= \frac{N_u}{2\pi\hbar}\mathrm{e}^{-2W(\vec{\mathbf{Q}})}\sum_\ell \mathrm{e}^{\mathrm{i}\vec{\mathbf{Q}}\cdot\vec{\ell}}(2\pi)\hbar\delta(\hbar\omega)$$

$$\mathrm{S}_{\mathrm{coh}}^{\mathrm{el.}}(\vec{\mathbf{Q}},0) = \mathrm{e}^{-2W(\vec{\mathbf{Q}})}\sum_\ell \mathrm{e}^{\mathrm{i}\vec{\mathbf{Q}}\cdot\vec{\ell}} \tag{3.32}$$

$$\mathrm{S}_{\mathrm{inc}}^{\mathrm{el.}}(\vec{\mathbf{Q}},0) = \mathrm{e}^{-2W(\vec{\mathbf{Q}})} \tag{3.33}$$

For small $\vec{\mathbf{u}}$, the exponential under the integral can be expanded in a power series as Equation 3.31. This is the phonon expansion. The first term, $p = 0$, corresponds to no change in neutron energy, and is elastic scattering, Equation 3.32 and Equation 3.33. Coherent elastic scattering is dependent on the angle to the crystal plane, $\vec{\mathbf{Q}} \cdot \vec{\ell}$, and is Bragg scattering.

$$S_{\text{coh}}^{\pm 1\text{ph.}}(\vec{\mathbf{Q}}, \omega) = \frac{N_u}{2\pi\hbar} e^{-2W(\vec{\mathbf{Q}})} \sum_{\ell} e^{\mathrm{i}\vec{\mathbf{Q}} \cdot \vec{\ell}} \left(\frac{\hbar}{2MN_u} \right) \sum_{j,q} \frac{\left(\vec{\mathbf{Q}} \cdot \vec{\mathbf{e}}_{jq} \right)^2}{\omega_{jq}}$$

$$\times \int_{-\infty}^{\infty} \mathrm{d}t\, e^{-\mathrm{i}\omega t} \left\{ e^{-\mathrm{i}\left(\vec{\mathbf{q}}_q \cdot \vec{\ell}_\ell - \omega_{jq} t \right)} \left\langle n_{jq} + 1 \right\rangle + e^{\mathrm{i}\left(\vec{\mathbf{q}}_q \cdot \vec{\ell}_\ell - \omega_{jq} t \right)} \left\langle n_{jq} \right\rangle \right\}$$

$$= \frac{1}{2M} e^{-2W(\vec{\mathbf{Q}})} \sum_{\ell} e^{\mathrm{i}\vec{\mathbf{Q}} \cdot \vec{\ell}} \left(\frac{\hbar}{2MN_u} \right) \sum_{j,q,\tau} \frac{\left(\vec{\mathbf{Q}} \cdot \vec{\mathbf{e}}_{jq} \right)^2}{\omega_{jq}} \frac{(2\pi)^3}{V_\tau}$$

$$\times \left\{ \delta\left(\omega - \omega_{jq} \right) \delta\left(\vec{\mathbf{Q}} - \vec{\mathbf{q}}_q - \vec{\tau}_\tau \right) \left\langle n_{jq} + 1 \right\rangle + \delta\left(\omega + \omega_{jq} \right) \delta\left(\vec{\mathbf{Q}} + \vec{\mathbf{q}}_q - \vec{\tau}_\tau \right) \left\langle n_{jq} \right\rangle \right\}$$

$$(3.34)$$

$$S_{\text{inc}}^{\pm 1\text{ph.}}(\vec{\mathbf{Q}}, \omega) = \frac{1}{2M} e^{-2W(\vec{\mathbf{Q}})} \sum_{j,q} \frac{\left(\vec{\mathbf{Q}} \cdot \vec{\mathbf{e}}_{jq} \right)^2}{\omega_{jq}} \left\{ \delta\left(\omega - \omega_{jq} \right) \left\langle n_{jq} + 1 \right\rangle + \delta\left(\omega + \omega_{jq} \right) \left\langle n_{jq} \right\rangle \right\} \quad (3.35)$$

Writing each term as creation and annihilation operators, it can be seen that the pth term corresponds to inelastic scattering with the creation or annihilation of phonons in p normal modes. The coherent single phonon creation and annihilation scattering function is given in Equation 3.34, where $\vec{\tau}$ are the reciprocal lattice vectors. $\tau = 1, 2, 3$, and V_τ is the volume of the reciprocal unit. The incoherent one phonon is likewise Equation 3.35.

$$W(\vec{\mathbf{Q}}) = \left\langle \vec{\mathbf{Q}} \cdot \vec{\mathbf{u}}_0(0) \right\rangle_T$$

$$= \frac{\hbar Q^2}{4MN_u} \sum_{j,q} \frac{(\vec{\mathbf{Q}} \cdot \vec{\mathbf{e}}_{jq})^2}{\omega_{jq}} \left\langle 2n_{jq}(\omega) + 1 \right\rangle \quad (3.36)$$

$$n_{jq}(\omega) = \left\langle \hat{\mathbf{a}}^\dagger \hat{\mathbf{a}} \right\rangle = \frac{1}{e^{\hbar\omega_0/k_\text{B}T} - 1} \quad (3.37)$$

$$\left\langle 2n_{jq}(\omega) + 1 \right\rangle = \frac{e^{\hbar\omega/k_\text{B}T} + 1}{e^{\hbar\omega/k_\text{B}T} - 1} = \coth\left(\frac{\hbar\omega}{2k_\text{B}T} \right) \quad (3.38)$$

$$Z(\omega) = \frac{1}{3N_u} \sum_{jq} \delta\left(\omega - \omega_{jq}(\vec{\mathbf{q}}) \right) \quad \text{where} \quad \int_0^{\omega_{\text{max}}} \mathrm{d}\omega\, Z(\omega) = 1 \quad (3.39)$$

$$W(\vec{\mathbf{Q}}) = \frac{3\hbar}{4M} \int_0^{\omega_{\max}} d\omega \frac{Z(\omega)}{\omega} \coth\left(\frac{\hbar\omega}{2k_B T}\right) \left(\vec{\mathbf{Q}} \cdot \vec{\mathbf{e}}_{jq}\right)^2 \tag{3.40}$$

Using the definition of displacement as creation and annihilation operators, Equation 3.24, the Debye-Waller factor becomes Equation 3.36. Quasiparticle phonons, which are collective excitations in the solid, obey Bose statistics, so the number operator $n_{jq}(\omega)$ is the Bose statistic, Equation 3.37. We define the phonon density of states $Z(\omega)$ as in Equation 3.39, and write the Debye-Waller factor as an integral over ω as Equation 3.40 where ω_{max} is the maximum phonon frequency. The phonon density of states (or the partial frequency distribution function) is defined where where $Z(\omega)d\omega$ is the fraction of normal vibration modes per frequency, between ω and $\omega + d\omega$.

A simplification can be made for cubic crystals, which have identical oscillator modes in each direction. This is also approximately true for many polycrystalline materials that are isotropic due to many small randomly-ordered crystals.

$$2W(\vec{\mathbf{Q}}) = \left\langle \left(\vec{\mathbf{Q}} \cdot \vec{\mathbf{u}}_0(0)\right)^2 \right\rangle_T \overset{\text{iso.}}{\approx} \frac{1}{3}Q^2 \left\langle u_0^2 \right\rangle \tag{3.41}$$

$$(\vec{\mathbf{Q}} \cdot \vec{\mathbf{e}}_{jq})^2 \overset{\text{iso.}}{\approx} \frac{1}{3}Q^2 \tag{3.42}$$

$$W(\vec{\mathbf{Q}}) \overset{\text{iso.}}{\approx} \frac{\hbar Q^2}{4M} \int_0^{\omega_{\max}} d\omega \frac{Z(\omega)}{\omega} \coth\left(\frac{\hbar\omega}{2k_B T}\right) \tag{3.43}$$

There are multiple solutions to this integral in Equation 3.43, so elastic scattering cannot be used to measure the structure of $Z(\omega)$ directly. (Some information can be extracted from the temperature-dependence however.) It is a common approximation to use the Debye spectrum, which has the correct shape at low energy, and which has only one adjustable parameter, the Debye temperature θ_D, where $\hbar\omega_D = k_B \theta_D$.

$$Z_D(\omega) = \begin{cases} \dfrac{3\omega^2}{\omega_D^3} & \omega \leq \omega_D \\ 0 & \omega > \omega_D \end{cases} \tag{3.44}$$

3.1.4 Incoherent approximation

The coherent and incoherent scattering functions have largely the same form, although calculation of the coherent scatting function is more difficult. In the incoherent approximation, the interference part of the coherent scattering is ignored, $\ell_1 \neq \ell_2$ terms are dropped in Equation 3.22, such that it has the same form as incoherent scattering. This term is still paired with the coherent scattering length, so the total scattering length is then used when calculating the cross-section from this approximated scattering function. Elastic scattering, and often the one-phonon term, are still treated coherently.

Hydrogen has a much larger incoherent cross-section (80.3 b) than coherent cross-section (1.76 b), so this approximation is reasonable for methane. The approximation is still used for many coherent scatterers where the many crystallites are randomly oriented or the incoming neutrons are unpolarized and isotropic, however the validity depends on the case in question.

3.2 Moderation in solid methane

I now focus on incoherent scattering in solid methane, our current choice for the cold moderator material in our Source. When cooled at low pressure, CH_4 molecules form a face-centered cubic crystal (fcc, also called cubic close-packed, ccp). There is a crystal phase transition at 20.4 K, and we are primarily interested in the phase above this temperature, called phase I. The hydrogens may rotate freely around the carbon in phase I, however become hindered rotors below that temperature in phase II.

3.2.1 Gaussian approximation

Although solid methane is cold enough that it can no longer be treated as a free-gas moderator, neutron energies are still well above the energies of available phonon modes, and scattering is inherently multi-phonon. For small values of $\hbar Q^2/M\omega_i$, the neutron response is given in small multiples of the available ω_i. But as $\hbar Q^2/M\omega_0 \to \infty$, the response becomes a Gaussian distribution centered at the change in energy. The many phonons created average out any characteristic frequencies of the lattice. Under the Gaussian approximation, we assume the response is exactly Gaussian at lower energies. The phonon expansion (still assuming a Bravis lattice) becomes that in Equation 3.46.

$$\left\langle \left(\vec{\mathbf{Q}} \cdot \vec{\mathbf{u}}_0(0)\right)\left(\vec{\mathbf{Q}} \cdot \vec{\mathbf{u}}_0(t)\right)\right\rangle = \frac{\hbar Q^2}{2M} \int_{-\infty}^{\infty} d\omega \, e^{-i\omega t} \frac{Z(\omega)}{\omega} n(\omega)$$

$$= \frac{\hbar Q^2}{2M} \gamma(t) \tag{3.45}$$

$$S(\vec{\mathbf{Q}}, \omega) = \frac{1}{2\pi\hbar} \int_{-\infty}^{\infty} dt \, e^{-i\omega t} \exp\left[\frac{\hbar Q^2}{2M}\left(\gamma(t) - \gamma(0)\right)\right]$$

$$= \frac{1}{2\pi\hbar} e^{-2W(\vec{\mathbf{Q}})} \sum_{p=0}^{\infty} \frac{1}{p!} \int_{-\infty}^{\infty} dt \, e^{-i\omega t} \left[\frac{\hbar Q^2}{2M} \gamma(t)\right]^p \tag{3.46}$$

3.2.2 S(α, β) notation

The scattering functions (e.g. Equation 3.29 and Equation 3.30) are often written in terms of dimensionless arguments, with momentum transfer α, energy transfer β, and the scattering angle θ. These are defined in Equation 3.47 through Equation 3.50, where A is the ratio of the atomic mass to the neutron mass.

$$\beta \equiv \frac{E_f - E_o}{k_\text{B} T} = \frac{\hbar \omega}{k_\text{B} T} \tag{3.47}$$

$$\alpha \equiv \frac{\hbar^2 (\vec{\mathbf{k}}_f - \vec{\mathbf{k}}_o)^2}{A k_\text{B} T} = \frac{\hbar^2 Q^2}{k_\text{B} T} \tag{3.48}$$

$$\mu \equiv \cos(\theta) = \frac{\vec{\mathbf{k}}_f \cdot \vec{\mathbf{k}}_o}{\left| k_f \right| \left| k_o \right|} \tag{3.49}$$

$$Q^2 = E_o^2 + E_f^2 - 2\mu \sqrt{E_o E_f} \tag{3.50}$$

I break from the usual notation for clarity. The scattering function as defined in Equation 3.51 is usually denoted with a script letter S as $\mathcal{S}(\alpha, \beta)$. This is difficult to distinguish, and I will use S(α, β) synonymously. However $S(\alpha, \beta)$ is used in the ENDF documentation to mean the symmetric scattering function as defined by Equation 3.52. Instead, I will denote the symmetric scattering function with $\widetilde{S}(\alpha, \beta)$. The principle of detailed balance in Equation 3.53 then becomes the symmetric detailed balance given in Equation 3.54. This allows half of the scattering function to be omitted in libraries of materials because they obey detail balance. This notably excludes hydrogen and deuterium which do not have randomly distributed molecular spin states.

$$\sigma(E_o \rightarrow E_f, \mu) = \frac{\sigma_\text{bound}}{k_\text{B} T} \sqrt{\frac{E_f}{E_o}} \, S(\alpha, \beta) \tag{3.51}$$

$$S(\alpha, \beta) = e^{\beta/2} \widetilde{S}(\alpha, \beta) \tag{3.52}$$

$$S(\alpha, \beta) = e^{-\beta} S(\alpha, -\beta) \tag{3.53}$$

$$\widetilde{S}(\alpha, \beta) = \widetilde{S}(\alpha, -\beta) \tag{3.54}$$

3.2.3   NJOY treatment

The Fortran-based NJOY2012[1] code includes many modular packages for managing and modifying ENDF and other nuclear data [100]. In particular, the `LEAPR`[2] module is used to process a user-provided density of states into an incoherent scattering function $S(\alpha, \beta)$ and the `THERMR` module produces a cross-section from the scattering function appropriate for use with MCNP.

The code operates under both the incoherent and Guassian approximations, which is appropriate for moderators containing hydrogen in the molecule. As implemented, the scattering function $S(\alpha, \beta)$ is given in Equation 3.55. For notation consistent with the NJOY documentation, the density of states previously denoted as $Z(\omega)$ is $\rho(\beta)$. Time t' is measured in units of $\hbar/k_B T$.

$$S(\alpha, \beta) = \frac{1}{2\pi} \int_{-\infty}^{\infty} dt' \, e^{i\beta t'} e^{-\gamma(t')} \tag{3.55}$$

$$\gamma(t) = \alpha \int_{-\infty}^{\infty} d\beta \, \frac{\rho(\beta)}{2\beta \sinh(\beta/2)} \left(1 - e^{-i\beta t'}\right) e^{-\beta/2} \tag{3.56}$$

$$\rho(\beta) = \sum_{j=1}^{K} \rho_j(\beta) \tag{3.57}$$

$$\rho_j(\beta) = \begin{cases} \rho_d(\beta) = w_j \delta(\beta_j) \\ \rho_s(\beta) \quad \text{and} \quad \int d\beta \, \rho_s = w_j \\ \rho_t(\beta) \quad \text{and} \quad \int d\beta \, \rho_t = w_j \end{cases} \quad \text{where} \quad \sum w_j = 1 \tag{3.58}$$

$$S(\alpha, \beta) = \frac{1}{2\pi} \int dt \, e^{i\beta t} \prod_{j=1}^{J} e^{-\gamma_j(t)}$$

$$= \int d\beta' \, S_{J-1}(\alpha, \beta') S_J(\alpha, \beta - \beta') \quad \text{for} \quad J = 1 \to K \tag{3.59}$$

The density of states is split into vibrational, phonon, and translational spectra, Equation 3.58. A partial scattering function is calculated from only the "solid-type" phonon spectrum ρ_s. This continuous spectrum should vary as β^2 as $\beta \to 0$. Neutrons scattering from the solid-type spectrum will create many phonons, and is treated with the Guassian approximation. Molecular vibrations ρ_d are included as "discrete" delta functions. We are considering neutrons of energies such that scattering

---

[1]As of the time of this writing, a newer version is available, NJOY2016. With great anticipation I note a C++ implementation is under development, see `https://njoy.github.io`

[2]LEAPR is based on the earlier code LEAP, and NJOY modules end with the letter R.
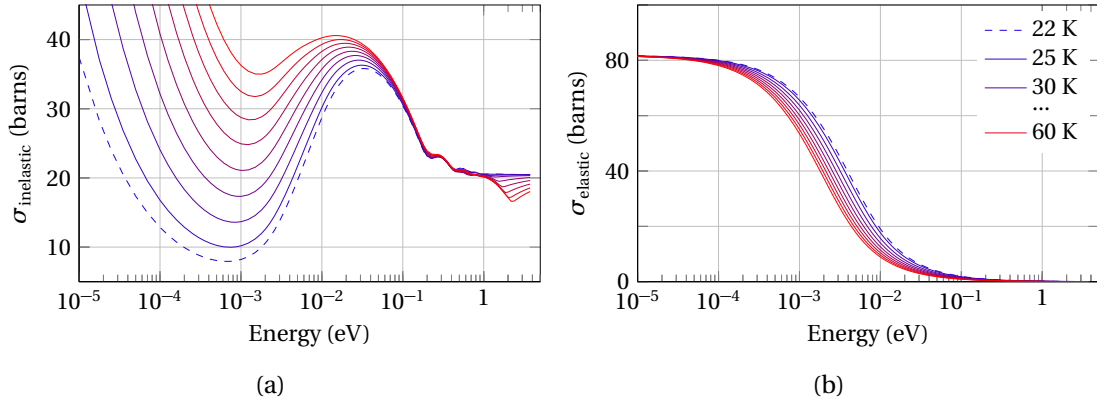
Figure 3.1: (a) Incoherent inelastic and (b) incoherent elastic cross-sections of methane per hydrogen produced from Harker-Brugger spectrum for various temperatures.

from the discrete oscillators will exchange a small number of quanta and can by treated by the phonon expansion. A partial scattering function is calculated with the first discrete mode, which is then convolved with the partial solid-type scattering function. The K partial discrete scattering functions are then serially convolved with the result of the previous convolution to produce the full scattering function, Equation 3.59. Finally ρ_t is the "translational" component for treating diffusion and liquids, and which is given zero weight for a solid. Elastic scattering (zero phonon), either coherent or incoherent, is calculated and included separately.

3.2.4 Methane temperature

The existing ENDF library[3] for thermal scattering of hydrogen bound in 22 K methane was produced by the NJOY code. Following the lead of R.E. MacFarlane [99], the continuous spectrum (only external modes) was taken from the spectrum calculated by Harker and Brugger [51] from their measurements. The internal vibrational modes at 162 meV, 190 meV, 361 meV, and 374 meV are included as discrete oscillators. This is valid for phase-I methane with temperatures warmer than 20 K. The input files are given in Appendix D

Numbers generated in processing methane in particular cover a large dynamic range. Again following R.E. MacFarlane, the NJOY code was modified to handle this large range; a cutoff value for truncating series in LEAPR was increased to save more terms. Methane thermal scattering libraries were generated over a range of temperatures, from 22 K to 60 K, Figure 3.1. The Source MCNP model was run with each. The MCNP tallies over the deuterium volume are shown in Figure 3.2.

---

[3]packaged with MCNP in the "A Compact ENDF" (ACE) format
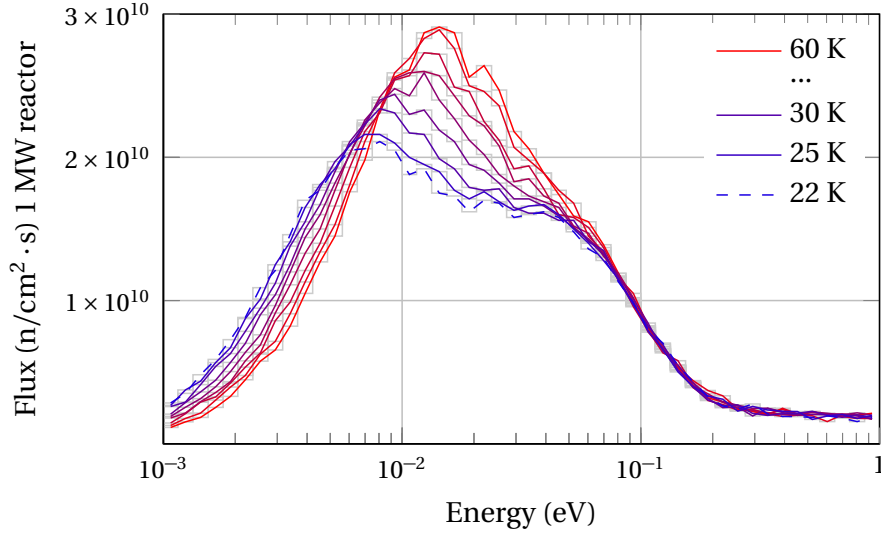
Figure 3.2: Group-averaged flux over the sD_2 in logarithmic width bins, 16 bins per decade, for various methane temperatures.

3.3 UCN production in deuterium

3.3.1 UCN production and storage time

The total production rate density of UCN P_{UCN} is given in Equation 3.60 as the product of the the incident flux Φ_o, the number density n of the converter, and the portion of the inelastic cross section to UCN energies σ_{UCN}.

$$P_{\text{UCN}} = n \int_0^\infty \mathrm{d}E_o\, \Phi(E_o) \cdot \sigma_{\text{UCN}}(E_o - E_{\text{UCN}}) \tag{3.60}$$

$$\rho = P \cdot \tau \tag{3.61}$$

$$\frac{1}{\tau} = \frac{1}{\tau_\beta} + \frac{1}{\tau_{\text{abs.}}} + \frac{1}{\tau_{\text{wall}}} + \frac{1}{\tau_{\text{holes}}} + \frac{1}{\tau_{\text{up.}}} + \frac{1}{\tau_{\text{para-}}} + \cdots \tag{3.62}$$

$$\frac{1}{\tau_{\text{loss}}} = \sum_j n_j\, v\, \sigma_{\text{loss}}^{(j)}(v) \tag{3.63}$$

$$\frac{1}{\tau_{\text{wall}}} = \bar{\mu} v \frac{1}{\lambda} = \bar{\mu} v \frac{A}{4V} \tag{3.64}$$

The achievable UCN density ρ in a closed converter volume is the product of this production rate with the mean storage time τ, Equation 3.61. The storage time will be the inverse of the sum of the decay constants of loss mechanisms. These may include, in no particular order, the beta decay of the neutron, nuclear absorption, loss on reflection from the walls, holes in the walls (to intentionally extract UCN or unavoidable gaps), phonon upscatter, upscatter from *para*-deuterium, and absorption and upscatter from isotopic and chemical impurities. Losses the in converter material can be written as a loss cross-section as in Equation 3.63. Loss due to reflection from walls is given in Equation 3.64 in terms of the probability of loss per bounce $\overline{\mu}$ and the mean free path λ in a vacuum. For convex volumes, the mean free path is four times the ratio of the volume V to wall surface area A [43]. Given a loss probability of 100%, the same form applies to UCN lost by extraction through a hole.

$$\nu \sigma_a(\nu) = \nu_{\text{th}} \sigma_a^{\text{th}} \tag{3.65}$$

$$\tau_{\text{D}_2\text{ abs.}} = \frac{1}{N_{\text{D}_2} \nu_{\text{th}} \sigma_a^{\text{th}}} = \frac{1}{\left(10^5 \, \text{mol/m}^3\right)\left(2200 \, \text{m/s}\right)\left(5.19 \times 10^{-4} \, \text{b}\right)} = 145 \, \text{ms} \tag{3.66}$$

UCN can remain in superfluid helium-4 that is below 500 mK for hundreds of seconds, limited primarily by wall loses and beta-decay. The mean storage time in deuterium however is inescapably limited by nuclear absorption to at best 150 ms [177]. This is calculated in Equation 3.66, where the thermal neutron velocity is 2200 $^{\text{m}}$/s and deuterium's thermal neutron absorption cross-section is 5.19×10^{-4} b [112]. The number density n_j of deuterium molecules at 5 K is memorably 1.00×10^5 $^{\text{mol}}$/m³ [151]. The lifetime for UCN in *para*-deuterium is significantly shorter, only 1.5 ms, due to a $J = 1 \rightarrow 0$ upscattering channel [93, 107]. A measurement by Morris, et al. [107] found a storage time of 30 ms, consistent with a few percent *para* content.

Likewise, while the mean free path in a superfluid helium source is set by the geometry of the container, in deuterium it is limited to a few centimeters in the converter material due to elastic incoherent scattering and scattering from inhomogeneities in the crystal. A deuterium-based converter will see diminishing production gains with increasing thickness.

$$V_{\text{mat.}} = n \frac{2\pi \hbar^2}{m_n} \sqrt{\frac{\sigma_{\text{tot.}}}{4\pi}} \tag{3.67}$$

The potential experienced by a UCN interacting with a material is the volume average of the point-like Fermi potentials (Equation 3.3) of the individual nuclei. This potential allows UCN to be stored in bottles, but also lowers the relative wall potential of the container by the same amount, and UCN leaving the material into vacuum will gain a boost with equal kinetic energy. As another point of comparison, the material potential of deuterium is roughly 100 neV, calculated as Equation 3.67, while the material potential of helium is an order of magnitude less.

A much higher UCN density can be achieved in superfluid helium. However, as deuterium has many more available phonon modes for downscattering, it can make use of a broad range of neutron energies. With an appropriate incident spectrum, deuterium still has an advantage over helium in production rate of two orders of magnitude [177]. For experiments with short UCN survival times, a deuterium-based source can provide a higher UCN current. As a practical consideration, since storage time in deuterium is limited by nuclear absorption, not by phonon upscatter as in helium, production is not enhanced significantly at temperatures lower than 5 K. This is appealing considering the < 1 K temperature required in a helium source.

$$\tau = \tau_{\text{conv.}} \frac{V}{V_{\text{conv.}}} \tag{3.68}$$

The UCN density ideally achievable in a storage volume open to a converter is approximately given by the ratio of their volumes as in Equation 3.68, but this is of limited use due to other losses. Pulsed sources can take advantage of a fast valve to separate the storage volume from the production volume, with the stored density set by the peak current. For our Source, with a continuous flux, a test volume cannot be filled to any greater density than steady-state density in the production volume and guide system. Thus it is critical to maintain the lifetime in the solid deuterium, in particular minimizing *para*-content and impurities, which will be discussed in Chapter 4.

3.3.2 Crystal structure

The freely rotating deuterium diatomic molecule in the $J = 0$ state is spherically symmetric. It forms a hexagonal close-packed (hcp) lattice, the most efficient means of packing spheres. At high percentage $J = 1$, which is not completely symmetric, or at high pressure it can form face-centered cubic (fcc), although this phase is not relevant to us. For the unit crystal with a height of c, seven molecules lie in a hexagon (with one in the center) of side length a at the $z = 0$ plane, and three molecules lie in a triangle also of side length a at the $z = c/2$ plane. This can be stated as two primitive hexagonal crystals where the unit atom of the second lies inside the unit cell of the first. This is shown in Figure 3.3. For the hydrogens, $c = \sqrt{8/3}$, and for deuterium at 5 K, $a = 0.360$ nm.

$$\vec{\ell} = \ell_1 \vec{\mathbf{t}}_1 + \ell_2 \vec{\mathbf{t}}_2 + \ell_3 \vec{\mathbf{t}}_3 \quad \text{where} \quad \ell_1 + \ell_2 + \ell_4 = 0 \tag{3.69}$$
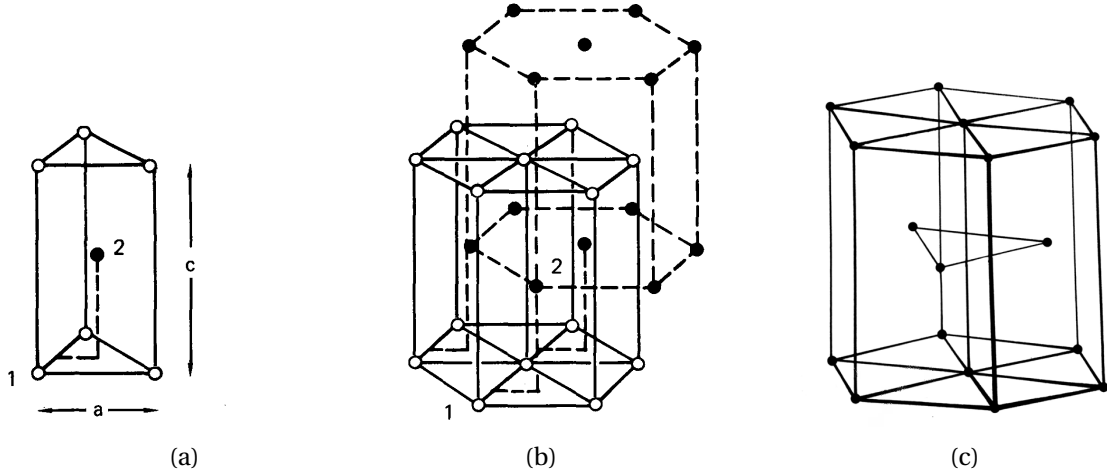
Figure 3.3: The deuterium hcp crystal. (a)(b) Each dot is a spherically symmetric deuterium molecule where (1) white is the first plane and (2) black is the second. Reproduced from P. C. Souers [150]. (c) Reproduced from S. Lovesey [97].

$$\frac{\vec{\tau}}{2\pi} = \frac{4}{3a^2}\left(\ell_1^2 + \ell_2^2 + \ell_1\ell_2\right) + \frac{1}{c^2}\ell_3^2 \tag{3.70}$$

This structure can be treated in our formulism with Bravais-Miller indexing, where we introduce a fourth index as in Equation 3.69 where $\ell_{1/2/3/4}$ run over all integers. Reciprocal lattice vector lengths $\tau_{1/2/3}$ are calculated as in Equation 3.70. The unit cell volume is $V_u = a^2 c \sqrt{3}/2$, with a volume of $V_u = a^2 c \sqrt{3}/4$ per molecule. The crystal is not cubic, but as our application averages over all angles of a polycrystal, it is a good approximation.

3.3.3   Production under Debye model

R. Golub and K. Böning [42] first considered production in deuterium using the Debye model. They evaluated the one-phonon downscattering cross section (one phonon creation), omitting spin and rotational correlations. Beginning with Equation 3.35, the lattice is assumed isotropic. Considering only the portion of the cross section to UCN energies, it can also be assumed both the temperature of the converter material and the final neutron energy are much less than the energy transfer, $\omega \gg T$ and $E_f \ll E_o$. For deuterium, at Debye temperature of $\theta_D = 110\,\mathrm{K}$ reproduces scattering results [114], and the Debye-Waller factor is integrated to ω_D where $\hbar\omega_D = k_B\theta_D$.

$$W(\vec{Q}) \overset{\text{iso.}}{\approx} \frac{\hbar Q^2}{4M} \int_0^{\omega_{\max}} d\omega \frac{Z(\omega)}{\omega}\left(\frac{2}{e^{\hbar\omega/k_B T} - 1} + 1\right)$$

$$\overset{\omega \gg T}{\approx} \frac{\hbar Q^2}{4M} \int_0^{\omega_{\max}} d\omega \, \frac{Z(\omega)}{\omega}$$

$$\overset{\text{Debye}}{\approx} \frac{3}{4} \left(\frac{\hbar^2 Q^2}{2M} \right) \left(\frac{1}{k_B \theta_D} \right)$$

$$S_{\text{inc}}^{+1\,\text{ph.}}(\vec{Q}, \omega) \overset{\text{iso.}}{\approx} \frac{N_u Q^2}{2M} e^{-2W(\vec{Q})} \frac{Z(\omega)}{\omega} \left(\frac{1}{e^{\hbar\omega/k_B T} - 1} + 1 \right)$$

$$\overset{\omega \gg T}{\approx} \frac{N_u Q^2}{2M} e^{-2W(\vec{Q})} \frac{Z(\omega)}{\omega}$$

$$\overset{\text{Debye}}{\approx} \frac{N_u Q^2}{2M} \exp \left\{ -2 \frac{3}{4} \left(\frac{\hbar^2 Q^2}{2M} \right) \left(\frac{1}{k_B \theta_D} \right) \right\} \frac{1}{\omega} \left(\frac{3\omega^2 \hbar^3}{(k_B \theta_D)^3} \right)$$

$$\overset{E_f \ll E_o}{\approx} \frac{3 N_u \hbar^2}{2M} \exp \left(\frac{-3\hbar^2 k_o^2}{4M k_B \theta_D} \right) k_o^2 E_o \frac{1}{(k_B \theta_D)^3} \tag{3.71}$$

Z.-Ch. Yu, et al. [177] further considered one-phonon downscattering with a more realistic density of states, based off the dispersion curve measurements of M. Nielsen [113], and found an increase in the production cross-section. With an incident Maxwellian flux, production was found to peak at a temperature of 29 K.

3.3.4 Molecular effects on production

C.-Y. Liu, et al. [93] included spin contributions, and in particular found the $J = 1 \to 0$ transition had a large cross-section for upscattering. Here I back up to Equation 3.11 and follow the development of Young and Koppel [176]. Taking the deuterium molecule as a dumbbell rotating at the lattice sites, the atom's vectors $\vec{R}_{\ell d}$ are given in Equation 3.72 where $\vec{\ell}_\ell$ is the sum over lattice vectors, $\vec{d}_d$ are displacements from those lattice sites, and $\vec{u}_\ell$ is the vector between the deuterium atoms. Splitting this into $\ell_1 = \ell_2$ "self" and $\ell_1 \neq \ell_2$ "interference" terms gives Equation 3.73. (This is analogous to applying the incoherent approximation on coherent scattering in Section 3.1.4.)

$$\vec{R}_{\ell d} = \vec{\ell}_\ell + \vec{d}_d + \vec{u}'_{\ell d} \quad \to \quad \vec{R}_{\ell d} = \vec{\ell}_\ell + (-1)^d \frac{\vec{u}_\ell}{2} \tag{3.72}$$

$$\frac{d^2 \sigma}{d\Omega \, dE_f} = \frac{k_f}{k_o} \sum_{\chi_f} \sum_{\chi_o} p_{\chi_o} \left| \sum_{\ell, d} \left\langle \chi_f \left| \hat{b}_{\ell d} e^{i\vec{Q} \cdot \vec{R}_{\ell d}} \right| \chi_o \right\rangle \right|^2 \delta(E_{\chi_o} - E_{\chi_f} + \hbar\omega)$$

$$
= \frac{k_f}{k_o} \left(\frac{1}{2\pi\hbar} \right) \sum_{\chi_f} \sum_{\chi_o} p_{\chi_o} \int_{-\infty}^{\infty} dt \, e^{i\left(\hbar\omega - E_{\chi_o} + E_{\chi_f}\right) t/\hbar}
$$

$$
\times \sum_{\ell_1 \neq \ell_2} \sum_{d_1=1}^{2} \sum_{d_2=1}^{2} \left\langle \chi_o \left| \hat{\mathbf{b}}_{\ell_1 d_1} e^{-i\vec{\mathbf{Q}} \cdot \left(\vec{\ell}_{\ell_1} + (-1)^{d_1} \vec{\mathbf{u}}_{\ell_1}/2 \right)} \right| \chi_f \right\rangle \left\langle \chi_f \left| \hat{\mathbf{b}}_{\ell_2 d_2} e^{i\vec{\mathbf{Q}} \cdot \left(\vec{\ell}_{\ell_2} + (-1)^{d_2} \vec{\mathbf{u}}_{\ell_2}/2 \right)} \right| \chi_o \right\rangle
$$

$$
+ \frac{k_f}{k_o} \left(\frac{1}{2\pi\hbar} \right) \sum_{\chi_f} \sum_{\chi_o} p_{\chi_o} \int_{-\infty}^{\infty} dt \, e^{i\left(\hbar\omega - E_{\chi_o} + E_{\chi_f}\right) t/\hbar}
$$

$$
\times \sum_{\ell} \sum_{d_1=1}^{2} \sum_{d_2=1}^{2} \left\langle \chi_o \left| \hat{\mathbf{b}}_{\ell d_1} e^{-i\vec{\mathbf{Q}} \cdot \left(\vec{\ell}_{\ell} + (-1)^{d_1} \vec{\mathbf{u}}_{\ell}/2 \right)} \right| \chi_f \right\rangle \left\langle \chi_f \left| \hat{\mathbf{b}}_{\ell d_2} e^{i\vec{\mathbf{Q}} \cdot \left(\vec{\ell}_{\ell} + (-1)^{d_2} \vec{\mathbf{u}}_{\ell}/2 \right)} \right| \chi_o \right\rangle
$$

$$(3.73)$$

Interactions with the deuterium molecule will include translation in the lattice (phonons), rotational states, vibrational states, and spin correlations with the incident neutron. We assume these states are independent, that is $\left| \chi \right\rangle = \left| \chi_t, J, S, n \right\rangle \simeq \left| \chi_t \right\rangle \left| J \right\rangle \left| S \right\rangle \left| n \right\rangle$, where S is the total spin, J is the total angular momentum, n is the vibrational state, and χ_t is the translational wavefunction in the crystal. The energy difference between the ground and first excited vibrational energy states is 0.37 eV (4300 K), calculated as Equation 4.6, so we can assume solid deuterium will begin in the ground state $n = 0$. Only the first few states will be accessible by the neutron energy. Excluding the interference term, we separate out the translational term, which can be treated as in Section 3.1.3 by separating a Debye-Waller term and applying the phonon expansion. (Young and Koppel address a free gas.) The primed terms are those without the translational components.

$$
\frac{d^2\sigma_{\text{self}}}{d\Omega \, dE_f} = \frac{k_f}{k_o} \left(\frac{1}{2\pi\hbar} \right) \sum_{\ell} \int_{-\infty}^{\infty} dt \sum_{\chi_o} p_{\chi_o} \left\langle \chi_o^{(\text{trans})} \left| e^{-i\vec{\mathbf{Q}} \cdot \vec{\ell}(0)} e^{i\vec{\mathbf{Q}} \cdot \vec{\ell}(t)} \right| \chi_o^{(\text{trans})} \right\rangle
$$

$$
\times \sum_{\chi_o'} p_{\chi_o'} \sum_{\chi_f'} e^{i\left(\hbar\omega - E_{\chi_o}' + E_{\chi_f}'\right) t/\hbar} \left| \left\langle \chi_f' \left| \hat{\mathbf{b}}_{\ell 1} e^{i\vec{\mathbf{Q}} \cdot \vec{\mathbf{u}}_{\ell}/2} + \hat{\mathbf{b}}_{\ell 2} e^{-i\vec{\mathbf{Q}} \cdot \vec{\mathbf{u}}_{\ell}/2} \right| \chi_o' \right\rangle \right|^2
$$

$$(3.74)$$

Young and Koppel then evaluate the remaining portions of the wavefunction specifically for the deuterium system. Explicitly, $\left| \chi' \right\rangle = \left| J, J_z, S, S_z, \sigma_z, n \right\rangle$ where S_z and J_z are their z components, and σ_z is the neutron spin. For unpolarized incident neutrons, $p_\sigma = \frac{1}{2}$. The scattering length operators in Equation 3.74 contain the spin dependent interaction with the nuclear spin I. These can be written in terms of the nuclear scattering lengths $b_\pm$ for the $I \pm 1/2$ states, which in turn can be

written in terms of the measured coherent and incoherent scattering lengths as Equation 3.75.

$$b_{\mathrm{coh}}^2 = \frac{1}{(2I+1)^2}\left\{(I+1)b_+ + I b_-\right\}^2$$

$$b_{\mathrm{inc}}^2 = \frac{I(I+1)}{(2I+1)^2}(b_+ - b_-)^2$$

(3.75)

$$\widehat{\mathbf{b}}_{\ell 1}\mathrm{e}^{\mathrm{i}\vec{\mathbf{Q}}\cdot\vec{\mathbf{u}}_\ell/2} + \widehat{\mathbf{b}}_{\ell 2}\mathrm{e}^{-\mathrm{i}\vec{\mathbf{Q}}\cdot\vec{\mathbf{u}}_\ell/2} = \left(2b_{\mathrm{coh}} + \sqrt{2}\,b_{\mathrm{inc}}\widehat{\mathbf{S}}\cdot\widehat{\boldsymbol{\sigma}}\right)\cos\left(\vec{\mathbf{Q}}\cdot\vec{\mathbf{u}}_\ell/2\right)$$

$$+\mathrm{i}\sqrt{2}\,b_{\mathrm{inc}}\widehat{\boldsymbol{\sigma}}\cdot\left(\widehat{\mathbf{I}}_1 - \widehat{\mathbf{I}}_2\right)\sin\left(\vec{\mathbf{Q}}\cdot\vec{\mathbf{u}}_\ell/2\right)$$

(3.76)

The vibrational matrix elements assume harmonic oscillators where ω_n is the vibrational energy. Under the conditions that there is no hindrance to the molecular rotation and no rotational-vibrational coupling, the rotational elements are the spherical harmonics, $\left|J J_z\right\rangle = Y_{J J_z}(\theta, \phi)$. For a more detailed derivation, see V. Sears [139].

$$\frac{\mathrm{d}^2\sigma_{\mathrm{self}}}{\mathrm{d}\Omega\,\mathrm{d}E_f} = \frac{k_f}{k_o}\left(\frac{1}{2\pi\hbar}\right)\sum_\ell\int_{-\infty}^{\infty}\mathrm{d}t\,\mathrm{e}^{\mathrm{i}\omega t}\sum_{\psi_o}p_{\chi_o}\left\langle\psi_o^{(\mathrm{trans})}\left|\mathrm{e}^{-\mathrm{i}\vec{\mathbf{Q}}\cdot\vec{\ell}(0)}\mathrm{e}^{\mathrm{i}\vec{\mathbf{Q}}\cdot\vec{\ell}(t)}\right|\chi_o^{(\mathrm{trans})}\right\rangle$$

$$\sum_{J_o}P_{J_o}\sum_{J_f}\mathcal{B}(J_o J_f)\left(2J_f+1\right)\sum_{n_f=0}^{\infty}\left(\frac{Q^2}{4M\omega_n}\right)^n\frac{\mathrm{e}^{\mathrm{i}\omega_n t}}{n!}\mathrm{e}^{\mathrm{i}\left(E_{J_f}-E_{J_o}\right)t/\hbar}$$

(3.77)

$$\times\sum_{L=\left|J_f-J_o\right|}^{J_f+J_o}\left|A_{nL}\right|^2\left\{C(J_o J_f; L)\right\}^2$$

$$A_{nL} = \frac{1}{2}\int_{-1}^{1}\mathrm{d}\mu\,\mu^n\exp\left(-\frac{Q^2\mu^2}{4M_{D_2}\omega_n} + \frac{iQ\langle u\rangle\mu}{2}\right)P_L(\mu)$$

(3.78)

This results in Equation 3.77, adopting a notation similar to C.-Y. Liu et al. [93]. $\mathcal{B}(J_o J_f)$ are rotational transition cross-section strengths resulting from the spin correlation, Equation 3.79. A_{nL} is an integral over the cosine of the angle of the molecule, $\mu = \cos(\theta)$, where $P_j(\mu)$ are Legendre polynomials[4]. $C(J_o J_f; L)$ is shorthand for $C(J_o, J_f, J_z^{(o)} = 0, J_z^{(f)} = 0; L, M = 0)$, which are the Clebsh-Gordon coefficients with the notation $C(j_1 j_2 m_1 m_2 | j m) = \left\langle j_1 j_2; m_1 m_2 \middle| j_1 j_2; j m\right\rangle$ and requirement that $J_o + J_f + J$ is even. (Koppel and Young use a different notation $C(j_1 j_2 j; m_1 m_2)$ with $m_1 + m_2 = m$

---

[4] A_{nL} is defined as by Lovesey [97], which differs from that by Young and Koppel [176] by a factor of 1/2, accounted for by differences in tabulated scattering lengths.

implicit.)

$$\mathcal{B}(J_o J_f) = \begin{cases} b_{\text{coh}}^2 + \frac{5}{8} b_{\text{inc}}^2 & J_o \text{ even} \to J_f \text{ even} \\ \frac{3}{8} b_{\text{inc}}^2 & J_o \text{ even} \to J_f \text{ odd} \\ \frac{3}{4} b_{\text{inc}}^2 & J_o \text{ odd} \to J_f \text{ even} \\ b_{\text{coh}}^2 + \frac{1}{4} b_{\text{inc}}^2 & J_o \text{ odd} \to J_f \text{ odd} \end{cases} \tag{3.79}$$

C.-Y. Liu et al. [93] explicitly identified the $J_o = 1 \to J_f = 0$ transition, that is upscattering of a neutron by *para*-to-*ortho*-deuterium conversion, as having a substantial cross-section of 31 b (approximately independent of UCN energy). The presence of *para*-deuterium significantly impacts the UCN survival time. Further, this *para* cross-section is largely temperature-independent. *Para*-deuterium must be converted to *ortho* prior to UCN production by the means discussed in Chapter 4.

3.3.5   Recent studies

So far, calculations of inelastic scattering of neutrons in deuterium has been made under the incoherent approximation. This is sufficient for calculating the total cold neutron cross-section, but may not be appropriate for scattering to UCN energies and in particular for calculating UCN upscattering rates. See the recent work by C. Lavelle, et al. [88] and C.-Y. Liu, et al. [95].

The UCN production in deuterium has been considered here in a perfect polycrystal of large grain size, but it is worth considering potential differences in a real crystal. Inhomogeneities will elastically scatter UCN, limiting the number that can escape the converter [29, 43, 125]. A. Adamczak [2] also suggests that as deuterium is largely a coherent scatterer, very small imperfections in the crystal may alter inelastic upscattering.

As a very light atom, deuterium is a quantum solid in which atoms undergo large zero-point motion. The assumption of a harmonic oscillator may not be good at very low temperatures, but it is likely a good approximation at 5 K [24, 25].

While inelastic neutron scattering studies of deuterium have been made [113, 133], these focus on thermal energies. Recently the groups at PSI [9, 11–13] and Munich [34, 35, 50] have made strong efforts in understanding the cross-section of deuterium at lower energies with a focus on UCN production. The two groups have produced energy-dependent UCN-production cross sections that will be used the the following section.
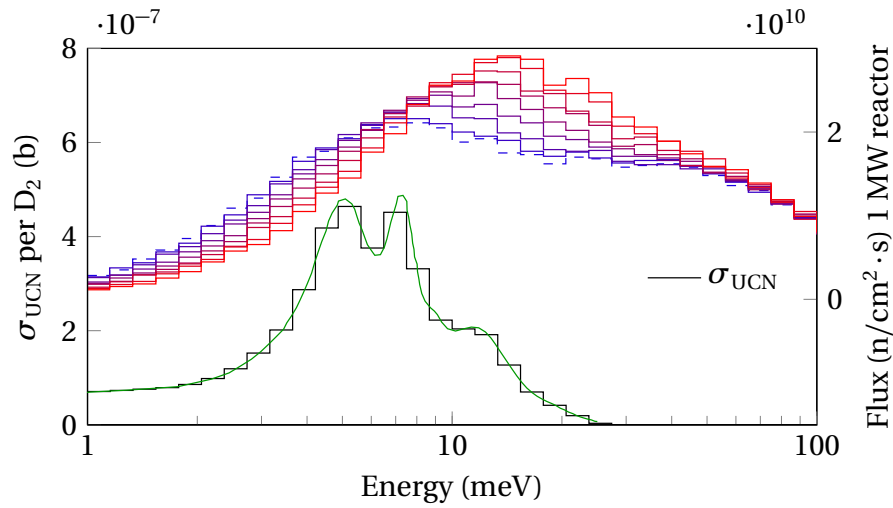
Figure 3.4: (Smooth line) UCN-production cross-section per molecule reproduced from A. Frei, et al. [35], binned to match the MCNP-calculated fluxes over the sD_2 for various methane temperatures from Figure 3.2, which are also plotted here.
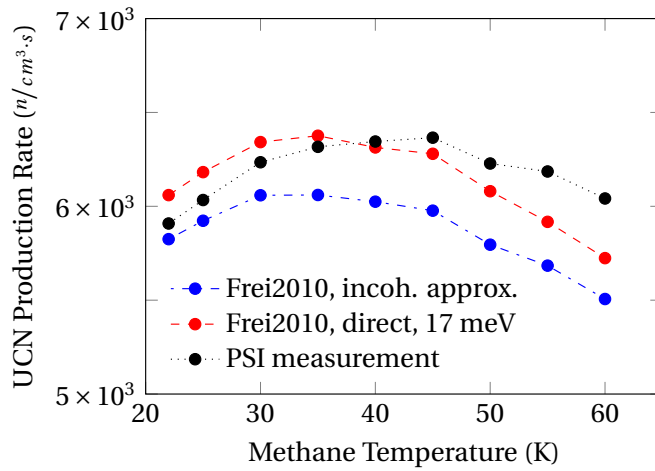
Figure 3.5: UCN production as a function of methane temperature for production cross-sections using the incoherent approximation from A. Frei, et al. [35], direct determination for 17 meV neutrons by taking S(Q,E) along the parabolic free-neutron dispersion curve from A. Frei, et al. [35], and measurements at PSI [11].
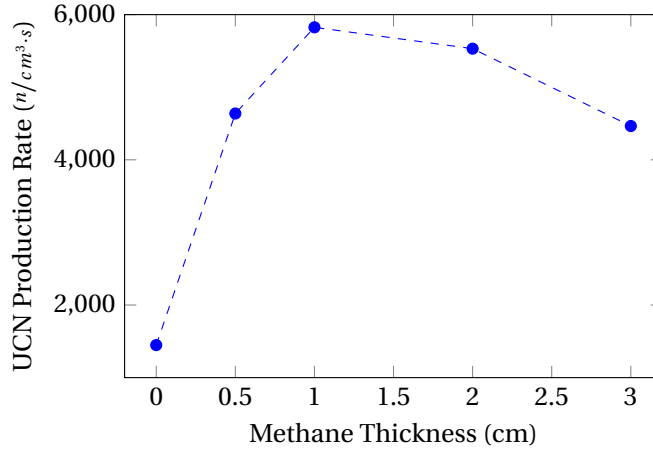
Figure 3.6:   UCN production with the thickness of methane at 22 K.

3.3.6   Cold moderator dependence in our Source

The UCN production in our Source as it depends on both cold moderator temperature and thickness was examined. Using the temperature-dependent neutron fluxes across the UCN converter calculated in Section 3.2.4, the UCN production rate was calculated as a function of temperature using the production cross sections from Atchison, et al. [11] and Frei, et al. [35]. The cold neutron fluxes and the production cross section per molecule are shown in Figure 3.4. The UCN production rate was calculated as in Equation 3.60. The cross-sections were split into average value logarithmic bins corresponding with the MCNP tallies. Calculations with smaller energy bins do not result in significantly different results.

Our cold flux is not fully thermalized, and as a result the temperature dependence is less pronounced. UCN production rate varies by only 3% with the temperature of the methane, rising from 22 K to a maximum between 30 K and 40 K. The total production-rate density calculated here is 6×10^3 n/cm³·s. This is roughly half of the original estimate for the source [78]. This means we are able run the cold source at higher temperatures, which will slow the degradation of methane under radiation, minimize hydrogen release, and avoid any concern over stored energy.

The UCN production was also calculated as a function of the cold moderator thickness, as shown in Figure 3.6. Increasing the thickness of the cold moderator from the current 1 cm to increase thermalization of the cold flux lowers the total flux and does not increase UCN production.

Chapter 4

Cryogenics and Gas Handling

4.1   Introduction

This chapter will describe the design and initial testing of the Source's cryostat, cryogenic helium system, and gas handling systems, in particular the deuterium spin-state converter and Raman spectrometer. Details of the most mature tests with deuterium are covered in the context of Chapter 5.

4.2   Cryogenics

4.2.1   Cryogenic helium system
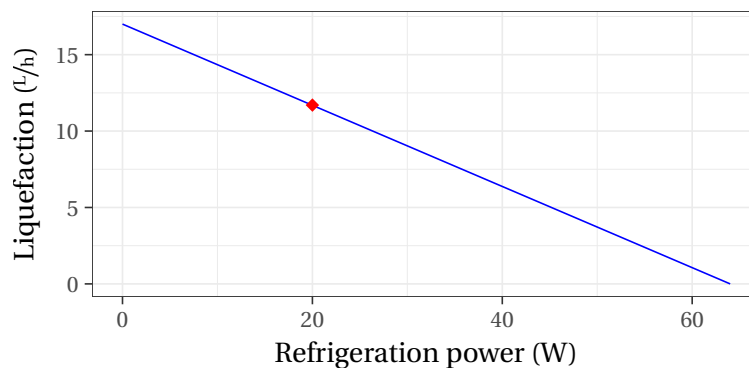
Figure 4.1:   Typical liquefaction and refrigeration capacity specification for the Linde model 1430 liquefier / refrigerator and model RS compressor. A potential operating point is highlighted (without liquid nitrogen assistance).
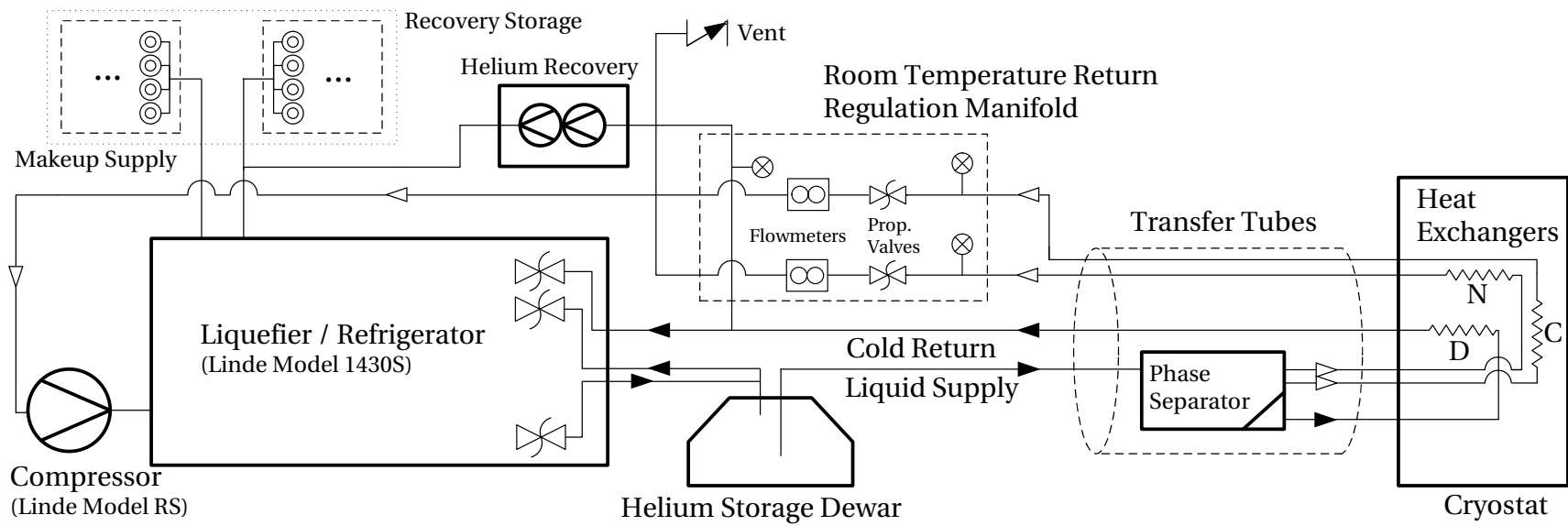
Figure 4.2:   Schematic of the helium cryogenic system. The labels D, N, and C in the cryostat designate the deuterium container, neutron guide, and methane heat exchangers respectively. Open arrows are pure gas flow.

The cryostat is cooled with liquid helium generated on site. An important feature of the cryostat and liquid helium cooling system is that it provides independent temperature control of the cold moderator container and the UCN-converter container. Our Linde model 1430S liquefier can produce liquid helium from room temperature gas, specified up to $17 \, ^L/_h$, or can operate as a closed loop refrigerator, providing up to 64 W refrigeration power. (If necessary, for example during initial cooling, it can provide up to $47 \, ^L/_h$ or 114 W using liquid nitrogen pre-cooling.) However, we are operating in a hybrid of the refrigeration and liquification modes. We return a portion of refrigeration flow while also boiling-off a portion of the stored liquid helium. For example, we might expect to utilize up to 20 W of refrigeration to maintain the UCN-converter and consume up to $12 \, ^L/_h$ to maintain the warmer cold moderator and neutron guide as in Figure 4.1 [78].

A schematic layout of the helium cryogenic system is shown in Figure 4.2. The full helium system and liqufier diagrams are given in Appendix A.5 and Appendix A.6. The helium liquefier supplies liquid helium to a 500 L helium storage dewar used as a buffer volume. The dewar can cool the cryostat for several hours in the event of power loss or liquefier maintenance. Helium pulled from the dewar by a variable-height withdrawal line enters a custom transfer tube. The transfer tube includes a built-in phase separator that gravitationally separates the liquid phase from the gas phase and into three parallel cooling loops. These are labeled D-, C-, and N-loops corresponding to the deuterium, methane ("C"H_4), and neutron guide cryostat heat exchangers. The mixed liquid-gas phase is delivered through the D-loop to cool the deuterium container to the coldest temperature, while the pure gas phase is delivered through the C-loop to the methane container. Depending on the level in the phase separator, a liquid-gas mixture may be delivered through the N-loop to the neutron guide.

After exiting the cryostat, return gas from the C- and N-loops are used as counter-flow to actively shield the supply lines, minimizing radiative heat loads in the transfer tube. The cold gas from the D-loop is returned directly to the liquefier through a low-temperature bayonet and cryogenic proportional valve. The C- and N-loop gas is warmed with heaters to room temperature in the return manifold and fed to the compressor's supply through two proportional valves. Helium flow is driven by pressure in the dewar, and flow through each loop is controlled by these three proportional valves. When the system is warmed up, helium is collected back into high pressure storage using the recovery system.

Modifying normal operation

Refrigeration demand will not always match the maximum output of the liquefier. The original intention was to cool the cryostat solely from the helium dewar for a period and operate the liquefier as needed to re-condense this recovered gas. For example, if the reactor is operating on a daily schedule, the liquefier would be run during the day, and the dewar would provide passive cooling

overnight while the reactor bay is locked. However, stopping and restarting the liquefier introduced changes in pressure to both the dewar and recovery lines, unavoidably changing the cryostat's temperatures daily. This is certainly a problem if actively producing UCN, and as shown in Chapter 5, cyclic changes in temperature can alter the deuterium crystal.

Instead we decided to operate the liquefier continuously, and limit its cooling power as needed to meet demand. (One could also imagine introducing an additional variable heat load such that the liquefier could be operated at a constant level just above the highest expected heat load.) Counter-current flow through the liquefier's heat exchangers is cooled by the expansion engine. A portion of the inlet high-pressure helium is expanded in two cylinders by pistons, driven by a variable frequency drive (VFD) and flywheel, and then added to the low-pressure return flow. (The expansion engine is analogous to an internal combustion engine driven in reverse.) Normally a control loop lowers the expansion engine speed to maintain inlet pressure, maximizing the use of compressor capacity. However, manually lowering the speed of the engine reduces the performance of the liquefier as desired. An additional control loop was programmed to the liquefier's control PLC to instead limit engine speed based off the return gas pressure (P-2 in Appendix A.6). This exactly limits the liquefier's cooling to match the liquefaction rate with the boil-off of the system. Continuously operating the liquefier at low speed should also lessen wear-and-tear on the liquefier associated with restarts and high-speed operation.

However, this control scheme is an actively maintained unstable equilibrium. We noticed the operating point would drift and oscillate in certain circumstances, particularly when the heat load on the cryostat was minimal. The engine's speed was designed to be limited in tandem with the supply pressure, and changing it's speed changes the supply pressure, moving the liquefier outside it's expected parameters. The compressor's bypass regulator (V345 in Appendix A.5) sets its outlet pressure and thus the liqufier's gas supply. Moving forward, replacing the compressor's manual bypass regulator with an machine-controlled equivalent, thus instead limiting the compressors performance, could provide this control and limit the systems cooling power inline with the system's original design.

4.2.2   Cryostat

Each heat exchanger in the cryostat is thermally isolated and paired with temperature sensors and electric heaters which, in conjunction with the parallel cooling loops, allows independent temperature control. The methane container is hung by titanium rods, providing thermal isolation. The deuterium container is separated from the neutron guide by a zircaloy ring explosively bonded with aluminum, allowing a large thermal gradient. Components are labeled in Figure 4.3, Figure 4.4 and Figure 4.5, with photos during assembly in Figure 4.6 and Figure 4.7
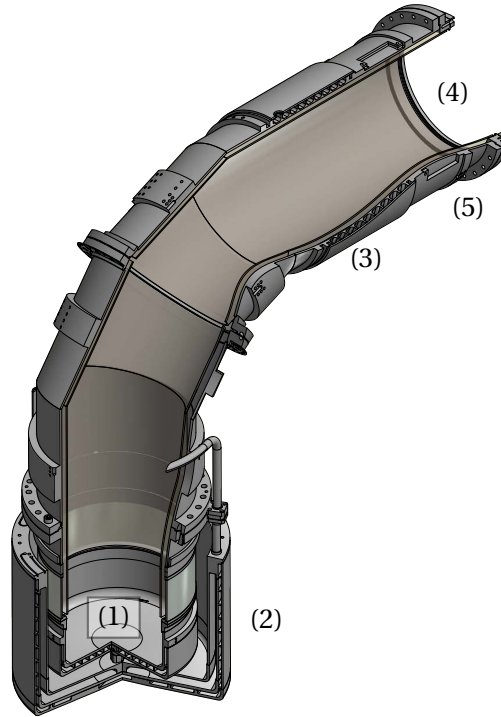
Figure 4.3:   Cutaway CAD rendering of the cryostat insert. (1) The deuterium container and (2) the methane container are shown detail in Figure 4.4 and Figure 4.5 respectively. The neutron guide runs co-axially from the deuterium container, through (3) the neutron guide's helium heat exchanger, to (4) the UCN foil window. There are (5) temperature sensors and an electric heater at the window's location.

The original electric heaters were roughly 1 foot lengths of 32 AWG nichrome wire at $10\,\Omega/\text{foot}$, but these proved unreliable. Breaks in insulation would cause short circuits, and breaks in thermal contact would lead to overheating. Potting epoxy was avoided to limit activation. Instead, the heaters were remade with three parallel lengths of nichrome wire, three times the length. For the deuterium container, these wires were wrapped between sheets of alumina fabric and clamped around the circumference of the container, Figure 4.9. For the methane container, the wire was clamped between alumina fabric and an alumina tube, which was then clamped to the top of the methane container, Figure 4.10. Both heaters were tested in a cryopump prior to installation.

Duplicate Lakeshore Cernox temperature sensors were installed on the deuterium container, methane container, above the temperature gradient ring, and at the UCN window. The deuterium sensors are 4-lead and calibrated, while the remainder are 2-lead calibration-banded with the response curves adjusted for the lead resistance.
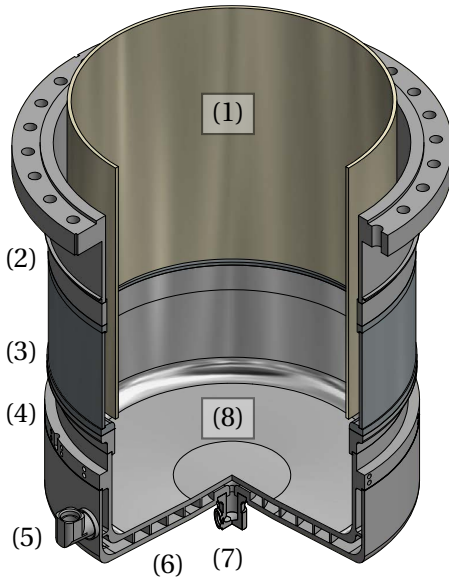
Figure 4.4: Cross-section CAD rendering of the deuterium container. Counter-clockwise from the top are (1) the neutron guide, (2) gradient ring heater and temperature sensors, (3) zircaloy gradient ring, (4) deuterium heater and temperature sensors, (5) cryogenic helium outlet, (6) helium heat exchanger in the double-wall of the container, (7) cryogenic helium inlet and its temperature sensor, and (8) the deuterium volume.

All temperature sensor and heater wires run 5 m to a disconnect to allow for the cryostat to be moved. Cables then run another 15 m to an electrical patch panel. Both transfer tube temperature sensors and cryostat sensors are read by three LakeShore model 218 temperature monitors which can be read by a PC via RS232. Each heater is paired with a power supply capable of providing at least 1.5 A and controlled either via RS232 or via a PCI analog output board.

The cryostat vacuum jacket is always actively pumped. See Appendix A.4 for pump details. A gate valve will close in the event of a power loss. A Pfeiffer model PKR capacitance/Pirani full-range gauge measures the pressure above the pump, which is typically 1×10^{-5} mbar when the cryostat is warm and 1×10^{-7} mbar when helium cooling is providing cryopumping. Three Varian model 531 Thermocouple pressure gauges are located on both helium transfer line's vacuum jackets and the safety relief line, read by a DigiVac model StrataVac 201 controller.

All cryostat and gas handling instrumentation is finally displayed and logged to file by LabView. A screenshot of this program is shown in Appendix B.1. In addition, the program provides control of the power supplies driving the cryostat heaters, allowing for example a linear increase in heater power. The helium liquefier's sensors and operation, including return proportional valves, are controlled by a separate HMI implemented in LookoutDirect. A screenshot of this program is shown in Appendix B.2.
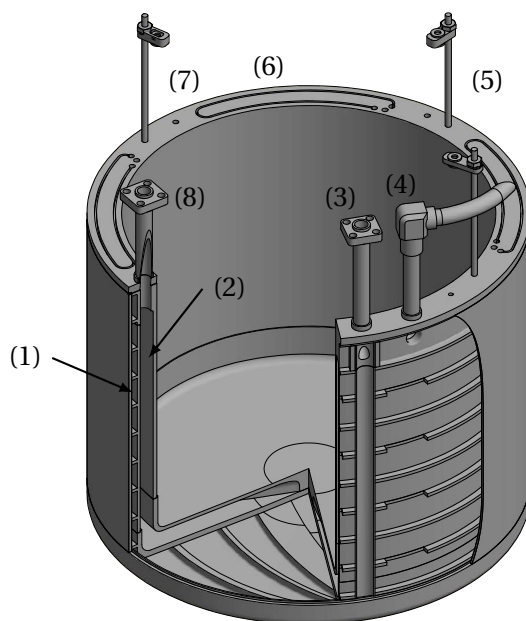
Figure 4.5: Cutaway CAD rendering of the methane container. It is a triple-walled container with (1) the helium heat exchanger between the outer walls and (2) the methane volume between the inner walls. A portion of the side, outside skin, and bottom of the container have been cut away to show the helium heat exchanger. Counter-clockwise are (3) the helium inlet, (4) the helium outlet, (5) one of the titanium rods suspending the container. The electric heaters and temperature sensors are located around the top rim of the container, for example at (6) and (7) respectively. (8) The methane tube serves as both inlet and outlet.

During assembly of the cryostat, the vacuum jacket, gas lines, and helium lines were all exten-sively leak checked, and all electronics were verified. The cryostat should be able to be moved from its testing position to the thermal column without any reassembly.

4.2.3   Initial testing

Previously the helium liquefier was commissioned with only the storage dewar. Prior to introducing the target cryogens, we characterized the cooling power of the cooling loops with the cryostat, as well as customized the automatic operation of the liquefier. For safety as well as accessibility, the initial cryogenic testing was performed with the source cryostat positioned outside of the reactor biological shield and without the room temperature UCN guide, see Figure 4.8.

The liquefier was operated at full power to both liquefy helium into the storage dewar and cool the cryostat. Between 200 liters and 250 liters (liquid) of the helium inventory were liquefied into the storage dewar. The cryostat was cooled first by cold gas from the top of the dewar, and then by liquid from the dewar. It took less than two days to reach minimum operating temperatures. Typical

Figure 4.6: Photograph of the cryogenic containers with the capped deuterium container on the left and methane container on the right.

| (a) | (b) |
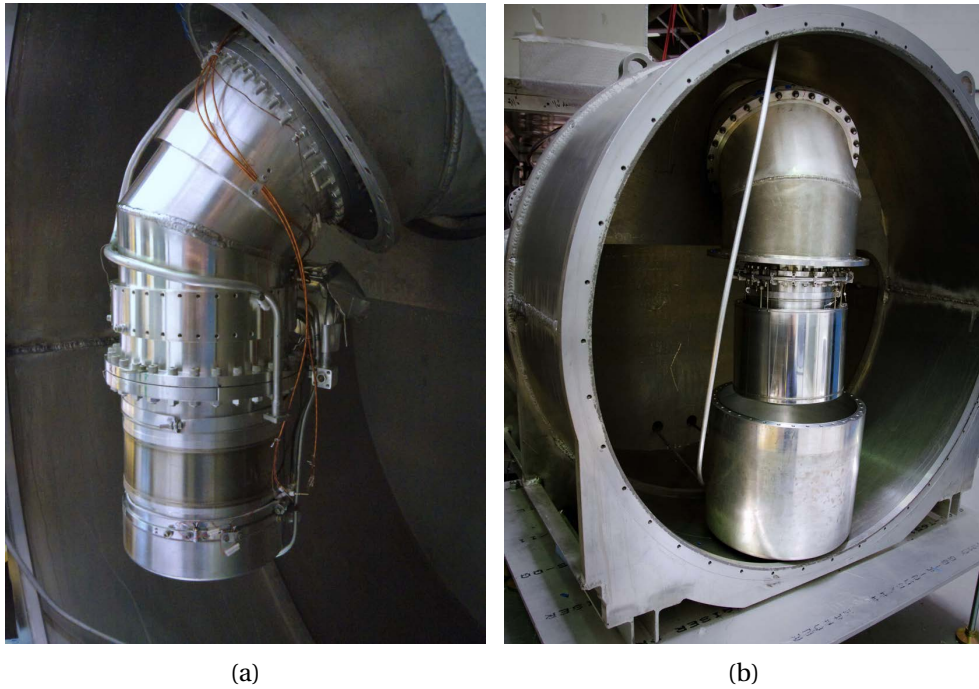
Figure 4.7: Photographs of the cryostat during assembly with the face of the heavy water tank removed, and (a) with the vacuum jacket and methane container removed showing the deuterium container and (b) with the bottom-most vacuum jacket segment lowered showing the methane container around the neutron guide.

Figure 4.8: Photograph of the completed cryostat vacuum jacket from behind. Gas lines and the helium transfer tube enter from the right. The vacuum jacket is removed at the neutron guide, showing the foil window.
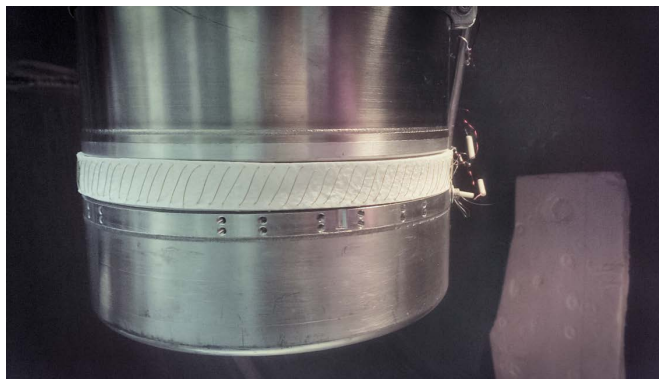
Figure 4.9: Photograph of the D_2 electric heater partially installed.

<div align="center">(a)   (b)</div>

Figure 4.10: Photographs of the methane electric heater (a) during assembly and (b) installed.

Table 4.1: Equilibrium temperature of the methane cryocontainer with electric heater input and helium flow, measured as room temperature return gas.

Helium Flow	Heater Power (W)		
(l/min)	0	10	25
34	10 K	25 K	35 K
27	10 K	30 K	40 K
15	10 K	30 K	60 K
10	15 K	40 K	80 K

base temperatures were 5.5 K, 12 K, and 35 K for the deuterium, methane, and neutron guide heat exchangers respectively. Once the cryostat reached base temperatures and the helium inventory had been condensed, the liquefier power was reduced, allowing the system to operate in steady-state mode, maintaining the net liquid helium inventory.

Heater power versus equilibrium temperature was then characterized for each cooling loop for several helium flow rates. During the measurements, typical return gas flow rates were 10 liters/min of gas at standard temperature-pressure (STP) for both the N- and C-loops. (We are unable to measure the cold D-loop return flow).

The system was able to maintain the desired temperatures in the cryogenic volumes with applied electric heater power well above the expected reactor heat load. The methane container requires the largest range of temperature control, so a subset of the heater power and helium flow versus temperature is shown in Table 4.1. A heater power of up to 10 W did not affect the temperature of the deuterium container, roughly the load expected during reactor operation.

These tests also showed that our parallel cryogenic loops allow independent temperature control of all three heat exchangers over a wide range of helium flows without disturbing the stability of the liquefier operation.
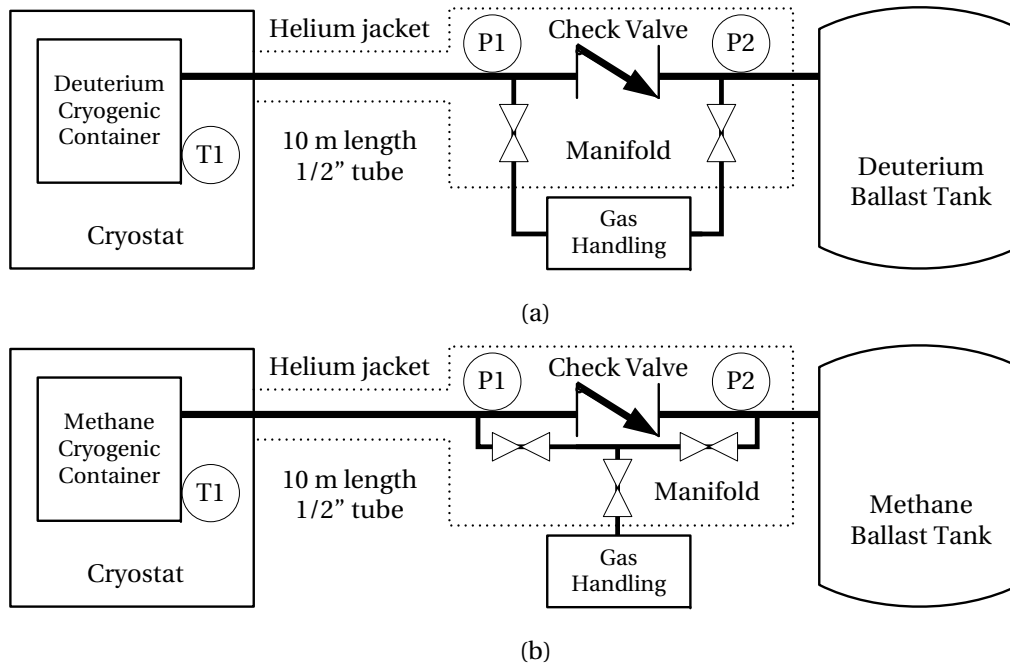
Figure 4.11: Simplified schematic diagrams of the (a) deuterium and (b) methane gas handling systems. "P1," "P2," and "T1" are abstractions of the existing instrumentation. The full gas handling diagram is given in Appendix A.2.

4.3 Gas handling

4.3.1 Description

Gas handling systems were designed and built to facilitate preparing and introducing deuterium and methane into the cryostat. The design of the deuterium gas handling system is based on the UCN source at the Los Alamos Neutron Science Center (LANSCE) [94, 173], and the methane gas handling system on the Low Energy Neutron Source (LENS) at the Indiana University Cyclotron facility [15, 89, 129].

The design of the gas handling systems for methane and deuterium both follow the same logic, shown in Figure 4.11. The full gas handling diagram is given in Appendix A.2. Each system has a ballast tank that is filled from high pressure cylinders via the gas handling panel to measure out a well-defined gas inventory given by the known tank volume and pressure, "P2" in Figure 4.11. The solid, cryogenic targets are prepared by permitting gas to flow, driven by the cryopumping of the
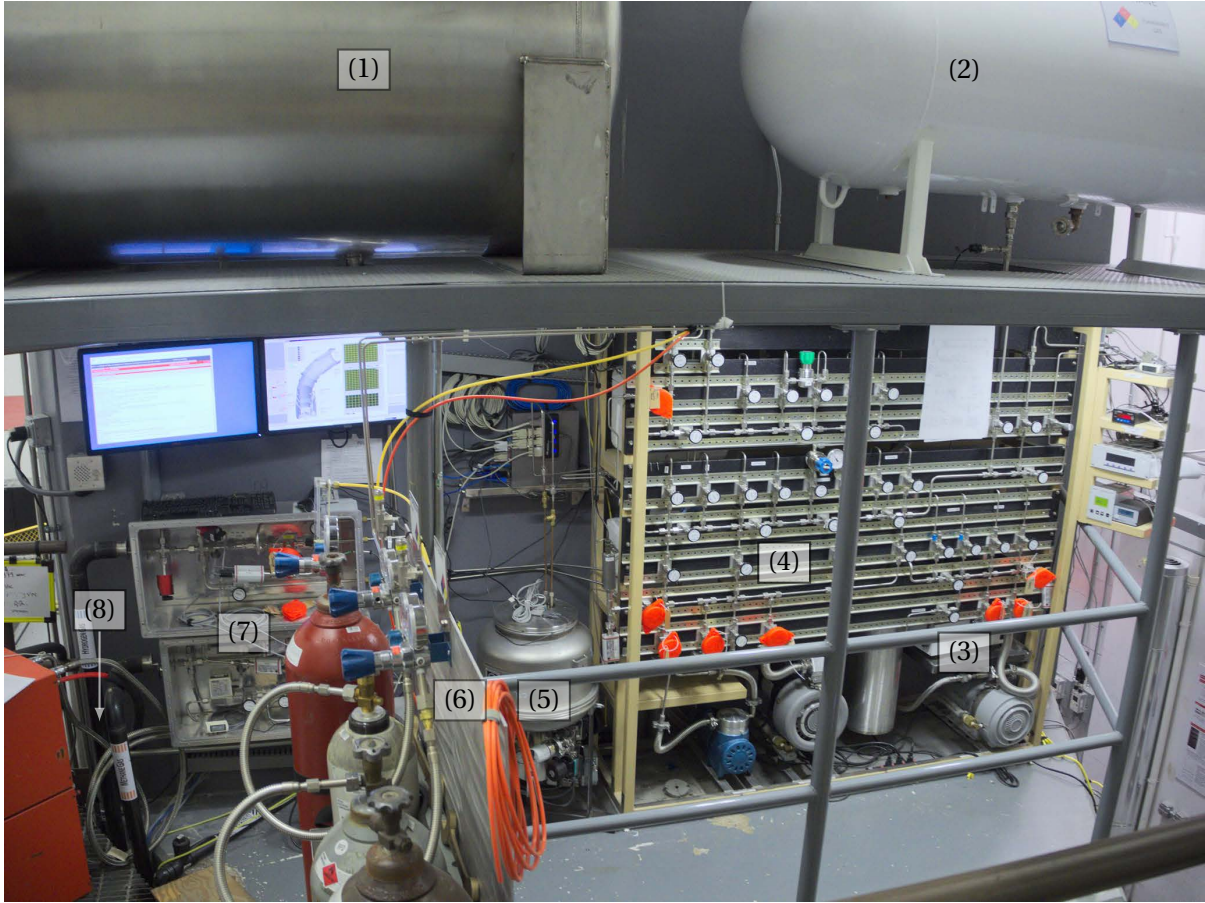
Figure 4.12: Photo of the gas handling systems area. Clockwise from the top is the (1) deuterium ballast tank, (2) methane ballast tank, (3) methane gas handling panel, (4) deuterium gas handling panel, (5) deuterium spin converter, (6) high pressure gas cylinders, (7) deuterium and methane manifolds inside helium-cover boxes, and (8) the direction of the helium covered connections to the cryostat.

cryostat, from their ballast tanks into their cryogenic volumes opposite the direction of the check valves. At the end of operation, the crystals are warmed through their melting and boiling points and the gas expands back into the ballast tanks through a check valve. Deuterium is stored in its ballast tank between operational runs, while methane is typically discarded.

The systems differ in the components of the gas handling panel and the panel's connection to the manifold box. As methane is always first liquefied, the gas flows directly through the manifold box and the ballast tank reflects the saturation pressure. The deuterium gas requires preparation, and may be sublimated at a lower pressure than the ballast tank, and so always flows through the gas handling panel.

Figure 4.13: (a) A CAD cross-section of the liquid nitrogen gas trap and styrofoam container and (b) a photo during assembly.

Panel components

The deuterium gas handling system includes many components which require flexibility in their use, so each was given an inlet, outlet, and bypass valve. A model "Mr. Hydrogen" palladium filter[1], provides purification of hydrogen (although cannot distinguish between hydrogen isotopes). Custom liquid nitrogen traps are placed both before and after the palladium filter to freeze out particularly hydrocarbons that could be introduced from the gas cylinder and palladium filter. The traps are stainless cylinders packed with copper wool suspended in a liquid nitrogen-filled styrofoam container, Figure 4.13, located behind the panel. An aluminum KNF model N143AN diaphragm pump may be used both to build pressure for the palladium filter and to recover deuterium remaining in the cryostat back to the ballast tank. The *para*-to-*ortho* converter is discussed later.

The deuterium ballast tank, built by Carolina Mechanical Services, is stainless pharmaceutical-grade and $1.8\,\text{m}^3$ in volume. The methane tank is a repurposed 250 gallon propane tank. It was flipped upside down to access the ports, and unused ports were capped.

All shutoff valves are Swagelok BG series stainless bellows-sealed valves. A Swagelok BMRW regulating valve was installed first and provided suitable control at the higher pressure required for liquefying. A Swagelok BMW metering valve currently provides flow control at the lower output pressures of the *para*-to-*ortho* converter, although it is not suitable for condensing liquid deuterium. A Sierra model 822S flowmeter measures the flow of deuterium into the cryostat up to $2\,^\text{L}/_\text{min}$ (STP), and an integrated flow can provide an estimate of the deuterium volume condensed.

---

[1]REB Research, www.rebresearch.com

69

A Swagelok series KPR 0 psig to 50 psig regulator before the palladium filter provides rough regulation from the high-pressure cylinder or diaphragm pump. A Matheson model 3494, 28" Hg vac–15 psig, absolute-pressure regulator provides fine control of the *para*-to-*ortho* converter inlet.

The methane gas handling system is far less sophisticated, including a dry-ice cooled gas trap, a volume for preparing gas mixtures, and a means for introducing helium to cover the frozen methane. The methane system does not require flow control, although the same model flowmeter is present.

The spring force of the return check valve is responsible for both setting its opening pressure and maintaining a seal in the reverse direction; a valve with a lower cracking pressure will typically re-seal less reliably. However, when the targets are warmed, the pressure in the cryostat will rise to the valve's cracking pressure above the ballast tank pressure. This is particularly a concern for the deuterium system. If a partial inventory is stored in the ballast tank, for example if condensation was not completed, a high pressure valve will put strain on UCN window foil. This prevents the use of a higher pressure check valve, and as such re-sealing will always be a problem to some extent. Resealing is then considered in the procedures. The return check valves were initially Swagelok CW series welded-poppet check valves with a cracking pressure of 140 mbar. However, the seal when closing proved unreliable, allowing gas to be cryopumped into the cryostat when not desired. These were replaced with Swagelok CH series check valves; the methane system has a cracking pressure of 350 mbar and the deuterium system 70 mbar.

Great care was taken in maintaining the cleanliness of the systems. Both gas handling systems are made entirely from instrumentation grade stainless tubing and almost exclusively with orbital welds and Swagelok VCR metal gasket seals. This is critical for the deuterium system, where deuterium is recycled and its purity over a long operational time is required to maintain performance. Heat sensitive instrumentation was placed around the perimeter of the panel to allow the panel to be completely baked without damaging them.

Instrumentation

The pressure gauge "P1" in Figure 4.11, measuring pressure above the cryogenic containers, is located at room temperature roughly 10 m away from the cryogenic volumes . While condensing, and later warming, "P1" and "T1" should show good agreement with the saturation vapor pressure.

In the methane gas handling system, the ballast tank, cryostat-side, and gas handling pressure gauges are all Pfeiffer model RPT100 piezo/pirani combination gauges with a range of 10^{-4} mbar to 1200 mbar. The deuterium gas handling system uses the same piezo/pirani combination gauges on the ballast tank and gas handling panel. In addition, the gas handling panel is redundantly read by a Mensor model 6000, 0 psia to 60 psia gauge. The deuterium cryostat-side requires the greatest precision as pressure affects sublimation and the measurement may be used to determine the temperature of the surface of the crystal. A Pfeiffer model CMR361 10^{-1} mbar to 1100 mbar

capacitance gauge and a Pfeiffer model CMR363 1×10^{-3} mbar to 11 mbar capacitance gauge are used in parallel. Initially a Pfeiffer model CMR365 10^{-5} mbar to 0.11 mbar was used instead of the CMR363, however this choice resulted in gap in the sensing range around 0.1 mbar that proved critical.

The RPT100 gauges are all read on a Pfeiffer model DPG109 controller. The capacitance gauges, along with Pfeiffer model PKR251 capacitance/pirini combination gauges on the cryostat and *para*-to-*ortho* converter vacuum jackets, are read on a Pfeiffer model TPG256 controller.

Panel

Because of the size of the gas handling panel and the large number of valves, we took a non-traditional approach to mounting small components to the panel. Components are bolted to small aluminum plates that are then clamped between rows of standard DIN rail[2]. This allows components to be placed on the panel without modifying the panel and without access to the rear of the panel, making modifications easier and, by loosening the rails, allowing expansion during bakeout. The horizontal rails do however limit vertical freedom, most noticeable when using VCR components of standard length. (A more flexible modification would be to place narrower rails close together for clamping bolt heads or T-nuts and machine vertical slots in the aluminum mounting plates.)

4.3.2 Procedures and safety

These systems present several safety concerns that were addressed. First, both methane and deuterium expand by hundreds of times during the phase change from liquid to gas, and in the confined volumes of the cryogenic containers, can generate a large pressure increase. As in Figure 4.11, check valves provide an always available route for gas to expand directly back into the ballast tanks. Uncontrolled warming, for instance due to a cooling failure, is passively expected by design, and in regards to gas flow, is identical to a planned warm-up.

There are valves for maintenance and deuterium storage that could potentially block this relief route. These valves are locked-out and procedures were established for their use. In the event of an unexpected blockage, the foil UCN window doubles as a burst disk into the vacuum jacket. It is not possible to cool the UCN window below the freezing point of deuterium, and the UCN guide diameter is very large, and so it cannot be blocked by solid deuterium. The methane container does not have a burst disk as it is itself a thin-walled aluminum container. The methane gas inlet tube is designed as the largest source of heat input, staying warmer than the container and discouraging blockage. Should the cryostat vacuum jacket be sealed, and either of these volumes ruptures, an independent relief path is provided back to the methane ballast tank.

---

[2]Our thanks to Paul Carter at TUNL for his help with construction.

Figure 4.14:   Photo of the exhaust line and flame arrestor entering the blower fan to the external stack.

Second, both gases are potentially flammable. Either a gross leak into the ballast tank, or a leak cryopumped into the cryogenic volumes over an extended operational run, could produce a flammable mixture. While both gas systems are designed as closed systems, and helium leak-tested for integrity, several valves are required for filling, evacuating, and sampling that are potentially open to atmosphere. These valves are also locked-out and procedures were established for their use. In the worst case, burst disks on both ballast tanks provide a relief path. It should be noted that small leaks are operationally problematic long before becoming safety concerns.

In addition, if the system is to be operated for an extended period, the gas line from check valve to cryostat is housed within a jacket that can be filled with an overpressure of helium gas. This prevents a leak from cryopumping oxygen into the cryogenic containers, and since the cryostat is necessarily above the liquefaction temperature of helium, provides measurable feedback of a large leak.

A few other safety features were also implemented. As many panel components are not high-pressure rated, the gas cylinders have low pressure regulators whose maximum output pressure is below the limits of the system. Should a regulator fail open, relief valves are installed on the regulators' outlet. Cylinders are also provided with flow restrictors from the gas supplier.

To evacuate and dispose of either gas, an exhaust system was built to remove the gas from the reactor hall. Gas is evacuated from the methane and deuterium gas handling panels independently by Varian model SH110 and Varian model TriScroll 300 scroll pumps respectively. Both pumps include anti-suckback valves should either pump fail. The gas is actively mixed with nitrogen, transported 15 m through a 1-1/2" schedule 40 ABS pipe, through a SuperFlash model Demax flame arrestor, and finally dumped into a ventilation stack that exhausts outside of the building, Appendix A.3.
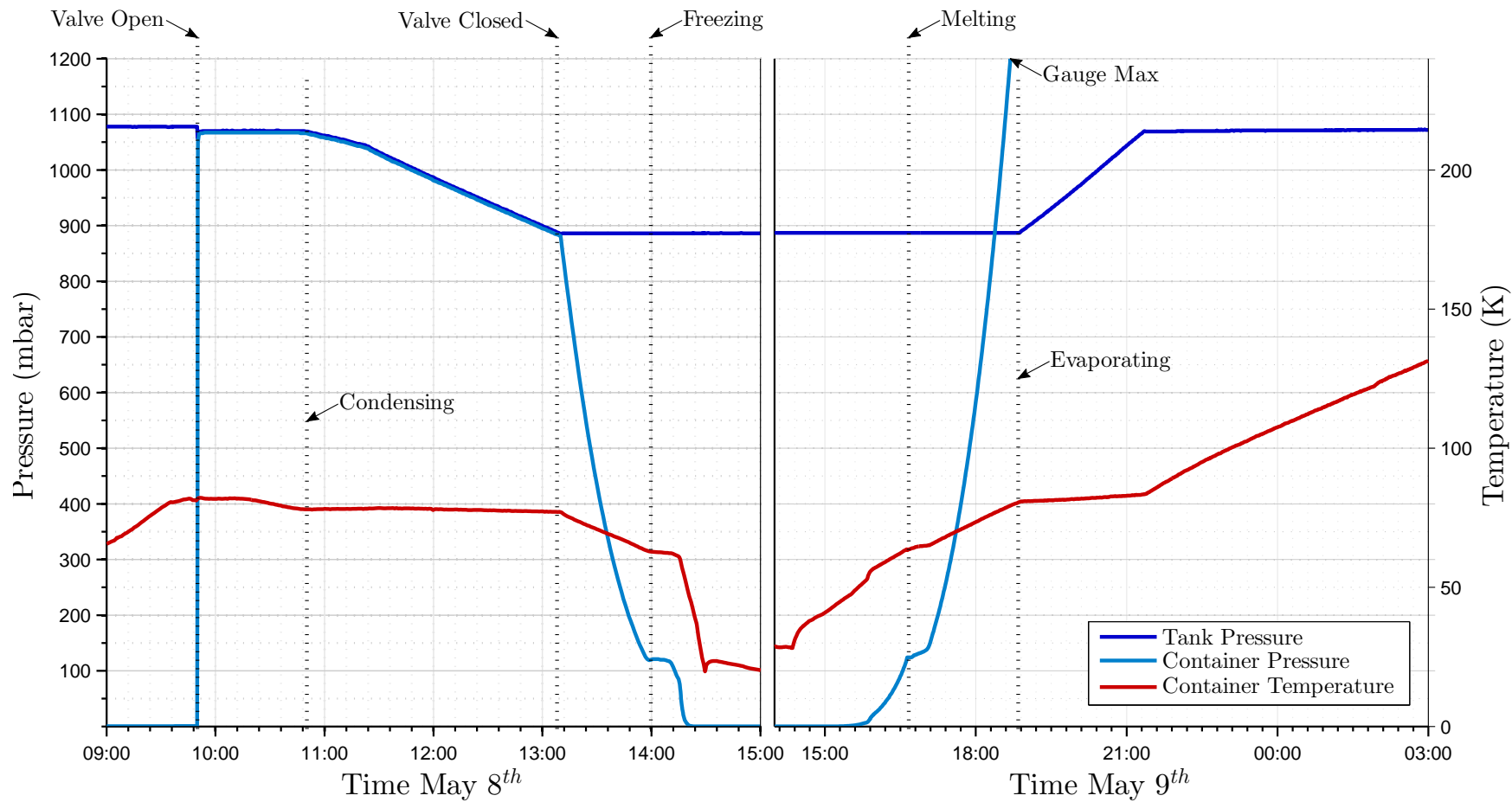
Figure 4.15: Measured pressures and temperature of nitrogen in the methane container while cooling and warming. Note the time axes are different.
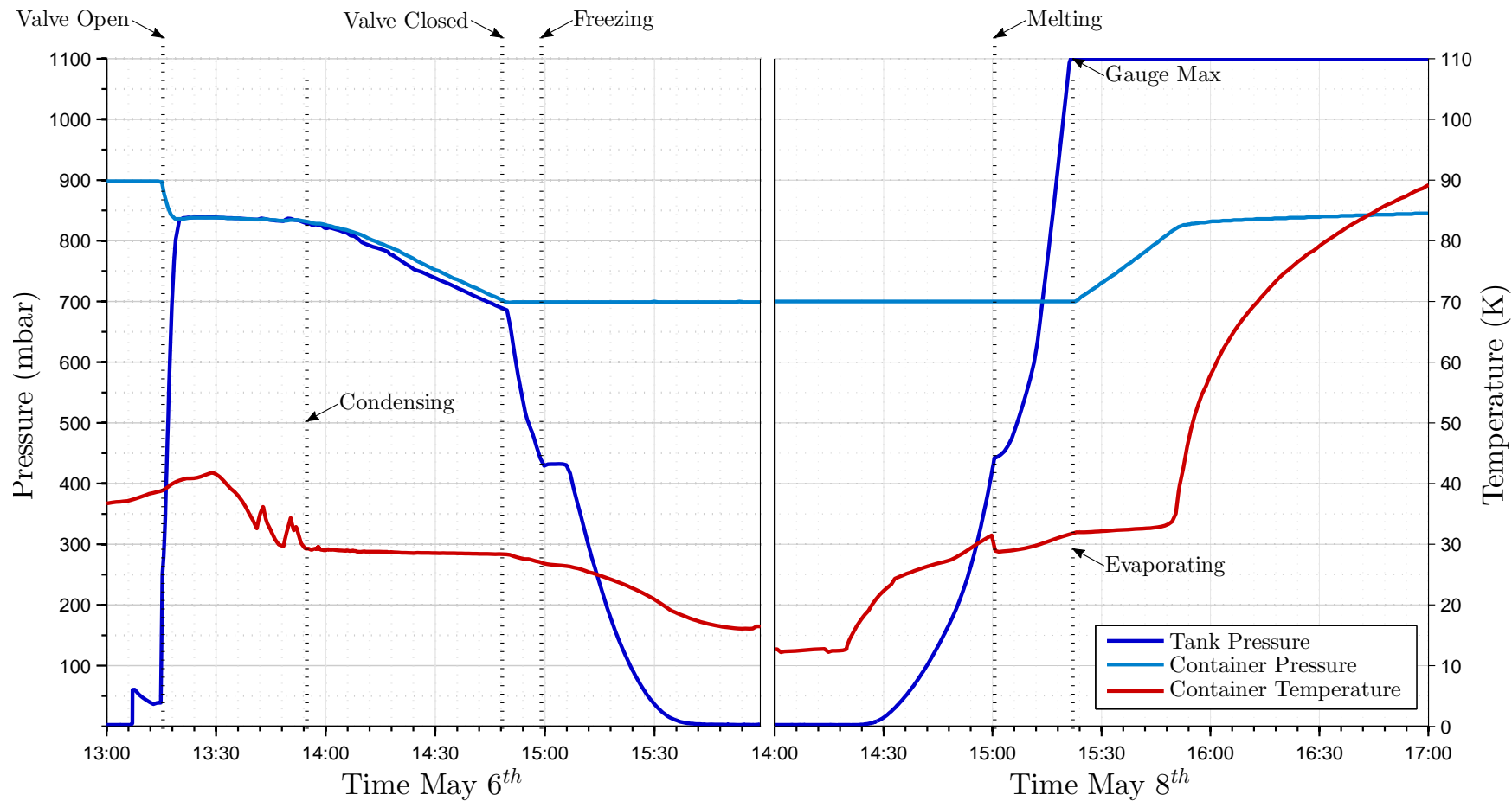
Figure 4.16: Measured pressures and temperature of neon in the deuterium container while cooling and warming.
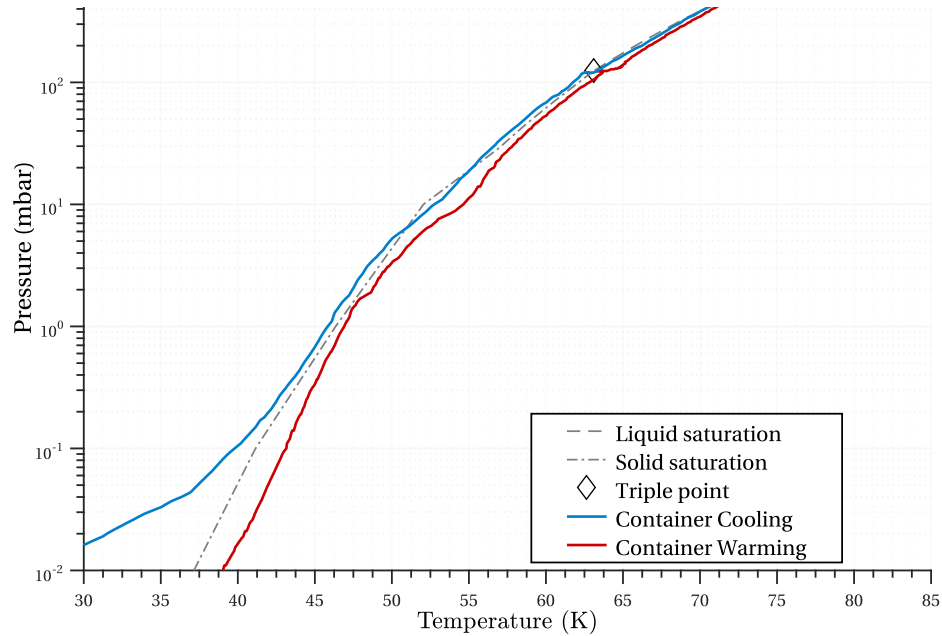
Figure 4.17:   Pressure versus temperature of nitrogen, compared with its saturation pressure, while condensing and warming nitrogen in place of methane.

4.3.3   Initial tests

Prior to condensing flammable methane and deuterium, to demonstrate the integrity and performance of the system, the gas handling systems were first used to condense nonflammable gases into the cryostat, nitrogen in place of methane and neon in place of deuterium. Both were first liquefied, then allowed to freeze while valved off from their ballast tanks. After some period at minimum temperature, the gases were allowed to warm passively, demonstrating the safe design of the system.

Data for gases in both containers showed easily identifiable phase transitions, Figure 4.15 and Figure 4.16, as well as good agreement with their saturation curves, Figure 4.17 and Figure 4.18. This shows that gases are saturated and near equilibrium with their cryogenic containers, an assumption necessary for modeling condensation, and that the pressures measured at the gas panel are an accurate representation of the pressures in the cryostat's containers.

Both flammable cryogens were then condensed. Methane and unconverted, liquid deuterium behaved as expected. However, when cooling solid deuterium, or sublimating deuterium, the container temperature did not always reflect the measured pressure. For example, Figure 4.20 shows a deuterium crystal warmed to melting point and then cooled again. This is addressed in detail in Chapter 5.
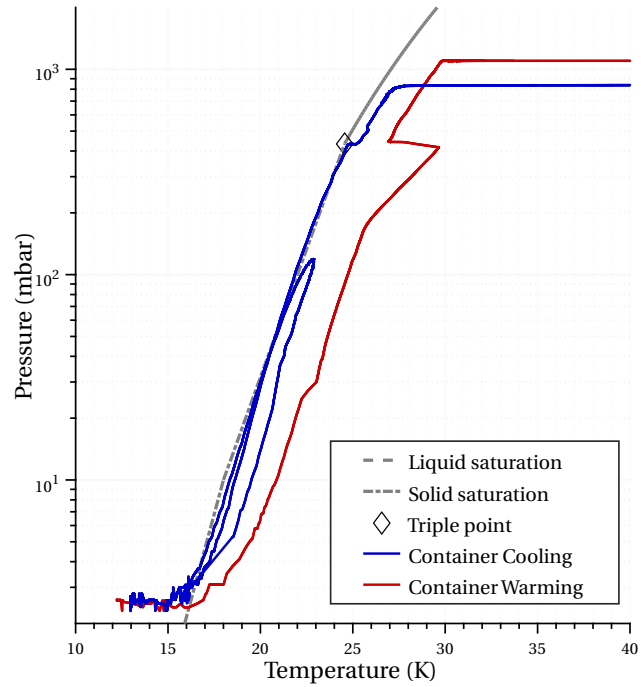
Figure 4.18: Pressure versus temperature of neon, compared with its saturation pressure while condensing, annealing, and warming neon in place of deuterium. The lowest pressures shown in the D_2 container are at the minimum of the high-range pressure gauge.
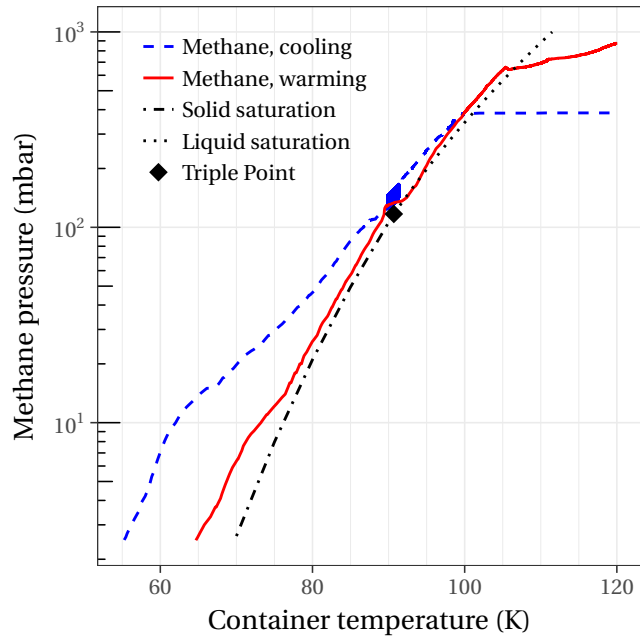
Figure 4.19: Pressure versus temperature of methane, compared with its saturation pressure, while condensing and warming.

77
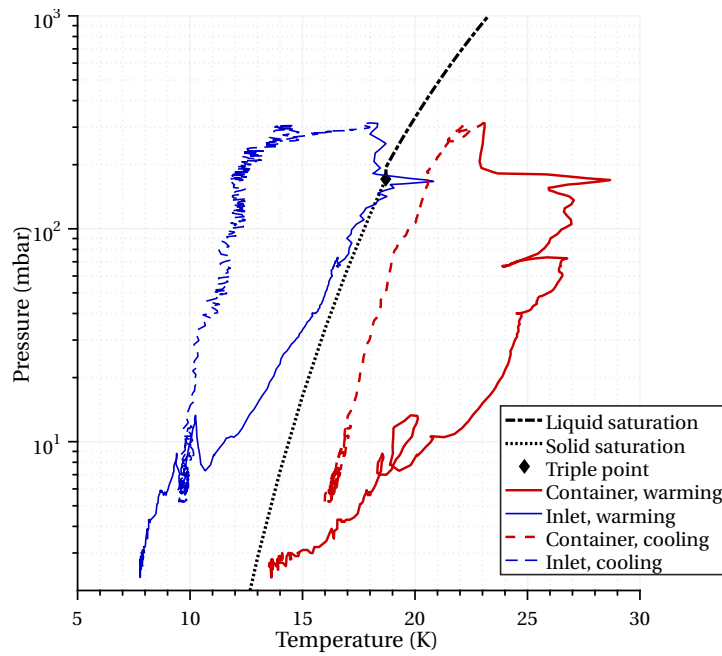
Figure 4.20:   Pressure versus temperatures of deuterium, compared with its saturation pressure, while warming a crystal to the melting point and cooling again. Temperature is measured both at the helium inlet and at the top of the container.

4.4   Spin conversion

4.4.1   Hydrogen spin isomers

Chemically pure hydrogen appears as diatomic molecules of the isotopes, in particular for this context: protium, $^1H_2$, deuterium, $^2H_2$ or D_2, and hydrogen deuteride, $^1H^2H$ or HD. In a wonderful display of quantum mechanics, the rotational excitations of the symmetric molecules couple with their nuclear spin to produce dramatic behavior at low temperature, but this behavior is not present with the asymmetric HD molecule.

$$\Psi_{\text{total}} = \psi_{\text{electronic}} \cdot \psi_{\text{rotation}} \cdot \psi_{\text{vibration}} \cdot \psi_{\text{spin}} \quad\quad (4.1)$$

Nucleons are indistinguishable fermions with ½ spin, so the atomic protons in the hydrogen molecule follow Fermi-Dirac statistics. Deuterons, with their extra neutron and integer nuclear spin, must obey Bose-Einstein statistics in the deuterium molecule. The total wavefunction of the deuterium molecule, including contributions from the molecular rotation and nuclear spins as in Equation 4.1, must be symmetric under permutation of the deuterons. This imposes restrictions on the molecular rotational state, J. The symmetric, even-numbered rotational levels, including the $J = 0$ ground state, must be paired with symmetric nuclear states, while the antisymmetric, odd-numbered rotational levels must be paired with the antisymmetric nuclear state. The electronic and vibrational components are always symmetric. Therefore, while changes in rotational number of ± 2 are readily allowed, changes in rotational number of just ± 1 would require a deuteron to change its nuclear spin. This effectively makes the even and odd rotational states independent species. The even rotational states ($J = 0, 2, ...$) are called *ortho*-deuterium, o-D_2, and the odd rotational states ($J = 1, 3, ...$) are called *para*-deuterium, p-D_2 [82]. This is opposite the familiar nomenclature of hydrogen, where the ground state is *para*-hydrogen. The prefix of *ortho* is applied to the states with the larger nuclear degeneracy and statistical weight, and *para* to the smaller [68].

The hydrogen molecule, analogous with a two electron system, forms triplet and singlet spin states for the odd-J and even-J rotational states respectively. At room temperature, molecules possess many units of angular momentum and so fill energy levels evenly in a Maxwell-Boltzmann distribution. The three-fold degeneracy of the triplet state compared to the non-degenerate singlet state means we expect to see a 1:3 ratio of the even-J states to the odd-J states. Likewise, *ortho*-deuterium with non-degenerate $S = 0$ and five-fold degenerate $S = 2$ states, and *para*-deuterium with a three-fold degenerate $S = 1$ state, have a 1+5:3 or 2:1 *ortho*-to-*para* ratio at room temperature. This high-temperature *ortho*-to-*para* ratio is called "normal" deuterium, denoted n-D_2.

Remarkably, if there is no fast mechanism present allowing for spin flips, this ratio will remain even after the deuterium is cooled to a temperature well below the energy of the $J = 1$ state [137]. When cooled sufficiently, *ortho*-deuterium will populate to the ground state $J = 0$. However *para*-deuterium, limited to changes in angular momentum of ± 2, will populate the $J = 1$ state with 7.4 meV.

This phenomenon was explored in the first hydrogen liquefiers. Liquid hydrogen was lost from storage dewars at a significantly faster rate than helium. The slow, natural conversion released this energy over time, evaporating the liquid [48]. (A significant problem for the storage of rocket fuel, for example.) Thankfully, this conversion can be accelerated and significant work was done on suitable catalysts and converter designs [171].

This conversion would have to be re-addressed with the deuterium-based UCN sources. The energetic *para*-deuterium provides a significant and unwanted channel for neutron upscattering via a spin flip to the *ortho* state, dramatically reducing UCN yield [93, 107, 147].

4.4.2 Spin state conversion

A nuclear spin flip, and therefore a *para*-to-*ortho* or *ortho*-to-*para* conversion, can be induced with a magnetic or electric field gradient. Magnetic dipoles and magnetic and electric quadrupoles present in *para*-deuterium and $S = 2$ *ortho*-deuterium can provide this gradient during molecular collisions. However conversion through these mechanisms happens at a very slow rate; the total rate constant for this $J = 1 \rightarrow 0$ relaxation is roughly 0.06 %/h in solid deuterium and unmeasurable slow in gas [147]. A faster rate may be provided by material walls or magnetic contaminates like oxygen. A radiation field will also facilitate *para*-to-*ortho* conversion, but is also too slow to be a practical solution at our source due to the small radiation flux. A dedicated converter is necessary.

A particularly efficient way to accelerate this process is to utilize the paramagnetism of a material as a catalyst. At a temperature below the $J = 1$ energy, with spin flips provided for by the catalyst, deuterium will approach an equilibrium ratio predominately in the $J = 0$ ground state, the *ortho* state. Potentially very high *ortho*-to-*para* ratios can be made by converting using a catalyst at very low temperature, e.g. 4.2 K, although a real converter may not practical below the triple point, 18.7 K. At the triple point temperature, the equilibrium ratio, denoted e-D_2, is 1.5 % *para*-deuterium. Although not directly useful for us, high percentage *para*-deuterium can be prepared by selective adsorption on certain materials [147, 158].

Work in the 1930s determined that for a catalyst to be effective, in addition to magnetic susceptibility, the material needed active surface adsorption. As proof, materials whose surfaces only became activate adsorbers above a certain temperature would not convert unless above that temperature [160]. The requirement of surface activity also means that catalysts will lose their conversion

power over time as active sites become filled by contaminants [157]. The catalyst can be regenerated, usually by baking under vacuum. A smaller granule size, and so larger surface area also improves conversion efficiency [170], although very small particles can potentially limit flow and contaminate other parts of the system.

Chromium(III) oxide gel was one of the first effective catalysts discovered [62, 159]. It was also found that many of the metallic oxides were good catalysts, in particular, iron(III) hydroxide [48, 159]. Both chromium(III) oxide and iron(III) hydroxide were common catalysts in practical hydrogen liquefiers [138, 170], and both remain common choices for UCN work [8, 53].

Based on the previous work of C.-Y. Liu and others [8, 94], a converter was developed to prepare deuterium to very high *ortho* fraction. A custom Raman spectroscopy setup, discussed in Section 4.5, was used to monitor the *para*-deuterium and hydrogen content. Both of these catalysts were prepared and tested, showing comparable converted *para*-to-*ortho* fractions.

4.4.3   Spin converter design

Our *para*-to-*ortho*-deuterium spin-state converter (informally "PO converter"), pictured in Figure 4.21, consists of a U-shaped copper cell with inlet and outlet gas lines, filled with a catalyst, and connected to the cold head of a cryopump. Gas can move through the converter in two different modes. Deuterium can be condensed and then evaporated in a batch process, or flow continuously while operating at the triple point of deuterium. The catalyst allows for spin flips, and at low temperature, deuterium rapidly reaches equilibrium with a large percentage of the lower energy *ortho* state.

We first attempted to solder prefabricated copper components, but it proved difficult to make reliably leak-tight. Instead, the cell was machined from a solid block of copper, which has the positive side-effect of significant thermal mass. Three 1.75 inch diameter bores form a U-shaped void roughly 0.5 liters in volume. The two parallel bores form the inlet and outlet on the top of the cell, see Figure 4.22. A lead-sealed lid covering these openings connects to $1/4$ inch tubes, an inlet and outlet from the heat exchanger, and a third going immediately to a burst disk. To save space, the lid is a single flange with the two bolt circles overlapping to form a figure eight pattern. Inside the cell, all three tubes are covered by fine aluminum wool held in place by copper mesh, Figure 4.23. This prevents small catalyst particles from migrating out of the cell and up-converting deuterium in a warmer region.
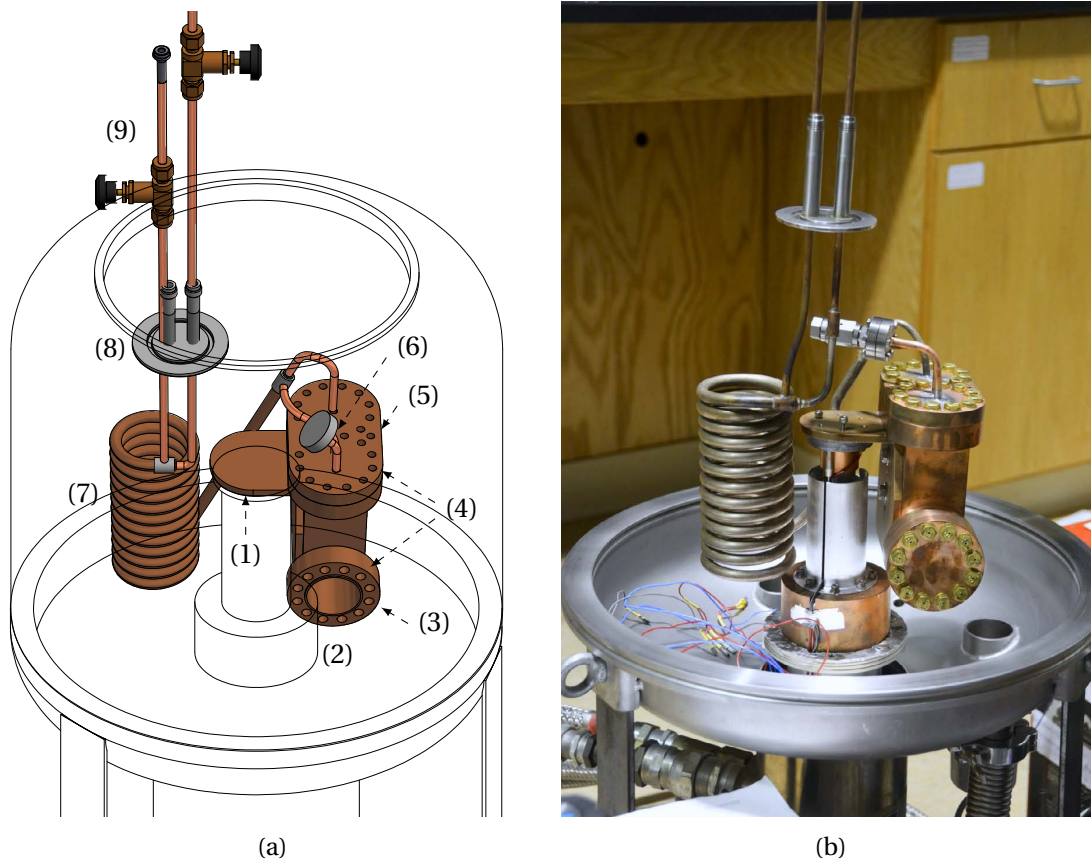
Figure 4.21: (a) A CAD rendering of the deuterium spin-converter and (b) a photo of the converter with the vacuum jacket removed. Labeled are (1) the cryopump second-stage cold-head, (2) catalyst cell, (3) blank flange (before the addition of the lower burst disk), (4) locations of the cell temperature sensors, (5) location of the electric heater, (6) lid burst disk (capped in photo), (7) tube-in-tube heat exchanger, (8) vacuum jacket gas feedthrough, and (9) disconnect valves (not pictured in photo).

The burst disk is a 0.002 inch copper foil soldered to a 1.33" ConFlat gasket, see Figure 4.24. A custom ConFlat flange was machined with knife edges on both sides, and tapped bolt holes rotated 30°. This allowed the disk to be leak tested separately and installed, without dismounting the burst disk, using the ConFlat flange on the opposite side. The perpendicular bore opening, necessary for machining, is capped with a lead-sealed blank flange. A second burst disk was added to this flange by soldered a 0.004 inch thick copper foil to the inside of a 0.64 inch inner diameter hole.

The electrical feedthrough on the cryopump vacuum jacket allows four 2-lead diode temperature sensors, LakeShore DT-470-SD, and one heater circuit. One sensor is mounted directly to the cold head, one to the lid of the cell, and a third to the bottom of the cell, see Figure 4.25. (A fourth sensor is mounted to the cryopump's first stage radiation shield, however the sensor has a short circuit with
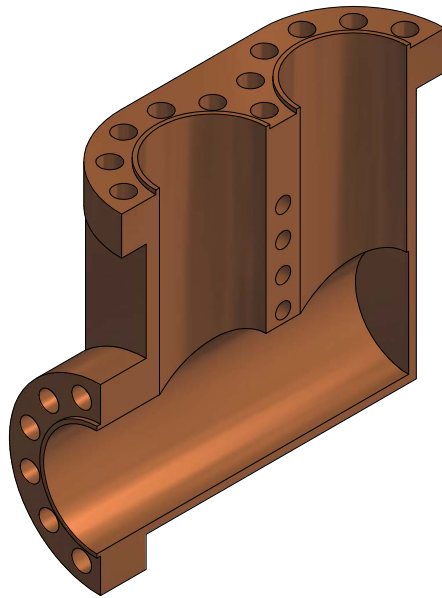
<center>(a)</center>
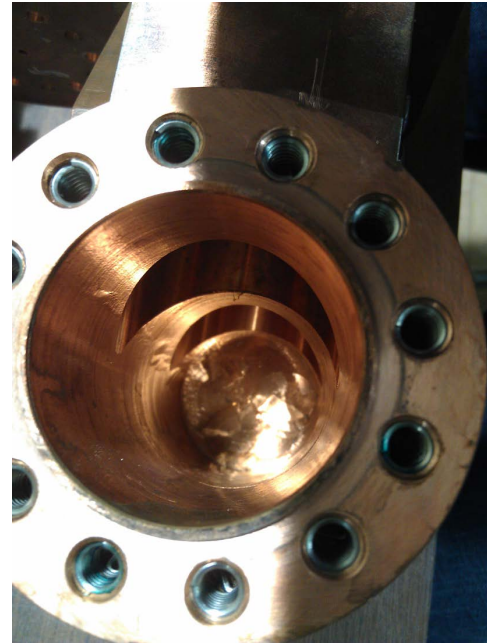
<center>(b)</center>

Figure 4.22: (a) Cross-section drawing of the spin-converter cell and (b) a view down the bottom horizontal bore of the cell.

<center>(a)</center>
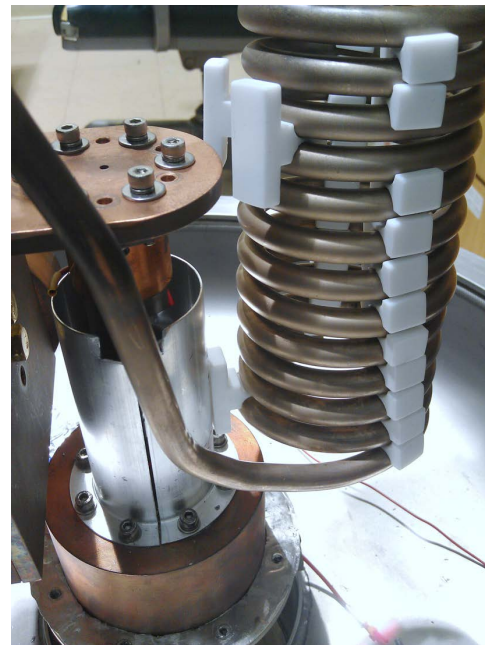
<center>(b)</center>

Figure 4.23: (a) Photos of the copper mesh and aluminum wool on the inlet line inside the spin-converter lid and (b) teflon spacers for heat exchanger.
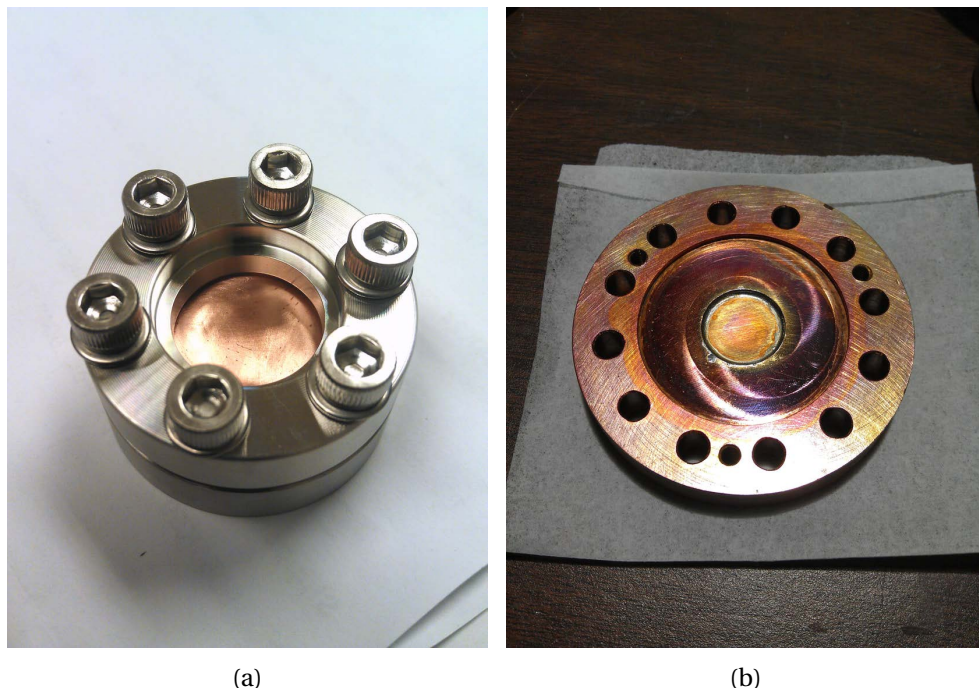
Figure 4.24:   (a) Photos of the spin-converter lid burst disk inside its ConFlat housing and (b) burst disk on the bottom horizontal bore flange.

its packaging and proved unreliable.) There is also a hydrogen vapor pressure sensor mounted to the cold head that proved unreliable. A $50\,\Omega$ cartridge heater, LakeShore HTR-50, is mounted to the lid with a clamp to provide temperature control. A LakeShore 335 temperature controller provides a temperature control feedback loop using the sensor mounted to the bottom of the cell.

A coaxial (tube-in-tube) counter-flow heat exchanger cools the incoming gas. Copper wire was wrapped in a large-pitch spiral around the inner $1/4$ inch tube to center it within the outer $3/8$ inch tube. (Both tubes have 0.035 inch wall thickness). The coaxial tubes were filled with water, frozen in liquid nitrogen, and wrapped around a mandrel to form to shape. The heat exchanger is allowed to support its own weight, with teflon spacers to avoid thermal contact with the rest of the cold head, Figure 4.23.

An L-shaped bracket connects the cell to the head of the cryopump. The cell and heat exchanger assembly mounted on the cold head fits inside the cryopump's vacuum jacket, see Figure 4.26. The cryopump is a Leybold RPK with Leybold RW3 helium compressor[3]. A Pfeiffer Vacuum, Inc. turbopump is connected directly to the vacuum jacket and is backed by a pumping station including a diaphragm roughing pump. A diagram is given in Appendix A.1.

---

[3]Our thanks to the IU Cyclotron staff for lending us two of these units.

(a)   (b)
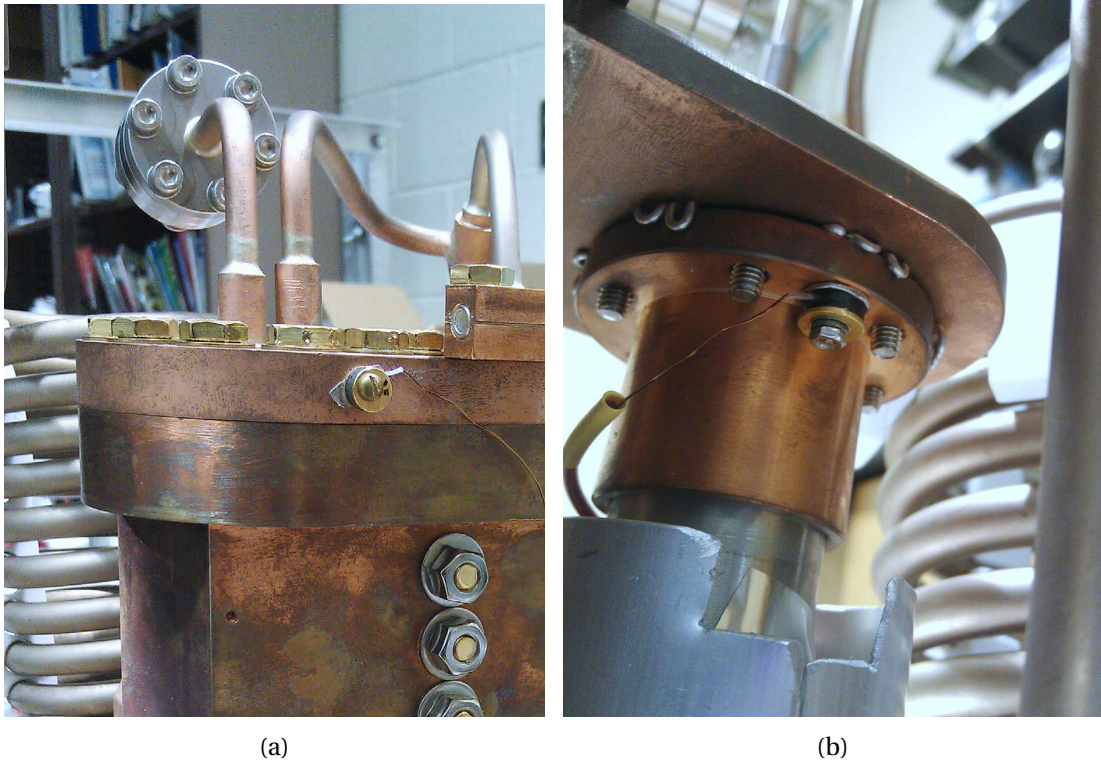
Figure 4.25:   (a) Photos of the heater mounted to the spin-converter cell lid and temperature sensors on the lid and base of the cell, as well as (b) the sensor mounted to the cold head.
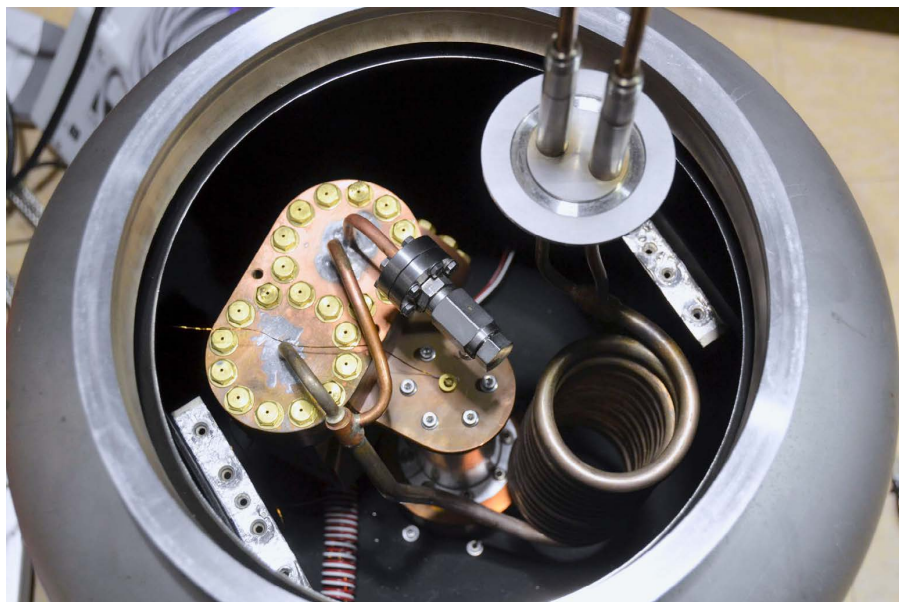
Figure 4.26:   Photo of the spin-converter cell and heat exchanger mounted inside the cryopump vacuum jacket. The burst disk is capped in this photo.

Figure 4.27:   Photo of glass Oxisorb canisters .

Two quick-connect tube-adapters mounted on a KF50 flange serve as a vacuum jacket feedthrough for the inlet and outlet gas lines. The KF50 flange extends inside the vacuum jacket, requiring an overpressure support-ring around the O-ring, allowing the vacuum jacket lid to be removed without removing the quick-connect tube fittings, see Figure 4.21. This configuration allows the cell to remain sealed by two disconnect valves on the inlet and outlet that also fit through the KF50 flange in the lid.

4.4.4   Oxisorb

Oxisorb overview

Various chromium oxides have historically been common choices due to commercially availability [49]. Likewise, chromium oxide is commercially available today as Oxisorb®, manufactured by Messer Griesheim GmbH, Germany, and available to us locally through GTS-Welco. It is an oxygen scrubber intended primarily for gas flow applications. Oxisorb is appealing as a commercially available and stable manufactured product. This is the catalyst material used by the PSI and Mainz groups [8, 33] in some hydrogen liquefiers [32], and is being considered for the European Spallation Source (ESS) [53]. The Oxisorb product consists of silica (SiO_2) gel granules (a water absorber) impregnated with the chromium (II) oxide, CrO.

The product is very hygroscopic, so the canisters were opened and filled in a nitrogen glove box. They can be easily opened by using a tube cutter on the metal end cap. Chromium oxide is brown to red in color, although the glass canisters purchased appear green because they contain a color changing oxygen indicator that turns brown to black once exposed to oxygen. The Oxisorb available in metal canisters may not have this indicator. The glass canisters are nominally 80 mL in volume, Figure 4.27, and the contents of six canisters, loosely packed, filled the cell roughly halfway up the vertical bores.

Oxisorb test

To test the converter separate from the Source gas handling system, one line was capped, and the other end was connected to a 1 L sample bottle, high pressure gas cylinder, pressure gauge, and vacuum pump. Gas can be condensed in a similar manner to a batch process mode with the gas handling system. The cell was initially cooled while empty, without a catalyst, with first nitrogen gas then deuterium gas to verify the pressure and temperature followed the vapor saturation curve.

Several cooldowns were then performed with the Oxisorb-filled cell. The first is outlined here. The cell was initially full of nitrogen gas from loading the catalyst in the glove box. The cell was baked at 350 K for 4 h while pumped until the pressure dropped, then cooled with the cryopump to 30 K, still well above the boiling point of deuterium. An atmosphere of deuterium was allowed into cell. After 5 min, the pressure had dropped below 10 mbar. Deuterium was repeatedly introduced and allowed to sit in the converter, and the pressure drop grew slower with each subsequent fill. Remarkably, after allowing roughly 10 g into the cell, the pressure was still very slowly dropping. The cell was cooled to 20 K, the valve closed, and the rest of the system evacuated.

After 40 min, the valve was opened and the cell warmed to 30 K. The pressure only rose to a few hundred millibar, but a higher pressure is desirable for Raman spectroscopy, so the cell was further warmed to roughly 40 K until the sample bottle could be filled to 1000 mbar. The system was evacuated and warmed, and when it had reached room temperature, filled to 500 mbar with deuterium to avoid storing the catalyst under vacuum.

Raman spectroscopy showed a *para*-to-*ortho*-fraction of less than 2%. The Oxisorb catalyst converts as expected, and quickly warming the cell to extract gas did not significantly up-convert the sample.

The large pressure drop is due to adsorption by the Oxisorb, and it is strongly temperature dependent. This is essentially what the product is designed to do as a gas scrubber; the large surface area that allows for physical adsorption, or physisorption, of gas and so is also ideal for rapid conversion. However the very large amount of gas stored was surprising, and requires consideration.

Figure 4.28:   Granules of iron hydroxide .

For determining the amount of solid deuterium held in the cryostat, this amount will need to be considered in addition to the pressure drop in the ballast tank. Also, the pressure does not follow the vapor pressure curve, and so cannot be used as an indicator of temperature, making it more difficult to pinpoint the deuterium triple point in the cell.

4.4.5   Iron hydroxide

Iron hydroxide overview

Because of the unexpected, very large absorption of Oxisorb, we next tried iron hydroxide as a catalyst. This is the catalyst used by the LANL UCN source [94]. Iron hydroxide is appealing because of the difficulty in handling of chromium oxide, however it may loose its effectiveness over fewer cycles than Oxisorb, particularly if contaminates are present [157].

$$
\begin{aligned}
&\mathrm{Fe_2O_3} && \text{Iron(III) oxide} \\
&\mathrm{Fe_2O_3 + H_2O \rightarrow FeO(OH)} && \text{Anhydrous iron(III) hydroxide} && (4.2) \\
&\mathrm{FeO(OH) + H_2O \rightarrow Fe(OH)_3} && \text{Monohydrous iron(III) hydroxide}
\end{aligned}
$$
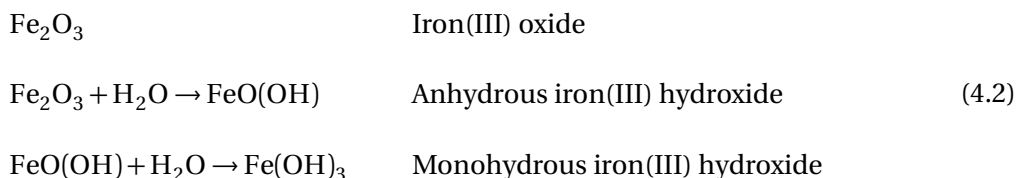
A variety of compounds are referred to as iron oxide and iron hydroxide. These iron oxides and hydroxides make up common rust. As non-chemists, we refer to the species we are interested in as iron(III) hydroxide, but the terminology can get a bit muddled. Iron(III) oxide is Fe_2O_3. Its hydroxide, iron(III) hydroxide (also called iron(III) oxide-hydroxide), may refer to either the anhydride FeO(OH)

88

Figure 4.29: The converter cell filled with roughly 350 mL iron hydroxide.

or any of the hydrates, FeO(OH)·nH$_2$O. The monohydrate in particular, FeO(OH)·H$_2$O or Fe(OH)$_3$, is also referred to as iron(III) hydroxide, hydrated iron oxide, or hydrous iron hydroxide. In this case, we are interested in the monohydrate, see Equation 4.2, as greater hydrations readily loose water. More details can be found in [74] and [156].

Iron hydroxide is available commercially as Ionex® [53], however ours was made in-house. We reacted ammonium hydroxide and iron chloride available from Sigma-Aldrich in solution. (We obtained our recipe for iron hydroxide from Steve Lamoreaux.) The precipitate was then filtered and heated to remove the water, although heating above 140 °C reduced it to iron oxide. After drying, submerging it back in water caused the solid cake to fracture into small granules without much dust, see Figure 4.28. Finally the granules are baked in the vacuum oven to remove the remaining water. These granules are small enough to provide a large surface area while also hopefully large enough to prevent small particles of catalyst material from migrating out of the converter volume.

Iron hydroxide test

To test the performance of the iron hydroxide catalyst in lab, a similar setup to the Oxisorb test was used. The cell was filled with roughly 350 mL of iron hydroxide, although again the packing ratio is not known, see Figure 4.29.

The cell was flushed several times with Argon to remove excess water, then baked at 350 K for 24 h before the pressure dropped. The cell was cooled to 25 K, and deuterium introduced. After 45 L gas (normal temperature and pressure, NTP) had been introduced, the pressure drop was very slow. The cell was cooled to 19 K, the valve closed, and the remainder of the system evacuated. The converter was allowed to sit for 15 min, then the valve was opened, and the cell was warmed until the pressure reached one atmosphere at 28 K. The cell was evacuated and allowed to warm to room temperature, then filled to slightly less than one atmosphere deuterium for storage.

The iron hydroxide also adsorbed deuterium at low temperature, although relatively less. It was nearly saturated with 8 g at a colder 25 K, compared with 10 g at 30 K with Oxisorb. However, this is still a significant amount of stored deuterium that must be accounted for.

24 h later, the sample was measured with the Raman spectrometer, determined to be 4% *para*-deuterium. The higher *para*-fraction could be due to a variety of things, including the different catalyst material, different warming procedure, accelerated relaxation in the sample bottle or Raman system, but the most likely candidate is the shorter residency time in the converter cell. Further investigation of deuterium conversion with iron hydroxide is planned for the near future.

4.5   Raman analysis

4.5.1   Deuterium energy levels

To first order, diatomic molecules like hydrogen are quantum linear rigid rotors. The wavefunctions are the spherical harmonics, and the rotational energy is given by Equation 4.3 where the moment of inertia is given in terms of the reduced mass, $I = \mu R^2$. A rotational constant is defined as $B_e = \hbar^2/2I$. The energy difference for a change in rotational number by two units is given by Equation 4.4. (Changes of one are disallowed without a spin flip, see Section 4.4.) Still to first order, the spacing between these energies is constant, Equation 4.5.

$$E_J = \frac{\hbar^2}{2I} J(J+1) \tag{4.3}$$

$$\Delta E_{J \to J+2} = 2B_e(2J+3) \tag{4.4}$$

$$\Delta(\Delta E) = 4B_e \tag{4.5}$$

More generally, we must include the vibrational energy levels, v, in particular because the ground state contributes to the total energy and the vibration modifies the distance between atoms. This is included as a modified rotational constant, B_v. Also, non-rigid centrifugal distortion with increasing angular momentum can be included through perturbation theory. Typically, the Dunham expansion [28, 58] is used, Equation 4.6, and the coefficients Y_{lk} are tabulated, e.g. *CRC Handbook of*

Physics and Chemistry [26, 56, 63]. (Sign changes are made to the sum to keep the value of constants positive.)

$$\frac{E_{v,J}}{hc} = \sum_{l,k} Y_{lk} \left(v + \frac{1}{2} \right)^l J^k (J+1)^k$$

$$= B_v J(J+1) - D_v J^2 (J+1)^2 + H_v J^3 (J+1)^3 + \cdots$$

where

$$B_v = \sum_l Y_{l1} \left(v + \frac{1}{2} \right)^l = B_e - \alpha_e \left(v + \frac{1}{2} \right) + \cdots$$

$$D_v = -\sum_l Y_{l2} \left(v + \frac{1}{2} \right)^l = D_e + \beta_e \left(v + \frac{1}{2} \right) + \cdots$$

(4.6)

etc.

The vibrational energy levels are significantly larger than the rotational energy levels. They are populated following the Maxwell-Boltzmann law, $\exp(-E_v/k_{\mathrm{B}}T)$, and at room temperature, light molecules like hydrogen are overwhelmingly in the ground state. For our Raman analysis, they can be treated as $v = 0$. The first few rotational energy levels are calculated in Table 4.2.

$$N_J = \frac{1}{Q} (2J+1) g_J \mathrm{e}^{-E_J/k_{\mathrm{B}}T}$$

where

$$Q = \sum_{i=0}^{\infty} (2i+1) g_i \mathrm{e}^{-E_i/k_{\mathrm{B}}T}$$

$$\sum_{J=0}^{\infty} N_J = 1$$

(4.7)

The rotational energy levels are also populated as the Maxwell-Boltzmann law, but in addition must include the $(2J+1)$ rotational state degeneracy and nuclear spin degeneracy, g_J (if present). The occupation of the Jth energy level goes as Equation 4.7, normalized by dividing by the sum over all states, Q. At 18.7 K, this statistical sum gives 1.5 % *para*-deuterium.

Table 4.2:   Molecular deuterium rotational energy levels to second order from Equation 4.6.

Level	H_2 (meV)	D_2 (meV)	HD (meV)
e_0	0.	0.	0.
e_1	14.7	7.41	11.1
e_2	43.9	22.2	33.2
e_3	87.4	44.3	66.3
e_4	145.	73.6	110.
e_5	215.	110.	166.

4.5.2   Raman scattering

The electric field of light incident on an atom or molecule induces a dipole moment, $\vec{P}$, that will re-radiate, scattering the incident light. The magnitude of the induced dipole moment is called the electric polarizability, α, Equation 4.8. The elastic process, Rayleigh scattering, produces light of the same wavelength, but the inelastic process, Raman scattering, produces light shifted by the energy difference of an internal excitation mode. Raman spectroscopy is then a useful method for probing the excitation modes of a target, and for us, can distinguish between spin isomers and hydrogen isotopes. The shifted photon frequency of Raman scattering is distinct from florescence in which the entire photon is absorbed and a portion emitted at a later time by a de-excitation. The frequency of the exciting Raman light is typically far off the frequency of the internal excitation.

$$\vec{P}_{\text{induced}} = \alpha \vec{E} \tag{4.8}$$

$$E_{J+2} - E_J = hc\left(\frac{1}{\Lambda} - \frac{1}{\lambda}\right) \tag{4.9}$$

Raman scattering accompanying a transition to a higher state, i.e. rotational $J \to J+2$, is called Stokes scattering, and to a lower state, $J \to J-2$, is called anti-Stokes scattering. (For this discussion, "Raman" scattering is used to mean rotational Raman scattering). Since states are populated as the Maxwell-Boltzmann distribution, anti-Stokes is suppressed, and we typically measure Stokes. (Though the ratio of Stokes to anti-Stokes could be exploited to measure temperature.) The frequency of the scattered photon is shifted by this change of energy between rotational states, Equation 4.9, where Λ is the exciting wavelength and λ is the observed. For our laser of wavelength of 488 nm, the wavelengths of Stokes Raman peaks are given in Table 4.3.

Table 4.3:   Wavelengths of Raman peaks to second order for Stokes transitions for incident 488 nm laser light.

Transition	H_2 (nm)	D_2 (nm)	HD (nm)
0→2	496.6	492.3	494.4
1→3	502.4	495.2	498.8
2→4	508.2	498.1	503.2
3→5	513.9	500.9	507.7
4→6	519.4	503.8	512.2
5→7	524.8	506.6	516.6

4.5.3   Relative intensity

The expected absolute intensity of a Raman line measured in our system depends on many unknown factors, e.g. the solid angle observed and the spectrometer efficiency. Thankfully, comparing a sample with a reference taken in the same system will exclude many contributions that are the same between measurements.

$$I \propto P N_o N_J \sigma_{J \to J+2} \tag{4.10}$$

For us, the intensity of the $J \to J + 2$ Stokes Raman line will depend on the laser power P, the total number density (pressure) N_o, the fractional occupation of the Jth state N_J, and the Raman scattering cross section of the transition from the Jth state $\sigma_{J \to J+2}$, Equation 4.10 [58].

$$\sigma_{J \to J+2} = (\text{const.}) b_{J \to J+2} (\omega_o + \Delta\omega_{J \to J+2})^4 \gamma^2$$

where

$$b_{J \to J+2} = \frac{3(J+1)(J+2)}{2(2J+1)(2J+3)}$$

$$\tag{4.11}$$

The Raman cross sections were first derived in detail by G. Placzek and E. Teller in 1933 [123]. For our setup, where the observation angle is perpendicular to both the direction of the incident light and its polarization, and transitions are purely rotational, C.M. Penney [119] has put this into a convenient form, Equation 4.11. Given the frequency of the incident light, ω_o, is far away from the rotational frequency, $\Delta\omega$, that term is roughly constant. Here γ is the anisotropic part (anti-symmetric components) of the polarizability tensor α, which is constant between the same states of the same species, and roughly constant between the first few rotational states among the hydrogens (e.g. $\gamma_{v=0, J=0}$ is 2.02 for H_2 and 1.96 for D_2) [75]. Differences are then primarily due to the angular
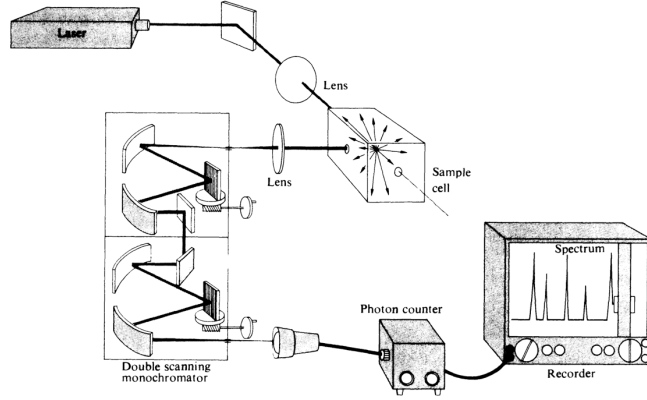
Figure 4.30: Reproduction of Figure 13.21 from *Optics* [57]. Our setup is identical, except includes optics of a second pass.

momentum dependence of the cross section, $b_{J \to J+2}$.

$$r^o = \frac{g^o_{\text{odd}}}{g^o_{\text{even}}} = \frac{1}{2} \tag{4.12}$$

$$\frac{f'}{f^o} = \frac{I'_{\text{para}}/I'_{\text{ortho}}}{I^o_{\text{para}}/I^o_{\text{ortho}}} = \frac{g'_{\text{odd}}/g'_{\text{even}}}{g^o_{\text{odd}}/g^o_{\text{even}}} = \frac{r}{r^o} \tag{4.13}$$

$$r = \frac{1}{2} \frac{I'_{\text{para}}/I'_{\text{ortho}}}{I^o_{\text{para}}/I^o_{\text{ortho}}} \tag{4.14}$$

For the *ortho*-to-*para* ratio within a single species, all terms contributing to the measured intensity, I, must be identical except the nuclear spin degeneracy term, g_J. As discussed in Section 4.4.1, for room-temperature deuterium, the *ortho*-to-*para* ratio, r^o, is known since $g_{\text{even}} = 6$ and $g_{\text{odd}} = 3$, Equation 4.12. If we define a fraction, f^o, between the measured *para*-to-*ortho* peak intensities of a reference, and a similar fraction, f', for the sample, the *ortho*-to-*para* ratio of a sample, r', is then trivially given by the ratio of these ratios, Equation 4.13. This is explicitly shown in Equation 4.14 where I^o and I' are the total counts in any identical set of Raman lines in the reference and sample respectively.

An *ortho*-to-*para* ratio can be determined by other means, such as a comparison of thermal conductivity at liquid nitrogen temperature [147] or via NMR, however these methods require calibration. Raman scattering is a direct measurement and is relatively straightforward to implement.
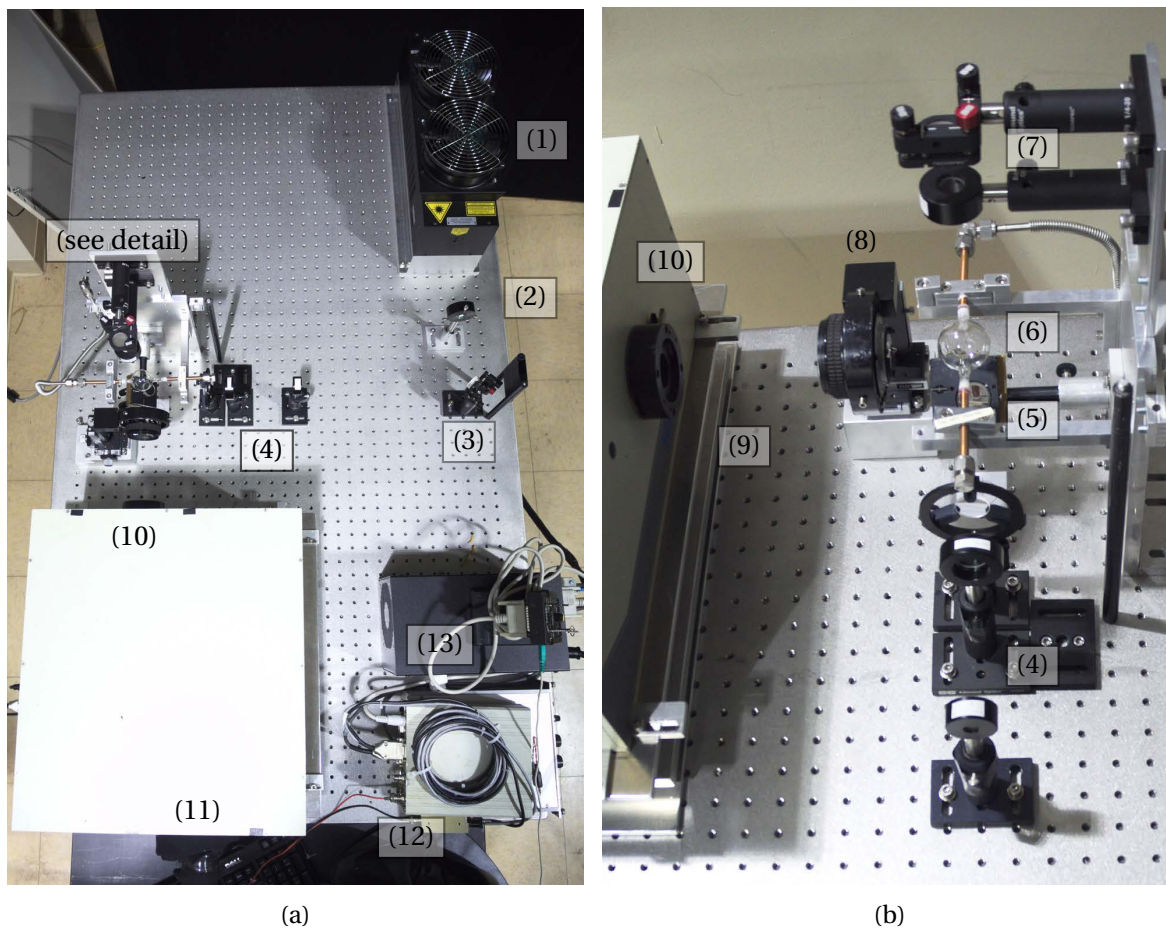
Figure 4.31: (a) Photo of the Raman spectroscopy table with (b) a detail photo of the gas cell and optics. The dark box cover has been removed and the gas management system has been disconnected. Following the path of the light from the upper-right corner of (a) is the (1) laser, (2) laser line filter, (3) mirror, (4) focusing optics, (5) vertically reflecting mirror, (6) gas cell, (7) retro-reflecting mirror and refocusing optic, (8) imaging camera lens, (9) spectrometer adjustment table, (10) spectrometer entrance slit, (11) PMT, (12) PMT power supply, PC, and data acquisition boxes, and (13) laser power supply and control.
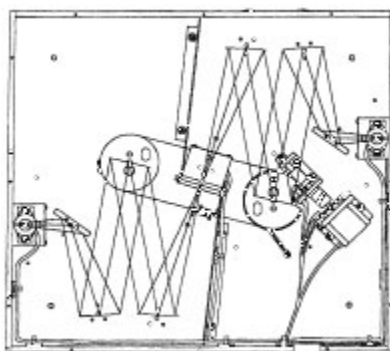
Figure 4.32: Internal light path in our double-grating, Horiba model Gemini 180 spectrometer.

95

4.5.4   Raman spectrometer setup

C.-Y. Liu et al. demonstrated Raman spectroscopy can be used to precisely determine the *para*-to-*ortho* ratio of the source deuterium, and is also sensitive to chemically indistinct hydrogen and HD contaminants [94]. Our Raman analysis setup follows theirs, and is a fairly standard design similar to one described in *Optics* by Hecht [57], reproduced in Figure 4.30.

The setup is built on a standard optical table and shown in Figure 4.31. Illumination is provided by an argon ion laser with a green, 488 nm wavelength. It is a National Laser model 800BL, vertically polarized to >250:1, and 80 mW in power. Although nominally 80 mW, running near this maximum, there were slow and persistent changes in output of up to 2% over a scan. Running at 60 mW, fluctuations in power measurement were less than 0.3% with no long term change in power output observed. The beam is first passed through a 488 nm laserline bandpass filter to exclude other frequencies produced by the Ar+ laser.

A 12 mm focal length plano-concave lens and a 12 mm focal length double-convex lens set 130 mm apart serve as a beam expander, and a 150 mm focal length plano-convex lens focuses the beam to a point in the gas cell. Before the cell, a second mirror redirects the beam vertically. Instead of a beamstop, a third reflector coupled with a diverging lens of the same focal length sends light back through the focus point to add intensity. This retro-reflector is adjusted so that the returning beam passes back through the system terminating just off-center of the laser beamport. A 50 mm camera lens images the focused laser point into a Horiba (Jbon Yvon) Gemini 180 double-grating spectrometer. A Hamamatsu photomultiplier tube with a dark count of roughly 10 per second serves as the detector, and a simple discriminator and the spectrometer controller provides the counting.

The sample volume is a spherical borosilicate-glass bulb[4] connected by a single tube to a simple gas management system. The sample cell is constructed with two inlet tubes, however this over-constrained the weak joints and several were broken. Instead of flowing gas through the cell, gas remaining in the cell can be repeatedly evacuated and flushed with inert gas. Pressure is measured with a Pfeiffer model RPT100 piezo-pirini combination full-range gauge, and a Pfeiffer model MVP015 diaphragm pump provides rough vacuum.

To account for scattering additional to the sample gas, a background scan is taken with the sample cell flushed with inert gas and near vacuum. The cell is first flushed with argon to remove any remaining deuterium and then evacuated to a few mbar. There a non-linear background signal that first rises and then falls over the scan region, Figure 4.34. There is no measurable difference between 5 mbar and 1 bar argon. The sample is then introduced on top of this partial pressure, which is subtracted from the sample pressure.

---

[4]Manufactured by Mike Souza at Princeton, chemistry.princeton.edu/research-facilities/glassblowing-shop
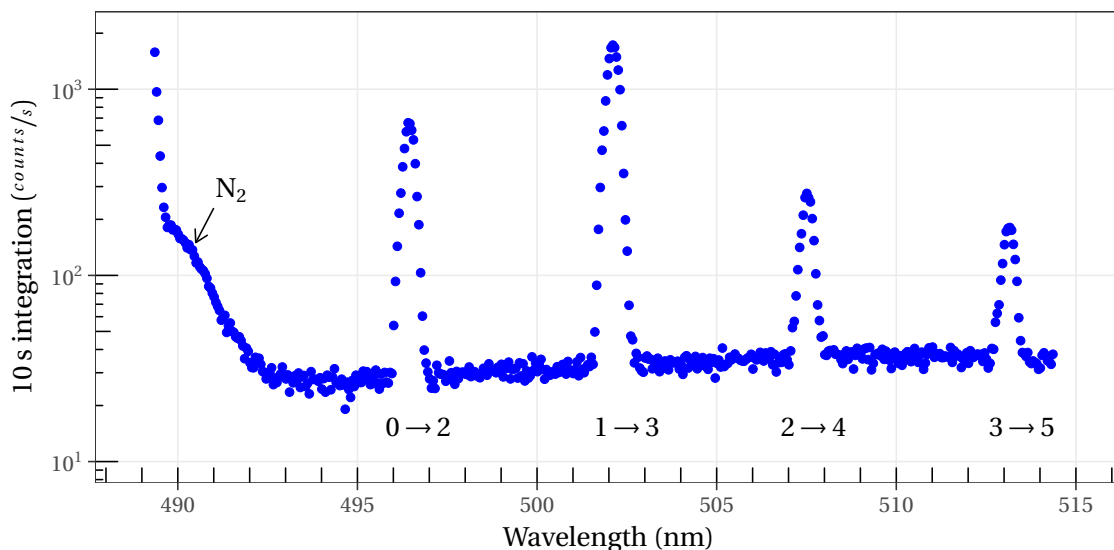
Figure 4.33: Representative measured Raman spectrum of hydrogen at 1 bar. The bulge on the tail of the laser line is caused by nitrogen contamination. Note the vertical axis is logarithmic, and the J=1→3 transition peak is nearly three times the leftmost, J=0→2 peak.

The Raman setup was previously demonstrated, however performance was poor. The spectrometer has three adjustable slits, at the entrance, between the gratings, and at the exit before the PMT, Figure 4.32. Ideally, with all focal lengths in the system well matched, these slits could be closed to the width of the focused laser scattering point in the gas sample cell without losing scattered light, only background. However, light reduction was seen closing the slits below 1 mm, and at a practical setting, only 300 counts per second were measured from the strongest Raman peak of hydrogen.

The two internal focal lengths of the spectrometer were not well matched. The manufacturer had installed baffles to crop the circular image produced by the aperature of the camera lens to account for this. This also created an asymmetrical peak shape as the cropped image was scanned across the PMT area.

The first and last plane mirrors were adjusted to change the path length in their respective halves of the spectrometer to match. The spectrometer was placed on a custom multi-axis table to allow it be aligned with the camera lens and laser point. This allowed slits to be narrowed and internal light baffles to be removed. The large Raman peak spacing allows peaks to be resolved with relatively large slit width. The entrance, middle, and exit slits were opened until the signal to background ratio began to increase, typically being set to 400 µm, 300 µm, and 500 µm respectively. This is presumably the size of the focused image at the slit. After these adjustments, roughly 2000 counts per second were observed in the strongest hydrogen scattering peak. A hydrogen spectrum is shown in Figure 4.33.
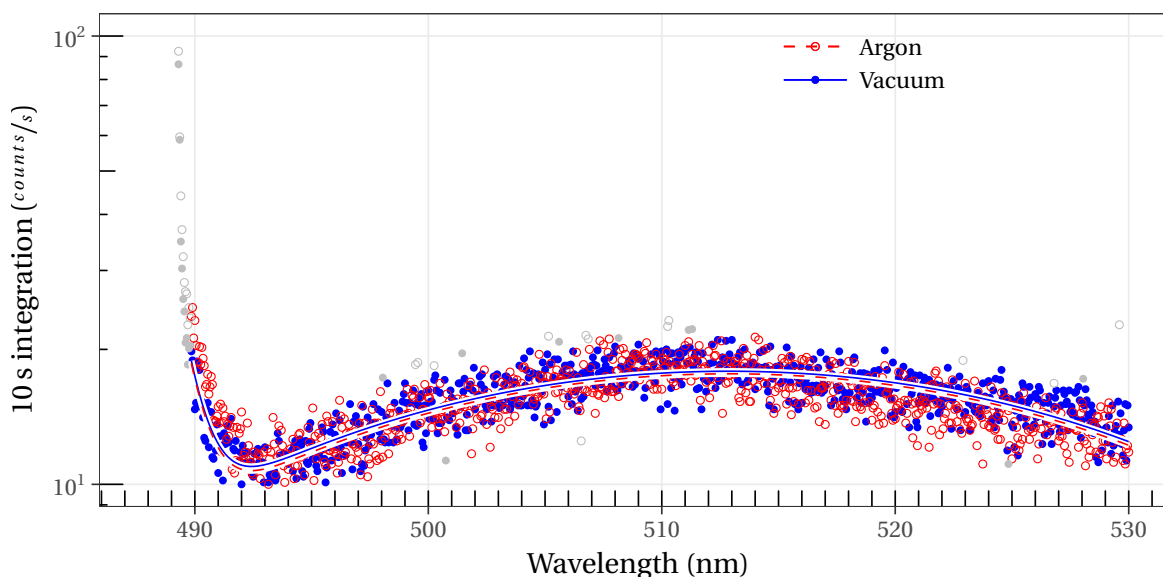
Figure 4.34: Representative measured background in the Raman sample cell with 3.5 mbar of argon (vacuum) and 1 bar of argon. The tail on the left is the edge of the 488 nm laser line, and the gradual rise then fall to longer wavelengths is likely due to fluorescence of the glass cell. The fit is given in Equation 4.15.

4.5.5 Analysis

Initially, the magnitude of each Raman peak was tallied individually. The background was fit locally as a line, using data immediately either side of a peak, and then subtracted from the total counts in the peak. Worryingly however, the calculated value depended on the pressure difference between the reference and sample. This is potentially a real effect, for example due to a contaminate introduced to the sample, but it also may be that this counting method is sensitive to background counts when tallying small peaks.

However, we can measure the shape of the background independently, and we know all peaks have the same shape, and that the ratio among even peaks, and separately among odd peaks, must be constant, and we might expect to decrease statistical error by including this information. The current method is as follows.
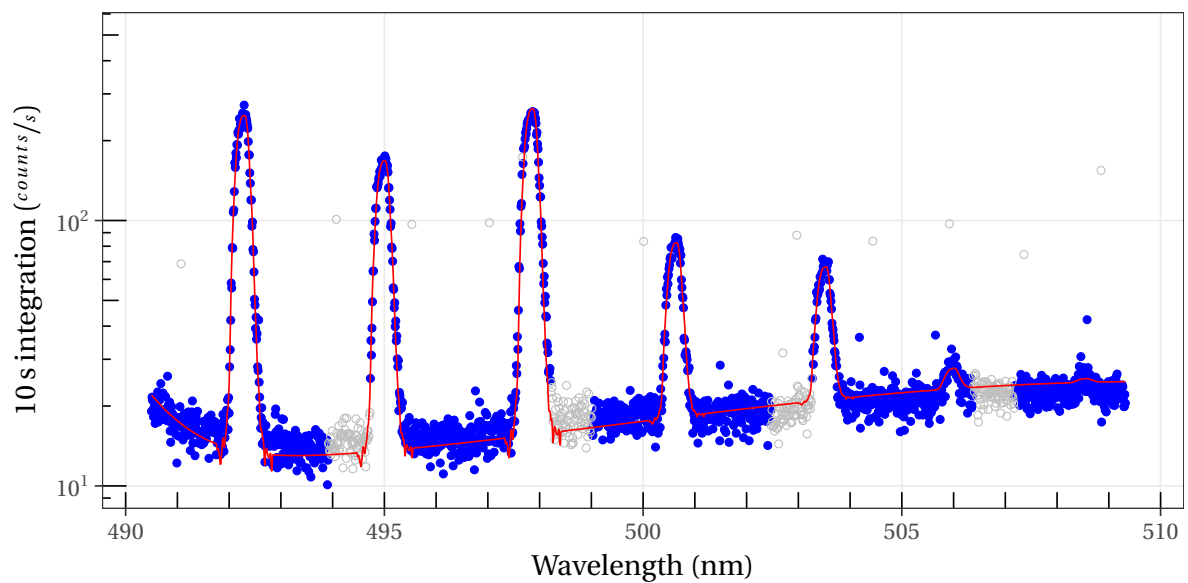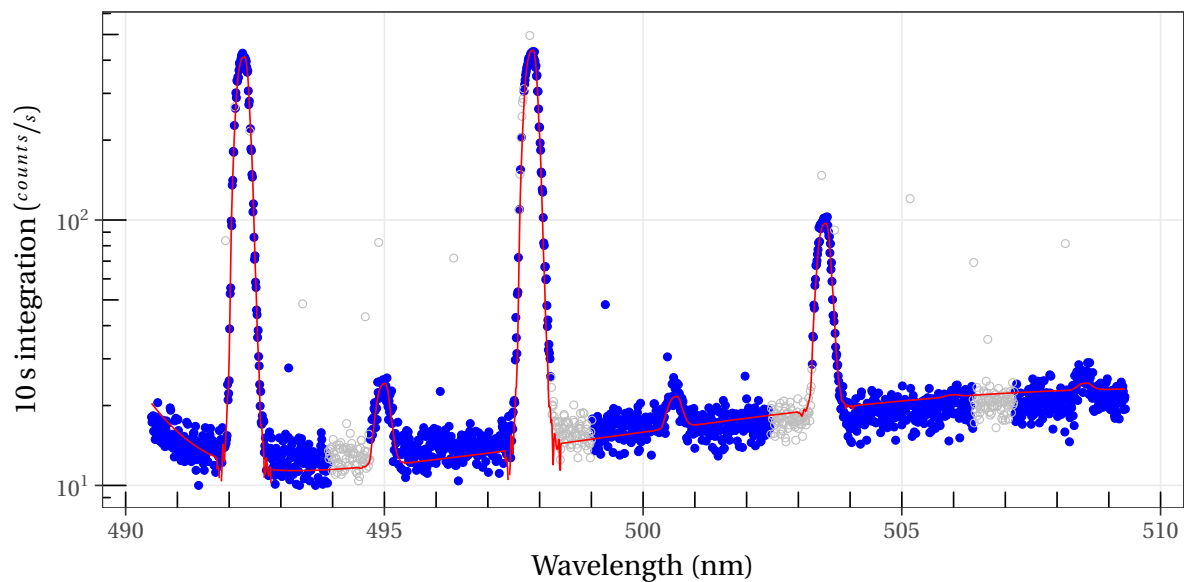
Figure 4.35: Representative measured Raman spectra of D_2. (a) The top is a 33% *para*-deuterium room-temperature reference, and (b) the bottom is a 2.3% *para*-deuterium converted sample.

Background

The background data is fit using non-linear least squares in MATLAB completely arbitrarily as two Gaussian functions, including the laser line tail and unknown background at longer wavelengths Equation 4.15, and a constant value, which would include components like the PMT dark rate. Data points greater than 3 standard deviations are excluded from the fit.

$$\mathcal{B}(x) = b_o + A_a \exp\left[-\left(\frac{x - A_b}{A_c}\right)^2\right] + B_a \exp\left[-\left(\frac{x - B_b}{B_c}\right)^2\right] \tag{4.15}$$

A comparison between a vacuum and 1 bar of argon shows no statistical difference over the wavelengths of the deuterium Raman peaks, so we may expect the background in a deuterium sample to be similar to this reference. The argon sample does show an increase along the laser line tail due to Rayleigh scattering, and possibly due to gas contamination.

Para-fraction

Even after the initial alignment, the peak shape is still slightly asymmetric. The $J = 0 \rightarrow 2$ peak was selected to model the shape for fitting the other peaks as the $J = 1 \rightarrow 3$ and $J = 2 \rightarrow 4$ may be modified by the presence of HD. The peak is processed through low-pass filter to remove noise, the local background is fit with a line and subtracted, and finally a linear interpolation is used between points.

$$\mathcal{F}_{\text{ref}}(x) = b_o + \mathcal{B}(x) + \sum_{i=1}^{7} a_i \mathcal{P}(x - x_i) \tag{4.16}$$

The first 7 peaks of a reference deuterium scan are then fit using this individually scaled peak shape on top of the previously fit background. (Fewer peaks are available at lower pressure.) For some spectra, the background had a constant offset from the independently measured background, and so an additional fitting parameter was included in the background. The cause of this offset is not known; it is potentially light leakage into the spectrometer, a change in the PMT darkrate with temperature, or drift in the discriminator level. The nonlinear least squares fit is given in Equation 4.16, were $\mathcal{B}$ is the previously fit background and $\mathcal{P}$ is the constant interpolated peak, and shown in Figure 4.35.

$$\mathcal{F}_{\text{sam}}(x) = b_o + \mathcal{B}(x) + a\left(\sum_{\text{even}} \mathcal{P}_i + 2r \sum_{\text{odd}} \mathcal{P}_i\right) \tag{4.17}$$

Then following Equation 4.14, the *ortho*-to-*para* ratio, r, of a sample is given by the ratio of the reference's and sample's respective ratios between even and odd peaks. The nonlinear least squares fit is given in Equation 4.17, where $\mathcal{B}$ is the previously fit background, $\mathcal{P}_i$ are the previously established peak shape and locations, and a is a constant multiple accounting for differences in the
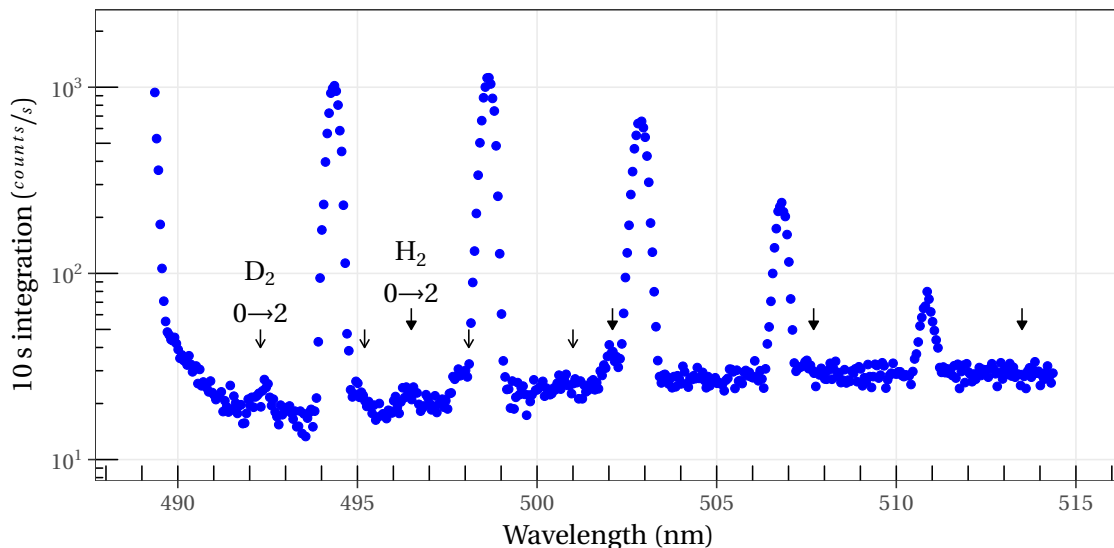
Figure 4.36: Representative measured Raman spectrum of hydrogen deuteride at 1 bar. The first four D_2 and H_2 Raman peaks are given by open arrows and closed arrows respectively, and contamination from both species is visible. Because HD lacks any nuclear degeneracy, the amplitude of the peaks is only modified by the Maxwell-Boltzman distribution at the given temperature.

leading factors of Equation 4.10 such as pressure. MATLAB calculates the covariance matrix during its fit algorithm, `lsqnonlin()`, and assuming everything is well behaved, provides a standard error on fitting parameters, including the ratio r. I assume the errors from the previous fits, and experimental error, is small relatively. This method is less sensitive to the pressure difference between the sample and reference than the raw counting method.

4.5.6 Hydrogen deuteride content

The Raman spectrometer can be used to set an upper limit on the hydrogen content of our deuterium, which will be predominately in the form of hydrogen deuteride (HD). Commercially available deuterium will be "dirtier" isotopically than chemically.

A reference HD sample with a 1012 mbar partial pressure was measured, Figure 4.36, and the first 5 peaks were fit using the same method as the deuterium reference, Equation 4.16. D_2 and H_2 are both visibly present as the HD sample has begun to decompose with age towards a statistical equilibrium between the three species. These contributions can be ignored however as they are a very small percentage of the HD reference at full pressure, and HD is a very small percentage of our sample deuterium.

$$\mathcal{F}_{HD}(x) = \mathcal{F}_{sam}(x) + a \sum_{i=1}^{4} \mathcal{P}_i \qquad (4.18)$$

101
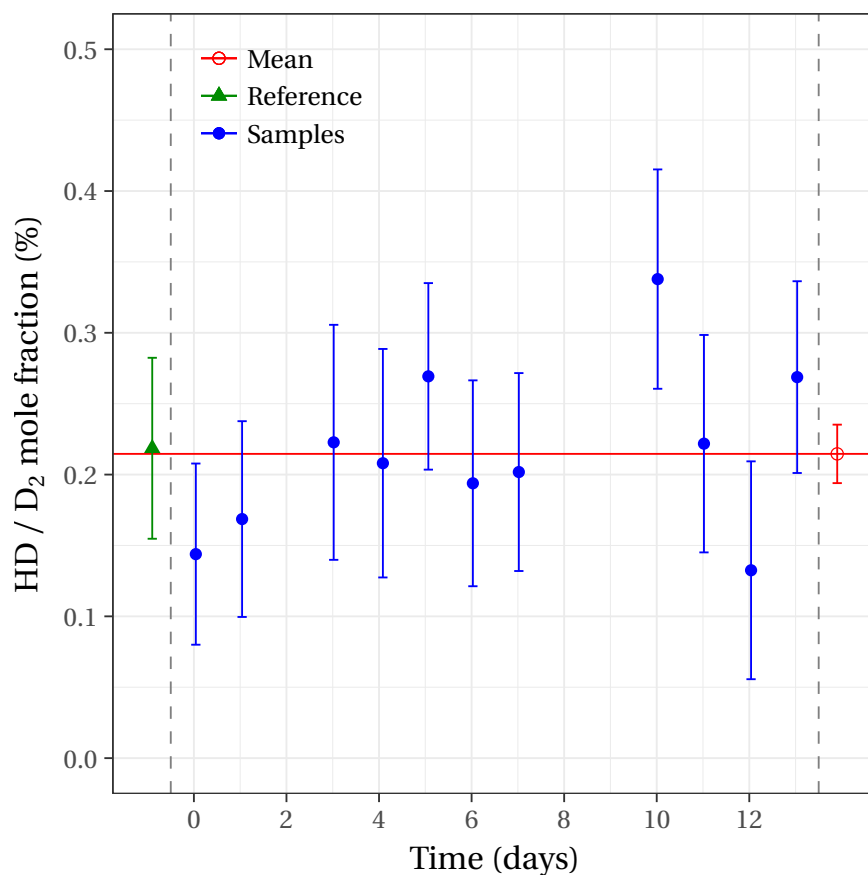
Figure 4.37:   HD content in the Raman cell relaxation study measurements and their weighted mean.

The domains covered by the HD peaks are excluded from the initial deuterium fits, Equation 4.16 and Equation 4.17, to avoid their influence on the background. These excluded domains are then included in a subsequent fit where the reference HD peaks are scaled by a factor, a in Equation 4.18. Following Equation 4.10, the measured intensity scales linearly with pressure, so the fitting parameter, scaled by the pressure of the reference, provides the partial pressure of HD in the sample.

Repeated measurements taken during the relaxation study shown later in Figure 4.41 provide the largest data set. These are shown in Figure 4.37, with a weighted mean of 0.21±0.02% HD mole fraction. It is entirely possible HD content is increasing over this series due to hydrogen contamination in the Raman system.
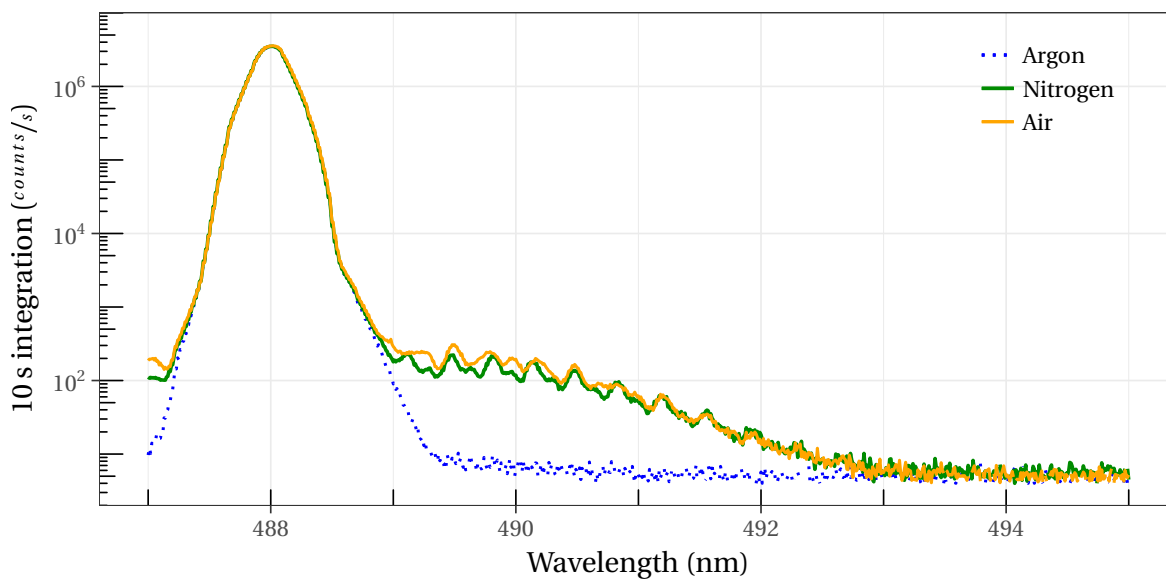
(a)
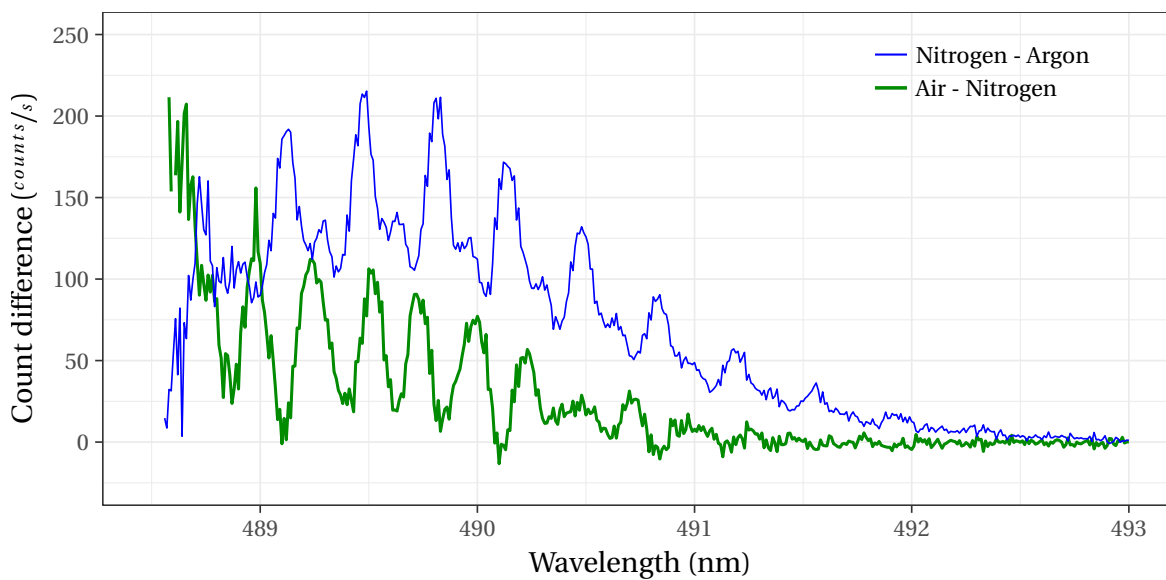
(b)

Figure 4.38: Measured Raman spectra of N_2 and air. (a) The argon background, nitrogen, and air scans include the laser line.(b) The oxygen Raman peaks are visible in the difference between the air and nitrogen spectra.

Table 4.4: Raman spectroscopy results from on-panel samples. The converted gas condensed on 2/24 was measured again after warming up on 3/4.

Sample	Date	Converter Temperature (K)	Sample pressure (mbar)	para-D_2 content Measured by Raman (%)	para-D_2 content Expected from Equation 4.7 (%)
Conversion	2016/2/2	20.6	215	2.0	2.3
Conversion	2016/2/17	24.0	795	3.6	4.0
Conversion	2016/2/24	19.5	163	2.2	1.8
Warm-up	2016/3/4		879	2.3	

4.5.7 Nitrogen and oxygen

Initially, the cell was flushed with nitrogen between scans. However, nitrogen is itself a dipole molecule and a strong Raman scatterer, so the signal from a very small amount of nitrogen was apparent in spectra, see figure Figure 4.33, and overlaps the first deuterium peak. This sensitivity could be used to place a limit on nitrogen or air contamination, particularly of deuterium stored in the ballast tank and cryostat for an extended period.

Narrowing the spectrometer slits relative to the deuterium scans allows individual nitrogen peaks to be resolved Figure 4.38. An air sample was also measured, and subtracting a nitrogen reference reveals the expected oxygen peaks. Oxygen is the heavier species, so we would expect the Raman peaks to be closer together, however the spin state paired with the odd rotational state is not present, so only Raman peaks from even rotational states are expressed.

The spectrometer should be tuned to maximize peak height versus background. In addition, peaks overlap the Rayleigh scattering signal, which would need to be addressed for a precision measurement of a small partial pressure in a sample.

4.5.8 Conversion on panel

The spin-state converter was moved to the reactor bay and installed on the gas handling panel prior to the tests discussed in Chapter 5. The converter was used in a flow-through mode, and operated near the triple point. Gas was sampled at the converter's outlet during the first few condensations and analyzed with the Raman setup. The results are shown in Table 4.4, and show agreement with the expected *para*-fraction. *Para*-fractions are not available during later condensations; the Raman spectroscopy setup needed to be moved to another lab during this time.

Figure 4.39:   Photo of sample cylinder used during tests.

4.5.9   Sample relaxation

The rate of spin-state relaxation in various parts of the system may be important, for example, if a sample cannot be immediately measured. Relaxation in both sample cylinder and Raman cell were measured.

The sample bottle used during these tests is a 1 L 304L stainless cylinder shown in Figure 4.39. After an initial sample, the Raman cell was evacuated and refilled from the sample bottle on each test, so the pressure dropped each subsequent measurement. Unfortunately this sudy was interrupted after only 4 measurements, and the results shown in Figure 4.40 are not particularly consistent. We can say the sample bottle does not cause a rapid relaxation if the sample is measured quickly.

The relaxation rate in the Raman cell itself was also measured. Since the measurement is in situ, the same gas is measured repeatedly, and the pressure is constant between measurements. Figure 4.41 shows a relaxation of 0.5% per day. This rapid relaxation is attributed to the pressure gauge present, although this was not confirmed.
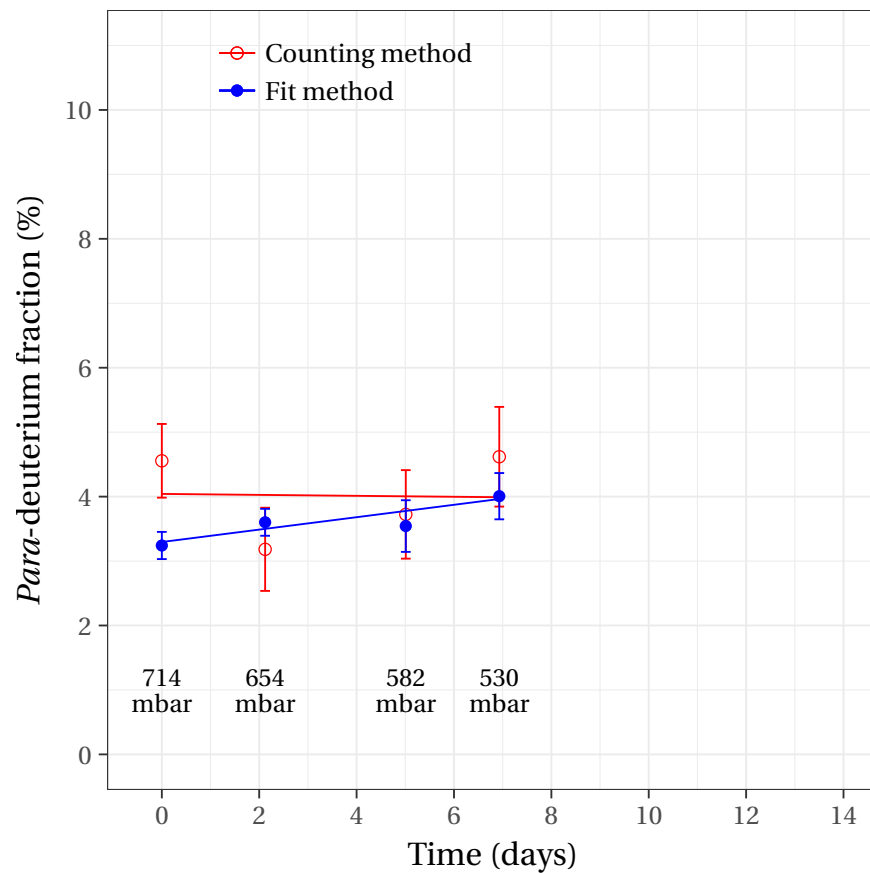
Figure 4.40: Spin-state relaxation in the stainless sample cylinder. During condensation on 2016/2/17, the cryostat was sampled and the *para*-deuterium fraction was repeatedly measured over the subsequent week. Each measurement, the contents of the Raman cell were flushed and the cell re-loaded, at a lower pressure, from the sample cylinder. The fraction was determined with both methods discussed in Section 4.5.5, and each given a weighted linear fit. The plot scale is the same as Figure 4.41.
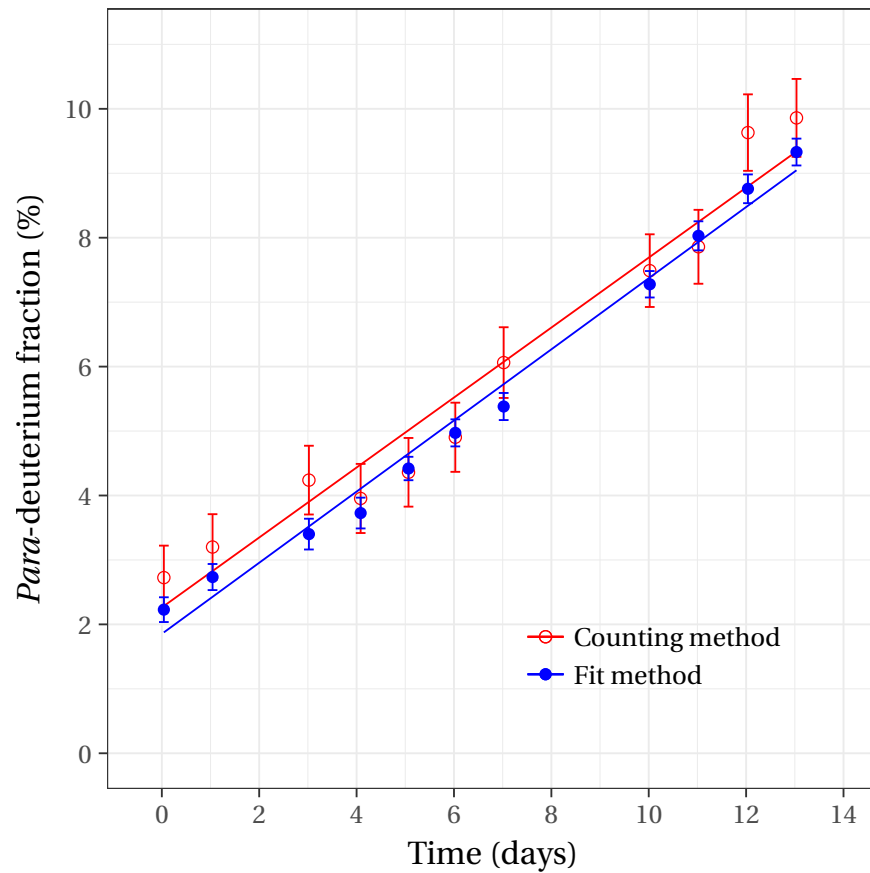
Figure 4.41: Spin-state relaxation in the Raman cell. After the warm-up on 2016/3/4, the cryostat was sampled and the *para*-deuterium fraction was repeatedly measured in situ over the subsequent two weeks. The fraction was determined with both methods discussed in Section 4.5.5, and each given a weighted linear fit.

Chapter 5

Deuterium Crystal Growth

5.1 Introduction

Ultracold neutron production in a physically realized crystal has several additional considerations over the theoretically ideal crystal ("spherical cow") discussed in Chapter 3, and some of these details are known to influence UCN production. How can we optimize our crystal's properties to maximize UCN production in our source?

Our crystal can be grown from deuterium gas either directly from gas or through the liquid phase. A single crystal will typically be polycrystalline in nature, with a given grain size, and with a larger scale geometry as well. On one extreme, the deuterium can rapidly sublimate into snow, like a bucket of water tossed into the Arctic air. On the other, deuterium can produce a monolithic and transparent crystal, like ice cubes suitable for a cocktail, as well as something in between the two extremes. What are suitable procedures and acceptable range of parameters for both processes? There is the potential for effects on the surface and at the shared boundary with its container, and these may be magnified by a thermal load or changes in temperature. Are these observed in our source, and can we extrapolate to the larger thermal pulses that would be seen at a spallation source? Solid deuterium has of course been explored in previous UCN sources, but we still need to verify there are no nasty surprises unique to our cryostat.

To answer these questions and verify the performance, we began a study to understand deuterium growth in our cryostat. As discussed below, the first part of this study was with the cryostat located outside of the reactor port, and a system was developed to directly monitor the crystal before measurements with neutrons.

5.1.1 Work at previous UCN sources

UCN production in deuterium is temperature dependent [93], and this dependence was one of the first measurements at the prototype sources at both PNPI [142] and LANSCE [107]. For proper accounting, the bulk temperature and temperature profile of the crystal must be known, and not just surmised from external sensors. To this end, without neutrons present, the prototype LANSE source embedded sensor diodes directly in the crystal [131]. In both sources, the surface temperature was indicated by vapor pressure.

The crystal structure, particularly non-uniformities in the crystal and grain size, also influence both cold neutron and UCN elastic cross sections. Deuterium's "transparency" to UCN, that is the extraction efficiency, is a factor in the total yield and the maximum equilibrium UCN density in the system. Serebrov, et al. [142] initially compared the temperature dependent UCN production for several different velocities, utilizing their different length scales to probe for non-uniformities, and found no deviation. Later the group at PNPI noted the method of preparation, particularly the rate of freezing from a liquid, had an impact on the neutron cross-section up to a factor of four change in total cross section! [144] However, it is not stated if the group had any feedback of crystal properties other than that provided by neutron data.

Morris, et al. [107] makes the point that the geometry of the crystal is also relevant. For a crystal in a bucket, such as our cryostat, the surface can range from concave to convex in shape and has the minimum exposed surface as a flat puck.

For the UCN source being developed there, the group at the Paul Scherrer Institut (PSI) has made a very strong effort to understand the solid deuterium in their source, in particular the transient heating of the crystal inherent in a pulsed-type source. They took a cryogenic cell on a cold neutron beam [10], with deuterium frozen from liquid, and observed that the neutron transmission deviates from the expected cross section upon cooling from 18 K to 5 K, and further deviates after thermal cycling [9]. They also observed changes in optical clarity with similar thermal cycling [17, 70, 108]. They conclude at 5 K, the total scattering cross section is dominated by the crystal properties, and attribute this to stress-induced imperfections introduced by the change in volume while cooling. More recently in that setup, they observed the crystal as transparent when grown from the liquid at 18 K, but opaque when grown from the gas phase at 12 K [13]. This is possibly attributed to the size of independent crystal domains [2].

In contrast, the prototype source run at the TRIGA reactor at Mainz produced a crystal by sublimation at 5 K. The group measured neutron yield as a function of the deuterium volume, and noted a nearly linear increase up to certain amount of solid deuterium, but that yield beyond that amount increased much less with thickness, which they attribute to the polycrystalline structure of the larger crystal. However, yield at these greater thicknesses could be dramatically improved by thermal cycling [33].

While these details provide great context for our Source, it is far from a complete picture, and serves to underscore the necessity of running our own study.

5.1.2 Goals

The primary goal of this study was to translate the pressure and temperature measured by instrumentation during Source operation to the actual pressure and temperature of the solid deuterium. These have the potential to be quite different. The pressure above the solid deuterium gives the temperature of the solid's surface. The pressure is measured at the gas handling area above the Source, separated by a 10 m length of 1.27 cm (½-inch) tubing. One temperature sensor is located on the outside of the deuterium container near the top, just under the gradient ring; a second is located on the helium inlet to the deuterium container. (See Chapter 4 for details.) It was expected that the container sensor would be warmer than the crystal, and the inlet sensor would be colder.

As a second priority, we wished to observe the quality of the deuterium crystal produced. While the general behavior of solid deuterium could be more easily studied in a different apparatus, it is crucial to the success of the Source that these observations are made in situ. Cold neutron scattering would provide a valuable tool for studying the neutron transport properties of crystals in our cryostat, but reproducing or transporting the Source to a neutron beam is very difficult. Instead, an optical system can be used to observe opacity and surface quality, and temperature sensors embedded in the solid deuterium can measure the temperature profile. A direct pressure measurement should also provide the surface temperature.

A tertiary goal was to determine the effect of an infrared load on the crystal. To increase neutron transmission, the UCN window foil might be removed in favor of a gate valve or another foil downstream (perhaps in a polarizer), thus exposing the Source volume to a load from a room temperature guide. It is also conceivable an infrared load could improve performance, perhaps by melting the surface of the crystal, aiding growth, and preventing a rough surface from affecting UCN production. Due to the geometry of the Source volume in particular, it is best to directly measure this effect.

5.1.3 Deuterium details and procedures

Deuterium was discovered by Harold Urey, et al. in 1931 [165], followed by significant work on its properties in the 30s. Very thorough investigations have more recently been made at low-pressure and high-temperature, as well as at high-pressure and low-temperature, with respect to fusion work, but there has been surprisingly little work in the meantime on deuterium at low-pressure and low-temperature owing possibly to the lack of applications.
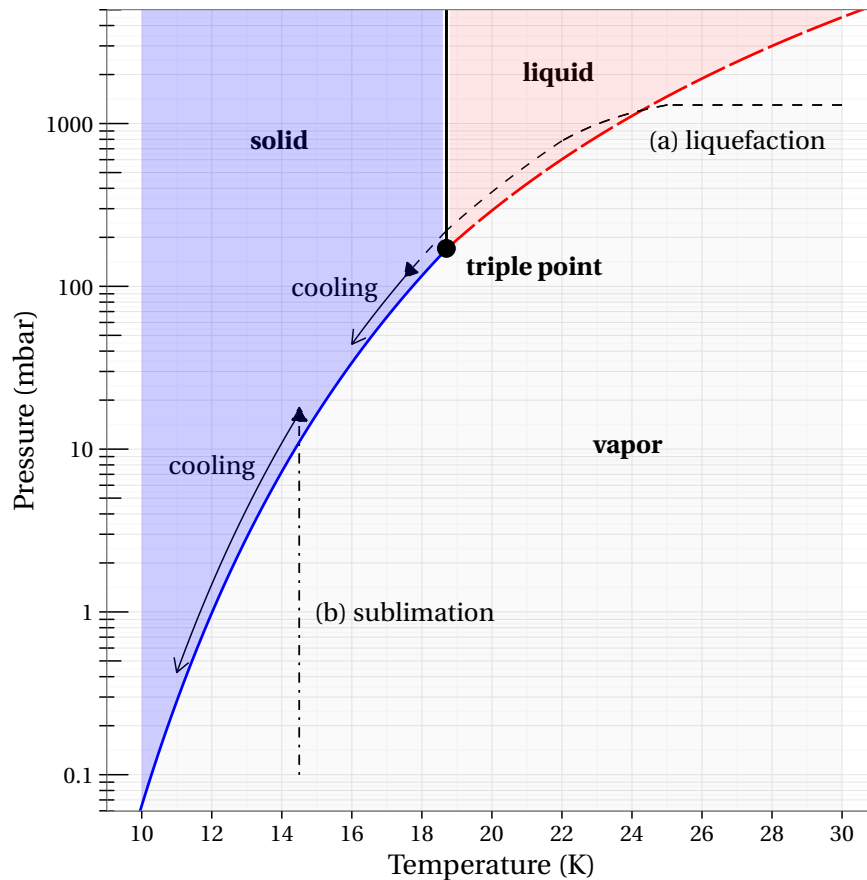
Figure 5.1: Phase diagram of deuterium with our two condensation processes. Generic examples of (a) liquefaction and (b) sublimation are shown. After each condensation, the deuterium is cooled at saturation to the operation temperature. The saturation curve is calculated from [151].

The crystal structure for low-temperature, low-pressure deuterium is primarily hexagonal close-packed (hcp), except for an enriched para ratio, which will grow as face-centered cubic (fcc). Interestingly however, equilibrium and lower para ratios has still been observed as fcc under certain conditions, but returning to hcp when heated near the triple point [23]. Quoting Silvera, et al. [147],

> Bulk H_2, and D_2, when grown from the melt in equilibrium with their vapor pressure, are always found to be hcp for both ortho and para species. As mentioned in the introduction of this section, diffraction studies showed that films of H_2, or D_2, grow from the vapor phase at low temperature in the fcc phase. However, Mills *et al.* (1978) grew D_2 at 4.2 K by injecting D_2 gas into boiling liquid helium to achieve a bulk powder of solid D_2. They found that the D_2, grew in the fcc structure for both ortho and para species. When heated to the diffusion region, it transformed to hcp and remained so when again lowered to 4.2 K.
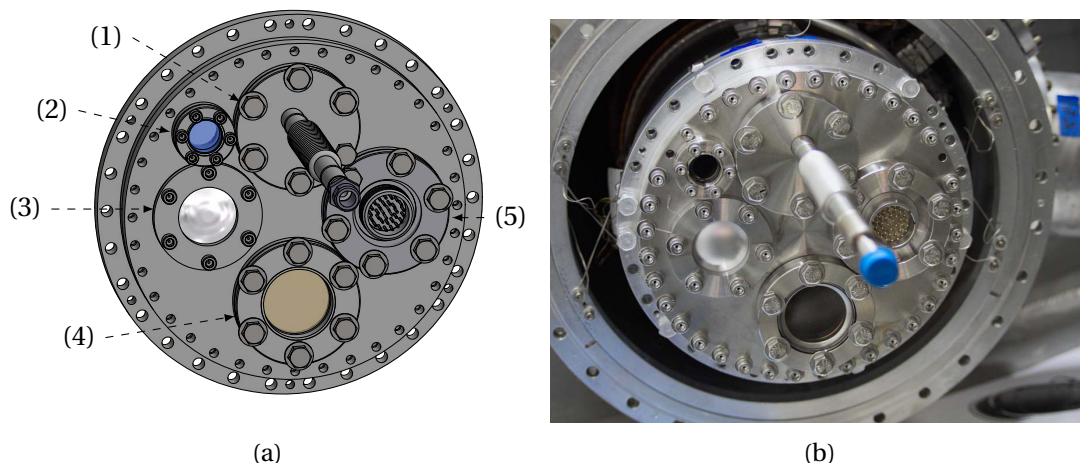
Figure 5.2: (a) CAD rendering and (b) photo of the monitoring system vacuum flange mounted on the Source cryostat, replacing the UCN window foil. Counterclockwise from the top is the (1) pressure feedthrough, (2) illumination window, (3) safety burst disk, (4) optical window, and (5) electrical feedthrough.

The details of deuterium's phase change and vapor pressure are critical to its behavior. Even at the triple point, its vapor pressure is significant, 171 mbar. However, by 10 K, its vapor pressure has dropped by four orders of magnitude. A phase diagram over our range of interest is given in Figure 5.1.

The vapor pressure of room temperature normal para-ortho ratio deuterium and that of low-temperature equilibrium para-ortho ratio deuterium are slightly different, roughly 5 mbar at 20 K to 1 mbar at 16 K [18]. The triple points of the two ratios differ by less than 0.1 K [151]. However, heat capacity and thermal conductivity are significantly different between the species [128].

Deuterium can be condensed from gas in our cryostat in two fundamentally different ways, shown in Figure 5.1. During liquefaction, the temperature is lowered and the deuterium gas present condenses into liquid. As the temperature continues to be lowered, the liquid freezes at the triple point. The temperature is lowered further still to reach operating temperature. In sublimation, with the temperature initially below the triple point, gas is introduced and condenses directly into solid. It is then cooled to operating temperature.

5.2 Methods

5.2.1 General design

There were a few important criteria to consider in the design. Because of the cost and complexity involved, this initial system will not be used in the radiation environment, and so cannot be used while producing UCNs. This is a serious trade-off given the goal of optimizing UCN production; we lose the direct feedback of UCN flux. We are further unable to verify the temperature profile under radiation heating, and are unable to search for crystal effects induced by radiation. Another study can, and should, be conducted in the future utilizing neutrons.

Thus, the recourse for this study is to examine the crystal over a range of possible conditions and growing procedures, and then later reproduce those conditions and procedures when the Source is installed in the reactor thermal column. As a benefit, this means the UCN window foil can be removed and the system installed in the neutron guide without consequence, greatly simplifying the setup. This monitoring system then becomes a practical diagnostic; it can be installed without significant modifications whenever the Source is removed from the reactor thermal column.

The UCN window foil is replaced with a solid flange that allows for electrical, pressure, and optical feedthroughs, as well as the mounting of any additional equipment. This flange was machined out of stainless steel to allow the use of ConFlat fittings by machining knife edges directly into the flange, Figure 5.2. This reduces the overall height and eliminates the need for welding. A safety burst disk identical to the one used on the vacuum jacket, which uses a crushed indium wire seal, provides the relief path previously provided by the UCN window foil.

5.2.2 Optical

Herculean efforts must be taken to avoid any contamination of the neutron guides and deuterium volume. This requirement, coupled with cost, eliminates a boroscope or similar optics to observe the crystal. Instead, a "dentist's mirror"-style component and optical windows can be constructed out of high-vacuum compatible materials.

The mirror itself is a commercially available 3.2 mm (⅛-inch) thick stainless steel plate with a #8, mirror-like, polish. It was mounted to its bracket by tapping threaded holes directly in the mirror. Unfortunately, this warped the mirror surface, distorting the image at the top of the mirror. A future replacement should use a different bracket. It is mounted to a ball joint, allowing for adjustment, and supported on aluminum rods extending from the flange, Figure 5.5. When the assembly is inserted into the guide, the mirror must be raised to avoid hitting the bottom of the guide, and it can be lowered with a screw and a very very long Allen key, Figure 5.3.

(a)   (b)
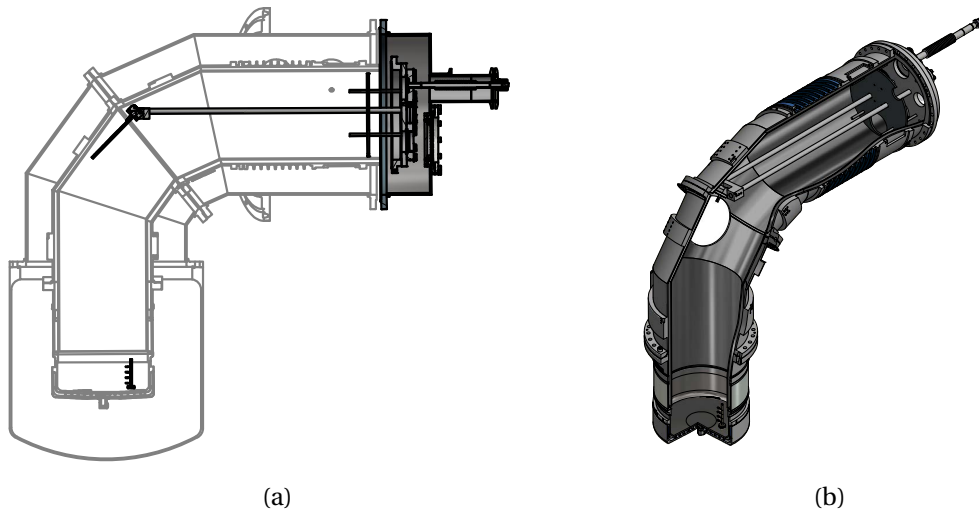
Figure 5.3:   (a) 2D CAD cross-section of the monitoring system, with the cryostat and vacuum jacket grayed out, and (b) 3D CAD rendering of the monitoring system and sectioned cryostat.

Figure 5.4:   Photo during guide installation at a similar angle to that provided by the monitoring system.
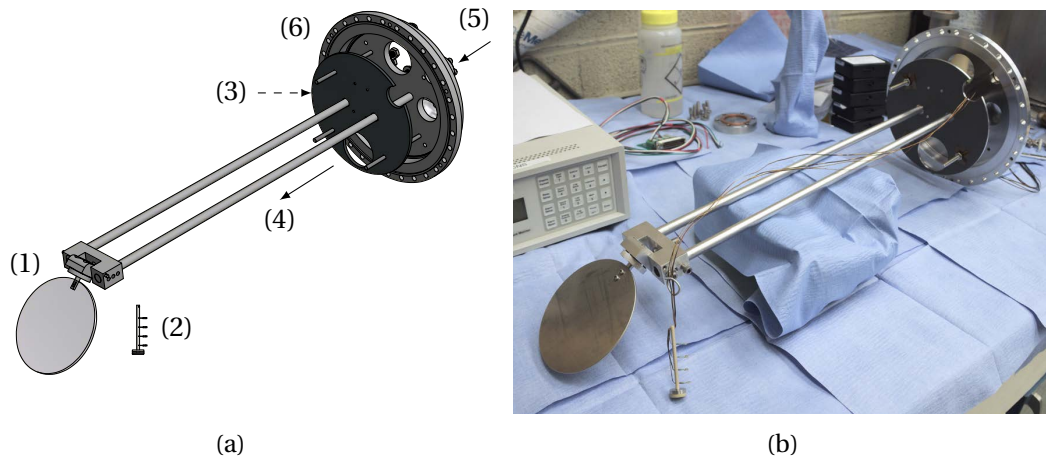
Figure 5.5: (a) CAD rendering and (b) photo of the monitoring system insert including (1) "dentist's mirror," (2) temperature sensor holder, (3) blackbody plate, (4) viewing path, (5) illumination path, and (6) vacuum flange. The components on the reverse of the vacuum flange are given in Figure 5.2.

The neutron guides and coated deuterium container have mirror-like surfaces leading to a "hall of mirrors" view through the window. This, along with the transparency of the solid deuterium, makes it tricky to decipher what is actually being seen in any given photo. It is necessary to compare each photo with a photo of the empty container, and it is also helpful to view a series of photos taken in time-lapse. It can also be difficult to re-focus on the surface of the deuterium after it has grown above the bottom of the container. Here the embedded temperature sensors provide a useful reference. An explanation of images taken is given in Figure 5.6, and an image from a similar view is given in Figure 5.4 for more context.

The cryostat window is an optical glass, fused silica, window in a 2.75 inch ConFlat with an aperture of 3.6 cm (1.4 inches). The vacuum jacket window is a polycarbonate plate seal with O-rings. As the cryostat "floats" only partially constrained inside the vacuum jacket, the vacuum jacket window is mounted on a top-hat shaped flange that can be replaced independent of the large vacuum jacket segment. This allows the outer window to be very close to the inner window, making the best use of the limited aperture.

Because the optical window is small, a partially-silvered mirror was initially planned to provide illuminations co-linear with the camera. However, this moved the camera farther from the aperture of the window, causing significant vignetting. (This approach may still be interesting for a study that uses a laser.) Instead, a 1.33 inch ConFlat window was added to the cryostat flange to allow separate illumination, and several white LEDs mounted to the vacuum jacket provide the illumination.

Figure 5.6: Photo of the empty deuterium container seen through the monitoring system. The view from above is shown in Figure 5.8. The residual deuterium in the cryostat has been condensed at center of the deuterium container, located below (1). This confirms that the center of the container is the coldest point. The lower arc at (2) is the bottom edge of the mirror. The upper arc at (3) is the edge of the container, a fillet where the bottom meets the vertical walls. (4) is the embedded temperature sensor holder. Unfortunately, there is evidence of issues with the neutron guides. The crossing lines at (5) are titanium wires used to support the lowest neutron guide. They should be located above the deuterium container, and out of the focal plane of the image, and so have evidently broken free and are lying on the bottom of the container. The container has a mirror finish, and the many specks seen, for example at (6), are most likely pieces of nickel coating fallen from the guides above. The distortion at (7) is caused by the screws used to mount the mirror.
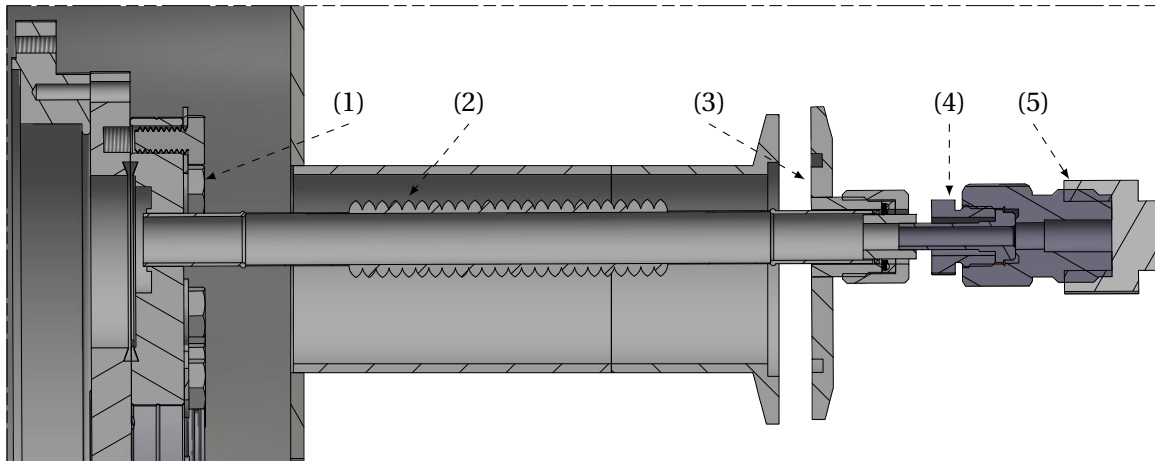
Figure 5.7: Cross-section CAD drawing of the pressure feedthrough. From left-to-right, (1) ConFlat fitting, (2) bellows and tube, (3) KF-to-Quick-Coupling fitting, and (4) VCR gland with split nut, which is attached to the (5) pressure gauge with a $^1/_4$ inch-to-$^1/_2$ inch VCR adapter.

As an interesting aside, the LEDs must be mounted to the room temperature vacuum jacket and not to the cryostat because the band-gap of diodes, and therefore the color of LEDs, is dependent on temperature. White LEDs are actually UV LEDs exciting a phosphor, and will cease to produce light at cold temperatures.

Photos were initially taken with an Olympus OMD-EM10II, with a four-thirds sized sensor, using a zoom lens at a 120 mm focal length. Later we switched to a Canon EOS Rebel T1i, with APS-C sized sensor, using a zoom lens at a 130 mm focal length. Of course, smaller areas of the crystal can be examined at higher resolution with longer focal lengths.

5.2.3 Pressure

The neutron guide is held between 40 K and 80 K and so requires a thermal break before a room temperature pressure gauge. A 1.27 cm (½-inch) stainless steel bellows was welded to the 2.75 inch ConFlat on the monitoring flange. This bellows and tubing extends out of a KF50 fitting, and the vacuum jacket is sealed with a KF-to-Quick-Coupling. A ¼-inch Swagelok VCR gland is smaller in diameter (if a split-nut is used) than the $^1/_2$ inch tube, allowing the gland to fit through the Quick-Coupling, Figure 5.7. This complicated arrangement allows the large vacuum jacket flange to be installed before the pressure feedthrough is secured, but unfortunately requires the cryostat to be briefly opened for the vacuum jacket flange to be installed or removed. The cryostat "floats" inside
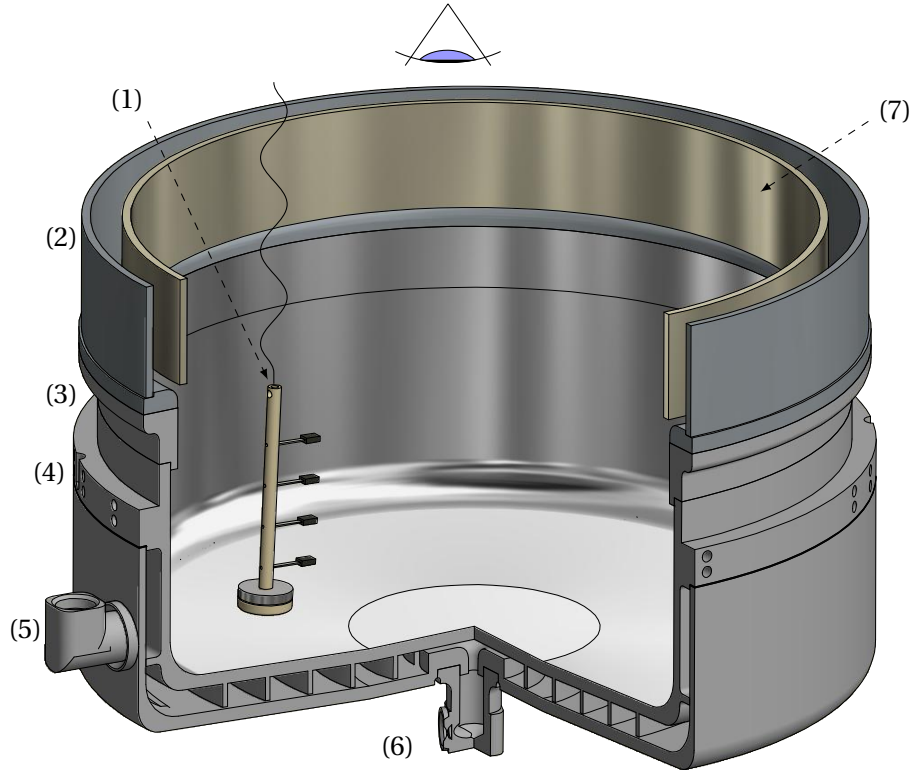
Figure 5.8: Cross-section CAD rendering of the deuterium volume at the bottom of the cryostat, up to the gradient ring. The eye symbol shows the view from above seen through the mirror. Counter-clockwise from the top is (1) the embedded temperature sensor stand and ribbon wire, (2) gradient ring, (3) the groove holding the electric heater band, (4) the location of the container temperature sensor, (5) cryogenic helium outlet, (6) cryogenic helium inlet and its temperature sensor, and (7) neutron guide.

the vacuum jacket, so both the ConFlat fitting and KF-to-Quick-Coupling fittings are mounted off-center and can be rotated to account for the bulk of the alignment while the bellows compensates for the remainder. This allows a pressure measurement as close to the cryostat volume as feasible, and provides a good point of comparison to the pressure gauges in the gas handling area.

5.2.4   Temperature

To directly measure the temperature profile of the solid deuterium, temperature sensors mounted to a stand are lowered from the mirror by their leads, much like line from a fishing rod. We use four Lake Shore model DT-670-SD-1.4L SD-packaged silicon diodes. They are calibrated by Lake Shore down to 1.4 K, and have an expected accuracy of ±12 mK. Further details are given in the Lake Shore catalog appendix D [84]. These sensors are mounted to the stand at heights of 1 cm, 2 cm, 3 cm, and 4 cm above the bottom surface of the deuterium container, Figure 5.8. The stand is machined

from PEEK plastic, which has a thermal conductivity much less than solid deuterium. This ensures a measured temperature gradient is due only to the solid deuterium. For temperature isolation, the sensors are supported by only their leads 1 cm from the stand. The bottom of the stand is a half torus, minimizing contact with the surface to a ring. A stainless steel disk is included as a (fishing) weight. Quad-lead ribbon cables run from each sensor to a multi-pin 2.75 inch ConFlat feedthrough on the flange, to a KF40 electrical feedthrough on the vacuum jacket, and finally to a Lake Shore model 218 temperature monitor.

Cryostat temperature instrumentation and control is discussed in greater detail in Chapter 4, but to briefly cover the important details: A calibrated Lake Shore Cernox designated TSD1a (redundant with TSD1b) is located on the the outside of the deuterium container, near the top, just under the gradient ring. A second Cernox designated TSD6 is located on the helium inlet to the deuterium container. The sensors embedded in the deuterium were not designated, and are just referred to as 1 cm, 2 cm, 3 cm, and 4 cm. One resistive wire heater, designated EHD1, is wrapped around the container just below the gradient ring, and another, designated EHN1, just above the gradient ring. Figure 5.8 gives the locations of these except for EHN1.

The temperature of the deuterium container can be adjusted in a few ways. The flow of cryogenic helium is determined by the pressure in the helium dewar, which is primarily set by the pneumatic proportional valve return to the liquefier (V308). The temperature of the helium is controlled some-what by the height of the withdrawal line in the dewar; from warmer gas completely when elevated out of the dewar, to two-phase and liquid flow when lowered completely into the dewar. Finally, the electric heaters can apply a heat load to offset the helium cooling.

During sublimation of every test, cold helium flow was returned through manual hand valve V389 ("40 K return"). The helium dewar fill level was 210 L to 250 L during all tests. When the deuterium container was cooled to its minimum temperature by fully lowering the withdrawal tube into the dewar, return flow is switched through pneumatic proportional valve V904.

5.2.5   Infrared load

An infrared load is provided by an anodized aluminum plate, available from McMaster-Carr, mounted on the flange just inside the usual location of the UCN window foil, Figure 5.5. A 25 Ω cartridge heater and a Lake Shore model PT-100 platinum resistance thermometer are mounted to the outside of the plate to provide temperature control, Figure 5.9. It is supported from the flange by three stainless steel threaded rods.

Table 5.1: Description of tests performed with the monitoring system. Separate gas handling cycles are designated A-E, and milestones within a cycle are given a subscript.

Date of test	Designation	Description
2016/02/02	A_1	New sublimation, small amount
2016/02/03	A_2	Unintentional warm-up
2016/02/23	B_1	New sublimation
2016/02/26	B_2	Full inventory
2016/02/27	B_3	Warmed for "annealing"
2016/02/29	B_4	After "annealing"
2016/03/01	B_5	Melt and re-freeze
2016/03/02	B_6	Frozen from liquid
2016/03/03	B_7	Cool to operating temperature
2016/03/04	B_8	Unintentional warm-up
2016/03/15	C_1	New sublimation, unstable growth
2016/03/25	C_2	Full inventory
2016/03/28	C_3	IR load test
2016/03/29	C_4	Heater pulsing
2016/04/04	C_5	Warm-up, temperature anomaly
2016/04/11	D_1	New sublimation
2016/04/13	D_3 [†]	Full inventory
2016/04/14	D_4	Cool to operating temperature
2016/04/15	D_5	Warm-up
2016/04/25	E_1	New sublimation
2016/04/26	E_2	Unintentional warm-up

[†] D_2 skipped to avoid confusion with deuterium.
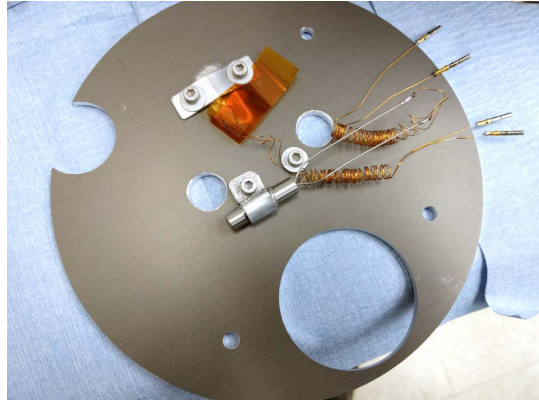
Figure 5.9: Infrared load plate facing away from the solid deuterium mounts a cartridge heater and temperature sensor.

Table 5.2: Conditions during initial sublimation at the beginning of each test. Instrument designations are in brackets.

Test	A_1	B_1	C_1	D_1	E_1
Date (2016)	2/2	2/23	3/15	4/11	4/25
Time	14:00	9:00	13:40	10:00	10:00
D_2 container top [TSD1a] (K)	8.2	8.3	18.3	16.2	17.8
Helium inlet [TSD6] (K)	<5.4[†]	<5.4[†]	9.5	8.4	9.7
Helium return [TSD2] (K)	6.8	7.3	18.6	12.6	16.3
D_2 container heater PS3a [EHD1] (W)[‡]	0	0	0	6.0	4.1
Gradient ring heater PS3b [EHN1] (W)[‡]	0	0	0	8.7	0
Withdrawal tube height (cm)	35	20	55	70	70
Dewar valve [V308] (%)	19	22	30	28	45
Dewar pressure [P308] (psig)	5.7	5.4	4.5	5.3	4.5
D_2 pressure [PD15] (mbar)	10	10	40	15	16
D_2 flow [MD01] (L/min)	0.4	0.3	0.8	0.8	0.7

[†] The helium inlet [TSD6] sensor response curve was not initially defined below 5.4 K.

[‡] Heater power is calculated from current and potential measured by the power supply and includes lead resistance. The gradient ring heater is 17 Ω and the deuterium container is 19 Ω including the leads. "PS" is short for power supply.

5.3 Results & Discussion

5.3.1 Summaries

A series of deuterium condensation tests were conducted under different conditions and observed with this monitoring system. I define a "cycle" as condensing deuterium gas stored in the ballast tank into the cryostat, then warming the solid deuterium and returning it to the tank. These cycles are essentially independent from one another. To distinguish these tests, I have designated each cycle with a capitol letter, and labeled individual treatments and milestones within each cycle with a numeric subscript, see Table 5.1.

A limited and highly variable chilled water supply proved a serious problem during all tests. Variations in the chilled water caused variations in the cooling power provided by the liquefier, and therefore container temperature. During cycles B and E, the liquefier compressor overheated, resulting in a loss of cooling and a loss of the deuterium crystal. Variations in the chilled water also impacted the para-ortho converter on the gas handling panel. This led to variations and interruptions in the deuterium flow rate into the cryostat. This infrastructure problem will have to be resolved for the Source to be reliable, and would improve the precision of future deuterium studies in the source.

Nonetheless, these tests provided a wealth of information. The range of behavior displayed by the solid deuterium was more dramatic than expected and underscores the need for this study. A brief summary of each cycle follows.

Cycle A

Cycle "A" was primarily a test of the gas handling system and monitoring setup. The ballast tank was initially charged with a minimal amount of gas, and only 100 mL of solid deuterium was condensed. Helium flow was likely two-phase, with the helium inlet less than 5.7 K, and the container at 8.2 K. Deuterium was allowed into the cryostat at a rate of 0.3 $^L/_{min}$ (STP), and cryostat pressure as measured at the manifold box was 10 mbar, see Table 5.2. Deuterium condensed as opaque islands around nucleation sites uniformly over the bottom of the container, see Figure 5.12a.

Cycle B

Cycle "B" initially reproduced the same conditions as "A," producing similar growth. The crystal was grown during the day when the reactor was open, and left to sit overnight. On the second day, the gradient ring heater was turned on and set to 5.8 W (10 V), and helium flow was adjusted to warm the neutron guide a few degrees. The final crystal produced was between 3 cm and 4 cm in height, and had a rough, crystalline surface like snow, see Figure 5.12b.
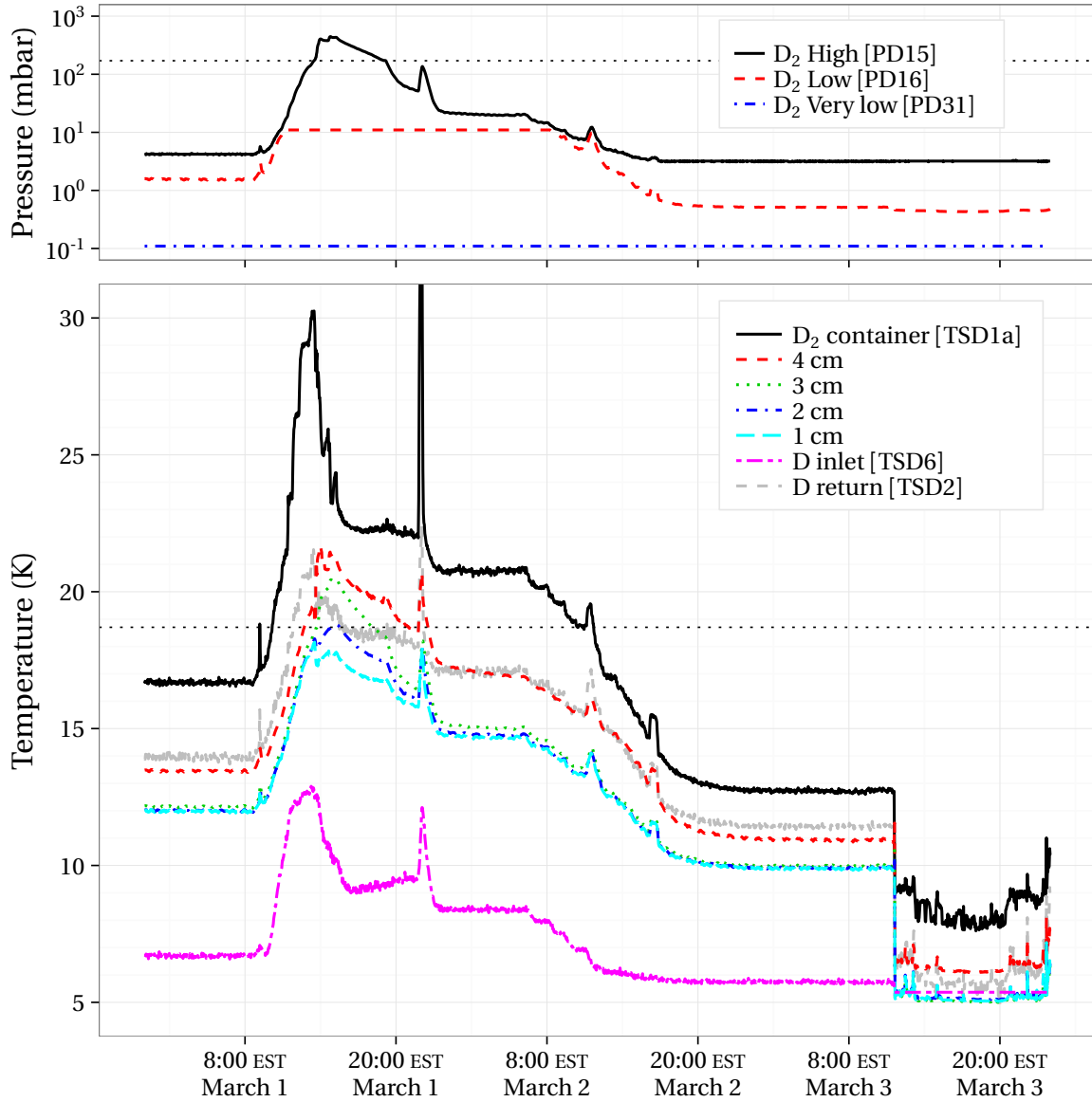
Figure 5.10: Pressures and temperatures during melting and re-freezing. Plot begins after annealing, B_4, and extends to until the crystal was cooled to operating temperature, B_7.

The crystal was then modified by maintaining an elevated temperature, which we will refer to as "annealing" the crystal. The electric heaters on the gradient ring and deuterium container were set to 8.6 W (12 V) and 2.6 W (7 V) respectively, and helium flow was then adjusted to raise the container temperature, and the crystal was held steady at this temperature for several days, with the helium inlet at 6.8 K, the container at 16.7 K, and the 1 cm embedded sensor at 12.0 K. The surface smoothed, and the crystal became slightly more translucent, see Figure 5.13a.

We melted and froze a new crystal from liquid. The container heater was then slowly stepped up until pressure reached the triple point, while taking care not to let pressure rise above the return check valve cracking pressure. With the heater at 17.75 V (17 W), the container at 29 K, the helium inlet at 12.6 K, and the manifold box pressure at 173 mbar, the embedded sensors cooled slightly as the surface started melting. The container heater was then slowly stepped down as the crystal melted over the next hour. With the helium inlet remaining cold, the bottom-center of the crystal likely did not melt. The embedded sensor at 1 cm did not reach the triple point temperature. Temperatures and pressures are plotted in Figure 5.10. The heater was further stepped down, and the crystal allowed to slowly freeze over the next 4.5 h. The crystal produced was transparent with large features.

The crystal was then cooled to minimum temperature. The appearance of the crystal did not change noticeably while cooling. Temperatures before and after are given in Table 5.5. Comparing B_6 with B_7, the temperature gradient is much smaller. The container cooled to 7.8 K and the helium inlet to 5.4 K. However, manifold box pressure did not drop below 0.4 mbar, above the range of the pressure gauge on the monitoring system. This corresponds to a saturation temperature, 9.5 K to 10 K, about equal with the container sensor near the top of the container.

Cycle C

For cycle "C," deuterium was condensed at a warmer temperature than the previous test, with the container sensor 17.2 K, and the helium inlet 9.1 K. Deuterium was condensed at a faster rate of 0.8 L/ min. This produced a perfectly clear crystal that grew radially outward from the center of the container, seen in Figure 5.12c. However, with the additional heat load from the flowing deuterium, the container began to continually warm. While trying to increase cooling, helium flow was interrupted, and the crystal melted then rapidly refroze, seen in Figure 5.14a.

To try to account for this additional heat load, we wished to increased the load from the electric heater such that it could later be decreased to offset the load introduced by the gas. To allow electric heaters to be applied, the withdrawal tube was lowered from 55 cm to 40 cm to first increase cooling. Overnight, the electric heaters were applied, and the crystal was slowly warmed, the container

back to 18 K, with pressure reaching 15 mbar. Interestingly, the crystal, still the same volume of deuterium well below melting temperature, migrated into an area of much smaller radius, as seen in Figure 5.14b. This confirms behavior seen before; at higher temperatures, deuterium is very mobile and will move away from areas of warmer temperature.

Deuterium was then sublimated over this crystal. Again it was left at high temperature, and again the deuterium migrated into a central crystal with smaller radius, see Figure 5.14c to Figure 5.14d. Over the next week, deuterium was repeatedly sublimated on the existing crystal under different conditions, then left to anneal. The surface of this composite crystal reached the sensor at 4 cm.

We then tested the infrared load plate. The plate was not sufficiently thermally isolated from the monitoring flange, and could not be warmed above 175 K with the present power supply delivering roughly 20 W. The neutron guide warmed from 58 K to 72 K, and deuterium container continued to warm after the heater was cut off, from 10.8 K to 11.7 K. After the neutron guide and plate had cooled again, the electric heater mounted at the UCN window was increased until the neutron guide was warming at the same rate as before. The system behaved identically, showing the rise in these temperatures was just a result of the poor thermal coupling. The plate will need to be properly isolated before it can be applied.

The crystal was then cooled to minimum temperature. We were still learning how to cool the container slowly. It was first cooled rapidly, then warmed, then cooled again. As seen in Figure 5.15, this rapid cooling created ripples on the crystal surface, possibly from the rapid sublimation of the remaining vapor. While modifying liquefier operation, the container temperature rose and fell multiple times. This strengthened the surface features, seen in Figure 5.16

We then purposely induced temperature changes by pulsing the electric heater. This is not dissimilar from what might be seen at pulsed neutron sources. Changes to the surface of the crystal, seen in Figure 5.17, were dramatic. The surface became increasingly rough and opaque.

The deuterium container was then slowly warmed. Interestingly, the deuterium must have been partially thermally disconnected from the crystal. With the container warmed to 32 K and the helium inlet to 15 K, the crystal remained 13 K. At this warmer temperature, the surface irregularities softened, but never became transparent, see Figure 5.18.

Cycle D

In preparation for cycle "D," the cryostat was initially not warmed and evacuated as usual, but evacuated only to 100 mbar at 100 K. When cooled, this residual vapor left a visible crystal in the center of the container. The fear was this would provide a poor seed for further growth. To remove it, the cryostat was warmed and fully evacuated. This is a significant logistical effort, and it would be worth exploring if it is really necessary.
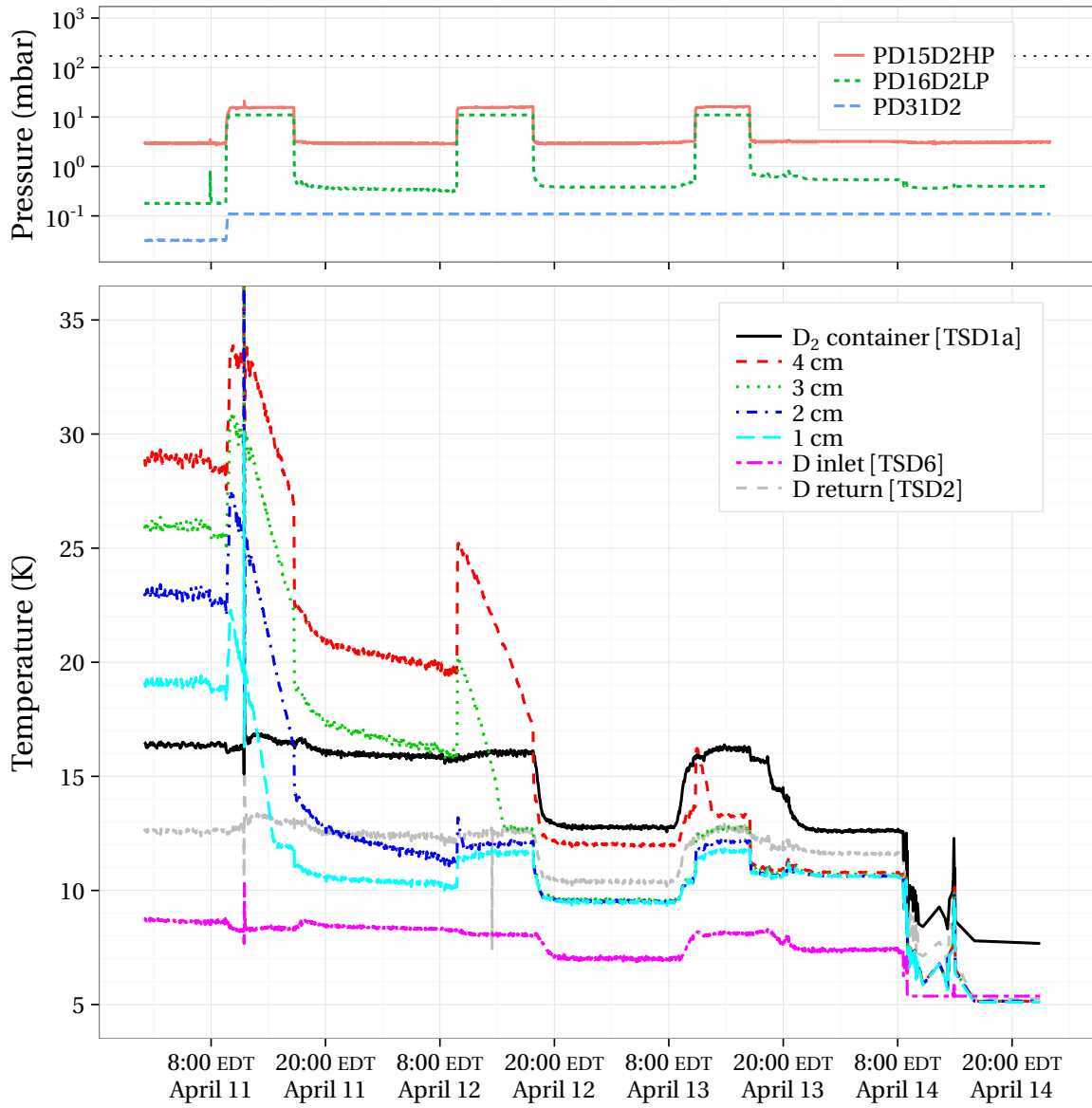
Figure 5.11: Pressures and temperatures during sublimation over three days. Plot begins with the cryostat under vacuum, gas was introduced, D_1, sublimated, and cooled to operating temperature, D_4.

For cycle "D," deuterium was condensed at a measured temperature similar to initial conditions in cycle "C." However, instead of limiting helium flow, the container was warmed primarily with electric heaters. Building from the previous experience, the electric heaters were lowered to offset the heat provided by deuterium flow. The initial growth was opaque. We observed the center of the container is much colder than the external temperature sensors indicated; they are inflated by the electric heaters.

On the first night, electric heaters were left on, and on the second night, electric heaters were turned off to observe the difference in movement, see Figure 5.11.

As the crystal grew in height, it became transparent. This tracks with an increase in pressure and temperature of the embedded temperature sensors with crystal height. As the crystal grows, the surface, farther from the cold container, is warmer.

Finally the crystal was cooled to operating temperature. Switching from gas to liquid cooling was not a smooth transition. The liquefier is touchy during this process, and a proper procedure will have to be mastered to avoid rapid variations in the temperature of the crystal.

Cycle E

For cycle "E," deuterium was condensed at a measured temperature similar to initial conditions in cycle "C." However, building on the previous experience, the container was warmed primarily by limiting helium flow, and electric heaters were applied only to the minimum needed to offset the heat introduced by deuterium gas flow. This produced a clear but textured crystal, contrasted with initial growth in cycle B. However, the liquefier compressor overheated due to limited chilled water supply, and the crystal was lost before it could be grown completely.

5.3.2 Volume condensed

Determining the amount of solid deuterium condensed prior to warming the converter at the end of the procedure is not straightforward because the amount of deuterium held in the converter is substantial and not precisely known. In a continuous flow mode, the amount held as a liquid need not be constant; deuterium can be cryopumped out of the converter and into the cryostat faster than it is cryopumped out of the ballast tank into the converter, and vice versa. In addition, a significant amount of deuterium is physisorbed by the catalyst. Both of these effects change with small changes in temperature of the converter. This was particularly noticable during these tests as the variable chilled water supply led to an unstable converter temperature.

During the condensation procedure, the mass of deuterium condensed was determined by the change in ballast tank pressure, less the mass initially stored in the converter. A more accurate measure of the final mass condensed is obtained when the converter is warmed and the gas remaining in the converter is returned to the ballast tank. This is currently a slight overestimate as the volume

Table 5.3: Pressures in the ballast tank and cryostat used to estimate condensed mass.

Test	Ballast tank pressure (mbar)						Cryostat pressure (mbar)	
	Initial	Converter filled	End of condensation	Before warm-up	After warm-up	After recovery	After warm-up	After recovery
A	342	298	234	234†	262	*	328 (110 K)	
B	925	725	294	402	907	*	995	
C	918	834	189	339	854	883	901 (100 K)	101 (100 K)
D	995	963	414	448	963	986	1010 (140 K)	4.5
E	985	944	771	771†	970	*	1033	

† Inventory remaining in the converter was not recovered to the ballast tank.
* Inventory remaining in the cryostat was not recovered to the ballast tank.

of gas evacuated from the gas panel is not yet precisely known and the volume of gas remaining in the converter at arbitrary temperatures has not been measured. Our most accurate measure is obtained when the cryostat is warmed to room temperature, and the final pressures in the ballast tank and cryostat are known and compared with the ballast tank pressure prior to warming.

Due to time constraints, and a leak in the safety burst foil, the cryostat was usually pumped out before it warmed to room temperature, and so in those cases, the cryostat's temperature must also be taken into account. Similarily, the pressures in the ballast tank and cryostat after recovering gas from the cryostat back to the ballast tank can be used to calculate a condensed mass, although this is a very small overestimate as some gas is evacuated from the gas panel after recovery.

$$\left(\rho(P_1) - \rho(P_2)\right) V_{\text{tank}} = m_{\text{condensed}} \tag{5.1}$$

These pressures are given in Table 5.3, and the estimated masses condensed are given in Table 5.4. Because deuterium deviates noticably from the ideal gas law, this mass was calculated using Equation 5.1 with densities, ρ, calculated from the NIST Standard Reference Database at each pressure and temperature [91]. A ballast tank volume of 1800 L and a cryostat volume of 23.2 L were used. (This does not include the volume of room-temperature tubing between the cryostat and ballast tank on either side of the dividing check valve.) These masses are also given as solid volumes at the triple point using a density of 173.94 kg/m³ [151].

Table 5.4: Estimates of condensed mass for each of the five tests.

Test	Estimated mass (g)					Solid volume (mL at triple point)				
	End of condensation	Before warm-up	After warm-up	After recovery	Integrated flowmeter	End of condensation	Before warm-up	After warm-up	After recovery	Integrated flowmeter
A	19.0	†	11.7	*	‡	109		67		
B	128	155	154	*	‡	736	891	885		
C	192	172	163	162	‡	1104	989	937	931	
D	163	163	161	160	155	937	937	926	920	891
E	51.4	†	63.1	*	47.1	296		363		270

† Converter was not recovered to ballast tank.
* Cryostat was not recovered to ballast tank.
‡ Flowmeter was not continuously logged.

The volume condensed can also be determined by integrating the mass flowmeter. This dead reckoning is susceptible to accruement of error over time, and so initially needs to be compared to several condensations of different volumes. Although the flowmeter is calibrated for instataneous values, error introduced by our logging system, in particular the ADC, has not been addressed. The mass flowmeter was not initially logged continuously, and so was only available on tests D and E. These volumes are also given in Table 5.4. The flowmeter provides a mass flow in NTP L/min (20 °C and 1 atm) and is converted to mass with a NTP density of $0.1652 \, \mathrm{kg/m^3}$ [91].

It is clear that the estimate of condensed mass made at the end of condensation is unreliable due to the unknown volume in the converter. Instead, during the procedure we will need to rely on the flowmeter. The accuracy of this integrated flow would best be determined by comparing its record with the estimated condensed mass, as determined after warming the cryostat, over a range of condensed masses.

5.3.3 Optical

Growth

Photos of the initial sublimations are shown in Figure 5.12. The small amounts shown are well below 1 cm, and so not yet registered on the first embedded sensor. The temperature should be approximately that of the helium inlet, TSD6 in Table 5.2, and potentially slightly warmer. Photos of the final inventory are shown in Figure 5.13.
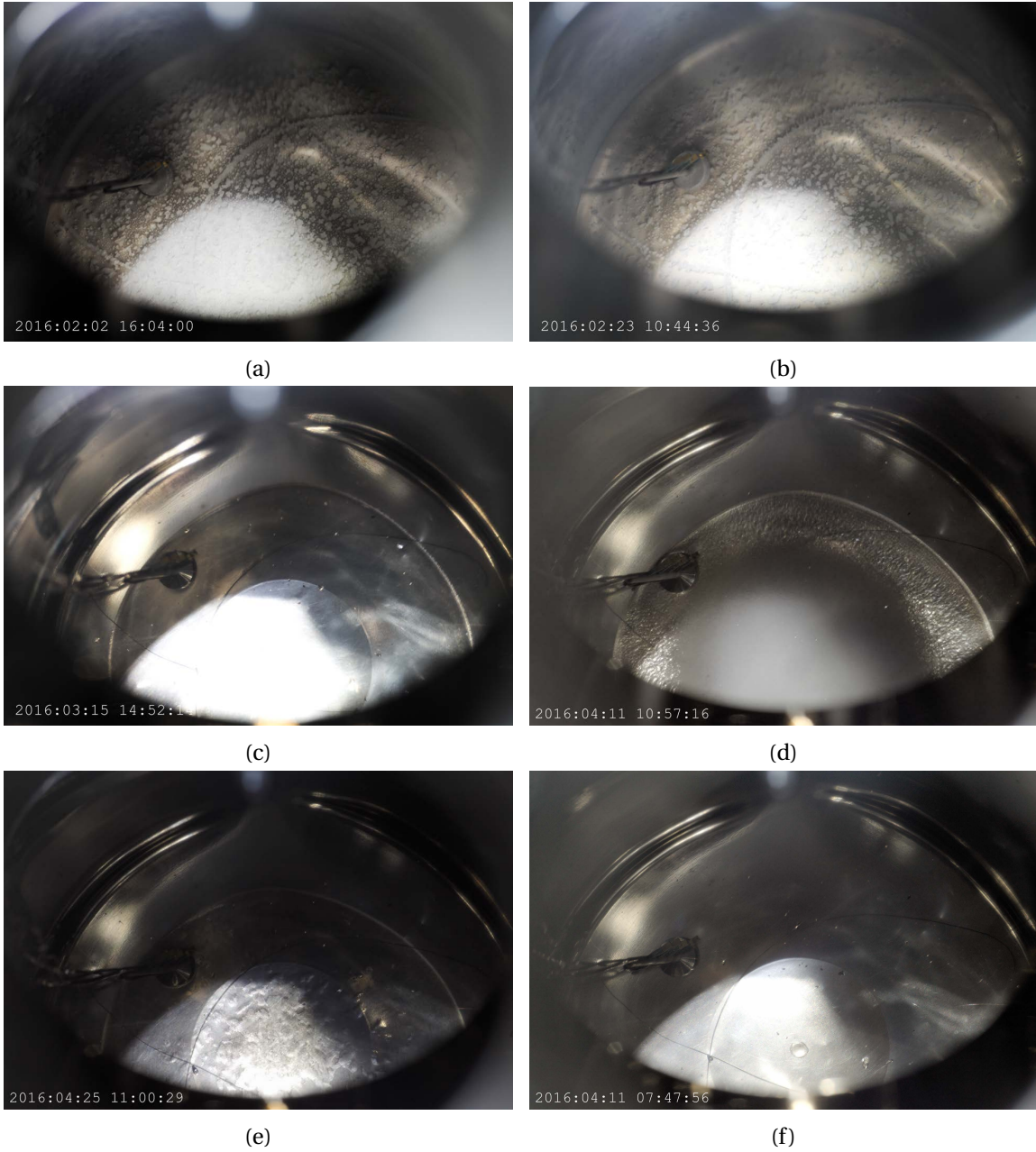
Figure 5.12: Photos during the initial sublimation of each cycle, with (a)-(e) corresponding to A_1, B_1, C_1, D_1, and E_1, and (f) of the empty container. The timestamps in (a)-(b) are one hour behind before daylight savings time.
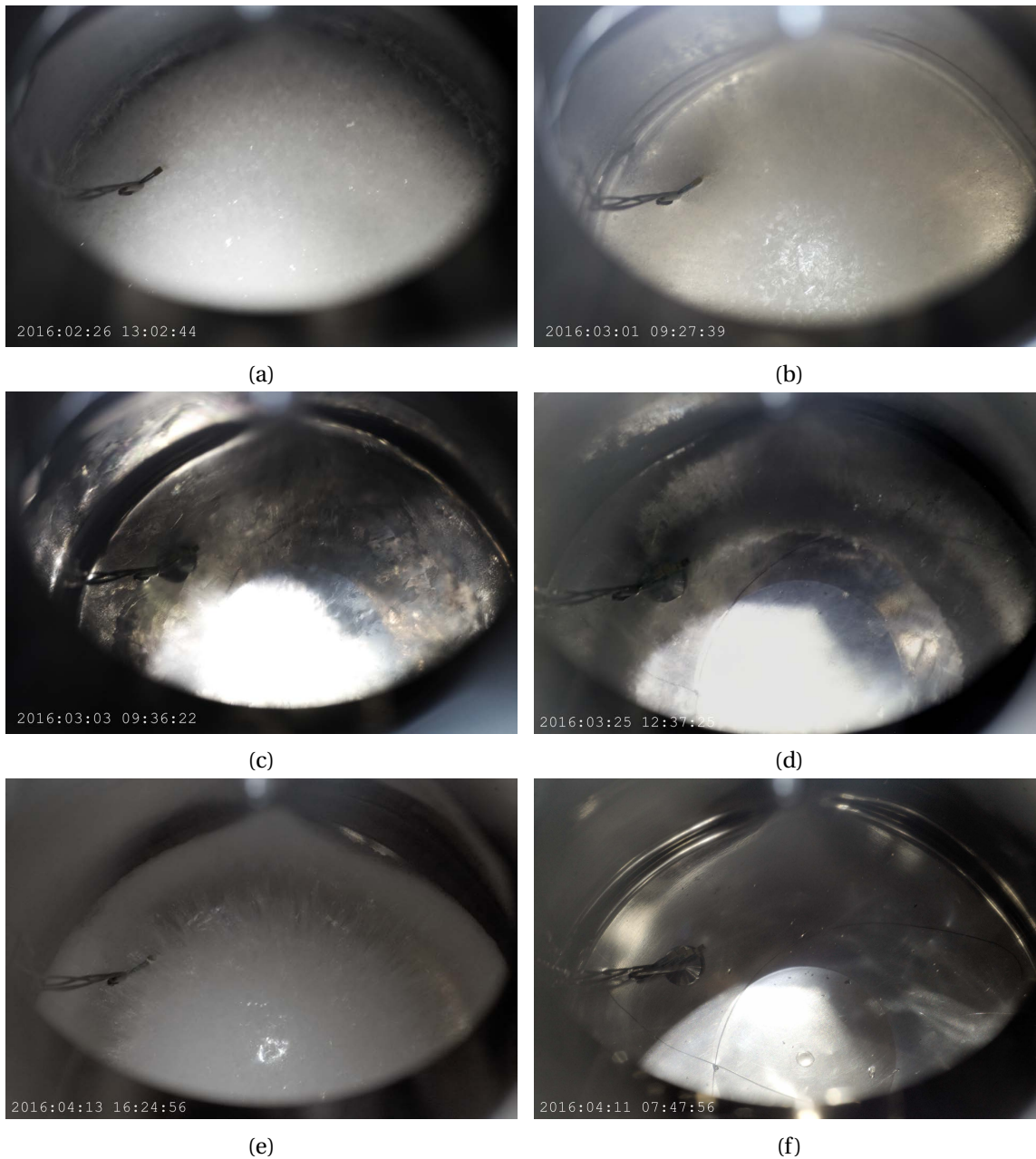
Figure 5.13: Photos at final inventory for several tests. (a) B_2 is a fast sublimation at a cold temperature, and (b) B_4 is the same crystal after "annealing" at 16.7 K for several days. (c) B_5 is the result of melting and slowly re-freezing from liquid the same inventory. (d) C_2 is the sum of repeated sublimations under various conditions as seen in Figure 5.14. (e) D_3 is another sublimation of full inventory. (f) The empty container is shown for comparison.

As mentioned, we saw a change in the initially opaque crystal of B_2 when left at a warm temperature, compare Figure 5.13a and Figure 5.13b. The surface smoothed, and the crystal became slightly more translucent. We refer to this as "annealing," and it could potentially be used to prepare an initial crystal or refresh an old crystal without melting and re-freezing.

There is clearly a transition from opaque to clear sublimation crystal growth from low temperature and pressure to high temperature and pressure. Between the two temperatures, the crystal grown is clear but has large scale non-uniformities. This is seen in Figure 5.12e when compared to opaque in Figure 5.12d and perfectly clear in Figure 5.12c. This transition was not exactly pinned down, but it is greater than 15 mbar and 10 K. A transparent crystal is likely a polycrystal with a large grain size, and so preferable for UCN production.

Deuterium Migration

Above 10 K, the difference in deuterium vapor pressure with temperature leads to an interesting effect. Deuterium will sublimate away from slightly warmer areas and re-condense in cooler areas leading to a net migration towards colder areas. This effect is quite dramatic. The bottom of the container is coldest in the center, and deuterium grown as a wide disk and left for a matter of hours will form a dome of smaller radius, see Figure 5.14. This effect in deuterium is known by those preparing fuel for fusion work. Interestingly, this effect is present in DT mixtures even in an isothermal setting; the self-heating from β-decay in tritium will create temperature variations due to differences in crystal thickness [60].

If a crystal is grown in separate stages, e.g. grown during working hours and left to migrate overnight, this could lead to a remarkably different geometry than if grown continuously. Also, in this data, deuterium tended to pull away from the embedded temperature sensor near the surface. Once cooled below 10 K, this effect was not observed over the course of days, but may still be present over longer time-scales.

Surface effects

Rapid variations in temperature can lead to surface irregularities. Cooling the full inventory C_2 leads to a visibly uneven surface, likely from rapid sublimation of the remaining vapor, see Figure 5.15. Further surface features appeared later, possibly related to liquefier operation, although there were no significant measured changes in temperature or pressure during this period, Figure 5.16. Eliminating changes in temperature and maintaining the crystal integrity becomes a matter of careful procedure.

Next, to amplify this effect, the container electric heater was pulsed for several days. The result was quite dramatic, Figure 5.17. The surface became quite rough, and visibility to the bottom of the container is lost.
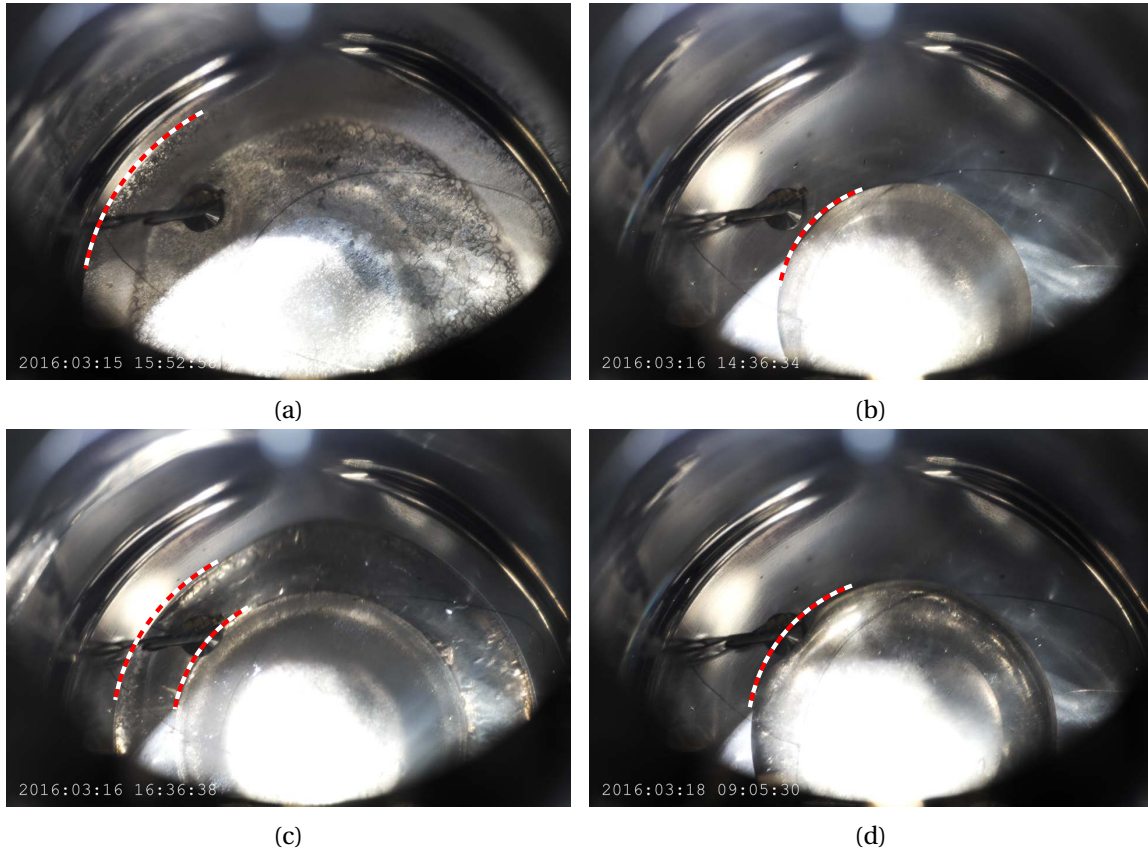
Figure 5.14: Photos of a small amount of deuterium overnight at warmer temperatures, taken before and after. The outer edges of the deuterium have been highlighted with a dashed line. (a) A small amount of deuterium was rapidly sublimated over an existing crystal and the bottom of the container. It was then left overnight with the helium inlet at 8 K and the container at 16 K. (b) Deuterium migrated into a smaller area in the colder region of the container. (c) Deuterium was then sublimated on top of that crystal and left for over a day with the helium inlet at 9.5 K and the container at 18.5 K. (d) Again, the deuterium migrated into a smaller area, forming an apparently uniform crystal.

Once these surface effects become present, it is not apparent how to smooth them other than re-condensing the crystal. The crystal was warmed slowly over several days, and although the roughness disappeared, the crystal stubbornly did not return to transparent, Figure 5.18.

(a)

(b)

Figure 5.15:   Photos of rough surface appearing while cooling.

5.3.4   Pressure

A Pfeiffer model CMR 375 pressure gauge, already on-hand, with a full scale of 0.1 mbar was selected. This maximum pressure corresponds to a deuterium vapor pressure just over 10 K. We expected to make a high-precision pressure measurement when the crystal was cooled to the minimum temperature just over 5 K, however the gauge was always over-scale when deuterium was present. Even at the coldest temperatures, pressure barely reached the 0.1 mbar mark. This prevented the primary goal of translating pressure read at the gas handling panel to cryostat pressure. It is straightforward to replace the gauge with a higher range one in the future.

However, this is still a useful observation. Even while the bulk of the solid deuterium is very cold, pressure should correspond to the warmest area where solid deuterium is present, such as a film along the container walls. Visual observations show the deuterium was readily mobile at warmer temperatures, but no longer mobile below 10 K. The pressure observed also corresponds

(a)

(b)

Figure 5.16:   Photos of rough surface appearing after cooling. There were no significant measured changes in temperature or pressure during this period.

with a deuterium temperature of 10 K, which may be coincidence, or may suggest further deuterium behavior. We might expect the deuterium frozen anywhere in the container that is warmer than this temperature to migrate to a colder area, and so the vapor pressure to correspond to the warmest temperature at which deuterium is no longer mobile.

We were unable to leave the crystal at minimum operating temperature for an extended period. It is possible that pressure may eventually fall as deuterium continues to slowly migrate to cooler areas.

(a)

(b)

Figure 5.17: Photos of a rough surface appearing while the electric heater is pulsed. In particular, the wire along the bottom of the container can no longer be seen.

The small amount of deuterium present during cycle "A" and between cycles "C" and "D" did register a pressure, however temperature was not varied, so they cannot be interpreted as a translation to temperatures. As a future test, less than 50 mL of solid deuterium could be condensed with the expectation that this small amount would condense primarily at the center, coldest part of the container. Its vapor pressure might then be used to measure the actual temperature of the coldest part of the container, as well as our original goal of translating pressure read at the gas handling panel to cryostat pressure.

5.3.5 Infrared load

Unfortunately, the threaded rods that support the infrared load plate did not sufficiently thermally isolate the plate from the flange, preventing it from being warmed to room temperature, and will have to be replaced. With the deuterium container cooled by helium gas, the container sensor was at 10.8 K, and the helium inlet sensor at 5.6 K, the power to the infrared plate heater was increased.

(a)

(b)

(c)

(d)

Figure 5.18: Photos of the change in surface irregularities as the crystal is warmed.

However, because the plate was not sufficiently thermally isolated from the monitoring flange, the neutron guide and deuterium container warmed with the plate. The plate could not be warmed above 175 K with the present power supply delivering roughly 20 W, at which point the neutron guide had warmed from 58 K to 72 K. The container, initially 10.8 K, continued to warm after the heater was cut off to 11.7 K. To attempt to exclude the effect of this rise in temperature, after the neutron guide had cooled again, the electric heater mounted at the UCN window was increased until the neutron guide was warming at the same rate as before. However the system behaved identically. This is to be expected, as the Stefan–Boltzmann law goes as T^4, the plate at 175 K is radiating a factor of 10 less than at 300 K. The isolation of the plate has since been improved, and is expected to function properly in the future.

Table 5.5: Full inventory conditions at various times averaged over 30 min. Instrument designations are in brackets. See Table 5.1 for dates and descriptions.

Test	B_2	B_3	B_4	B_6	B_7	C_2	C_4	C_5	D_3	D_4
Date (2016)	2/26	2/27	2/29	3/3	3/3	3/25	4/1	4/4	4/14	4/15
Start of 30 min average	15:00	6:00	15:00	5:00	18:00	15:00	5:00	6:00	6:00	6:00
D_2 container top [TSD1a] (K)	10.58	16.68	16.79	12.74	7.76	14.80	10.33	21.16	12.62	7.68
Embedded 4 cm (K)	10.287[‡]	13.408[‡]	13.492[‡]	10.945[‡]	6.100[‡]	11.781	8.210	11.168	10.781	5.156
Embedded 3 cm (K)	8.450	12.407	12.189	9.980	5.015	11.660	8.159	11.015	10.708	5.074
Embedded 2 cm (K)	8.334	12.220	12.040	9.909	5.104	11.545	8.148	10.840	10.622	5.152
Embedded 1 cm (K)	8.184	12.167	12.020	9.890	5.050	11.473	8.119	10.740	10.618	5.105
Helium inlet [TSD6] (K)	<5.4[†]	6.81	6.82	5.76	<5.4[†]	6.62	5.52	13.06	7.40	<5.4[†]
Helium return [TSD2] (K)	8.26	13.96	14.03	11.43	5.55	12.95	8.72	12.18	11.60	5.27
D_2 container heater PS3a [EHD1] (W)	0	2.6	2.6	8.2	0	2.0	0	11.6	0	0
Gradient ring heater PS3b [EHN1] (W)	5.8	8.6	8.6	8.6	0	5.1	0	11.8	0	0
Withdrawal tube height (cm)	35	35	35	35	0	45	40	40	70	0
Dewar valve [V308] (%)	25	40	40	40	27	30	22	19	40	36
Dewar pressure [P308] (psig)	5.4	4.1	4.1	4.1	4.2	4.8	4.9	5.8	4.6	5.2
D_2 pressure [PD15/PD16] (mbar)	0.48	1.93	1.60	19.86	0.58	1.06	0.41	0.73	0.53	0.40

[†] The helium inlet [TSD6] sensor response curve was not initially defined below 5.4 K.
[‡] Above surface of solid.

5.3.6 Temperature

The embedded temperature sensors performed as expected and provided temperature profiles in the solid deuterium. There were two interesting anomalies observed that are worth looking at more closely.

First, when cooled to minimum temperature, the embedded sensors recorded an unusual temperature profile, see B_7 and D_4 in Table 5.5. Above $8\,\mathrm{K}$, there was a monotonically increasing temperature with height, e.g. D_3. However, when the withdrawal line to the dewar was lowered, and the container cooled with two-phase helium flow, the profile became; $1\,\mathrm{cm}$ was cold, $2\,\mathrm{cm}$ was warm, $3\,\mathrm{cm}$ was the coldest, and $4\,\mathrm{cm}$ is the warmest. This effect was small, on the order of $0.1\,\mathrm{K}$, but was reproducible. The top sensor, being near the surface of the solid, is expected to be warmed by an infrared load. However, we have no explanation for the temperature inversion seen in the other sensors.

Second, we repeatedly noticed the helium inlet sensor TSD6 would not return to a previous value when returned to the same conditions. With a change to the heat provided by the electric heater on the container, we expect the response of the helium inlet sensor to lag behind the response of both the container and helium return sensors. This is expected as the container sensor is located at the top of the container near the heater, and helium flow similarly exits at the top of the container, while the helium inlet sensor is at the bottom of the container, farthest from the heater. But looking at the data afterwards, there is something amiss.

Figure 5.19 shows the adjustment of electric heaters, with the container empty, in preparation for a test. After the heater was turned on, at a point while the helium inlet was warming and both the container and helium return had reached equilibrium, there is an unexpected dip in both the container and helium return, the container started to warm, and the helium inlet warmed at an increased rate. Conversely, after the heater had been reduced and all sensors were cooling, there was a point when the container and helium return peaked, the container started to cool, and the helium inlet cooled at an increased rate. Finally, the heater was turned up again, and while both the container and helium return returned to their previous equilibrium temperature, the helium inlet reached equilibrium at a much cooler temperature.

The response of the container and the helium return sensors indicate it is not simply a case of poor contact between the inlet sensor and the container. The simultaneous response rules out unrecorded changes in the heater power, as we would expect the hysteresis normally seen. Instead, it appears cooling power is sometimes stolen from the system. One possible culprit is contact between the helium line or container and some other part of the system as the geometry changes with temperature. Another possibility is cryopumping of deuterium in the vacuum jacket on to the container, and in particular the large surface area of the alumina fabric insulation. We know there was a leak
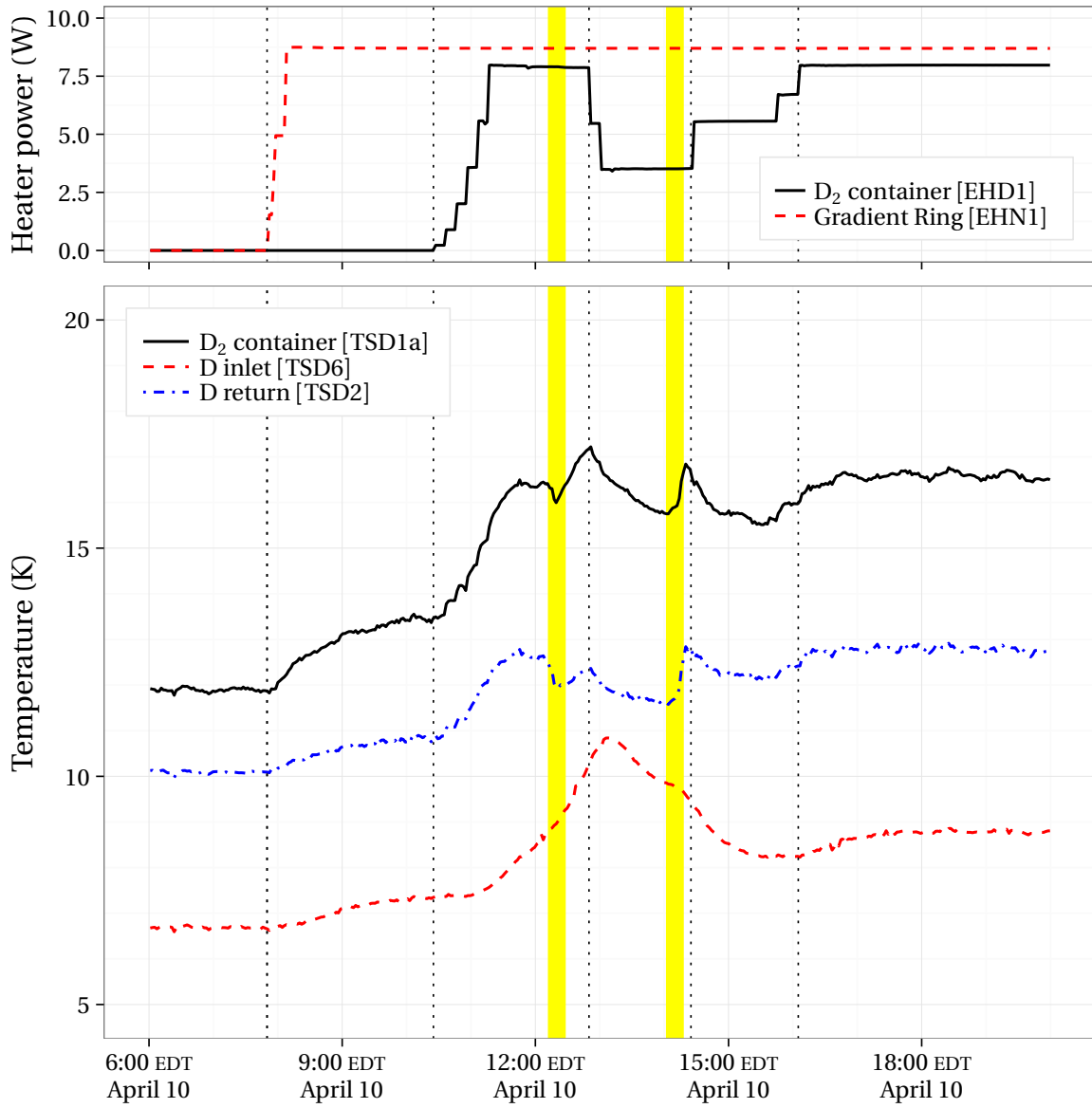
Figure 5.19: Temperatures and heater power while adjusting the temperature of the empty container in preparation for condensation. Unexpected behavior is highlighted.
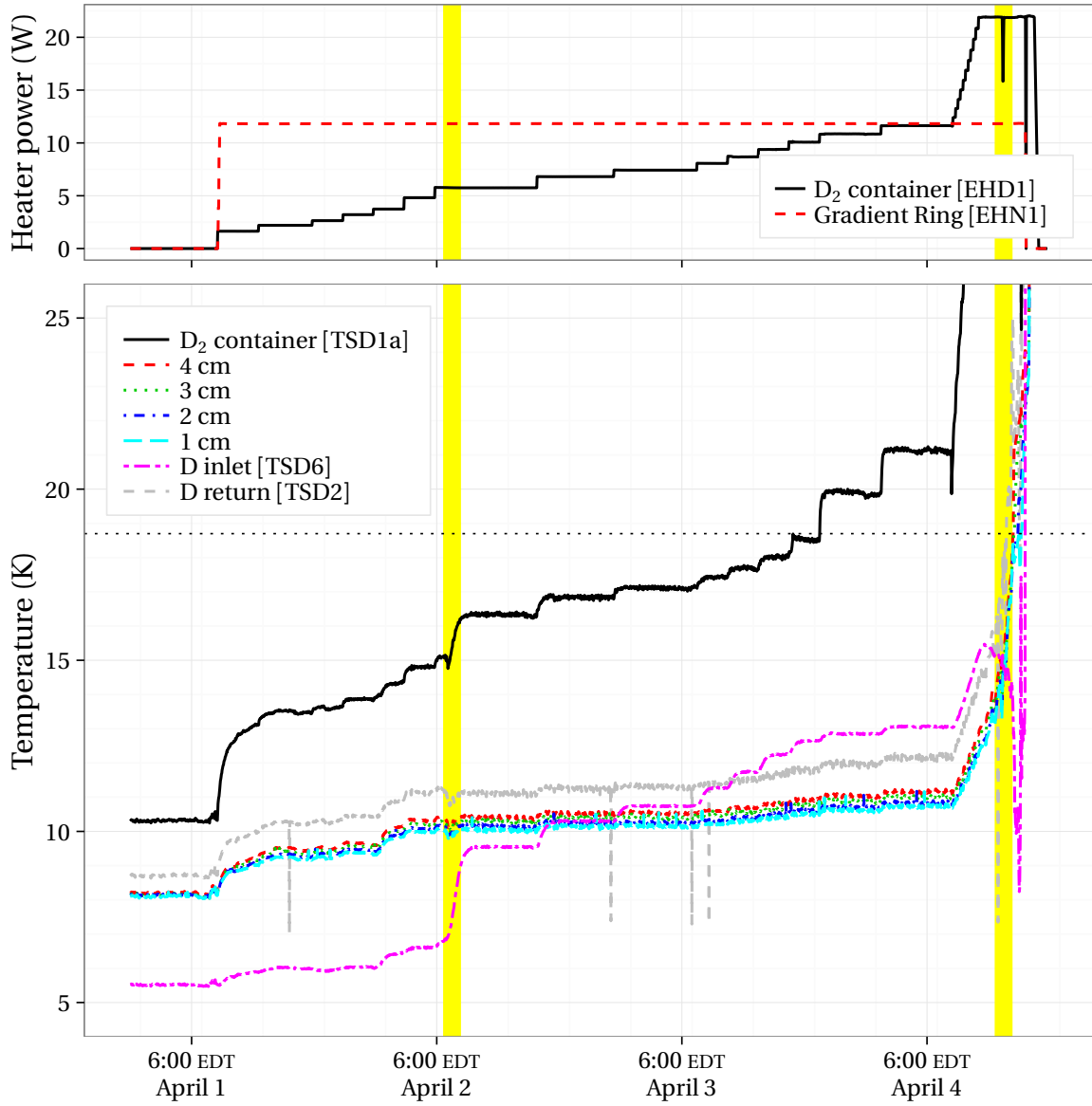
Figure 5.20: Pressures and temperatures during warming over three days. Plot shows full inventory C_4 to melting C_5. Unexpected behavior is highlighted.

of deuterium through the burst foil on the monitoring flange. When the container temperature is initially raised, this deuterium boils off, increasing the local vacuum jacket pressure. On subsequent warming, this deuterium is no longer present. Whatever the cause, this phenomenon must be kept in mind when looking at data from these tests.

Figure 5.20 shows the slow warming of a deuterium crystal. Like the previous example, at a certain point the helium inlet warms to a significantly higher temperature, coupled with dips in the container temperature and helium return. Particularly notable in this case however is that with solid deuterium in the container, the embedded sensors behave similarly to the helium return. Potentially related observation is that, as the container starts to warm, the helium inlet sensor cools dramatically.

Temperature translation

Although pressure can provide an accurate surface temperature, it may be helpful to translate the externally measured temperature to the bulk deuterium temperature after the monitoring system, and embedded temperature sensors, have been removed. The temperatures of the deuterium container (TSD1a), helium inlet (TSD6), and helium return (TSD2) have been plotted against the 1 cm embedded sensor for the periods this sensor was covered with deuterium during cycles B, C, and D in Figure 5.21. As expected, cryogenic conditions, primarily helium cooling, electric heaters, and flowing deuterium, prevent these from being one-to-one translations.

Instead, we can map out translations during the (usually overnight) periods when deuterium was not condensing, electric heaters were constant, and cooling was largely steady. These periods are given in Figure **??** by heater values. There is too little data to extrapolate to a future test, and so it may only be useful when replicating the exact circumstances.

5.4   Conclusions

While these tests were limited by the chilled water infrastructure issue, they provided a much needed learning process for procedural details. More importantly, they showed the range of solid deuterium behavior, some of which is specific to this cryostat.

5.4.1   Procedure when growing from liquid

Growing a crystal from liquid can produce a clear and flat crystal in our cryostat. The procedure appears straightforward. The electric heater provides sufficient temperature control such that the vapor pressure can be kept below the cracking pressure of the return check valve to the ballast tank. The only modification from the procedure in cycle "B" that the dewar withdrawal must be elevated to warm the helium flow and allow the coldest part of the container to melt.
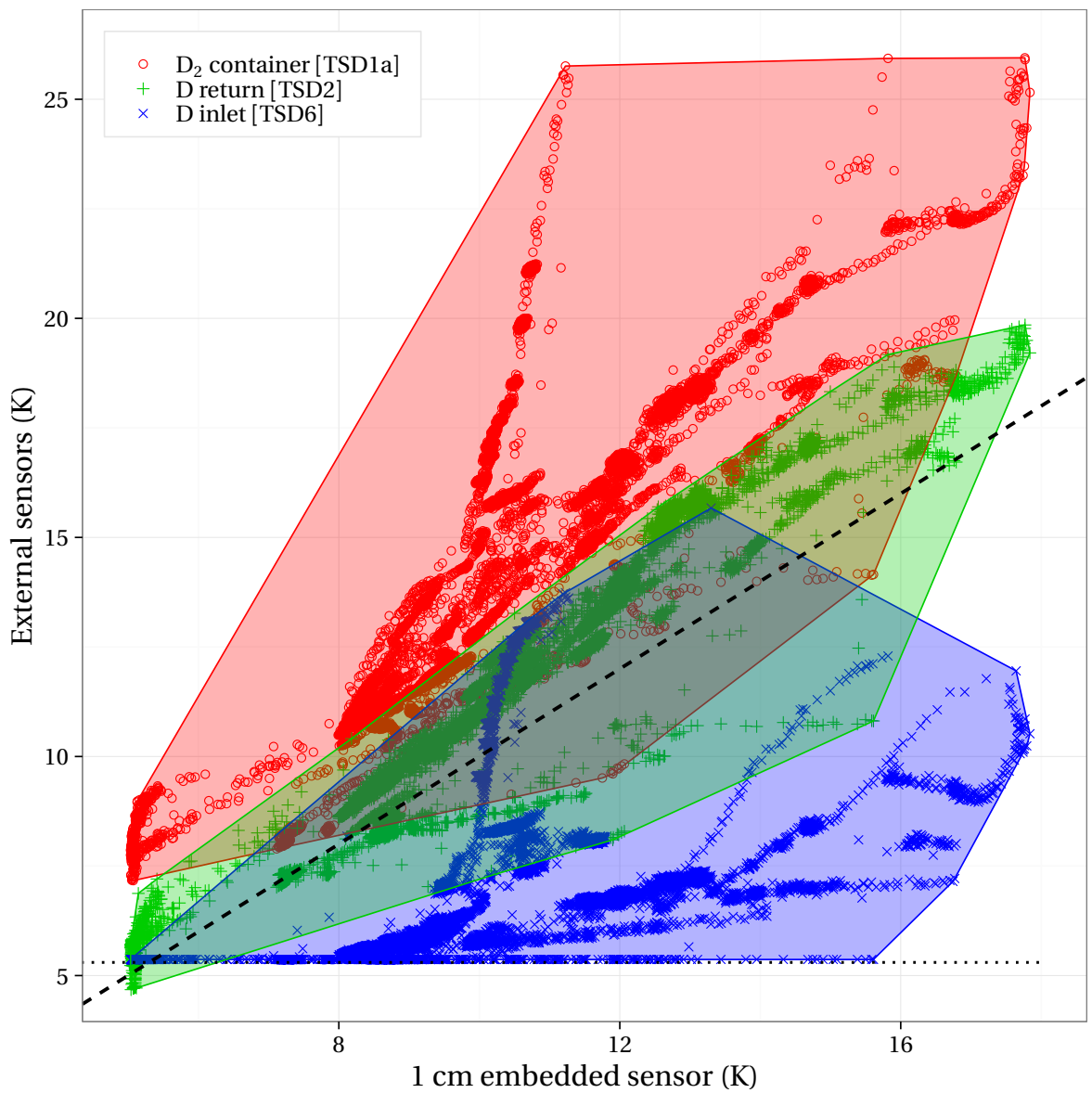
Figure 5.21: 1 cm embedded sensor compared with the external sensors during periods when there was greater than 1 cm height of deuterium condensed. An $x = y$ line is shown for reference. The D inlet [TSD6] sensor was not defined below 5.4 K. The periods are specifically 2/23 18:00 — 3/3 22:00, 3/22 15:00 — 4/4 10:00, and 4/11 18:00 — 4/15 8:00.

Figure 5.22: Comparing 1 cm sensor with the external sensors under constant conditions during periods when there was greater than 1 cm height of deuterium condensed. Specifically, deuterium was not being condensed, heater power was constant, and cooling was relatively stable.
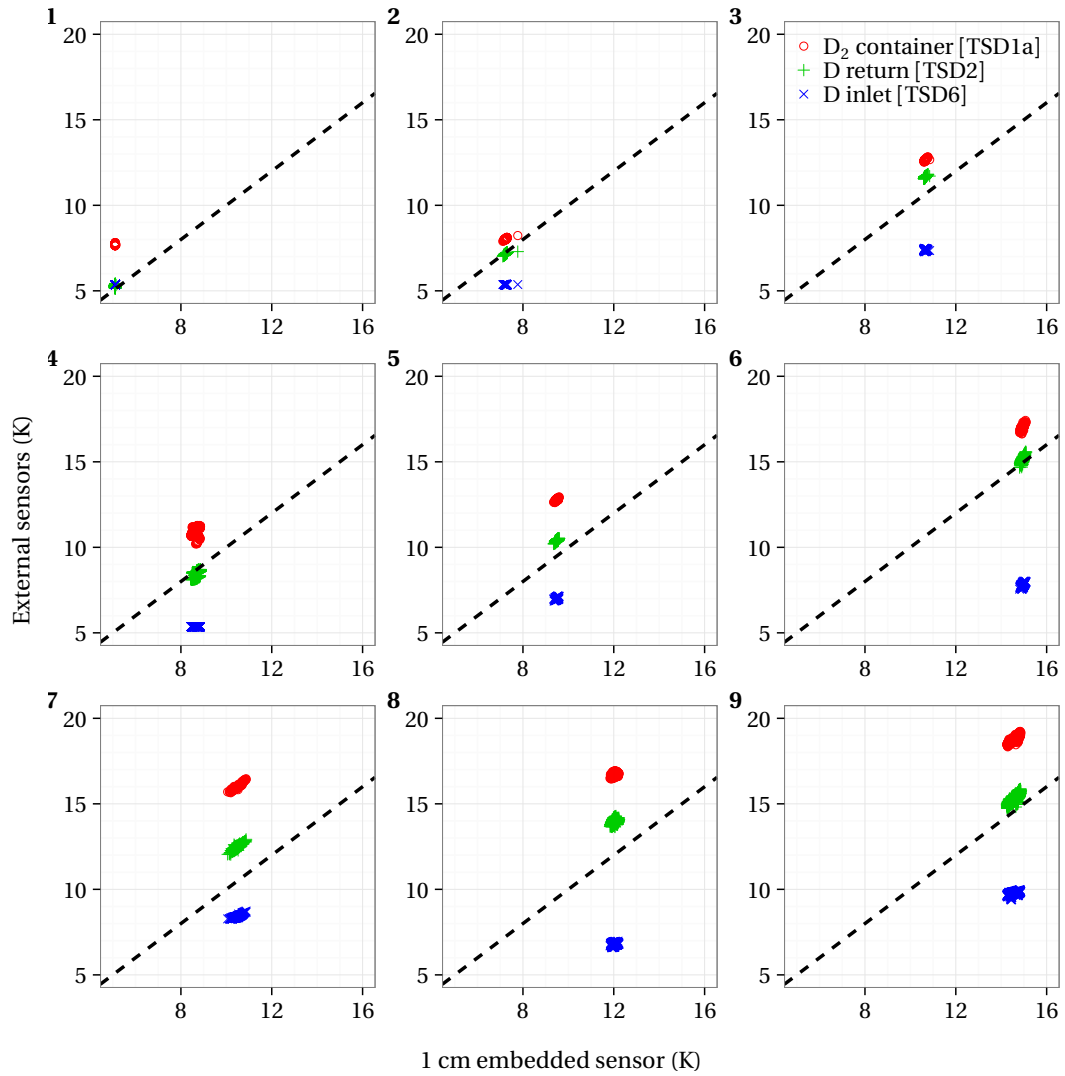
Plot	Begin	End	EHD1 (V)	EHN1 (V)
1	4/14 16:00	4/15 8:00	0	0
2	2/23 18:00	2/24 8:00	0	0
3	4/13 22:00	4/14 8:00	0	0
4	2/24 20:00	2/25 10:00	0	10
	2/25 18:00	2/26 8:00		
5	4/12 20:00	4/13 8:00	0	12
6	3/21 15:00	3/22 8:00	0	12
7	4/11 18:00	4/12 8:00	11	12
8	2/27 6:00	3/1 8:00	7	12
9	3/16 18:00	3/18 12:00	10	12

145

5.4.2   Procedure when sublimating from gas

Lessons

Sublimating a crystal directly from gas however proved more restrictive. Adjusting the height of the withdrawal tube proved an unreliable means of controlling the deuterium container temperature. Although container temperature tracks with withdrawal tube height, any given temperature is not easily reproducible. This is likely in part because the liquid level is not constant and changes with liquefier operation. Also, just as when melting prior to growing from liquid, the electric heater alone is not sufficient to warm the very bottom of the container unless the dewar withdrawal line is completely elevated and helium flow limited. A large heater power can simply create a large heat gradient across the container. With the withdrawal line completely elevated, dewar return proportional valve V308 provides the best control. Small changes in the proportional valve are not reflected in the dewar pressure P308, but can easily be seen on the helium inlet temperature sensor TSD6. The center of the deuterium container is colder than the temperature recorded by the helium inlet sensor. The temperature of initial sublimation should be adjusted accordingly.

The electric heater should be used to pre-heat the container, and reduced with the added heat input of deuterium gas flow, to keep the system in thermal equilibrium. Initial sublimation at C_1 produced a clear crystal, but temperature and pressures continually increased leading to a de-stabilization of cooling. In E_1, with the heater used to pre-heat the container, a clear crystal was grown with stable conditions.

As the crystal grows in height, the surface becomes warmer due to the thermal gradient. To maintain constant growing conditions on the surface, the temperature of the container should be slowly lowered.

Finally, fluctuations in temperature can lead to crystal defects, particularly on the surface. This can be eliminated largely by establishing strict procedures for condensing and cooling.

Procedure

With these lessons, a proper procedure is then established, although further tests are needed to pin down the specifics. First, the container is warmed primarily by completely elevating the dewar withdrawal line while the dewar return proportional valve V308 limits helium flow and provides precise temperature control. Electric heaters are applied only to the minimum needed to offset the heat introduced by deuterium gas flow, and are then reduced accordingly when gas begins to flow. As the crystal grows, cooling power should be slowly increased by using dewar return proportional valve V308 to maintain surface temperature and vapor pressure to keep conditions constant for crystal growth. Finally, when the crystal is to be cooled to operating temperature, the withdrawal line can then be lowered.

5.4.3 Solid deuterium observations

Most importantly, when sublimating from gas, it may not be possible with our current cryostat configuration to grow a crystal that is both transparent and of uniform thickness. We have seen deuterium over approximately 10 K remains mobile and will migrate to form an isothermal surface. With the warmer walls of our container, it will form a dome. However, below approximately 11 K, the crystal is opaque.

The LANL UCN source at LANSCE experiences a much larger infrared head load on the crystal. It is possible a large IR load could aid in growing a transparent crystal by preferentially heating the surface while the bulk remains at a colder temperature. This can be explored when the IR load plate is repaired.

The dramatic degradation of the crystal surface under a pulsed heat load is also interesting. Over an extended run, the daily power cycle of the PULSTAR reactor may be an issue, but this phenomenon should definitely be a concern for pulsed sources such as the LANL or PSI sources. Our monitoring system will be a useful platform for further study.

Chapter 6

Conclusion

6.1 Potential obstacles

Before concluding, I should identify potential obstacles to successfully concluding the PULSTAR Source commissioning and transitioning to routine operation. I see no issues with the application of the physics involved. However, while this work has added confidence to the Source's already excellent conceptual design, the engineering implementation of the apparatus pushes the limits of a small program. Enthusiasm may have gotten the better of us, and instead of a modular prototype, the Source was constructed as complex and fully-mature apparatus. To give a specific example, though the temporary shield discussed in Chapter 2 will allow the shield door to remain open with the Source installed, access will still be quite limited, further compounding maintenance. And as is, the fragile assembly must still be removed from the shield cart to be cryogenically tested. The cryostat insert itself, including UCN guides, cannot be removed without disassembling large portions of the vacuum jacket and temperamental helium and gas connections.

Moving forward, I advise looking for opportunities to improve access and simplify the design, accepting any compromises therein. I believe it is still worthwhile to use our limited resources for such potentially major modifications in the interest of long-term reliability.

To identify one potential place for improvement, the Source's vacuum jacket includes over 30 unique aluminum vacuum-flange connections. Vacuum leaks present upon assembly require the disassembly of multiple additional flanges, invariably creating more leaks. I propose reconstructing the vacuum jacket, with a large primary seal on top allowing the cryostat insert to be lifted directly out of the top of the moderator tank with limited disassembly. This improves access. The remaining

connections should be limited to 3-4 independent vacuum seals, improving reliability. The vacuum connections currently submerged in heavy water are a concern as, given the right conditions, the water can corrode the lead sealing wire. This modification would allow these submerged vacuum connections to be removed.

6.2   Current status and outlook

While I identify these concerns, they are relatively small and the overall outlook for the Source is very positive. The hardest work has already been done, and the Source should deliver a competitive UCN flux in the near future. As of the time of this writing, all components of the PULSTAR UCN Source have been completed and tested. The Source assembly was previously installed on the thermal column door to test-fit the UCN guide, so we anticipate no issues with final assembly. The temporary shield has been constructed in preparation. Installation is currently awaiting improvements to the chilled water supply and final safety approval.

A systematics study apparatus in support of the nEDM project is being built in parallel and will be ready to make immediate use of the Source when the Source comes online.

I also want to emphasis the impact of an accessible UCN user-facility. I take a *build it, and they will come* attitude. Having a facility available as a platform for small projects and exploratory work can only promote an interest in UCN as a tool. Much like cold neutron sources decades ago, this can only be a positive for fundamental physics in the process.

BIBLIOGRAPHY

[1] H. Abele, "The neutron. Its properties and basic interactions", Prog. Part. Nucl. Phys. 60 (1) (2008) 1–81, DOI: 10.1016/j.ppnp.2007.05.002 (cited on page 5).

[2] A. Adamczak, "Cold neutron scattering in imperfect deuterium crystals", Nucl. Instr. Meth. Phys. Res. B 269 (21) (2011) 2520–2526, DOI: 10.1016/j.nimb.2011.07.104 (cited on pages 54, 109).

[3] I. Altarev, "Universal liquid-hydrogen source of polarized cold and ultracold neutrons at the VVR-M reactor of the Leningrad Institute of Nuclear Physics", JETP Lett. 44 (6) (1986) 344–348, URL: http://www.jetpletters.ac.ru/ps/1389/index.shtml (cited on page 7).

[4] I. Altarev et al., "A liquid hydrogen source of ultra-cold neutrons", Phys. Lett. A 80 (5-6) (1980) 413–416, DOI: 10.1016/0375-9601(80)90784-7 (cited on page 8).

[5] E. Amaldi, E. Fermi, "On the absorption and the diffusion of slow neutrons", Phys. Rev. 50 (10) (1936) 899–928, DOI: 10.1103/PhysRev.50.899 (cited on page 6).

[6] O. L. Andreev et al., "Absolute measurement of the yield of a neutron source by the gold-foil activation method", Sov. At. Energy 16 (3) (1964) 304–305, DOI: 10.1007/BF01122978 (cited on page 22).

[7] A. Anghel et al., "The PSI ultra-cold neutron source", Nucl. Instr. Meth. Phys. Res. A 611 (2-3) (2009) 272–275, DOI: 10.1016/j.nima.2009.07.077 (cited on pages 10, 11).

[8] F Atchison et al., "Investigation of solid D_2 for UCN sources", J. Res. Natl. Inst. Stand. Technol. 110 (4) (2005) 491, DOI: 10.6028/jres.110.076 (cited on pages 81, 86).

[9] F. Atchison et al., "Measured Total Cross Sections of Slow Neutrons Scattered by Solid Deuterium and Implications for Ultracold Neutron Sources", Phys. Rev. Lett. 95 (18) (2005) 182502, DOI: 10.1103/PhysRevLett.95.182502 (cited on pages 54, 109).

[10] F. Atchison et al., "Production of ultracold neutrons from a cold neutron beam on a $^2H_2$ target", Phys. Rev. C 71 (5) (2005) 054601, DOI: 10.1103/PhysRevC.71.054601 (cited on page 109).

[11] F. Atchison et al., "Cold Neutron Energy Dependent Production of Ultracold Neutrons in Solid Deuterium", Phys. Rev. Lett. 99 (26) (2007) 262502, DOI: 10.1103/PhysRevLett.99.262502 (cited on pages 54–56).

[12] F. Atchison et al., "Investigation of solid D2, O2 and CD4 for ultracold neutron production", Nucl. Instr. Meth. Phys. Res. A 611 (2-3) (2009) 252–255, DOI: 10.1016/j.nima.2009.07.072 (cited on page 54).

[13] F. Atchison et al., "Production of ultracold neutrons from cryogenic ^{2}H, O_2, and C^2H_4 converters", Europhys. Lett. 95 (1) (2011) 12001, DOI: 10.1209/0295-5075/95/12001 (cited on pages 54, 109).

[14] C. Baker et al., "Experimental measurement of ultracold neutron production in superfluid ^{4}He", Phys. Lett. A 308 (1) (2003) 67–74, DOI: 10.1016/S0375-9601(02)01773-5 (cited on page 8).

[15] D. Baxter et al., "Status of the low energy neutron source at Indiana University", Nucl. Instr. Meth. Phys. Res. B 241 (1) (2005) 209–212, DOI: 10.1016/j.nimb.2005.07.027 (cited on page 67).

[16] H. Becker et al., "Neutron production and thermal moderation at the PSI UCN source", Nucl. Instr. Meth. Phys. Res. A 777 (2015) 20–27, DOI: 10.1016/j.nima.2014.12.091 (cited on pages 11, 14).

[17] K. Bodek et al., "An apparatus for the investigation of solid D_2 with respect to ultra-cold neutron sources", Nucl. Instr. Meth. Phys. Res. A 533 (3) (2004) 491–504, DOI: 10.1016/j.nima.2004.06.157 (cited on page 109).

[18] F. G. Brickwedde et al., "The Difference in Vapor Pressures of Ortho and Para Deuterium", J. Chem. Phys. 3 (11) (1935) 653, DOI: 10.1063/1.1749571 (cited on page 112).

[19] J. M. Carpenter, "Thermally activated release of stored chemical energy in cryogenic media", Nature 330 (6146) (1987) 358–360, DOI: 10.1038/330358a0.

[20] R. R. E. Carter, B. B. E. Leonard, "PULSTAR fuel, low enrichment, long lifetime, economical, proven", English (1993), URL: https://inis.iaea.org/search/search.aspx?orig_q=RN:26017044 (cited on page 15).

[21] J. Chadwick, "The Existence of a Neutron", Proc. R. Soc. A Math. Phys. Eng. Sci. 136 (830) (1932) 692–708, DOI: 10.1098/rspa.1932.0112 (cited on page 6).

[22] M. Chadwick et al., "ENDF/B-VII.1 Nuclear Data for Science and Technology: Cross Sections, Covariances, Fission Product Yields and Decay Data", Nucl. Data Sheets 112 (12) (2011) 2887–2996, DOI: 10.1016/j.nds.2011.11.002 (cited on page 34).

[23] G. W. Collins et al., "Metastable structures of solid hydrogen", Phys. Rev. B 53 (1) (1996) 102–106, DOI: 10.1103/PhysRevB.53.102 (cited on page 111).

[24] D. Colognesi et al., "Lattice dynamics and molecular rotations in solid hydrogen deuteride: Inelastic neutron scattering study", Phys. Rev. B 79 (14) (2009) 144307, DOI: 10.1103/PhysRevB.79.144307 (cited on page 54).

[25] V. V. Danchuk et al., "Orientational order parameter in the ordered phase of solid deuterium from neutron-diffraction data", Low Temp. Phys. 30 (2) (2004) 118–121, DOI: 10.1063/1.1645162 (cited on page 54).

[26] J. Demaison et al., "Diatomic Molecules, Data and References", Landolt-Börnstein - Gr. II Mol. Radicals, Landolt-Börnstein - Group II Molecules and Radicals 24A (1998), edited by W. Hüttner, DOI: 10.1007/b60165 (cited on page 91).

[27] D. Dubbers, M. G. Schmidt, "The neutron and its role in cosmology and particle physics", Rev. Mod. Phys. 83 (4) (2011) 1111–1171, DOI: 10.1103/RevModPhys.83.1111 (cited on page 5).

[28] J. L. Dunham, "The Energy Levels of a Rotating Vibrator", Phys. Rev. 41 (6) (1932) 721–731, DOI: 10.1103/PhysRev.41.721 (cited on page 90).

[29] G. Engelmann et al., "Comparison between very-slow-neutron transmission and small-angle neutron-scattering experiments", Z. Phys. B 35 (4) (1979) 345–349, DOI: 10.1007/BF01332696 (cited on page 54).

[30] E. Fermi, L. Marshall, "Interference Phenomena of Slow Neutrons", Phys. Rev. 71 (10) (1947) 666–677, DOI: 10.1103/PhysRev.71.666 (cited on page 6).

[31] E. Fermi, W. H. Zinn, "Reflection of Neutrons on Mirrors", Phys. Rev. 70 (1–2) (1946) 103, DOI: 10.1103/PhysRev.70.99 (cited on page 6).

[32] F. Fernandez-Alonso et al., "Solid para-hydrogen as the paradigmatic quantum crystal: Three observables probed by ultrahigh-resolution neutron spectroscopy", Phys. Rev. B 86 (14) (2012) 144524, DOI: 10.1103/PhysRevB.86.144524 (cited on page 86).

[33] A. Frei et al., "First production of ultracold neutrons with a solid deuterium source at the pulsed reactor TRIGA Mainz", Eur. Phys. J. A 34 (2) (2007) 119–127, DOI: 10.1140/epja/i2007-10494-2 (cited on pages 14, 86, 109).

[34] A. Frei et al., "Density of states in solid deuterium: Inelastic neutron scattering study", Phys. Rev. B 80 (6) (2009) 064301, DOI: 10.1103/PhysRevB.80.064301 (cited on page 54).

[35] A. Frei et al., "Understanding of ultra-cold–neutron production in solid deuterium", Europhys. Lett. 92 (6) (2011) 62001, DOI: 10.1209/0295-5075/92/62001 (cited on pages 33, 54–56).

[36] M. R. Gibbs et al., "The collective excitations of normal and superfluid : the dependence on pressure and temperature", J. Phys. Condens. Matter 11 (3) (1999) 603–628, DOI: 10.1088/0953-8984/11/3/003 (cited on page 8).

[37] M. R. Gibbs et al., "Pressure Dependence of the Multiphonon Excitations of Superfluid 4He", J. Low Temp. Phys. 120 (1/2) (2000) 55–64, DOI: 10.1023/A:1004656818842 (cited on page 8).

[38]   R Golub, "Ultracold neutrons: Their role in studies of condensed matter", Rev. Mod. Phys. 68 (2) (1996) 329–347, DOI: 10.1103/RevModPhys.68.329 (cited on page 5).

[39]   R. Golub, K. Böning, "New type of low temperature source of Ultra-cold neutrons and production of continous beams of UCN", Z. Phys. B 51 (2) (1983) 95–98, DOI: 10.1007/BF01308763 (cited on page 8).

[40]   R. Golub, J. Pendlebury, "Super-thermal sources of ultra-cold neutrons", Phys. Lett. A 53 (2) (1975) 133–135, DOI: 10.1016/0375-9601(75)90500-9 (cited on page 8).

[41]   R. Golub, J. Pendlebury, "The interaction of Ultra-Cold Neutrons (UCN) with liquid helium and a superthermal UCN source", Phys. Lett. A 62 (5) (1977) 337–339, DOI: 10.1016/0375-9601(77)90434-0 (cited on page 8).

[42]   R Golub et al., "Operation of a superthermal ultra-cold neutron source and the storage of ultra-cold neutrons in superfluid Helium^4", Z. Phys. B 51 (3) (1983) 187–193, DOI: 10.1007/BF01307673 (cited on pages 7, 8, 50).

[43]   R. Golub et al., *Ultra-Cold Neutrons*, Adam Hilger, 1991, URL: https://books.google.com/books?id=QPUjlcWNg78C (cited on pages 5, 48, 54).

[44]   T. Goorley et al., "Initial MCNP6 Release Overview", Nucl. Technol. 180 (3) (2012) 298–315, DOI: 10.13182/NT11-135 (cited on pages 14, 24).

[45]   J. R. Granada, "Neutron scattering kernel for solid deuterium", Europhys. Lett. 86 (6) (2009) 66007, DOI: 10.1209/0295-5075/86/66007 (cited on page 32).

[46]   J. R. Granada, F Cantargi, "Development of Cold Neutron Scattering Kernels for Advanced Moderators", in: 2010 8–13, DOI: 10.1063/1.3295617 (cited on page 32).

[47]   J. R. Granada et al., "Neutron Cross Sections Libraries for Methane in Phase II and Solid Deuterium", J. Korean Phys. Soc. 59 (23) (2011) 1076, DOI: 10.3938/jkps.59.1076 (cited on page 32).

[48]   E. R. Grilly, "The Liquefaction and Storage of Partially Converted Liquid Hydrogen", Rev. Sci. Instrum. 24 (1) (1953) 1, DOI: 10.1063/1.1770507 (cited on pages 80, 81).

[49]   E. R. Grilly, "The Regular Production of 85 Percent Para Liquid Hydrogen", Rev. Sci. Instrum. 24 (10) (1953) 899, DOI: 10.1063/1.1770544 (cited on page 86).

[50]   E. Gutsmiedl et al., "Understanding UCN production in solid : The generalized density of states measured via inelastic neutron scattering", Nucl. Instr. Meth. Phys. Res. A 611 (2-3) (2009) 256–258, DOI: 10.1016/j.nima.2009.07.082 (cited on page 54).

[51]   Y. D. Harker, "Investigation of the Low-Temperature Phase Transition in Solid Methane by Slow Neutron Inelastic Scattering", J. Chem. Phys. 46 (6) (1967) 2201, DOI: 10.1063/1.1841024 (cited on page 46).

[52] Y. D. Harker, R. M. Brugger, "Slow-Neutron Inelastic Scattering from Low-Temperature Gaseous Methane, Liquid Methane, and Solid Methane", J. Chem. Phys. 42 (1) (1965) 275, DOI: 10.1063/1.1695688.

[53] M. Hartl et al., "Hydrogen adsorption on two catalysts for the ortho- to parahydrogen conversion: Cr-doped silica and ferric oxide gel", Phys. Chem. Chem. Phys. 18 (26) (2016) 17281–17293, DOI: 10.1039/C6CP01154C (cited on pages 81, 86, 89).

[54] A. I. Hawari, J. L. Wormald, "Investigation of Mixed Enrichment Core Loadings for the PULSTAR Reactor", in: IGORR Conf. Bariloche, Argentina, 2014, URL: http://www.igorr.com/scripts/home/publigen/content/templates/Show.asp?P=942&L=EN (cited on page 15).

[55] A. I. Hawari, "PULSTAR Reactor Power Upgrade from 1- to 2-MWth", English, in: IGORR Conf. Daejeon, South Korea, 2013, URL: http://www.igorr.com/home/liblocal/docs/IGORR2013/02_1030.pdf (cited on page 15).

[56] W. M. Haynes, editor, CRC Handbook of Chemistry and Physics, 96th edition, CRC Press, 2016, URL: http://www.hbcpnetbase.com (cited on page 91).

[57] E Hecht, Optics, 4th, Adison-Wesley, 2002, URL: https://books.google.com/books?id=7aG6QgAACAAJ (cited on pages 94, 96).

[58] G. Herzberg, Molecular spectra and molecular structure, Vol. 1 Spectra of diatomic molecules, 1950, URL: https://books.google.com/books?id=tSVRAAAAMAAJ (cited on pages 90, 93).

[59] R. E. Hill et al., "Performance of the prototype LANL solid deuterium ultra-cold neutron source", Nucl. Instr. Meth. Phys. Res. A 440 (3) (2000) 674–681, DOI: 10.1016/S0168-9002(99)01060-8 (cited on page 9).

[60] J. K. Hoffer, L. R. Foreman, "Radioactively induced sublimation in solid tritium", Phys. Rev. Lett. 60 (13) (1988) 1310–1313, DOI: 10.1103/PhysRevLett.60.1310 (cited on page 132).

[61] A. T. Holley, "UCN polarimetry in measurement of the beta asymmetry" (2012) 160, DOI: 10.1017/CBO9781107415324.004.

[62] J. Howard, H. S. Taylor, "The Adsorption of Gases by Chromium Oxide Gel", J. Am. Chem. Soc. 56 (11) (1934) 2259–2264, DOI: 10.1021/ja01326a016 (cited on page 81).

[63] K. P. Huber, G. Herzberg, Molecular Spectra and Molecular Structure: IV. Constants of Diatomic Molecules, Springer US, 1979, DOI: 10.1007/978-1-4757-0961-2 (cited on page 91).

[64] P. R. Huffman et al., "Magnetic trapping of neutrons", Nature 403 (6765) (2000) 62–64, DOI: 10.1038/47444 (cited on page 8).

[65] V. K. Ignatovich, *The Physics of Ultracold Neutrons*, Clarendon Press, 1990, URL: `https://books.google.com/books/?id=40LuAAAAIAAJ`.

[66] S. Imajo et al., "Pulsed ultra-cold neutron production using a Doppler shifter at J-PARC", Prog. Theor. Exp. Phys. 2016 (1) (2016) 013C02, DOI: `10.1093/ptep/ptv177` (cited on page 9).

[67] T. Jenke, H. Abele, "Experiments with Gravitationally-bound Ultracold Neutrons at the European Spallation Source ESS", Phys. Procedia 51 (51) (2014) 67–72, DOI: `10.1016/j.phpro.2013.12.016` (cited on page 5).

[68] F. Kalckar, E. Teller, "On the Theory of the Catalysis of the Ortho-Para Transformation by Paramagnetic Gases", Proc. R. Soc. A Math. Phys. Eng. Sci. 150 (871) (1935) 520–533, DOI: `10.1098/rspa.1935.0120` (cited on page 79).

[69] J. Karch et al., "Performance of the solid deuterium ultra-cold neutron source at the pulsed reactor TRIGA Mainz", Eur. Phys. J. A 50 (4) (2014) 78, DOI: `10.1140/epja/i2014-14078-9` (cited on pages 11, 14).

[70] M. Kasprzak, "Thermal up-scattering of very cold and ultra-cold neutrons in solid deuterium", PhD thesis, 2004, URL: `http://arxiv.org/abs/nucl-ex/0407022` (cited on page 109).

[71] R. Khan et al., "Monte Carlo simulation of the thermal column and beam tube of the TRIGA Mark II research reactor", Nucl. Eng. Des. 241 (8) (2011) 2859–2864, DOI: `10.1016/j.nucengdes.2011.04.025` (cited on page 14).

[72] A. Kilvington et al., "Scattering of ultra-cold neutrons (UCN) by superfluid helium at temperatures around 1 K", Phys. Lett. A 125 (8) (1987) 416–420, DOI: `10.1016/0375-9601(87)90174-5`.

[73] D. E. Knuth, *The TEXbook*, Addison-Wesley Pub. Co, 1984 483, URL: `https://books.google.com?id=hEYuAQAAIAAJ` (cited on page iv).

[74] M. Kobayashi, M. Uda, "Structure of "ferric hydroxide gel"", J. Non. Cryst. Solids 29 (3) (1978) 419–422, DOI: `10.1016/0022-3093(78)90163-1` (cited on page 89).

[75] W. Kolos, L. Wolniewicz, "Polarizability of the hydrogen molecule", J. Chem. Phys. 46 (4) (1967) 1426, DOI: `10.1016/S0031-8914(53)80017-0` (cited on page 93).

[76] J. U. Koppel, J. A. Young, "Slow neutron spectra in molecular hydrogen at low temperatures", Nukleonik 8 (1965).

[77] E. Korobkina et al., "Production of UCN by downscattering in superfluid He^4", Phys. Lett. A 301 (5-6) (2002) 462–469, DOI: `10.1016/S0375-9601(02)01052-6` (cited on page 8).

[78] E. Korobkina et al., "An ultracold neutron source at the NC State University PULSTAR reactor", Nucl. Instr. Meth. Phys. Res. A 579 (1) (2007) 530–533, DOI: `10.1016/j.nima.2007.04.116` (cited on pages 11, 14, 33, 56, 59).

[79]   E. Korobkina et al., "Ultracold neutron source at the PULSTAR reactor: Engineering design and cryogenic testing", Nucl. Instr. Meth. Phys. Res. A 767 (2014) 169–175, DOI: `10.1016/j.nima.2014.08.016` (cited on page 11).

[80]   K. Krane, *Introductory Nuclear Physics*, Wiley, 1987, URL: `https://books.google.com/books?id=ConwAAAAMAAJ` (cited on page 3).

[81]   M. Kreuz et al., "A method to measure the resonance transitions between the gravitationally bound quantum states of neutrons in the GRANIT spectrometer", Nucl. Instr. Meth. Phys. Res. A 611 (2) (2009) 326–330, DOI: `10.1016/j.nima.2009.07.059` (cited on page 5).

[82]   H. Kuhn et al., *Principles of Physical Chemistry*, 2nd, John Wiley & Sons, 2009 1084, URL: `http://books.google.com/books?id=E5SBRSKR53EC` (cited on page 79).

[83]   E Kulagin et al., "Radiation effects in cold moderator materials: Experimental study of accumulation and release of chemical energy", Nucl. Instr. Meth. Phys. Res. B 215 (1-2) (2004) 181–186, DOI: `10.1016/j.nimb.2003.08.026`.

[84]   Lake Shore Cryotronics, *Temperature Measurment and Control Catalog*, 2016, URL: `http://www.lakeshore.com/Documents/LakeShoreTC_l.pdf` (cited on page 118).

[85]   S. K. Lamoreaux, R Golub, "Experimental searches for the neutron electric dipole moment", J. Phys. G 36 (10) (2009) 104002, DOI: `10.1088/0954-3899/36/10/104002` (cited on page 5).

[86]   B. Lauss, "Ultracold Neutron Production at the Second Spallation Target of the Paul Scherrer Institute", Phys. Procedia 51 (2014) 98–101, DOI: `10.1016/j.phpro.2013.12.022` (cited on page 11).

[87]   B. Lauss, "The ultracold neutron facility at the Paul Scherrer Institute UCN", in: *International Workshop: Probing Fundamental Symmetries and Interactions with UCN*, Mainz, 2016, URL: `https://indico.mitp.uni-mainz.de/event/59/session/17/contribution/116/material/slides/0.pdf` (cited on page 10).

[88]   C. M. Lavelle et al., "Ultracold-neutron production in a pulsed-neutron beam line", Phys. Rev. C 82 (1) (2010) 015502, DOI: `10.1103/PhysRevC.82.015502` (cited on page 54).

[89]   C. Lavelle et al., "Neutronic design and measured performance of the Low Energy Neutron Source (LENS) target moderator reflector assembly", Nucl. Instr. Meth. Phys. Res. A 587 (2) (2008) 324–341, DOI: `10.1016/j.nima.2007.12.044` (cited on page 67).

[90]   K. K. H. Leung et al., "Ultracold-neutron production and up-scattering in superfluid helium between 1.1 K and 2.4 K", Phys. Rev. C 93 (2) (2016) 025501, DOI: `10.1103/PhysRevC.93.025501` (cited on page 10).

[91] P. Linstrom, W. Mallard, editors, *NIST Chemistry WebBook, NIST Standard Reference Database Number 69*, National Institute of Standards and Technology, Gaithersburg MD, DOI: `10.18434/T4D303` (cited on pages 128, 129).

[92] C.-Y. Liu, "A Superthermal Ultra-Cold Neutron Source", PhD thesis, Princeton University, 2002, URL: `http://search.proquest.com/docview/305526157` (cited on page 11).

[93] C. Y. Liu et al., "UCN Upscattering rates in a molecular deuterium crystal", Phys. Rev. B 62 (6) (2000) 3, DOI: `10.1103/PhysRevB.62.R3581` (cited on pages 8, 48, 51, 53, 54, 80, 109).

[94] C.-Y. Liu et al., "An apparatus to control and monitor the para-D_2 concentration in a solid deuterium, superthermal source of ultra-cold neutrons", Nucl. Instr. Meth. Phys. Res. A 508 (3) (2003) 257–267, DOI: `10.1016/S0168-9002(03)01666-8` (cited on pages 67, 81, 88, 96).

[95] C. Y. Liu et al., "Coherent Neutron Scattering in Polycrystalline Deuterium and its Implications for Ultracold Neutron Production" (2010), URL: `https://arxiv.org/abs/1005.1016v1` (cited on page 54).

[96] D. A. Long, *The Raman effect: a unified treatment of the theory of Raman scattering by molecules. 2002*, volume 8, 2002 21–22, DOI: `10.1002/0470845767`.

[97] S. W. Lovesey, *Theory of neutron scattering from condensed matter*, Clarendon Press, 1984, URL: `https://books.google.com?id=xfLvAAAAMAAJ` (cited on pages 34, 50, 53).

[98] V. Lushchikov et al., "Observation of Ultracold Neutrons", JETP Lett. 9 (1) (1969) 23, URL: `http://www.jetpletters.ac.ru/ps/1639/article_25024.pdf` (cited on page 7).

[99] R. E. MacFarlane, *New Thermal Neutron Scattering Files for ENDF/B-VI, Release 2*, technical report, LANL Report, LA-12639-MS, 1994, URL: `http://t2.lanl.gov/nis/publications/thermal.pdf` (cited on page 46).

[100] R. E. MacFarlane, *The NJOY Nuclear Data Processing System, Version 2012*, technical report, LA-UR-12-27079, 2013, URL: `http://t2.lanl.gov/nis/codes/NJOY12` (cited on page 45).

[101] R. E. MacFarlane, A. Kahler, "Methods for Processing ENDF/B-VII with NJOY", Nucl. Data Sheets 111 (12) (2010) 2739–2890, DOI: `10.1016/j.nds.2010.11.001` (cited on page 34).

[102] J. MacPhee, R. Lumb, "The Transient Characteristics of a New Pulse Research Reactor", English, in: *Pulsed Neutron Res. Vol. II. Proc. Symp. Pulsed Neutron Res.* International Atomic Energy Agency, Vienna (Austria), 1965, URL: `https://inis.iaea.org/search/search.aspx?orig_q=RN:44078830` (cited on page 15).

[103] Y. Masuda et al., "Spallation Ultracold Neutron Source of Superfluid Helium below 1 K", Phys. Rev. Lett. 108 (13) (2012) 134801, DOI: `10.1103/PhysRevLett.108.134801` (cited on page 10).

[104] C. Mattoni et al., "A long wavelength neutron monochromator for superthermal production of ultracold neutrons", Physica B 344 (1-4) (2004) 343–357, DOI: 10.1016/j.physb.2003.10.023 (cited on page 8).

[105] R. McConn et al., *Compendium of Material Composition Data for Radiation Transport Modeling, Revision 1*, technical report, PNNL-15870 Rev. 1, 2011, URL: www.pnnl.gov/main/publications/external/technical_reports/PNNL-15870Rev1.pdf (cited on page 25).

[106] K Mishima et al., "Production of ultra cold neutrons by a doppler shifter with pulsed neutrons at J-PARC", J. Phys. Conf. Ser. 528 (1) (2014) 012030, DOI: 10.1088/1742-6596/528/1/012030 (cited on page 9).

[107] C. L. Morris et al., "Measurements of Ultracold-Neutron Lifetimes in Solid Deuterium", Phys. Rev. Lett. 89 (27) (2002) 272501, DOI: 10.1103/PhysRevLett.89.272501 (cited on pages 9, 48, 80, 109).

[108] A. R. Mueller, "Characterization of solid D_2 as source material for ultra cold neutrons and development of a detector concept for the detection of protons from the neutron decay", PhD thesis, 2008, URL: http://mediatum.ub.tum.de/doc/672350/672350.pdf (cited on page 109).

[109] *National Nuclear Data Center*, 2017, URL: www.nndc.bnl.gov (cited on pages 22, 23).

[110] V. V. Nesvizhevsky et al., "Measurement of quantum states of neutrons in the Earth's gravitational field", Phys. Rev. D 67 (10) (2003) 102002, DOI: 10.1103/PhysRevD.67.102002 (cited on page 5).

[111] V. V. Nesvizhevsky et al., "Quantum states of neutrons in the Earth's gravitational field", Nature 415 (6869) (2002) 297–299, DOI: 10.1038/415297a (cited on page 5).

[112] *Neutron scattering lengths and cross sections*, URL: https://ncnr.nist.gov/resources/n-lengths/list.html (visited on 01/01/2017) (cited on page 48).

[113] M. Nielsen, "Phonons in solid hydrogen and deuterium studied by inelastic coherent neutron scattering", Phys. Rev. B 7 (4) (1973) 1626–1635, DOI: 10.1103/PhysRevB.7.1626 (cited on pages 51, 54).

[114] M. Nielsen et al., "Lattice Dynamics of Solid Deuterium by Inelastic Neutron Scattering", Phys. Rev. B 3 (12) (1971) 4383–4385, DOI: 10.1103/PhysRevB.3.4383 (cited on page 50).

[115] T. Oetiker, *The Not So Short Introduction to LaTeX2ε*, Version 5., 2015, URL: http://mirrors.ctan.org/info/lshort/english/lshort.pdf (cited on page iv).

[116]   G. Palmquist, "Design and Construction of the Ultracold Neutron Source at the NC State PUL-STAR Research Reactor", PhD thesis, 2014, URL: http://www.lib.ncsu.edu/resolver/1840.16/9572 (cited on pages 11, 22).

[117]   D. E. Parks, *Slow Neutron Scattering and Thermalization*, edited by W. A. Benjamin, New York (cited on page 34).

[118]   R. W. Pattie, "Status of the Ultracold neutron source upgrade at LANSCE", in: *International Workshop: Probing Fundamental Symmetries and Interactions with UCN*, Mainz, 2016 (cited on page 11).

[119]   C. M. Penney et al., "Absolute rotational Raman cross sections for N_2, O_2, and CO_2", J. Opt. Soc. Am. 64 (5) (1974) 712, DOI: 10.1364/JOSA.64.000712 (cited on page 93).

[120]   *PF2 - Ultracold neutron facility*, URL: https://www.ill.eu/instruments-support/instruments-groups/instruments/pf2 (visited on 01/01/2017) (cited on page 6).

[121]   R. Picker, "How the Minuscule Can Contribute to the Big Picture: The Neutron Electric Dipole Moment Project at TRIUMF", in: *Proc. 14th Int. Conf. Meson-Nucleon Phys. Struct. Nucleon*, Journal of the Physical Society of Japan, 2017, DOI: 10.7566/JPSCP.13.010005 (cited on pages 5, 10).

[122]   F. M. Piegsa et al., "New source for ultracold neutrons at the Institut Laue-Langevin", Phys. Rev. C 90 (1) (2014) 015501, DOI: 10.1103/PhysRevC.90.015501 (cited on page 10).

[123]   G. Placzek, E. Teller, "Die Rotationsstruktur der Ramanbanden mehratomiger Moleküle", Z. Phys. 81 (11-12) (1933) 839–839, DOI: 10.1007/BF01342084 (cited on page 93).

[124]   Y. Pokotilovski, "Production and storage of ultracold neutrons at pulse neutron sources with low repetition rates", Nucl. Instr. Meth. Phys. Res. A 356 (2-3) (1995) 412–414, DOI: 10.1016/0168-9002(94)01325-X (cited on page 9).

[125]   Y. Pokotilovski, "UCN transport simulation in solid deuterium crystals", Nucl. Instr. Meth. Phys. Res. A 675 (2012) 29–33, DOI: 10.1016/j.nima.2012.01.070 (cited on page 54).

[126]   S. V. Pullela, "Determination of the PULSTAR reactor neutron energy spectrum", Energy Convers. Manag. 38 (10-13) (1997) 1015–1023, DOI: 10.1016/S0196-8904(96)00131-8 (cited on page 22).

[127]   J. Raffle, "Determination of absolute neutron flux by gold activation", J. Nucl. Energy. Part A 10 (1) (1959) 8–13, DOI: 10.1016/0368-3265(59)90090-8 (cited on page 22).

[128]   I. A. Richardson et al., "Fundamental Equation of State for Deuterium", J. Phys. Chem. Ref. Data 43 (1) (2014) 013103, DOI: 10.1063/1.4864752 (cited on page 112).

[129]   T. Rinckel et al., "LENS Operating Experience", Phys. Procedia 26 (2012) 161–167, DOI: 10.1016/j.phpro.2012.03.021 (cited on page 67).

[130] J. J. Sakurai, J. Napolitano, *Modern Quantum Mechanics*, Addison-Wesley, 2011, URL: https://books.google.com?id=N4I-AQAACAAJ (cited on page 36).

[131] A Saunders et al., "Demonstration of a solid deuterium source of ultra-cold neutrons", Phys. Lett. B 593 (1-4) (2004) 55–60, DOI: 10.1016/j.physletb.2004.04.048 (cited on pages 9, 109).

[132] A Saunders et al., "Performance of the Los Alamos National Laboratory spallation-driven solid-deuterium ultra-cold neutron source.", Rev. Sci. Instrum. 84 (1) (2013) 013304, DOI: 10.1063/1.4770063 (cited on pages 9, 11).

[133] J. W. Schmidt et al., "Coherent inelastic neutron scattering study of solid orthodeuterium at high pressure", 30 (11) (1984), DOI: 10.1103/PhysRevB.30.6308 (cited on page 54).

[134] P. Schmidt-Wellenburg, "The quest for an electric dipole moment of the neutron", AIP Conf. Proc. 1753 (2016), DOI: 10.1063/1.4955363 (cited on page 5).

[135] P. Schmidt-Wellenburg et al., "Ultracold-neutron infrastructure for the gravitational spectrometer GRANIT", Nucl. Instr. Meth. Phys. Res. A 611 (2-3) (2009) 267–271, DOI: 10.1016/j.nima.2009.07.096 (cited on page 10).

[136] P Schmidt-Wellenburg et al., "Experimental study of ultracold neutron production in pressurized superfluid helium", Phys. Rev. C 92 (2) (2015) 024004, DOI: 10.1103/PhysRevC.92.024004 (cited on page 10).

[137] R. B. Scott et al., "The Vapor Pressures and Derived Thermal Properties of Hydrogen and Deuterium", J. Chem. Phys. 2 (8) (1934) 454, DOI: 10.1063/1.1749509 (cited on page 80).

[138] R. B. Scott, *Cryogenic engineering*, D. Van Nostrand, Princeton, 1959 (cited on page 81).

[139] V. F. Sears, "Theory of cold neutron scattering by homonuclear diatomic liquids: I. free rotation", Can. J. Phys. 44 (6) (1966) 1279–1297, DOI: 10.1139/p66-108 (cited on page 53).

[140] A. Serebrov et al., "Studies of a solid-deuterium source for ultra-cold neutrons", Nucl. Instr. Meth. Phys. Res. A 440 (3) (2000) 658–665, DOI: 10.1016/S0168-9002(99)01058-X (cited on pages 8, 9, 14).

[141] A. P. Serebrov, A. K. Fomin, "Calculation of the ultracold neutron yield from a superfluid helium source in the WWR-M reactor", Tech. Phys. 60 (8) (2015) 1238–1242, DOI: 10.1134/S106378421508023X (cited on page 10).

[142] A. P. Serebrov, V. A. Mityukhlyaev, "Experimental study of a solid-deuterium source of ultra-cold neutrons", JETP Lett. 62 (10) (1995) 785–790, URL: http://www.jetpletters.ac.ru/ps/1221/article_18455.pdf (cited on pages 16, 109).

[143] A. P. Serebrov et al., "High-density ultracold neutron sources for the WWR-M and PIK reactors", Crystallogr. Reports 61 (1) (2016) 144–148, DOI: 10.1134/S1063774516010211 (cited on pages 10, 14, 16).

[144] A. Serebrov et al., "Experimental studies of very cold neutrons passing through solid deuterium", JETP Lett. 74 (6) (2001) 302–305, DOI: 10.1134/1.1421404 (cited on page 109).

[145] A. Serebrov et al., "Ultracold neutron diffractometry for nanostructural studies", Nucl. Instr. Meth. Phys. Res. A 562 (1) (2006) 365–370, DOI: 10.1016/j.nima.2006.02.070.

[146] A. Serebrov et al., "Preparation of facilities for fundamental research with ultracold neutrons at PNPI", Nucl. Instr. Meth. Phys. Res. A 611 (2) (2009) 276–279, DOI: 10.1016/j.nima.2009.07.078 (cited on page 10).

[147] I. F. Silvera, "The solid molecular hydrogens in the condensed phase: Fundamentals and static properties", Rev. Mod. Phys. 52 (2) (1980) 393–452, DOI: 10.1103/RevModPhys.52.393 (cited on pages 80, 94, 111).

[148] K. Sköld, D. L. Price, "Neutron scattering", in: *Methods Exp. Phys.* Volume 23, 1986, DOI: 10.1016/S0076-695X(08)60554-2 (cited on page 34).

[149] Y. Sobolev et al., "Status of the UCN source at beamport D of the research reactor TRIGA Mainz", in: April, 2016, URL: https://indico.mitp.uni-mainz.de/event/59/session/17/contribution/119 (cited on page 11).

[150] P. C. Souers, *Cryogenic hydrogen data pertinent to magnetic fusion energy*, 1979, URL: http://www.iaea.org/inis/collection/NCLCollectionStore/_Public/10/490/10490410.pdf (cited on page 50).

[151] P. C. Souers, *Hydrogen Properties for Fusion Energy*, University of California Press, 1986, URL: https://books.google.com/books/?id=I2K6DKA1IMwC (cited on pages 48, 111, 112, 128).

[152] G. L. Squires, *Introduction to the Theory of Thermal Neutron Scattering*, Cambridge University Press, Cambridge, 2012 260, DOI: 10.1017/CBO9781139107808 (cited on page 34).

[153] A. Steyerl, "Measurements of total cross sections for very slow neutrons with velocities from 100 m/sec to 5 m/sec", Phys. Lett. B 29 (1) (1969) 33–35, DOI: 10.1016/0370-2693(69)90127-0 (cited on page 7).

[154] A. Steyerl, "A "neutron turbine" as an efficient source of ultracold neutrons", Nucl. Instr. Meth. 125 (3) (1975) 461–469, DOI: 10.1016/0029-554X(75)90265-7 (cited on page 7).

[155] A Steyerl et al., "A new source of cold and ultracold neutrons", Phys. Lett. A 116 (7) (1986) 347–352, DOI: 10.1016/0375-9601(86)90587-6 (cited on pages 7, 9).

[156] T. Sugimoto, K. Sakata, "Preparation of monodisperse pseudocubic α-Fe$_2$O$_3$ particles from condensed ferric hydroxide gel", J. Colloid Interface Sci. 152 (2) (1992) 587–590, DOI: `10.1016/0021-9797(92)90062-Q` (cited on page 89).

[157] N. Sullivan et al., "Precise and efficient in situ ortho — para-hydrogen converter", Cryogenics 30 (8) (1990) 734–735, DOI: `10.1016/0011-2275(90)90240-D` (cited on pages 81, 88).

[158] N. Sullivan et al., "Multistage separator column for ortho-hydrogen and para-deuterium production", 1993, URL: `http://www.sciencedirect.com.prox.lib.ncsu.edu/science/article/pii/001122759390233E` (cited on page 80).

[159] H. S. Taylor, H. Diamond, "The Para-Hydrogen Conversion at Paramagnetic Surfaces", J. Am. Chem. Soc. 55 (6) (1933) 2613–2614, DOI: `10.1021/ja01333a515` (cited on page 81).

[160] H. S. Taylor, A. Sherman, "The Ortho-Para-Hydrogen Conversion at Surfaces", J. Am. Chem. Soc. 53 (4) (1931) 1614–1615, DOI: `10.1021/ja01355a506` (cited on page 80).

[161] *The PULSTAR reactor*, 2016, URL: `https://www.ne.ncsu.edu/nrp/about/pulstar-reactor` (cited on page 15).

[162] U. Trinks et al., "Concepts of UCN sources for the FRM-II", Nucl. Instr. Meth. Phys. Res. A 440 (3) (2000) 666–673, DOI: `10.1016/S0168-9002(99)01059-1` (cited on pages 11, 14).

[163] E. P. Tsentalovich, "The nEDM experiment at the SNS", Phys. Part. Nucl. 45 (1) (2014) 249–250, DOI: `10.1134/S1063779614011073` (cited on page 9).

[164] V. F. Turchin, *Slow Neutrons*, Israel Program for Scientific Translations, 1965, 1965, URL: `https://books.google.com?id=9Z8sAAAAYAAJ` (cited on page 34).

[165] H. C. Urey et al., "A Hydrogen Isotope of Mass 2", Phys. Rev. 39 (1) (1932) 164–165, DOI: `10.1103/PhysRev.39.164` (cited on page 110).

[166] L. Van Hove, "Correlations in space and time and born approximation scattering in systems of interacting particles", Phys. Rev. 95 (1) (1954) 249–262, DOI: `10.1103/PhysRev.95.249` (cited on page 37).

[167] V. Vladimirskii, "Magnetic Mirrors, Channels and Bottles for Cold Neutrons", JETP 12 (4) (1961) 740 (cited on page 6).

[168] B. Wehring, *Personal communication*, 2012 (cited on page 24).

[169] B. Wehring, A. Young, "Ultracold Neutron Source at the North Carolina State Research Reactor", Trans. Am. Nucl. Soc. 83 (2001) 120 (cited on page 11).

[170] D. H. Weitzel, O. E. Park, "Iron Catalyst for Production of Liquid para-Hydrogen", Rev. Sci. Instrum. 27 (1) (1956) 57, DOI: `10.1063/1.1715369` (cited on page 81).

[171] D. Weitzel et al., "Ortho-para catalysis in liquid-hydrogen production", J. Res. Natl. Bur. Stand. 60 (3) (1958) 221, DOI: `10.6028/jres.060.026` (cited on page 80).

[172] F. E. Wietfeldt, G. L. Greene, "Colloquium : The neutron lifetime", Rev. Mod. Phys. 83 (4) (2011) 1173–1192, DOI: `10.1103/RevModPhys.83.1173` (cited on page 5).

[173] Y. Xu, "Characterization of solid deuterium ultracold neutron source production and UCN transport", PhD thesis, 2006, URL: `http://www.lib.ncsu.edu/resolver/1840.16/4239` (cited on pages 11, 24, 67).

[174] H. Yoshiki et al., "Observation of ultracold-neutron production by 9-Å cold neutrons in superfluid helium", Phys. Rev. Lett. 68 (9) (1992) 1323–1326, DOI: `10.1103/PhysRevLett.68.1323` (cited on page 8).

[175] A. R. Young et al., "Beta decay measurements with ultracold neutrons: a review of recent measurements and the research program at Los Alamos National Laboratory", J. Phys. G 41 (11) (2014) 114007, DOI: `10.1088/0954-3899/41/11/114007` (cited on pages 5, 9).

[176] J. A. Young, J. U. Koppel, "Slow Neutron Scattering by Molecular Hydrogen and Deuterium", Phys. Rev. 135 (3A) (1964) A603–A611, DOI: `10.1103/PhysRev.135.A603` (cited on pages 51, 53).

[177] Z.-C. Yu et al., "A thin film source of ultra-cold neutrons", Z. Phys. B 62 (2) (1986) 137–142, DOI: `10.1007/BF01323423` (cited on pages 8, 48, 49, 51).

[178] Y. Zel'dovich, "Storage of Cold Neutrons", JETP 9 (6) (1959) 1389, URL: `http://www.jetp.ac.ru/cgi-bin/dn/e_009_06_1389.pdf` (cited on page 6).

[179] O Zimmer, R Golub, "Ultracold neutron accumulation in a superfluid-helium converter with magnetic multipole reflector", Phys. Rev. C 92 (1) (2015) 015501, DOI: `10.1103/PhysRevC.92.015501` (cited on page 10).

[180] O Zimmer et al., "Superfluid-Helium Converter for Accumulation and Extraction of Ultracold Neutrons", Phys. Rev. Lett. 99 (10) (2007) 104801, DOI: `10.1103/PhysRevLett.99.104801` (cited on page 8).

[181] O. Zimmer, "New results on ultracold neutron production in superfluid helium at ILL", in: *4th Int. Work. Neutron Deliv. Syst.* September, 2015, URL: `https://www.ill.eu/fileadmin/users_files/media/Events/NDS2015/O_Zimmer_2015_09_30_NDS2015_ILL_UCN-source.pdf` (cited on page 10).

[182] O. Zimmer et al., "Superthermal Source of Ultracold Neutrons for Fundamental Physics Experiments", Phys. Rev. Lett. 107 (13) (2011) 134801, DOI: `10.1103/PhysRevLett.107.134801` (cited on pages 9, 10).

APPENDICES

Appendix A

Additional diagrams

A.1 Spin-state converter PID
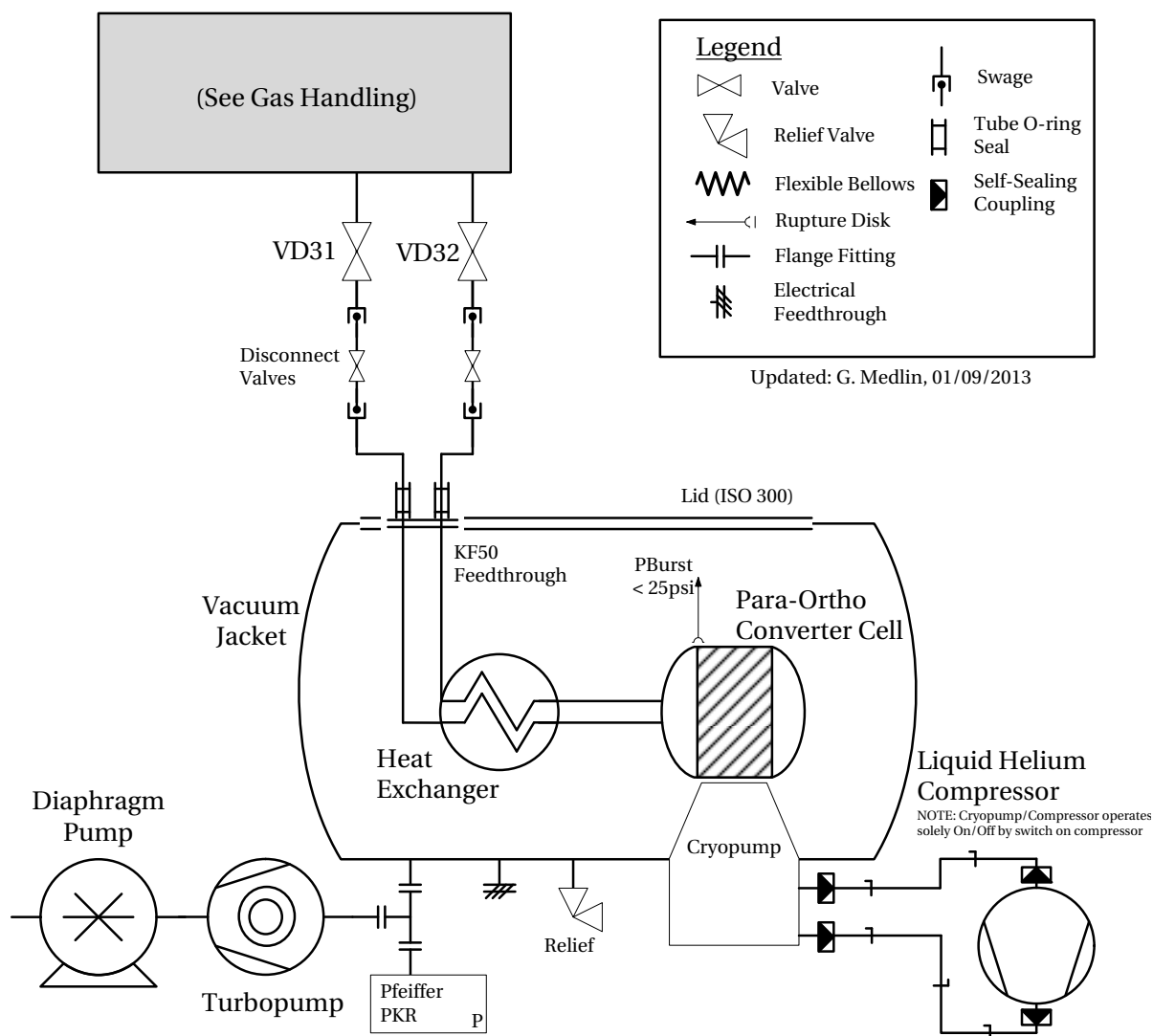
A.2 Gas handling PID
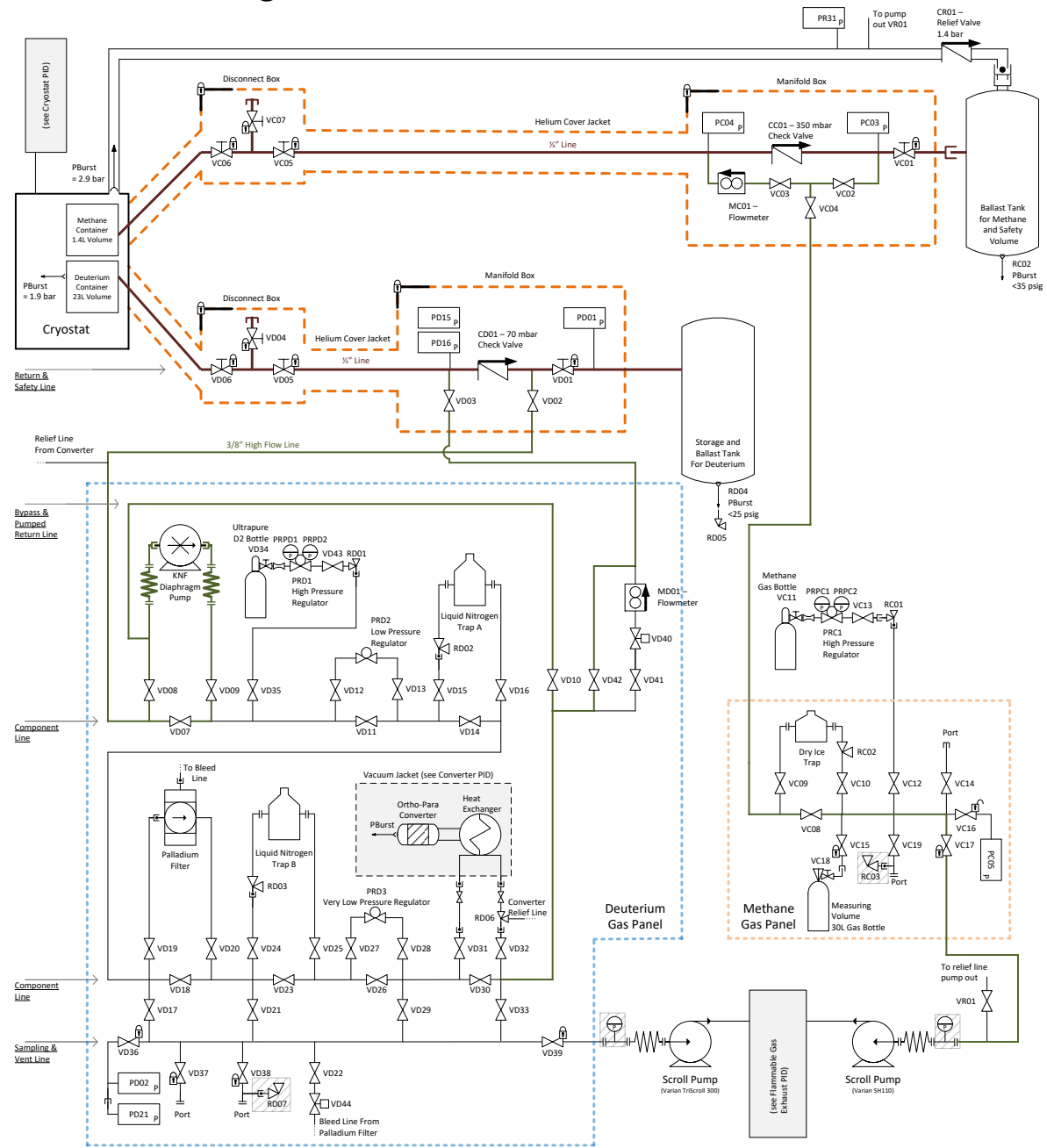
Updated: G. Medlin, 2016/09/13

Legend

- ¼" Bellows Valve
- ½" Bellows Valve
- Metering Valve
- Regulator
- Bar Handle Valve
- Check Valve
- Relief Valve
- Cylinder Flow Restrictor
- Pipe Cap
- Indicator
- Locked Closed During Cooldown
- Locked Open During Cooldown
- Flexible Bellows
- Rupture Disk
- KF Flange Fitting
- Swage Fitting
- NPT Fitting
- 1/2" Tube
- 3/8" Tube
- 1/4" Tube
- Planned but not yet present

NOTE: VCR and ConFlat Fittings not shown

Key

- V – Valve
- P – Pressure Gauge
- C – Check Valve
- R – Relief Valve
- M – Mass Flowmeter
- PR – Pressure Regulator

Gauges

PD01, PC02, PC03, PC04, PC05
 – Pfeiffer RPT-100 Piezo – 10^{-4}-1200 mbar
PD15 – Pfeiffer CMR 361 – 1100-10^{-1} mbar
PD16 – Pfeiffer CMR 375 – 0.11-10^{-5} mbar
PD21 – Mensor 6000 – 0-60psia (4 bar)
PR31 – Thermocouple – 1200-0 mTorr

MD01, MC01 – Sierra 822S Flowmeter – 0-50 slpm

Valves

Standard – Bellows-Sealed Swagelok BG Series
VD40 – Metering Valve SS-4BMW
CC01 – Swagelok CH Series 0.35 bar nominal
CD01 – Swagelok CH Series 0.07 bar nominal
PRD02 – Swagelok KPR Series 0 to 50 psi
PRD03 – Swagelok KPR Series 0 to 10 psi
RC01, RC02, RC03, RD01, RD02, RD03, RD06, RD07
 – Swagelok RL3 Series Adjustable 0.7 to 15.5 bar
RD04 – Burst disk 15-25 psig
RC03 – Burst disk Fike CPV Series 31-35 psig

A.3   Gas exhaust PID
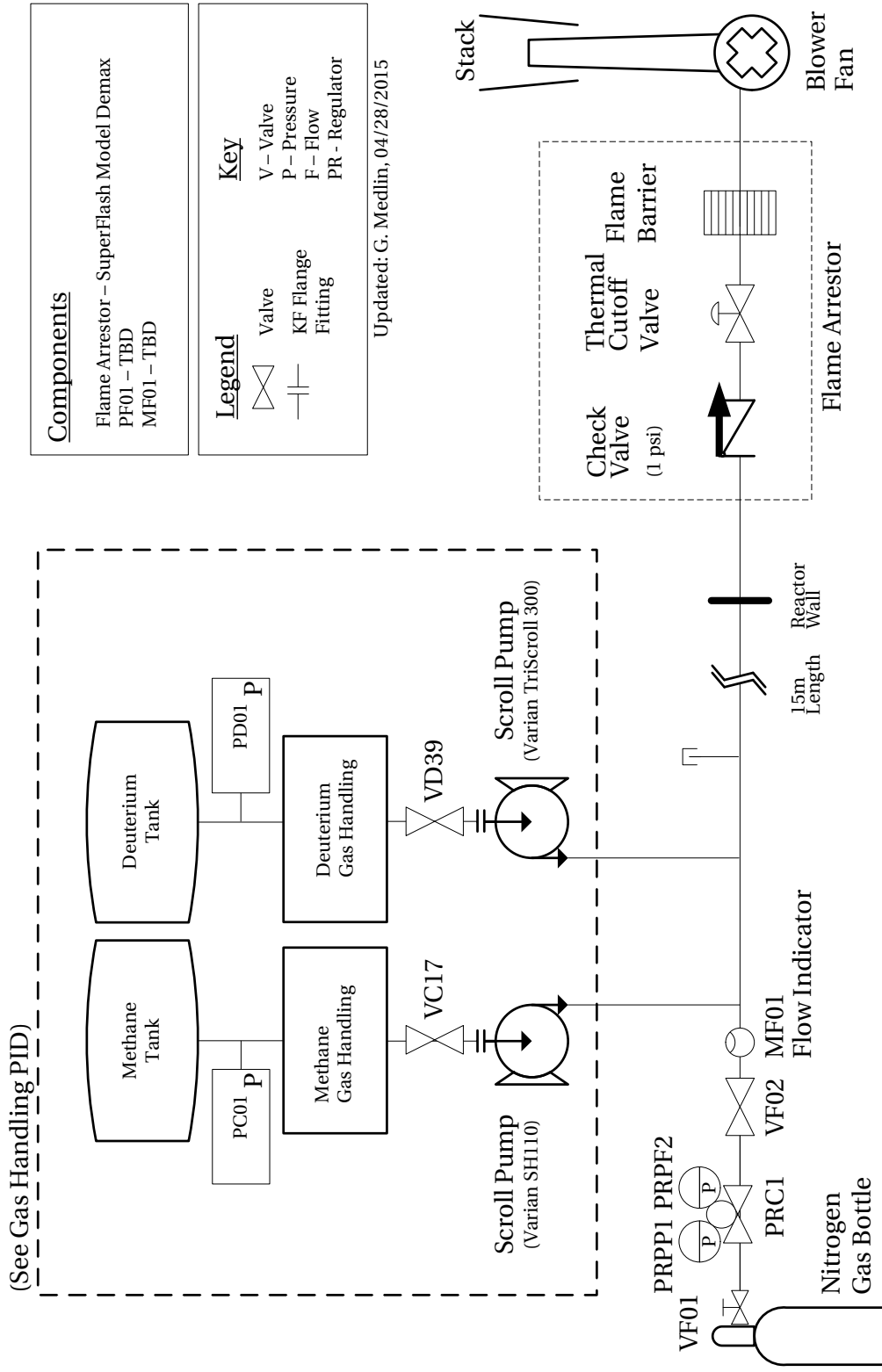
A.4 Cryostat vacuum PID
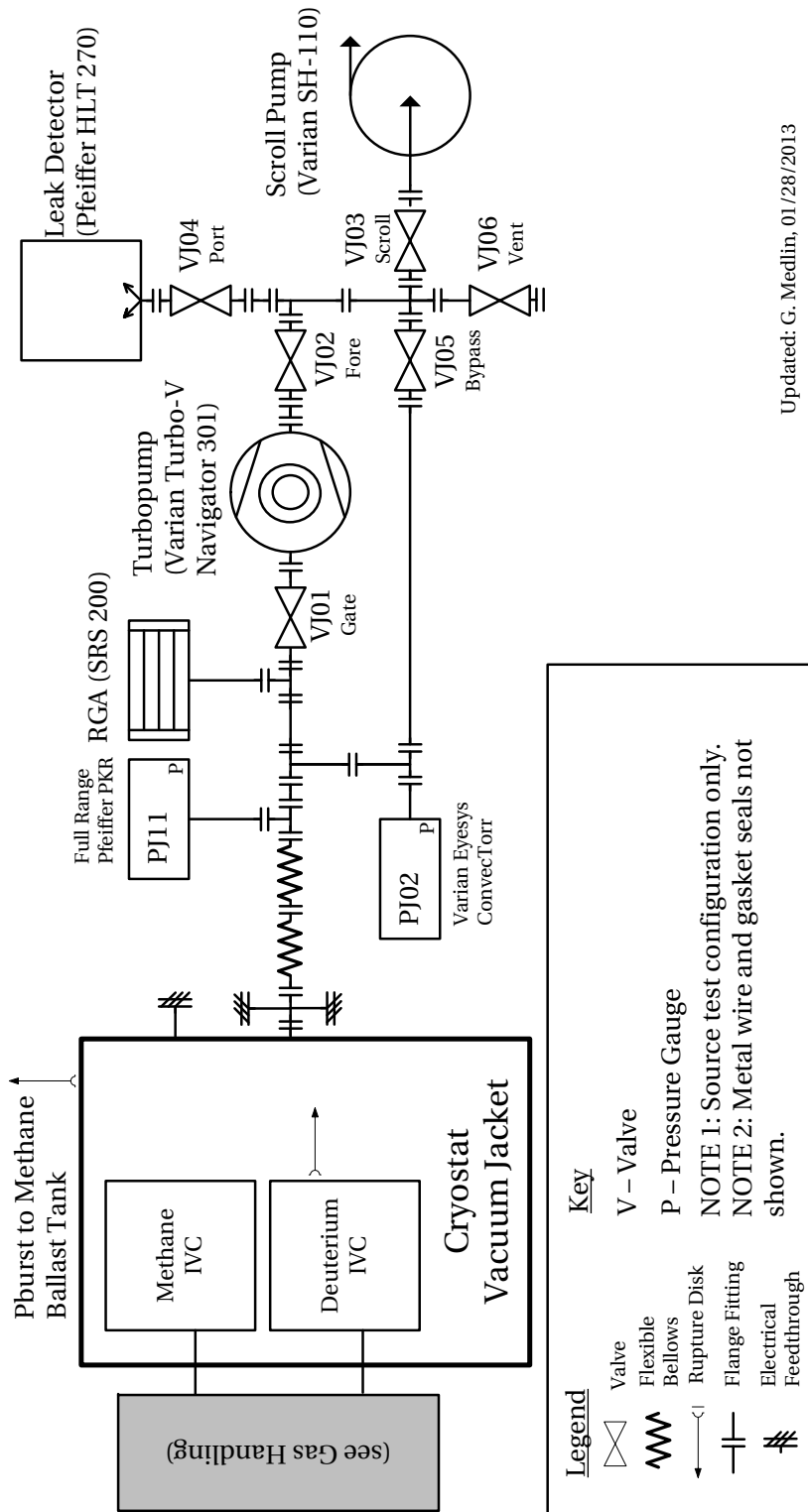
A.5 Helium PID
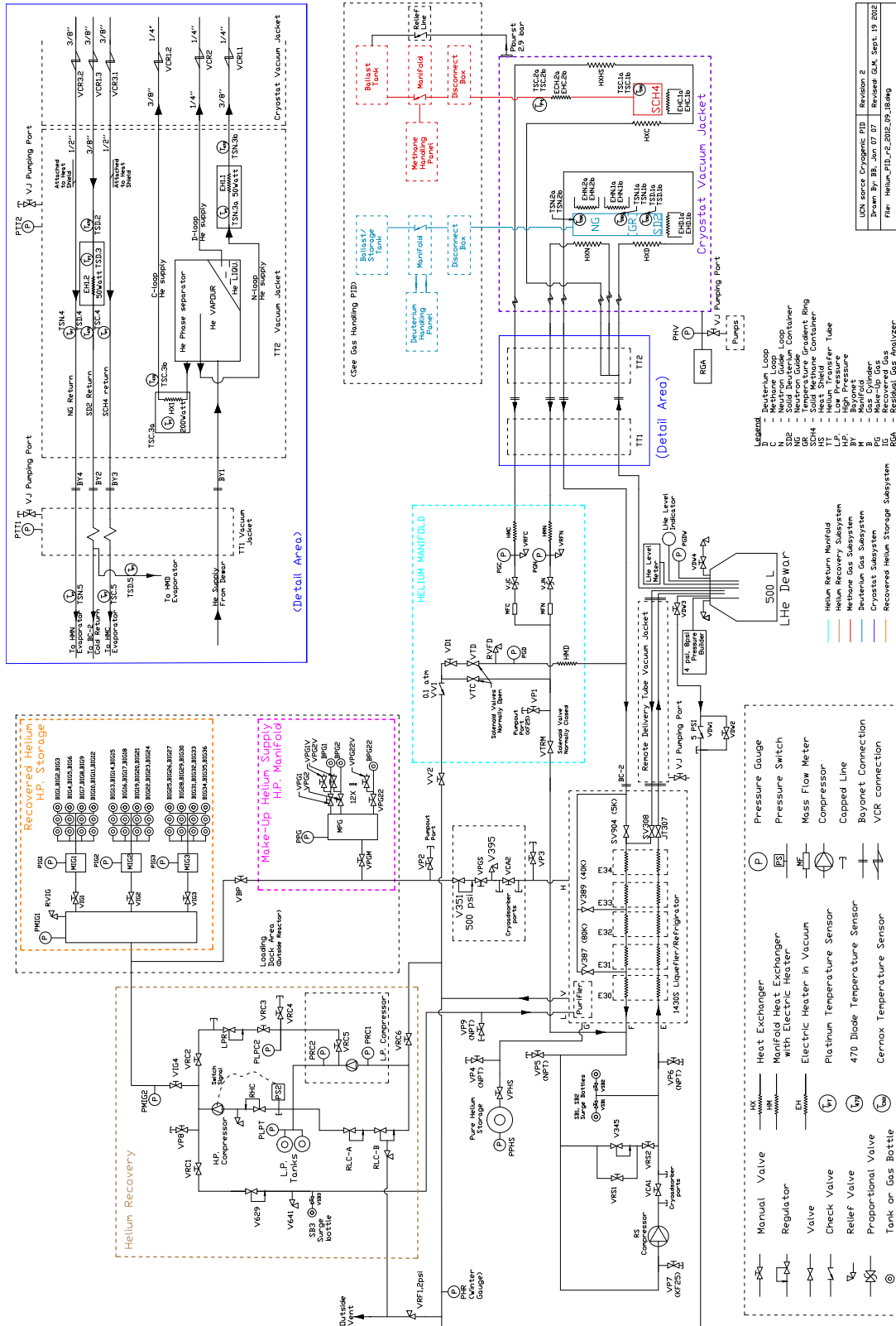
A.6 Liquefier PID
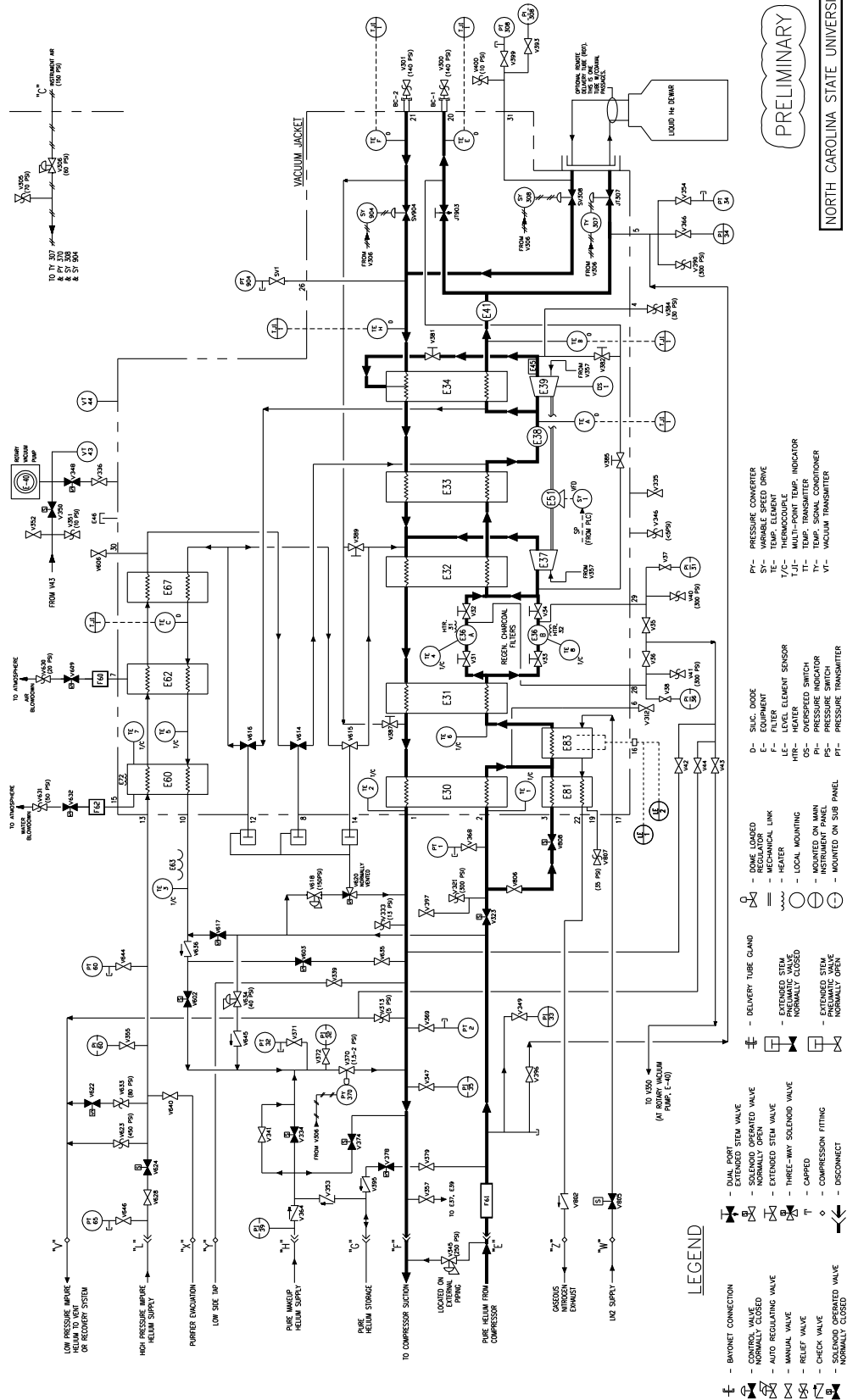
B

Additional images

B.1 LabVIEW Source Human-Machine Interface (HMI)

B.2 Helium Liquefier HMI
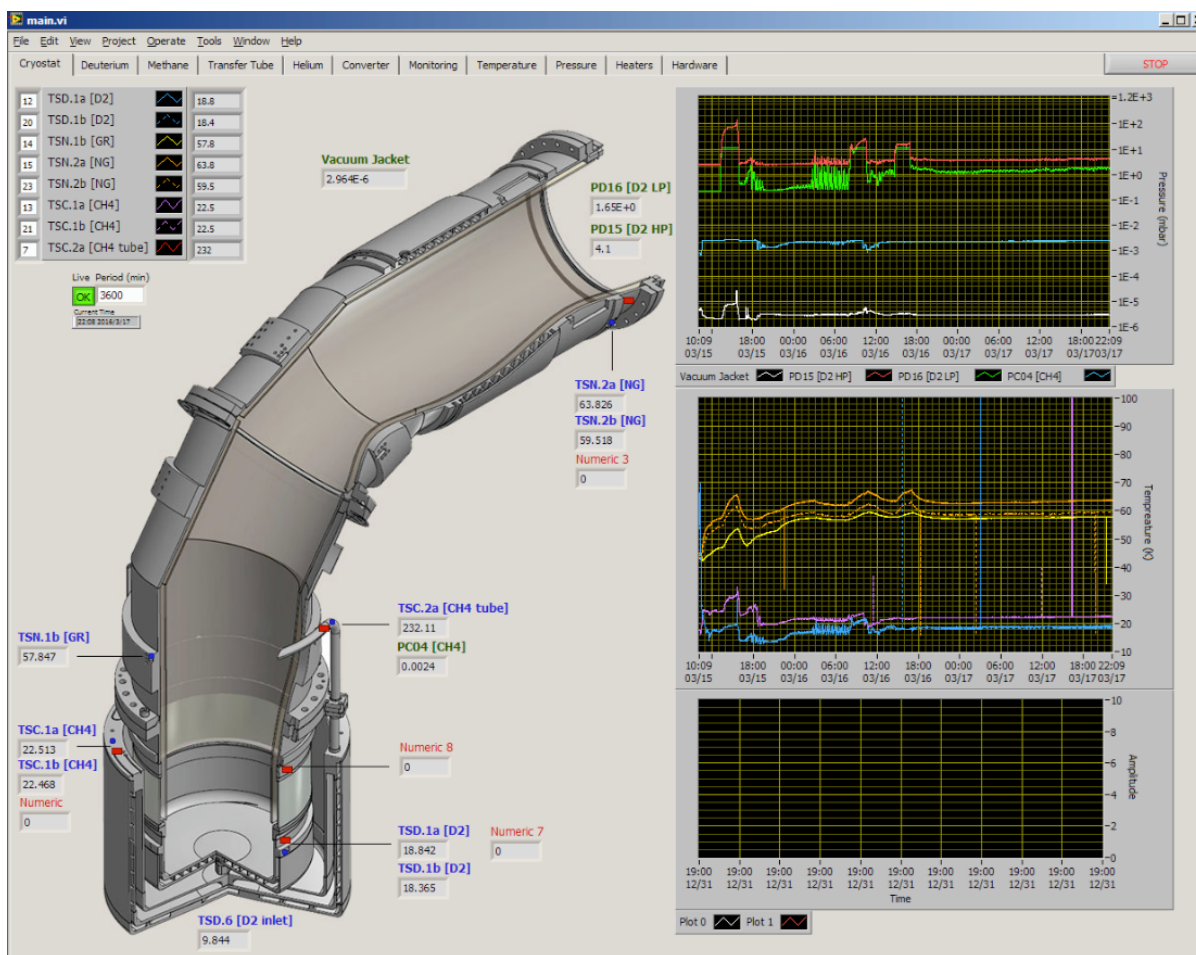
Appendix C

Selected gas handling procedure example

[Document begins on following page]

13 Condensing Deuterium using Para-Ortho Converter

A Purpose

The appropriate amount of deuterium stored in the ballast tank is prepared through the gas panel and para-ortho converter and condensed into the deuterium cryocontainer.

B Summary

The deuterium cryocontainer may first be warmed from the minimum operating temperature to the desired temperature for sublimation or liquefaction. The ballast tank is opened to the panel and flow is allowed into the para-ortho converter, optionally purified through the liquid nitrogen traps. The para-ortho converter may be used in a continuous flow or batch operation. Once flow is established, the palladium filter may be used to further purify the gas, and the diaphragm pump can be used increase pressure on the filter inlet. The outlet of the diaphragm pump cannot be allowed to exceed 3 bar, so the pump bypass is opened whenever flow is interrupted, such as during batch operation. The sampling line may be evacuated and used to sample gas or purge the palladium filter's bleed line. Once the desired amount has been condensed, forward valves are closed, and the container is cooled to the desired operating temperature below the freezing point. Deuterium may be recovered from the para-ortho converter and panel to the ballast tank. Finally, deuterium remaining in the system and the warmed LN traps are evacuated.

C Procedure

Reference Appendix C for a schematic of component locations. Refer to the Cryostat Procedures for procedures for warming and cooling the cryocontainer.

Holding

If any condition is not met, close valves VD02, VD03, and VD39. If the system must be shut down, follow Procedure 8. If the experimenter is required to leave, the system can be left in its current state.

13.1 Verifying the initial state of the system

1. The system has been purged or evacuated, leak checked, and the ballast tank filled, Procedure 3 through Procedure 6. Verify using gauge PD01 that 200 mbar to 1000 mbar of deuterium gas is in the ballast tank.
2. If desired, the para-ortho converter has been baked for cleanliness following in Procedure 11. Ensure the vacuum jacket is evacuated, and the converter has been cooled to the desired temperature.
3. The helium system is ready to operate.
4. Tank valve VD01 (green) in the manifold box may be closed for deuterium storage.
5. Ensure safety return valves VD05 and VD06 in the disconnect box and panel pressure gauge valve VD36 are locked and tagged open.
6. Ensure panel valves VD37, VD38, and VD39 and disconnect box valve VD04 are locked and tagged closed.
7. Ensure that all other valves are in the closed position, and PRD01, PRD02, and PRD03 are set to their minimum value.
8. Ensure pressure and temperature instrumentation is active if desired.

13.2   Preparation

Note: Gas sampling Procedure 9 may be performed when desired at any point between Step 9 and Step 59.

9. If they will be used, cool either or both LN cryogenic traps A and B. Maintain liquid level until at least Step 49.
10. If the palladium filter will be used, turn it on and set to desired temperature.
11. Warm the cryocontainer to the desired temperature.
12. Warm the para-ortho converter to the desired temperature.
13. Open and lock tank valve VD01 (green handle) in manifold box.
14. Notify the reactor operator that deuterium condensation is beginning and safety valves locked open.

13.3   Initial setup

15. To open the ballast tank to the gas panel, open manifold box valve VD02, and to open the gas panel to the cryostat, open manifold box valve VD03.
16. Open KNF diaphragm pump bypass valve VD07.
17. Open low pressure regulator bypass valve VD11.
18. If LN cryogenic trap A is to be used, open valves VD15 and VD16, else open bypass VD14.
19. Open palladium filter bypass VD18.
20. If LN cryogenic trap B is to be used, open valves VD24 and VD25, else open bypass VD23.
21. Open very low pressure regulator PRD3 valves VD27 and VD28.
22. To monitor para-ortho converter inlet pressure on PD02, ensure closed VD17, VD21, and VD33, and open VD29.
23. Adjust very low pressure regulator PRD3 as desired for the para-ortho converter inlet pressure while monitoring pressure PD02.
24. To allow gas into the para-ortho converter, open para-ortho converter valve VD31. If desired, wait and allow the catalyst to saturate with deuterium.

Note: PRD3 and para-ortho converter temperature may now be adjusted as desired at any time until Step 42. Any one, and only one, of VD17, VD21, VD29, and VD33 may be open to monitor pressure.

13.4   Continuous flow operation

Note: If not using continuous flow operation, skip to Step 29, and then follow Section 13.6.

25. To monitor para-ortho converter outlet pressure on PD02, ensure closed VD17, VD21, and VD29, and open VD33.
26. To allow gas out of the para-ortho converter, open valve VD32.
27. To begin condensing deuterium into the cryocontainer, open valve VD41.
28. Adjust needle valve VD40 as desired. Record the pressures on both sides of the check valve, PD01 and PD15. Mass flowmeter MD01 is not necessarily used. See Appendix K.

13.5   Palladium filter

Note: If not using the palladium filter, skip to Step 33.

29. To monitor the palladium filter inlet pressure on PD02 and PD21, ensure closed VD21, VD29, and VD33, and open VD17.

30. To include the palladium filter, open valves VD19 and VD20, and close bypass VD18.

Note: The palladium filter bleed line may be evacuated following Procedure 10 as desired up to Step 59.

31. If the KNF diaphragm pump will be used to build pressure for the palladium filter, open valves VD08 and VD09 and turn on the pump.
32. While monitoring the palladium filter inlet pressure on PD02 and PD21, close VD07. If PD21 rises above 55 psia, reopen VD07.

13.6   Batch operation

Note: If not using batch operation, having performed Section 13.4, skip to Step 42.

33. If using the KNF pump, open VD07.
34. To monitor para-ortho converter outlet pressure on PD02, ensure closed VD17, VD21, and VD29, and open VD33.
35. Close VD31, wait the desired period of time, then open VD32.
36. To begin condensing deuterium into the cryocontainer, open valve VD41.
37. Adjust needle valve VD40 as desired. Record the pressures on both sides of the check valve, PD01 and PD15. Mass flowmeter MD01 is not necessarily used. See Appendix K.
38. When the desired amount of deuterium has been condensed, close VD32 and reopen VD31.
39. If using the palladium filter, to monitor the palladium filter inlet pressure on PD02 and PD21, ensure closed VD21, VD29, and VD33, and open VD17.
40. If using the KNF pump, while monitoring the palladium filter inlet pressure on PD02 and PD21, close VD07. If PD21 rises above 55 psia, reopen VD07.
41. If using batch operation, repeat Step 33 through Step 40 as desired.

13.7   Finishing condensation

42. When the desired amount of deuterium has been condensed from the ballast tank into the deuterium cryocontainer, first reopen KNF pump bypass VD07 if closed, then close valve VD03 in manifold box

Note: Maintain liquid nitrogen level in LN traps until at least Step 49.

43. Cool the cryocontainer to the desired operating temperature.

13.8   Recovering the deuterium remaining in the gas panel

Note: If not recovering gas from the gas panel, skip to Step 49.

44. If not recovering gas from the para-ortho converter, close VD31 and VD32, and open VD30.
45. To monitor pressure on PD02, close VD21, VD29, and VD33 if open, and open VD17.
46. To reverse the flow of the KNF pump, close valves VD11, VD12 and VD08, and open VD07 and VD10. Start the KNF diaphragm pump, if not already running.
47. If recovering gas from the para-ortho converter, warm para-ortho converter to desired temperature.
48. When PD02 reaches the desire pressure, close manifold box valve VD02 and turn off KNF diaphragm pump.

13.9   Evacuating the deuterium remaining in the converter

49. LN traps will not be evacuated until warm, following Procedure 12, to avoid evacuating for an extended period while the cryocontainer is cold. Close valves VD15, VD16, VD24, and VD25.
50. Follow procedures in Procedure 2 for turning on the exhaust system.
51. Turn on the Varian TriScroll 300 pump.
52. Verify valves VD02 and VD03 in manifold box are closed.
53. If not already, open valves VD08, VD11, VD12, VD14, VD18, VD23, VD26, VD30-VD33.
54. Unlock and open VD39, monitoring the pressure using PD02.
55. Warm the para-ortho converter to at least 250 K.
56. When the pressure at PD02 drops below 10 mbar, follow procedures in Procedure 2 for turning off the exhaust system.
57. When the desired pressure is reached, close and lock valve VD39.
58. Turn off the Varian TriScroll 300 pump.
59. Close all panel valves, VD07-VD33, VD41, and VD42 if open, and turn down PRD2 and PRD3.

13.10   Back-filling para-ortho converter cell

Note: Step 60 to Step 62 are optional.

60. Only if the para-ortho converter is warmer than 250 K, it may be back-filled with deuterium for storage. Open valves VD02, VD07, VD12, VD13, VD14, VD18, VD23, VD26, VD29, and VD31.
61. Increase low pressure regulator PRD3 until PD02 reads the desired pressure, then turn down PRD3.
62. Close valves VD02, VD07, VD12, VD13, VD14, VD18, VD23, VD26, VD29, and VD31.

13.11   Confirming the final state of the system

63. Verify that safety return valve VD01 (green) in the manifold box is locked and tagged open.
64. Verify safety return valves VD05 and VD06 in the disconnect box and panel pressure gauge valve VD36 are locked and tagged open.
65. Verify panel valves VD37, VD38, and VD39 and disconnect box valve VD04 are locked and tagged closed.
66. Verify that all other valves are in the closed position, and PRD01, PRD02, and PRD03 are set to to their minimum value.
67. Record the pressures at gauges PD01, PD15, and PD02.
68. Verify pressure and temperature instrumentation is active if desired.

D

Code

D.1   NJOY methane bash file 'smeth_multi.sh'

```
echo "=== Solid Methane Multiple Temperatures ==="
echo "--- cleaning up ---"
rm -f tape*
echo "--- getting endf H-1 tape ---"
cp ../ref/1-H.ENDFB-VII tape20
echo "--- running njoy - LEAPR ---"
../../njoy2012/bin/xnjoy < smeth_multi_leapr.dat
echo "--- copying output ---"
cp tape24 out_leapr
echo "--- getting leapr output ---"
cp out_leapr tape24
echo "--- fixing masses in leapr output ---"
sed -i 's/1.340000+2 9.992000-1/1.340000+2 1.589400+1/g' tape24
sed -i 's/327.237843 0.000000+0/8.174400+1 0.000000+0/g' tape24
echo "--- running njoy ---"
../../njoy2012/bin/xnjoy < smeth_multi.dat
echo "--- copying output ---"
cp tape29 out_reconr
cp tape28 out_broadr
cp tape30 smetm12
cp tape31 xsdir12
echo "--- converting ACER PS plots ---"
ps2pdf tape60 plot_ace12.pdf
echo "--- converting PLOTR PS plots ---"
ps2pdf tape91 plot_thermr12.pdf
ps2pdf tape95 plot_all.pdf
ps2pdf tape97 plot_leapr.pdf
echo "--- cleaning up ---"
rm -f tape*
```

D.2 NJOY main input file 'smeth_multi.dat'

```
  moder /                               Convert H–1 ENDF from ASCII to binary
     ↪ format
    20 −21 /                              [1] nin nout
  reconr /                            Generate PENDF, pointwise for linear
     ↪ interpolation within accuracy
   −21 −22 /                             [1] nendf:(input endf) npend:(output
     ↪ pendf)
    "  H–1 from ENDF/B–VII " /            [2] tlabel
    125 1 /                               [3] mat ncards ngrid
    0.001 0.0 /                           [4] err tempr errmax errint
    'Methane Test' /                      [5] cards:(description)
    0 /                                   [6] enode:(user energy grid)
  moder /                             Convert THERMR output PENDF to ASCII
   −22 29 /                               [1] nin nout
  broadr /                            Add temperature dependance by doppler
     ↪ broadening PENDF
   −21 −22 −23 /                          [1] nendf:(input endf) nin:(input pendf
     ↪ ) nout:(output penf)
    125 8 /                               [2] mat1 ntemp2 istart istrap temp1
    0.001 /                               [3] errthn thnmax errmax errint
    22 30 35 40 45 50 55 60 /             [4] temp2
    0 /                                   [5] mat1:(next material, 0 term.)
  moder /                             Convert THERMR output PENDF to ASCII
   −23 28 /                               [1] nin nout
  thermr /                            Add thermal range using S(alpha,beta)
     ↪ into PENDF
    24 −23 −25 /                          [1] nenf nin nout
    34 125 20 8 2 0 0 4 237 1 /           [2] matde matdp nbin:(angles) ntenp
       ↪ iinc icoh natom mtref iprint
    22 30 35 40 45 50 55 60 /             [3] tempr
    0.001 4 /                             [4] tol emax
  moder /                             Convert THERMR output PENDF to ASCII
   −25 26 /                               [1] nin nout
  acer /                              Generate ACE file for MCNP
   −21 −25 0 30 31 /                      [1] nendf npend ngend nace ndir
    2  1  1  .12  0 /                     [2] iopt iprint itype suff nxtra
    "Solid Methane 22K" /                 [3] hk:(description)
    125 22 smetm /                        [8] matd tempd tname
    1001 0 0 /                            [8a] iza01 iza02 iza03
    237 80 238 1 1 4 /                    [9] mti nbint:(# of energies) mte ielas
       ↪ :(1=incoh) nmix emax iwt
  acer /
   −21 −25 0 32 33 /
```

179

```
      2   1   1   .13   0  /
      "Solid  Methane  30K"  /
      125  30  smetm  /
      1001  0  0  /
40    237  80  238  1  1  4  /
   acer  /
    −21  −25  0  34  35  /
      2   1   1   .14   0  /
      "Solid  Methane  35K"  /
45    125  35  smetm  /
      1001  0  0  /
      237  80  238  1  1  4  /
   acer  /
    −21  −25  0  36  37  /
50    2   1   1   .15   0  /
      "Solid  Methane  40K"  /
      125  40  smetm  /
      1001  0  0  /
      237  80  238  1  1  4  /
55 acer  /
    −21  −25  0  38  39  /
      2   1   1   .16   0  /
      "Solid  Methane  45K"  /
      125  45  smetm  /
60    1001  0  0  /
      237  80  238  1  1  4  /
   acer  /
    −21  −25  0  40  41  /
      2   1   1   .17   0  /
65    "Solid  Methane  50K"  /
      125  50  smetm  /
      1001  0  0  /
      237  80  238  1  1  4  /
   acer  /
70  −21  −25  0  42  43  /
      2   1   1   .18   0  /
      "Solid  Methane  55K"  /
      125  55  smetm  /
      1001  0  0  /
75   237  80  238  1  1  4  /
   acer  /
    −21  −25  0  44  45  /
      2   1   1   .19   0  /
      "Solid  Methane  60K"  /
80    125  60  smetm  /
      1001  0  0  /
```

```
     237 80 238 1 1 4 /
  acer /                                  Generate ACE file test plots
     0 30 70 /                              [1] nendf npend ngend nace ndir
85   7 /                                    [2] iopt iprinr ntype suff nxtra
     /                                      [3] hk:(description)
  acer /
     0 32 72 /
     7 /
90   /
  acer /
     0 34 74 /
     7 /
     /
95 acer /
     0 36 76 /
     7 /
     /
  acer /
100  0 38 78 /
     7 /
     /
  acer /
     0 40 80 /
105  7 /
     /
  acer /
     0 42 82 /
     7 /
110  /
  acer /
     0 44 84 /
     7 /
     /
115 plotr /                                 Plotting THERMR output
     90 /                                    [0] nplt nplt0:(input commands)
     /                                       [1] lori:(orientation) istyle:(2=swiss)
        ↪   size ipcol
     1 /                                     [2] iplot iwcol factx facty xll,yll ww,
        ↪ wh,wr
     "Solid Methane 22K" /                   [3] t1:(1st line title)
120  /                                       [3a] t2:(2nd line title)
     4 0 3 1 2e−5 2e−1 /                     [4] itype jtype igrid ileg xtag ytag
     1e−5 5 /                                [5] el eh xstep
     /                                       [5a] xlabl
     1e−2 1e3 /                              [6] yl yh ystep
125  /                                       [6a] ylabl
```

181

```
       6 −25 125 3 1 22 /                       [8] iverf nin matd mfd mtd temper
       /                                        [9] icon isym idash iccol ithck ishade
       "H−1 elastic+(n,g)" /                    [10]
       2 /                                      [2] iplot
130    6 −25 125 3 2 22 /                       [8]
       0 0 1 1 /                                [9]
       "H−1 elastic" /                          [10]
       3 /                                      [2] iplot
       6 −25 125 3 102 22 /                     [8]
135    0 0 2 2 /                                [9]
       "H−1 (n,g)" /                            [10]
       4 /                                      [2] iplot
       6 −25 125 3 237 22 /                     [8]
       0 0 3 3 /                                [9]
140    "phonon inelastic" /                     [10]
       5 /                                      [2] iplot
       6 −25 125 3 238 22 /                     [8]
       0 0 4 4 /                                [9]
       "phonon elastic" /                       [10]
145    99 /                                     [2] iplot:(99=term)
   plotr /                                      Plotting THERMR output
       94 /                                     [0] nplt nplt0:(input commands)
       /                                        [1] lori:(orientation) istyle:(2=swiss)
           ↪  size ipcol
       1 /                                      [2] iplot iwcol factx facty x11,y11 ww,
           ↪ wh,wr
150    "Solid Methane Various Temperatures" /  [3] t1:(1st line title)
       /                                        [3a] t2:(2nd line title)
       4 0 3 1 2e−5 2e−1 /                      [4] itype jtype igrid ileg xtag ytag
       1e−5 5 /                                 [5] el eh xstep
       /                                        [5a] xlabl
155    1e−2 1e3 /                               [6] yl yh ystep
       /                                        [6a] ylabl
       6 −25 125 3 237 22 /                     [8] iverf nin matd mfd mtd temper
       0 0 0 0 /                                [9] icon isym idash iccol ithck ishade
       "22 K, inelastic" /                      [10]
160    2 /                                      [2] iplot
       6 −25 125 3 237 30 /                     [8]
       0 0 1 1 /                                [9]
       "30 K, inelastic" /                      [10]
       3 /                                      [2] iplot
165    6 −25 125 3 237 40 /                     [8]
       0 0 2 2 /                                [9]
       "40 K, inelastic" /                      [10]
       4 /                                      [2] iplot
       6 −25 125 3 237 50 /                     [8]
```

```
170   0  0  3  3  /                          [9]
      "50 K,  inelastic"  /                  [10]
      5 /                                    [2] iplot
      6 −25  125  3  238  22  /              [8]
      0  0  4  4  /                          [9]
175   "22 K,  elastic"  /                    [10]
      6 /                                    [2] iplot
      6 −25  125  3  238  60  /              [8]
      0  0  5  5  /                          [9]
      "60 K,  elastic"  /                    [10]
180   99 /                                   [2] iplot:(99=term)
    plotr /                              Plotting LEAPR output
      96 /                                   [0] nplt nplt0:(input commands)
      /                                      [1] lori:(orientation) istyle:(2=swiss)
          ↪   size ipcol
      1 /                                    [2] iplot iwcol factx facty x11,y11 ww,
          ↪ wh,wr
185   "Solid  Methane 22K"  /                [3] t1:(1st line title)
      /                                      [3a] t2:(2nd line title)
      2  0  3  0  /                          [4] itype jtype igrid ileg xtag ytag
      0  450  50  /                          [5] el eh xstep
      "beta"  /                              [5a] xlabl
190   1e−10  1e−1  /                         [6] yl yh ystep
      "SS(alpha,−beta)"  /                   [6a] ylabl
      6  24  34  7  4  22  9  2  2/          [8] iverf nin matd mfd mtd temper
      /                                      [9] icon isym idash iccol ithck ishade
      2 /                                    [2]
195   6  24  34  7  4  22  27  2  2/         [8]
      /                                      [9]
      3 /                                    [2]
      6  24  34  7  4  22  44  2  2/         [8]
      /                                      [9]
200   99 /                                   [2] iplot:(99=term)
    viewr /                              Generate PS
      70  60/                                [1] infile nps
    viewr /                              Generate PS
      72  62/                                [1] infile nps
205 viewr /                              Generate PS
      74  64/                                [1] infile nps
    viewr /                              Generate PS
      76  66/                                [1] infile nps
    viewr /                              Generate PS
210   78  68/                                [1] infile nps
    viewr /                              Generate PS
      80  85/                                [1] infile nps
    viewr /                              Generate PS
```

```
      82  86 /                          [1] infile nps
215   viewr /                           Generate PS
      84  87/                           [1] infile nps
      viewr /                           Generate PS
      90  91 /                          [1] infile nps
      viewr /                           Generate PS
220   94  95 /                          [1] infile nps
      viewr /                           Generate PS
      96  97 /                          [1] infile nps
      stop
```

D.3 NJOY LEAPR input file 'smeth_multi_leapr.dat'

```
leapr /                                 Generate S(alpha,beta), ENDF file 7
  24 /                                   [1] nout:(endf output)
  SOLID METHANE AT multiple T, HARKER & BRUGGER SPECTRUM /[2] title:(not in
      ↪ output)
  8 2 /                                  [3] ntempr iprint nphon:(def=100)
  34 134 0 1 /                           [4] mat za isabd ilog
  0.9992 20.436 4 /                      [5] awr spr npr:(num principle atoms)
      ↪ iel ncold
  1 1 11.898 4.7392 1 /                  [6] nss:(secondary scatterer, 0/1) b7:(
      ↪ type) aws sps mss:(num secondary atoms)
  70 80 /                                [7] nalpha nbeta lat
  .1742 .3488 .4059 .4644 .5215 .6386 .7547 .8703
    .9860 1.1601 1.3932 1.6245 1.9148 2.2050 2.6105
    3.0177 3.5393 4.1198 4.8740 5.6871 6.6159 7.7760
    9.0522 10.6200 12.4187 14.5066 16.9443 19.8464 23.2115
    27.0995 31.7421 37.0805 43.4052 50.7168 59.1889 69.6343
    81.2403 87.0431 94.0059 101.5493 110.2545 120.1198 129.9834
    151.4547 177.5682 188.0122 204.2604 207.1629 209.4831 214.7058
    217.0265 220.5090 232.1145 242.5599 261.1291 272.7347 282.0199
    287.2413 298.2667 304.6496 311.0342 319.1575 327.2810 331.9236
    350. 370. 390. 410. 450. 500. /       [8] (alpha values increasing)
  0. .1742 .3488 .4059 .4644 .5215 .6386 .7547 .8703
    .9860 1.1601 1.3932 1.6245 1.9148 2.2050 2.6105
    3.0177 3.5393 4.1198 4.8740 5.6871 6.6159 7.7760
    9.0522 10.6200 12.4187 14.5066 16.9443 19.8464 23.2115
    27.0995 31.7421 37.0805 43.4052 50.7168 59.1889 69.6343
    81.2403 85.451 89.650 94.0059 96.0 100.221 104.6 110.2545
    120.1198 129.9834 151.4547 170.90 177.5682 181.6 185.67 190.419
    193.8 197.276 200.8 204.2604 207.1629 209.4831 214.7058
    217.0265 220.5090 232.1145 242.5599 261.1291 272.7347 282.0199
    287.2413 298.2667 304.6496 311.0342 319.1575 327.2810 331.9236
    350. 370. 390. 410. 430. 450. /       [9] (beta values increasing)
  22 /                                   [10] (temperature K)
  0.0005 45 /                            [11] delta ni
  0. 1.75 7 15.75 26 36 37.5 38.5 41 42.5 43.3 43.5
   43.5 43.6 45 46.3 48 44.5 39 35 33.6 32 28.3 25 22 17 16
   13 9.7 7 4.5 2.3 1.2 1.5 2 2.5 3 2.7 2.2 2.1 2.2 3 3 1.5
   0. /                                  [12] rho
  0. 0. .32 /                            [13] twt c tbeta
  4 /                                    [14] nd:(number of oscillators)
  .162 .190 .361 .374 /                  [15] (oscillator energies)
  .308 .186 .042 .144 /                  [16] (oscillator weights)
  −30 /                                  [10] (temp K, − skip 11−18)
```

```
     -35  /
     -40  /
     -45  /
     -50  /
45   -55  /
     -60  /
     ' S-CH4 LANL     EVAL-APR93 MACFARLANE'/
     ' REF. 1     DIST-'/
     '------ENDF/B-6      MATERIAL 33'/
50   '------THERMAL DATA' /
     '------ENDF-6'/
     ' SOLID METHANE AT multiple T, MODEL OF PICTON BASED ON THE '/
     ' SPECTRUM OF HARKER AND BRUGGER.'/
     ' '/
55   ' 1. R.E.MACFARLANE, NEW THERMAL NEUTRON SCATTERING FILES  FOR '/
     '     ENDF/B-VI RELEASE  2, LOS ALAMOS NATIONAL LABORATORY REPORT '/
     '     LA-12639-MS (TO  BE PUBLISHED). '/
     ' '/
     ' Modified by G.Medlin 2015/01/16 '/
60   ' '/
     /                              [20] (comments until blank line)
   stop
```

D.4 MCNP test tank geometry

```
   c ******************************************************************
   c ***                      Cell Cards                          ***
   c ******************************************************************
   c
   c (num) (mat) [den] (geom) [params] (n) (list)
 5 c      or
   c (num) LIKE (n) BUT (list)
   c
   c Geometry
   c      : Union
10 c      # Compliment
   c      intersection implicit
   c
   c Translate:
   c      trcl = ( x y z )
15 c
```
[Reactor details omitted]
```
   c
   c === Experimental Geometry ===
   c thermal column nose port (C/void–He/Pb)
20 c graphite
   520    11   −1.69   ((8835 −8837 8838 −8836) (−831 −8836 −833 834) −8842 8843)
          #(−857 858 −8842 8843 −855 856) imp:n=1 imp:p=1
   c he in nose port
   523    2   −0.000178   −857 858 −8842 8843 −855 856 imp:n=1 imp:p=1
25 c nose port box
   5523   9 −2.699 ((−9837 9835 −9836 9840 −842 843) −8831 −8833 −9836 8834)
          #520 #(−857 858 −8842 8843 −855 856) #5524 imp:n=1 imp:p=1
   5524   6 −1.0 (−8838 9839 8843 834 −8837 8835) imp:n=1 imp:p=1
   6527   9   −2.699 ((835 −837 838 −836) −8943 839) imp:n=1 imp:p=1
30 c
   c 5525 9 −2.699 (−7631 1831 (−7633 7634 −7733 7742)) imp:n=1 imp:p=1
   c 5526 9 −2.699 (7632 −1832 (−7633 7634 −7733 7742)) imp:n=1 imp:p=1
   c 5527   9 −2.699 ((−7631 7632 −7633 7634) −733 7733)  imp:n=1 imp:p=1
   c 5528   9 −2.699 ((−7631 7632 −7633 7634) −7742 7842)  imp:n=1 imp:p=1
35 c water between lead box and nose port
   527    6 −1.0 ((835 −837 838 −836) −843 8943)  imp:n=1 imp:p=1
   c lead
   526   16   −11.34 ((−1831 1832 −1833 1834) −7733 7834)  imp:n=1 imp:p=1
   c he in lead box
40 5529   2   −0.000178   ((−1831 1832 −1833 1834) −7834 7742)  imp:n=1 imp:p=1
   c lead box
   5525   9 −2.699 (−7333 842 −2833 2834 −2831 2832) #5529 #526 imp:n=1 imp:p=1
   c thermal column wall   (Al)
```

187

```
     521     9   −2.699   ((835 −837 838 −836) −839 8840)    imp:n=1 imp:p=1
45   c
     c thermal column lining
     5927   9   −2.699  (−8936 836 −8937 8935 −8943 713) imp:n=1 imp:p=1
     5928   9   −2.699  (−838 8938 −8937 8935 −8943 713) imp:n=1 imp:p=1
     5929   9   −2.699  (−836 838 −8937 837 −8943 713) imp:n=1 imp:p=1
50   5930   9   −2.699  (−836 838 −835 8935 −8943 713) imp:n=1 imp:p=1
     c
     c Graphite webbing
     700    9   −2.699   (−8840 2300 −2323 2325 −837 835) &
                         :(−8840 2300 −2326 2324 −837 835) &
55                       :(−8840 2300 −2331 2333 −836 838) &
                         :(−8840 2300 −2334 2332 −836 838) imp:n=1 imp:p=1 $ aluminium
                            ↪ webbing
     701    11  −1.69   −8840 2300 −2325 2326 −2333 2334 &
                         #(−2327 2328 −2335 2336) imp:n=1 imp:p=1 $ inner graphite
     702    22  −0.00129 −8840 9915 −2327 2328 −2335 2336 imp:n=1 imp:p=1 $ inner air
60   7702   22  −0.00129 −9915 2301 −2327 2328 −2335 2336 imp:n=1 imp:p=1 $ inner air
     7703   22  −0.00129 −2301 2300 −2327 2328 −2335 2336 imp:n=1 imp:p=1 $ inner air
     703    11  −1.69   −8840 2300 −2321 2323 −2332 2330 imp:n=1 imp:p=1 $ top left
     704    11  −1.69   −8840 2300 −2321 2323 −2333 2334 imp:n=1 imp:p=1 $ top middle
     705    11  −1.69   −8840 2300 −2321 2323 −2329 2331 imp:n=1 imp:p=1 $ top right
65   706    11  −1.69   −8840 2300 2330 −2332 −2325 2326 imp:n=1 imp:p=1 $ middle left
     707    11  −1.69   −8840 2300 2331 −2329 −2325 2326 imp:n=1 imp:p=1 $ middle
        ↪ right
     708    11  −1.69   −8840 2300 −2324 2322 −2332 2330 imp:n=1 imp:p=1 $ bottom left
     709    11  −1.69   −8840 2300 −2324 2322 −2333 2334 imp:n=1 imp:p=1 $ bottom
        ↪ middle
     710    11  −1.69   −8840 2300 −2324 2322 −2329 2331 imp:n=1 imp:p=1 $ bottom
        ↪ right
70   711    22  −0.00129 −8840 2300 −836 2323 −2332 835 &
                         #(−2321 2323 −2332 2330) imp:n=1 imp:p=1 $ top left
     712    22  −0.00129 −8840 2300 −836 2321 −2333 2334 imp:n=1 imp:p=1 $ top middle
     713    22  −0.00129 −8840 2300 −836 2323 −837 2331 &
                         #(−2321 2323 −2329 2333) imp:n=1 imp:p=1 $ top right
75   714    22  −0.00129 −8840 2300 −2325 2326 835 −2330 imp:n=1 imp:p=1 $ middle
        ↪ left
     715    22  −0.00129 −8840 2300 −2325 2326 2329 −837 imp:n=1 imp:p=1 $ middle
        ↪ right
     716    22  −0.00129 −8840 2300 −2324 838 −2332 835&
                         #(−2324 2322 −2332 2330) imp:n=1 imp:p=1 $ bottom left
     717    22  −0.00129 −8840 2300 −2322 838 −2333 2334 imp:n=1 imp:p=1 $ bottom
        ↪ middle
80   718    22  −0.00129 −8840 2300 −2324 838 −837 2331 &
                         #(−2324 2322 −2329 2331) imp:n=1 imp:p=1 $ bottom right
```

```
    719     22    -0.00129 -836 838 -837 835 -2300 2203 imp:n=1 imp:p=1 $ tiny air gap
        ↪ for detector
    c D2O test tank
    809     22    -0.00129  2200 -2203  2230  838 -836 -837  835   imp:n=1 imp:p=1  $ air
        ↪  outside tank
85  810     9     -2.699     2200 -2201 -2230 &
                             #(2200 -2203  2253 -2252  2257 -2255)  imp:n=1 imp:p=1    $
                                ↪ front wall D2O tank
    3055   13    -1.105      6015 -6045 -6065  imp:n=1 imp:p=1 $ D2
    811    13    -1.105      -2205 2202 -2230 &
                             #(2200 -2203  2253 -2252  2257 -2255)  &
90                           #(6015 -6045 -6065) imp:n=1 imp:p=1   $ D2O tank 1st part
                                ↪ flipped away
    c 811   13   -1.105      2201 -2202 -2230 &
    c                        #(2200 -2203  2253 -2252  2257 -2255)  imp:n=1 imp:p=1   $
        ↪ D2O tank 1st part
    c 813   9    -2.699      2200 -2202  2253 -2252  2257 -2255 &
    c                        #(2200 -2203  2251 -2250  2256 -2254)  imp:n=1 imp:p=1   $
        ↪ stringer channel wall before well
95  c 814    22   -0.00129 2202 -2204  2253 -2252  2257 -2255 &
    c                        #(2200 -2203  2251 -2250  2256 -2254)  imp:n=1 imp:p=1   $
        ↪ stringer channel wall in well
    c 815   9    -2.699      2204 -2203  2253 -2252  2257 -2255 &
    c                        #(2200 -2203  2251 -2250  2256 -2254)  imp:n=1 imp:p=1   $
        ↪ stringer channel wall after well
    813    9    -2.699      2200 -2204  2253 -2252  2257 -2255 &
100                          #(2200 -2203  2251 -2250  2256 -2254)  imp:n=1 imp:p=1   $
                                ↪ stringer channel wall before well flipped away
    814    22   -0.00129 -2202 2204  2253 -2252  2257 -2255 &
                             #(2200 -2203  2251 -2250  2256 -2254)  imp:n=1 imp:p=1   $
                                ↪ stringer channel wall in well flipped away
    815    9    -2.699      2202 -2203  2253 -2252  2257 -2255 &
                             #(2200 -2203  2251 -2250  2256 -2254)  imp:n=1 imp:p=1   $
                                ↪ stringer channel wall after well flipped away
105 c 820    9    -2.699      2201 -2202  2229 -2231  imp:n=1 imp:p=1   $ its  wall
    c 811    22   -0.00129   2202 -2204 -2231  2229  imp:n=1 imp:p=1   $ air inside
        ↪ ucn-cylinder
    821    13   -1.105      -2202 2204  2232 -2230 &
                             #(2200 -2203  2253 -2252  2257 -2255)  imp:n=1 imp:p=1   $
                                ↪ D2O tank 2nd part
    822    22   -0.00129 -2233 -2230  2226         imp:n=1 imp:p=1   $ ucn-cylinder
110 823    9    -2.699   -2233 -2224  2223         imp:n=1 imp:p=1   $ ucn-cylinder
        ↪ bottom wall
    824    22   -0.00129 -2233 -2225  2224         imp:n=1 imp:p=1   $ ucn-cylinder
        ↪ part
    825    22   -0.00129 -2233  2225 -2226 &
```

189

```
                        #(2200 −2203  2253 −2252  2257 −2255)  imp:n=1 imp:p=1    $
                          ↪ ucn−cylinder central disk
   827    9    −2.699      2233 −2232 −2230  2223 &
                        #(2200 −2203  2253 −2252  2257 −2255)  imp:n=1 imp:p=1    $
                          ↪ wall of ucn−cylinder
   828    13   −1.105    −2232 −2230 −2223           imp:n=1  imp:p=1  $ D2O space under
       ↪  ucn−cylinder
   829    13   −1.105    −2204 2201 −2230 &
                        #(2200 −2203  2253 −2252  2257 −2255)  imp:n=1 imp:p=1    $
                          ↪ D2O tank 3rd part, flipped away
   c 829     13   −1.105    −2204 2205 −2230 &
   c                     #(2200 −2203  2253 −2252  2257 −2255)  imp:n=1 imp:p=1    $
       ↪ D2O tank 3rd part
   832    9    −2.699      2205 −2203  2229 −2230 &
                        #(2200 −2203  2253 −2252  2257 −2255)  imp:n=1 imp:p=1    $
                          ↪ D2O back wall
   833    22   −0.00129 −2200  713   −837    835 838 −836 imp:n=1 imp:p=1 $ behind
       ↪ tank
   c rect stringer channel subdivided for surface detectors
   840    9   −2.699 9901 −2203  2251 −2250  2256 −2254  imp:n=1 imp:p=1
   841    9   −2.699 9902 −9901  2251 −2250  2256 −2254  imp:n=1 imp:p=1
   842    9   −2.699 9903 −9902  2251 −2250  2256 −2254  imp:n=1 imp:p=1
   843    9   −2.699 9904 −9903  2251 −2250  2256 −2254  imp:n=1 imp:p=1
   844    9   −2.699 9905 −9904  2251 −2250  2256 −2254  imp:n=1 imp:p=1
   845    9   −2.699 9906 −9905  2251 −2250  2256 −2254  imp:n=1 imp:p=1
   846    9   −2.699 9907 −9906  2251 −2250  2256 −2254  imp:n=1 imp:p=1
   847    9   −2.699 9908 −9907  2251 −2250  2256 −2254  imp:n=1 imp:p=1
   848    9   −2.699 9909 −9908  2251 −2250  2256 −2254  imp:n=1 imp:p=1
   849    9   −2.699 9910 −9909  2251 −2250  2256 −2254  imp:n=1 imp:p=1
   850    9   −2.699 9911 −9910  2251 −2250  2256 −2254  imp:n=1 imp:p=1
   851    9   −2.699 9912 −9911  2251 −2250  2256 −2254  imp:n=1 imp:p=1
   852    9   −2.699 9913 −9912  2251 −2250  2256 −2254  imp:n=1 imp:p=1
   853    9   −2.699 9914 −9913  2251 −2250  2256 −2254  imp:n=1 imp:p=1
   854    9   −2.699 2200 −9914  2251 −2250  2256 −2254  imp:n=1 imp:p=1


   C ***************************************************************
   C ***                      Surface Cards                      ***
   C ***************************************************************
   c
   c Plane normal to x−axis:
   c     px (distance)
   c Cylinder on x−axis
   c     cx (radius)
   c Cylinders parallel to axes
   c     c/x (y) (z) (radius)
   c     c/y (x) (z) (radius)
```

```
c      c/z (x) (y) (radius)
c
```
[Reactor details omitted]
```
c thermal column nose and main body
1831     pz   25.4
1832     pz   −25.4
1833     px   26.0298
1834     px   −18.9702
2831     pz   26.3525
2832     pz   −26.3525
2833     px   26.9823
2834     px   −19.9227
831      p    −1.732   1    0    13.3097 $15.2147
833      p     1.732   1    0    25.1161 $27.0211
834      p     0   −0.57735    1    −11.52714825 $−12.6270
8831     p    −1.732   1    0    14.3097 $16.2147
8833     p     1.732   1    0    26.1161 $28.0211
8834     p     0   −0.57735    1    −12.52714825 $−13.6270
8835     px   −38.652
8836     pz    42.182
8837     px    45.712
8838     pz   −42.182 $ xuf2
8839     pz   −65042
9835     px    −39.922
9836     pz   43.452
9837     px   46.982
9839     pz   −66.312
9840     pz   −67.582
835      px   −56.7955 $ −56.319
836      pz    60.325 $ 60.98
837      px    63.8545 $ 63.378
838      pz   −60.325 $ −60.98
839      py   −107.8591 $−105.9541
c thermal column liner
8935     px   −58.0655 $ −57.589
8936     pz    61.595 $ 62.25
8937     px    65.1245 $ 64.648
8938     pz   −61.595 $ −62.25
c
8840     py   −110.3991 $−108.4941
8842     py   −36.815 $−34.91
8843     py   −105.8766 $−103.9716
842      py   −35.86277 $−33.95777
843      py   −106.8291 $−104.9241
8943     py   −107.2241 $−105.3191
855      pz   25
```

191

```
     856     pz   −25
     857     px   25.5298
200  858     px   −18.4702
     c
     c Graphite Webbing
     2300     py   −115.5 $ end of web plate
     2301     py   −115.4 $ surface just before end of web plate for detector
205  2321     pz    43.0 $ top of graphite
     2322     pz   −43.0
     2323     pz    30.1625 $ top of aluminium webbing
     2324     pz   −30.1625
     2325     pz    29.21 $ bottom of aluminium webbing
210  2326     pz   −29.21
     2327     pz    22.5 $ bottome of graphite
     2328     pz   −22.5
     2329     px    46.5298 $ right of graphite
     2330     px   −39.4702
215  2331     px    33.5333 $ right of aluminium webbing
     2332     px   −26.4743
     2333     px    32.5808 $ left of aluminium webbing
     2334     px   −25.5218
     2335     px    26.0298  $ left of graphite
220  2336     px   −18.9702
     c
     c D2O test tank
     2200     py     −186.5
     2201     py     −185.2
225  c 2202     py     −147.2
     2202     py     −154.8 $ flipped away
     2203     py     −115.501
     c 2204     py     −119.4
     2204     py     −182.6 $ flipped away
230  2205     py     −116.8
     2206     py     −181.4
     2207     py     −176.3
     2208     py     −171.2
     2209     py     −166.1
235  2210     py     −161.0
     2211     py     −155.9
     2212     py     −150.8
     22211     py     −145.7
     22212     py     −140.6
240  22213     py     −135.5
     22214     py     −130.4
     22215     py     −125.3
     22216     py     −120.2
```

```
      2217      pz     22.5 $ half size of 45
245   2218      pz    −22.5 $ half size 45
      2219      px    −18.9702 $ −22.5 +3.5298
      2220      px     26.0298  $ 22.5 +3.5298
      2221      pz     43.0 $ sets   x−collimator thickness, was 43.0
      2222      pz    −43.0 $
250   2223      pz    −14.0 $bottom of ucn−cylinder
      2224      pz    −13.35 $wall bottom of ucn−cylinder
      2225      pz    −2.0 $bottom of ucn−cylinder
      2226      pz     2.0
      2227      px    −39.4702 $ sets  y−collimator thickness, 43.0 +3.5298
255   2228      px     46.5298 $ 43.0 +3.5298
      2229      c/y   3.5298 0 −1.07  $ for 'effective' cylindrical stringer
      2230      c/y   3.5298 0 −55.0  $ for cylinder tank
      2231      c/y   3.5298 0 −1.72  $ for stringer wall
      c 2232      c/z   3.5298 −133.2991   13.80   $ 0 −167.2 $ outer R for ucn−cylinder,
          ↪ +3.5298 change z=132.2
260   c 2233      c/z   3.5298 −133.2991   13.15   $ 0 −167.2 $ R of ucn−cylinder +3.5298
      2232      c/z   3.5298 −168.7   13.80   $ outer R for ucn−cylinder, +3.5298 change z
          ↪ =132.2
      2233      c/z   3.5298 −168.7   13.15   $ R of ucn−cylinder +3.5298
      c stringer cavity
      2250      pz     0.635
265   2251      pz    −0.635
      2252      pz     1.270
      2253      pz    −1.270
      2254      px     5.4345
      2255      px     6.0695
270   2256      px     1.6245
      2257      px     0.9895
      c detector surfaces
      c from front face of tank (2300: −115.5)
      9901      py    −118.04   $   2.54
275   9902      py    −123.12   $   7.62
      9903      py    −128.20   $   12.7
      9904      py    −133.28   $   17.78
      9905      py    −138.36   $   22.86
      9906      py    −143.44   $   27.94
280   9907      py    −148.52   $   33.02
      9908      py    −153.60
      9909      py    −158.68
      9910      py    −163.76
      9911      py    −168.84
285   9912      py    −173.92
      9913      py    −179.00
      9914      py    −184.08
```

```
     9915       py   −112.96
     c 9916       py   −107.88 $ in aluminium plate
290  9917       py   −102.8
     9918       py   −97.72
     9919       py   −92.64
     9920       py   −87.56
     9921       py   −82.48
295  9922       py   −77.40
     9923       py   −72.32
     9924       py   −67.24
     9925       py   −62.16
     9926       py   −57.08
300  9927       py   −52.00
     9928       py   −46.92
     9929       py   −41.84
     c 9930       py   −36.76 $ front of nose port
     c (2203: −186.5)
305  c D2 volume
     6015     pz   −13.2951    $ inside of volume
     6045     pz   −7.940      $ D2 level, 1.2 L
     6046     px   16.3985     $ Tangent to outside of D2
     6047     px   −0.4935     $ Tangent to outside of D2
310  6065     c/z   7.9525  −135.810 8.446 $ inside of container


     c ****************************************************************
     c ***                        Data Cards                       ***
     c ****************************************************************
315  c
     mode   n p
     c
     [Reactor details omitted]
     c
320  c ******************  Materials Specification  ******************
     c
     c (+) Atomic fraction or (−) Weight fraction
     c MTn = S(alpha,beta) thermal neutron treatment for material n
     c
325  [Reactor details omitted]
     c
     c —— Helium Gas
     m2     2004          1.000000   gas=1.0     $
     c —— H2O (Coolant & Moderator)
330  m6     1001          0.666670   & $ H
            8016          0.333330     $ O
     mt6    lwtr.20t
     c —— Aluminum
```

```
    m9      13027         1.000000      $
335 mt9     al27.22 t
    c ──── Graphite
    m11     6000          1.000000      $
    mt11    grph.20 t
    c ──── Heavy Water
340 m13     1002          0.666670    & $
            8016          0.333330      $
    mt13    hwtr.20 t
    c ──── Lead
    m16     82204         0.014000    & $ Pb−204   1.4%
345         82206         0.241000    & $ Pb−206  24.1%
            82207         0.221000    & $ Pb−207  22.1%
            82208         0.524000      $ Pb−208  52.4%
    c ──── Air (Experimental geometry)
    m22     6000          0.020000    gas=0.02   & $
350         7014          0.660000    gas=0.66   & $
            8016          0.320000    gas=0.32     $
    c ──── Acrylic
    m33     1001          0.534      $ H
            6012          0.333      $ C
355         8016          0.133      $ O
    c
    c ****************** Detectors  ******************
    c
    c Virtual surface detectors
360 c Fn:N S (or C)
    c FSn S1 ... Sk T (optional)
    c
    c   default energy bins:
    e0  6.25e−7   5.53e−3   0.821   20.0
365 c
    c Stringer
    f12:n 9901
    f22:n 9902
    f32:n 9903
370 f42:n 9904
    f52:n 9905
    f62:n 9906
    f72:n 9907
    f82:n 9908
375 f92:n 9909
    f102:n 9910
    f112:n 9911
    f122:n 9912
    f132:n 9913
```

```
380  f142:n 9914
     f152:n 9915
     f162:n 839
     fS162 −2251 2250 −2256 2254 T
     f202:n 2300
385  c
     c Performance of thermal column
     c log bins , 4 per decade:
     e301  1.00E−09  1.78E−09  3.16E−09  5.62E−09  &
           1.00E−08  1.78E−08  3.16E−08  5.62E−08  &
390        1.00E−07  1.78E−07  3.16E−07  5.62E−07  &
           1.00E−06  1.78E−06  3.16E−06  5.62E−06  &
           1.00E−05  1.78E−05  3.16E−05  5.62E−05  &
           1.00E−04  1.78E−04  3.16E−04  5.62E−04  &
           1.00E−03  1.78E−03  3.16E−03  5.62E−03  &
395        1.00E−02  1.78E−02  3.16E−02  5.62E−02  &
           1.00E−01  1.78E−01  3.16E−01  5.62E−01  &
           1.00      1.78      3.16      5.62      &
           1.00E+01  1.78E+01  3.16E+01  5.62E+01  &
           1.00E+02
400  e302  1.00E−09  1.78E−09  3.16E−09  5.62E−09  &
           1.00E−08  1.78E−08  3.16E−08  5.62E−08  &
           1.00E−07  1.78E−07  3.16E−07  5.62E−07  &
           1.00E−06  1.78E−06  3.16E−06  5.62E−06  &
           1.00E−05  1.78E−05  3.16E−05  5.62E−05  &
405        1.00E−04  1.78E−04  3.16E−04  5.62E−04  &
           1.00E−03  1.78E−03  3.16E−03  5.62E−03  &
           1.00E−02  1.78E−02  3.16E−02  5.62E−02  &
           1.00E−01  1.78E−01  3.16E−01  5.62E−01  &
           1.00      1.78      3.16      5.62      &
410        1.00E+01  1.78E+01  3.16E+01  5.62E+01  &
           1.00E+02
     c e304  1.00E−09  1.78E−09  3.16E−09  5.62E−09  &
     c       1.00E−08  1.78E−08  3.16E−08  5.62E−08  &
     c       1.00E−07  1.78E−07  3.16E−07  5.62E−07  &
415  c       1.00E−06  1.78E−06  3.16E−06  5.62E−06  &
     c       1.00E−05  1.78E−05  3.16E−05  5.62E−05  &
     c       1.00E−04  1.78E−04  3.16E−04  5.62E−04  &
     c       1.00E−03  1.78E−03  3.16E−03  5.62E−03  &
     c       1.00E−02  1.78E−02  3.16E−02  5.62E−02  &
420  c       1.00E−01  1.78E−01  3.16E−01  5.62E−01  &
     c       1.00      1.78      3.16      5.62      &
     c       1.00E+01  1.78E+01  3.16E+01  5.62E+01  &
     c       1.00E+02
     fC301 core side of lead plate , current
425  f301:n 7733
```

```
     fS301 −6015 6045 6046 −6047 T
     c
     fC302 end of web plate / front of tank, flux
     f302:n 2301
430  fS302 −6015 6045 6046 −6047 T
     c
     c fC304 D2 Volume, flux
     c f304:n 3055
     c
435  c ****************** Source Specification ******************
     c
     c ** Reactor Source Specification **
     c Form: KCODE NSRCK RKK IKZ KCT MSRK KNRM MRKP KC8
     c NSRCK = number of source histories per cycle
440  c RKK = initial guess for keff
     c IKZ = number of cycles to be skipped before beginning tally accumulation
     c KCT = number of cycles to be done
     c MSRK = number of source points to allocate storage for
     c KNRM = normalize tallies by 0=weight / 1=histories
445  c MRKP = maximum number of cycle values on MCTAL or RUNTPE
     c KC8 = summary and tally information averaged over
     c 0 = all cycles
     c 1 = active cycles only
     c
450  kcode 50000 1.000000 20 5020
     c
     [Reactor details omitted]
     c
     c Print and dump cycle
455  c PRDMP NDP NDM MCT NDMP DMMP
     c    NDP = increment for printing tallies (in cycles)
     c    NDM = increment for dumping to RUNTPE file (in cycles)
     c    MCT = flag to write MCTAL file and for OUTP comparisons
     c    NDMP = maximum number of dumps on RUNTPE file
460  prdmp    0   0   1
     c nps     10000
     c ctme    3600
     c Which tables to print
     print −160 −161 −162 $−175
```

D.5 MCNP Source geometry

```
 0   c ******************************************************************
     c ***                       Cell  Cards                           ***
     c ******************************************************************
     c
     c (num) (mat) [den] (geom) [params] (n) (list)
 5   c      or
     c (num) LIKE (n) BUT (list)
     c
     c Geometry
     c      : Union
10   c      # Compliment
     c       intersection  implicit
     c
     c Translate:
     c       trcl = ( x y z )
15   c
```
[Reactor details omitted]
```
     c
     c === Experimental  Geometry ===
     c thermal column nose port (C/void–He/Pb)
20   c graphite
     520    11   −1.69   ((8835 −8837 8838 −8836) (−831 −8836 −833 834) −8842 8843)
            #(−857 858 −8842 8843 −855 856) imp:n=1 imp:p=1
     c he in nose port
     523    2    −0.000178    −857 858 −8842 8843 −855 856 imp:n=1 imp:p=1
25   c nose port box
     5523  9 −2.699 ((−9837 9835 −9836 9840 −842 843) −8831 −8833 −9836 8834)
            #520 #(−857 858 −8842 8843 −855 856) #5524 imp:n=1 imp:p=1
     5524   6 −1.0 (−8838 9839 8843 834 −8837 8835) imp:n=1 imp:p=1
     6527   9 −2.699 ((835 −837 838 −836) −8943 839) imp:n=1 imp:p=1
30   c
     c 5525 9 −2.699 (−7631 1831 (−7633 7634 −7733 7742)) imp:n=1 imp:p=1
     c 5526 9 −2.699 (7632 −1832 (−7633 7634 −7733 7742)) imp:n=1 imp:p=1
     c 5527   9 −2.699 ((−7631 7632 −7633 7634) −733 7733)  imp:n=1 imp:p=1
     c 5528    9 −2.699 ((−7631 7632 −7633 7634) −7742 7842)  imp:n=1 imp:p=1
35   c water between lead box and nose port
     527    6 −1.0 ((835 −837 838 −836) −843 8943)  imp:n=1 imp:p=1
     c lead
     526   16   −11.34 ((−1831 1832 −1833 1834) −7733 7834)  imp:n=1 imp:p=1
     c he in lead box
40   5529  2   −0.000178    ((−1831 1832 −1833 1834) −7834 7742)  imp:n=1 imp:p=1
     c lead box
     5525   9  −2.699 (−7333 842 −2833 2834 −2831 2832) #5529 #526 imp:n=1 imp:p=1
     c thermal column wall  (Al)
```

```
     521    9   −2.699   ((835 −837 838 −836) −839 8840)    imp:n=1 imp:p=1
c
c thermal column lining
5927   9   −2.699  (−8936 836 −8937 8935 −8943 713) imp:n=1 imp:p=1
5928   9   −2.699  (−838 8938 −8937 8935 −8943 713) imp:n=1 imp:p=1
5929   9   −2.699  (−836 838 −8937 837 −8943 713) imp:n=1 imp:p=1
5930   9   −2.699  (−836 838 −835 8935 −8943 713) imp:n=1 imp:p=1
c Graphite webbing
c 800     22  −0.00129   −8840  2200 2218 −2217 −2220 2219  imp:n=1 imp:p=1 $ web
    ↪ opening
c 801     11  −1.69       −8840 2200 2217 −2221 −2228 2227  imp:n=1 imp:p=1 $ web
    ↪ upper  graphite   plate  6  −1.66
c 802     11  −1.69       −8840 2200 2222 −2218 −2228 2227  imp:n=1 imp:p=1 $ web
    ↪ bottom graphite   plate  6  −1.66
c 803     11  −1.69       −8840 2200 2218 −2217 −2219 2227  imp:n=1 imp:p=1 $ web
    ↪ left  graphite   plate ∗    6  −1.66
c 804     11  −1.69       −8840 2200 2218 −2217 −2228 2220  imp:n=1 imp:p=1 $ web
    ↪ right graphite    plate∗    6  −1.66
c 805     22  −0.00129   −8840 2200 2221 −836 −837 835  imp:n=1 imp:p=1 $ above
    ↪ web graphite water plate
c 806     22  −0.00129   −8840 2200 838 −2222 −837 835  imp:n=1 imp:p=1 $ below
    ↪ web graphitr water plate
c 807     22  −0.00129   −8840 2200 2222 −2221 −2227 835  imp:n=1 imp:p=1 $ left
    ↪ web   graphite water plate
c 808     22  −0.00129   −8840 2200 2222 −2221 −837 2228  imp:n=1 imp:p=1 $ right
    ↪ web graphite water  plate
c
c Graphite webbing
700     9   −2.699  (−8840 2300 −2323 2325 −837 835) &
                    :(−8840 2300 −2326 2324 −837 835) &
                    :(−8840 2300 −2331 2333 −836 838) &
                    :(−8840 2300 −2334 2332 −836 838) imp:n=1 imp:p=1 $ aluminium
                        ↪ webbing
701     11  −1.69  −8840 2300 −2325 2326 −2333 2334 &
                #(−2327 2328 −2335 2336) imp:n=1 imp:p=1 $ inner graphite
702     22  −0.00129 −8840 2301 −2327 2328 −2335 2336 imp:n=1 imp:p=1 $ inner air
719     22  −0.00129 −2301 2300 −2327 2328 −2335 2336 imp:n=1 imp:p=1 $ inner air
703     11  −1.69   −8840 2300 −2321 2323 −2332 2330 imp:n=1 imp:p=1 $ top left
704     11  −1.69   −8840 2300 −2321 2323 −2333 2334 imp:n=1 imp:p=1 $ top middle
705     11  −1.69   −8840 2300 −2321 2323 −2329 2331 imp:n=1 imp:p=1 $ top right
706     11  −1.69   −8840 2300 2330 −2332 −2325 2326 imp:n=1 imp:p=1 $ middle left
707     11  −1.69   −8840 2300 2331 −2329 −2325 2326 imp:n=1 imp:p=1 $ middle
    ↪ right
708     11  −1.69   −8840 2300 −2324 2322 −2332 2330 imp:n=1 imp:p=1 $ bottom left
709     11  −1.69   −8840 2300 −2324 2322 −2333 2334 imp:n=1 imp:p=1 $ bottom
    ↪ middle
```

```
710     11   -1.69   -8840 2300 -2324 2322 -2329 2331 imp:n=1 imp:p=1 $ bottom
    right
711     22   -0.00129 -8840 2300 -836 2323 -2332 835 &
                    #(-2321 2323 -2332 2330) imp:n=1 imp:p=1 $ top left
712     22   -0.00129 -8840 2300 -836 2321 -2333 2334 imp:n=1 imp:p=1 $ top middle
713     22   -0.00129 -8840 2300 -836 2323 -837 2331 &
                    #(-2321 2323 -2329 2333) imp:n=1 imp:p=1 $ top right
714     22   -0.00129 -8840 2300 -2325 2326 835 -2330 imp:n=1 imp:p=1 $ middle
    left
715     22   -0.00129 -8840 2300 -2325 2326 2329 -837 imp:n=1 imp:p=1 $ middle
    right
716     22   -0.00129 -8840 2300 -2324 838 -2332 835&
                    #(-2324 2322 -2332 2330) imp:n=1 imp:p=1 $ bottom left
717     22   -0.00129 -8840 2300 -2322 838 -2333 2334 imp:n=1 imp:p=1 $ bottom
    middle
718     22   -0.00129 -8840 2300 -2324 838 -837 2331 &
                    #(-2324 2322 -2329 2331) imp:n=1 imp:p=1 $ bottom right
c 719     22   -0.00129 -836 838 -837 835 -2300 2200 imp:n=1 imp:p=1 $ tiny air
    gap for detector
c D2O Tank
900     9   -2.699   -2300 3000 -3035 3002 imp:n=1 imp:p=1 $ front wall of tank
901     9   -2.699   -2300 3001 -3002 3004  imp:n=1 imp:p=1 $ front wall of tank
    0.5" well
c 902     13 -1.105   -3001 3000 -3002 3004  imp:n=1 imp:p=1 $
903     9   -2.699   -2300 3003 -3004  imp:n=1 imp:p=1 $ front wall of tank 0.25"
    well
c 904     13 -1.105   -3003 3000 -3004  imp:n=1 imp:p=1 $
905     22 -0.00129   -2300 3020  3035 -837 835 838 -836  imp:n=1 imp:p=1 $
    outside tank
910     13   -1.105 -3003 3005 -3040 -4045 $ first section of tank bottom half
            #(-2300 3000 -3035 3002 )  #(-2300 3001 -3002 3004 )
            #(4000 -4025 -4010 -4045 ) #(-4020 -4045 -4005 )
            #(4000 -4005 4020) imp:n=1 imp:p=1 $
911     13   -1.105 -3003 3005 -3040 4045 & $ first section of tank
            #(-2300 3000 -3035 3002 ) #(-2300 3001 -3002 3004 ) &
            #(4045 -4060 -4050 ) #(-4075 4060 -4065 ) #(-4090 4075 -4080 ) &
            #(-4105 4090 -4095 )   imp:n=1 imp:p=1 $
915     9   -2.699   -3000 3005  3040 -3035  imp:n=1 imp:p=1 $ wall of first
    section of tank
920     13 -1.105   -3005 3015 -3040 -3030  imp:n=1 imp:p=1 $ second section of
    tank
925     9   -2.699   -3005 3010 -3035  3025 4095 imp:n=1 imp:p=1 $ front wall of
    second section of tank
930     9   -2.699   -3005 3020 -3035 -3025 3030  imp:n=1 imp:p=1 $ top wall of
    second section of tank
```

```
935     9   −2.699   −3005 3015   3040 −3035 −3030 imp:n=1 imp:p=1 $ wall of second
  ↪ section of tank
940      22 −0.00129    −3010 3020 −3035   3025  &
             #(−4095 −4105) imp:n=1 imp:p=1 $ above second section of tank
945     9   −2.699   −3015 3020 −3035 −3030   imp:n=1 imp:p=1 $ back wall of tank
c
c Vacuum Jacket
1000     9   −2.699    4000 −4015 −4005 4010   imp:n=1 imp:p=1 $ wall of section 1
1005      0            −4025 −4045 −4010 #1025 #1035 #(5000 −5050 −5040 ) &
                      #(6000 −6050 −4060) & $ exclude D2 volume
                      imp:n=1 imp:p=1 $
1010     9   −2.699   −4000 −4020   4025   imp:n=1 imp:p=1 $ wall of bottom of
  ↪ section 1
1011      9   −2.699 4025 4000 −4010 −4045 imp:n=1 imp:p=1  $ fix for the corner,
1025     9   −2.699    4015 −4035 −4005 4030   imp:n=1 imp:p=1 $ wall
1035     9   −2.699    4035 −4045 −4005 4040   imp:n=1 imp:p=1 $ wall
1045     9   −2.699    4045 −4060 −4050 4055   imp:n=1 imp:p=1 $ wall
1050     0             4045 −4060 −4055 6050   imp:n=1 imp:p=1 $
1055     9   −2.699   −4075 4060 −4065 4070   imp:n=1 imp:p=1 $ wall of section 2
1060     0            −4075 4060 −4070 6080   imp:n=1 imp:p=1 $
1065     9   −2.699   −4090 4075 −4080 4085   imp:n=1 imp:p=1 $ wall of section 3
1070     0            −4090 4075 −4085 6100   imp:n=1 imp:p=1 $
1075     9   −2.699   −4105 4090 −4095 4100   imp:n=1 imp:p=1 $ wall of section 4
1080     0            −4105 4090 −4100 #(−6140 −6120) imp:n=1 imp:p=1 $
1090     0            5025 −5040 −5075   &
                     #(−6050 6000) imp:n=1 imp:p=1 $
1100     0            6025 −6030 −6050 6060   imp:n=1 imp:p=1 $
c
c Methane Container
2000     9   −2.699    5000 −5035 −5050 5055   imp:n=1 imp:p=1 $ methane container
  ↪ outer wall
2005     9   −2.699    5000 −5005 −5055   imp:n=1 imp:p=1 $ methane container
  ↪ bottom wall
2010     25 −0.017    5005 −5035 −5055 5060   imp:n=1 imp:p=1 $ lHe
2015     25 −0.017    5005 −5010 −5060   imp:n=1 imp:p=1 $ lHe bottom
2020     9   −2.699   5010 −5030 −5060 5065   imp:n=1 imp:p=1 $ middle wall
2025     9   −2.699   5010 −5015 −5065   imp:n=1 imp:p=1 $ middle wall bottom
c 2030    15 −0.42      5015 −5030 −5065 5070   imp:n=1 imp:p=1 $ methane
c 2035    15 −0.42      5015 −5020 −5070   imp:n=1 imp:p=1 $ methane bottom
2030     15 −0.42      (5015 −5030 −5065 5070):(5015 −5020 −5070)  &
                      imp:n=1 imp:p=1 $ methane
2040     9   −2.699   5020 −5030 −5070 5075   imp:n=1 imp:p=1 $ inner wall
2045     9   −2.699   5020 −5025 −5075   imp:n=1 imp:p=1 $ inner wall bottom
2050     9   −2.699   5035 −5040 −5050 5060   imp:n=1 imp:p=1 $ outer top
2055     9   −2.699   5030 −5040 −5060 5075   imp:n=1 imp:p=1 $ inner top
c
```

```
c Deuterium Volume
3000    9   -2.699     6000 -6025 -6050 6055   imp:n=1 imp:p=1 $
3005    9   -2.699     6000 -6005 -6055   imp:n=1 imp:p=1 $
c 3010    25  -0.017      6005 -6020 -6055 6060   imp:n=1 imp:p=1 $
3010    25  -0.017     (6005 -6020 -6055 6060) : (6005 -6010 -6060 6065)
                       imp:n=1 imp:p=1 $
3015    25  -0.017     6005 -6010 -6065   imp:n=1 imp:p=1 $
3020    9   -2.699     6020 -6025 -6055 6060   imp:n=1 imp:p=1 $
c 3035    9   -2.699      6010 -6035 -6060 6065   imp:n=1 imp:p=1 $
3035    9   -2.699     6015 -6035 -6060 6065   imp:n=1 imp:p=1 $
c 3040    9   -2.699      6010 -6015 -6065   imp:n=1 imp:p=1 $
3040    9   -2.699     6010 -6015 -6060   imp:n=1 imp:p=1 $
3045    9   -2.699     6030 -6035 -6050 6060   imp:n=1 imp:p=1 $
3050    3   -6.4       6035 -6040 -6050 6055   imp:n=1 imp:p=1 $
3055    0             6015 -6045 -6065   imp:n=1 imp:p=1 $ D2
3060    9   -2.699     6040 -4045 -6050 6055   imp:n=1 imp:p=1 $
3065    0             6045 -6035 -6065   imp:n=1 imp:p=1 $
3070    0             6035 -4045 -6055 6070 imp:n=1 imp:p=1 $
3075    0             6035 -4045 -6075 imp:n=1 imp:p=1 $
c Guides
3090    26  -2.2       6035 -4045 -6070 6075   imp:n=1 imp:p=1 $
3095    9   -2.699     4045 -4060 -6050 6055   imp:n=1 imp:p=1 $
3100    0             4045 -4060 -6055 6070   imp:n=1 imp:p=1 $
3105    26  -2.2       4045 -4060 -6070 6075   imp:n=1 imp:p=1 $
3110    0             4045 -4060 -6075   imp:n=1 imp:p=1 $
c section 2
3115    9   -2.699     4060 -4075 -6080 6085   imp:n=1 imp:p=1 $
3120    0             4060 -4075 -6085 6090   imp:n=1 imp:p=1 $
3125    26  -2.2       4060 -4075 -6090 6095   imp:n=1 imp:p=1 $
3130    0             4060 -4075 -6095   imp:n=1 imp:p=1 $
c section 3
3135    9   -2.699     4075 -4090 -6100 6105   imp:n=1 imp:p=1 $
3140    0             4075 -4090 -6105 6110   imp:n=1 imp:p=1 $
3145    26  -2.2       4075 -4090 -6110 6115   imp:n=1 imp:p=1 $
3150    0             4075 -4090 -6115   imp:n=1 imp:p=1 $
c section 4
3155    9   -2.699     4090 -6140 -6120 6125   imp:n=1 imp:p=1 $
3160    0             4090 -6140 -6125 6130   imp:n=1 imp:p=1 $
3165    26  -2.2       4090 -6140 -6130 6135   imp:n=1 imp:p=1 $
3170    0             4090 -6140 -6135   imp:n=1 imp:p=1 $
c
830     21  -2.5   -3020 713 -837 835 838 -836 &
             #(-4105 4090 -4095 4100 )#(-4105 4090 -4100 )  imp:n=1 imp:p=1 $
                ↪ behind tank


c ****************************************************************
```

```
c ***                        Surface  Cards                           ***
c ********************************************************************
c
c Plane normal to x-axis:
c     px (distance)
c Cylinder on x-axis
c     cx (radius)
c Cylinders parallel to axes
c     c/x (y) (z) (radius)
c     c/y (x) (z) (radius)
c     c/z (x) (y) (radius)
c
```
[Reactor details omitted]
```
c
c thermal column nose and main body
1831     pz   25.4
1832     pz  -25.4
1833     px   26.0298
1834     px  -18.9702
2831     pz   26.3525
2832     pz  -26.3525
2833     px   26.9823
2834     px  -19.9227
831      p   -1.732    1    0    13.3097 $15.2147
833      p    1.732    1    0    25.1161 $27.0211
834      p    0   -0.57735   1   -11.52714825 $-12.6270
8831     p   -1.732    1    0    14.3097 $16.2147
8833     p    1.732    1    0    26.1161 $28.0211
8834     p    0   -0.57735   1   -12.52714825 $-13.6270
8835     px  -38.652
8836     pz   42.182
8837     px   45.712
8838     pz  -42.182 $ xuf2
8839     pz  -65042
9835     px  -39.922
9836     pz   43.452
9837     px   46.982
9839     pz  -66.312
9840     pz  -67.582
835      px  -56.7955 $ -56.319
836      pz   60.325  $  60.98
837      px   63.8545 $  63.378
838      pz  -60.325  $ -60.98
839      py -107.8591 $-105.9541
c thermal column liner
8935     px  -58.0655 $ -57.589
```

```
     8936     pz    61.595  $ 62.25
245  8937     px    65.1245 $ 64.648
     8938     pz   −61.595  $ −62.25
     c
     8840    py   −110.3991 $−108.4941
     8842    py   −36.815   $−34.91
250  8843    py   −105.8766 $−103.9716
     842     py   −35.86277 $−33.95777
     843     py   −106.8291 $−104.9241
     8943    py   −107.2241 $−105.3191
     855     pz   25
255  856     pz   −25
     857     px   25.5298
     858     px   −18.4702
     c
     c  Graphite Webbing
260  c 2200       py   −115.5 $ end of web plate
     2300       py   −115.5 $ end of web plate
     2301       py   −115.4 $ surface just before end of web plate for detector
     2217       pz    22.5
     2218       pz   −22.5
265  2219       px   −18.9702
     2220       px    26.0298
     2321       pz    43.0 $ top of graphite
     2322       pz   −43.0
     2323       pz    30.1625 $ top of aluminium webbing
270  2324       pz   −30.1625
     2325       pz    29.21 $ bottom of aluminium webbing
     2326       pz   −29.21
     2327       pz    22.5 $ bottome of graphite
     2328       pz   −22.5
275  2329       px    46.5298 $ right of graphite
     2330       px   −39.4702
     2331       px    33.5333 $ right of aluminium webbing
     2332       px   −26.4743
     2333       px    32.5808 $ left of aluminium webbing
280  2334       px   −25.5218
     2335       px    26.0298  $ left of graphite
     2336       px   −18.9702
     2227       px   −39.4702
     2228       px    46.5298
285  c
     c  *****************  Source Geometry  ******************
     c
     c D2O tank
     c front at 2300
```

```
3000      py   −118.04     $ end of front wall 1" thick
3001      py   −116.77     $ front wall 0.5" thickness
3002      c/y   3.5295 0 41.91
3003      py   −116.135  $ front wall 0.25" thickness
3004      c/y   3.5295 0 31.75
3005      py   −160.4453 $ end of front section
3010      py   −162.9853 $ end of front section wall 1" thick
3015      py   −196.5133 $ end of back section
3020      py   −199.0533 $ end of back section wall 1" thick
3025      pz    14.2875    $ top of back section 4.8" above centerline
3030      pz    13.6525    $ top of back section bottom of wall 0.25" thick
3035      c/y   3.5295 0 57.4675   $ tank wall
3040      c/y   3.5295 0 56.8325   $ tank inner wall 0.25"
c
c Sphere: n   S   x y z R
c Plane:  n   P   A B C D
c        where: A=nx,  B=ny,  C=nz,  d=nx*xo+ny*yo+nz*zo  Ax+By+Cz=D
c Arbitrary Geometric:
c         n  GQ A B C D E F G H J K
c        where: Ax^2+By^2+Cz^2+Dxy+Eyz+Fzx+Gx+Hy+Jz+K=0
c
c Vacuum jacket
c p1,c1=(xo,yo,zo,asi,pol)=(7.9525,−135.81,−19.7891,0,0): bottom
4000      pz   −19.7891    $ bottom of section 1
4005      c/z   7.9525 −135.810 17.78     $ section 1
4010      c/z   7.9525 −135.810 17.4625  $ inside wall of section 1
4015      pz    7.343    $
4020      s     7.9525 −135.810 4.12754 29.801 $ curved bottom of section 1
4025      s     7.9525 −135.810 4.12754 29.4835 $ 29.613 $ inside of curved bottom
4030      c/z   7.9525 −135.810 15.812     $
4035      pz    9.883    $ bottom of
4040      c/z   7.9525 −135.810 14.745      $ inside
4045      pz   10.823    $ bottom
4050      c/z   7.9525 −135.810 14.795      $
4055      c/z   7.9525 −135.810 14.478      $ inside wall
c
c p2=(xo,yo,zo,asi,pol)=({7.9525, −135.81, 22.2089,(18)0.314159, (250)4.36332)
c c2=(xo,yo,zo,asi,pol)=({7.9525, −135.81, 22.2089,(36)0.314159, (250)4.36332)
4060      p   −0.10569  −0.290381  0.951057  59.7181 $ bottom of section 2
4065      gq   0.959585   0.694923   0.345492 &
             −0.222078    0.893701   0.32528  &
             −52.647      170.673     103.441      10431.3 $ r=14.7955
4070      gq   0.959585   0.694923   0.345492 &
             −0.222078    0.893701   0.32528  &
             −52.647      170.673     103.441      10440.6 $ r=14.478
c
```

```
c  p3=(xo,yo,zo,asi,pol)=({5.38718, −142.858, 32.5325, (51)0.890118, (250)
    ↪ 4.36332)
c  c3=(xo,yo,zo,asi,pol)=({5.38718, −142.858, 32.5325, (66)1.15192, (250)4.36332)
   4075    p    −0.2658 −0.730278  0.62932 123.368 $ bottom of section 3
   4080    gq    0.902374   0.26306    0.834565 &
                −0.536448   0.698328   0.25417  &
                −94.6273    55.3322    44.0919    3271.11 $ r=14.7955
   4085    gq    0.902374   0.26306    0.834565 &
                −0.536448   0.698328   0.25417  &
                −94.6273    55.3322    44.0919    3280.4  $ r=14.478
c
c  p4=(xo,yo,zo,asi,pol)=({1.37118, −153.892, 37.7604, (78)1.36136, (250)4.36332)
c  c4=(xo,yo,zo,asi,pol)=({51.37118, −153.892, 37.7604, (90)1.5708, (250)4.36332)
   4090    p    −0.334546 −0.919158  0.207912  148.843 $ bottom of section 4
   4095    gq    0.883022   0.116978   1.0         &
                −0.642788   0.0        0.0         &
                −101.341    36.8853    −75.5208   4114.59  $ r=14.7955
   4100    gq    0.883022   0.116978   1.0         &
                −0.642788   0.0        0.0         &
                −101.341    36.8853    −75.5208   4123.89 $ r=14.478
c
c   p5=(xo,yo,zo,asi,pol)=({−13.6713, −195.221, 37.7604, (90)1.5708, (250)
    ↪ 4.36332)
   4105    p    −0.34202 −0.939693  0          188.123 $ end of section 5
c
c Methane container
   5000    pz   −19.6191    $ bottom of container
   5005    pz   −19.3011    $ bottom of lHe
   5010    pz   −18.8831    $ top of lHe bottom
   5015    pz   −18.5651    $ bottom of methane
   5020    pz   −17.5341    $ top of methane bottom
   5025    pz   −17.2861    $ top of container bottom
   5030    pz   −1.6611     $ top of methane
   5035    pz   −0.1121     $ top of lHe
   5040    pz    0.6119     $ top of container
   5050    c/z  7.9525 −135.810 12.6135     $ Outside of container
   5055    c/z  7.9525 −135.810 12.4135     $ outside of lHe
   5060    c/z  7.9525 −135.810 12.0175     $ inside of lHe
   5065    c/z  7.9525 −135.810 11.8105     $ outside of methane
   5070    c/z  7.9525 −135.810 10.8965     $ inside of methane
   5075    c/z  7.9525 −135.810 10.6425     $ inside of container
c
c Deuterium volume
c
   6000    pz   −14.5281    $ bottom of container 1/8"
   6005    pz   −14.2101    $ bottom of lHe
```

```
380 6010      pz    −13.6131    $ top of lHe bottom 1/8"
    6015      pz    −13.2951    $ inside of volume
    6020      pz    −9.7291     $ top of lHe
    6025      pz    −8.5191     $ top of container
    6030      pz    −6.7101     $ bottom of guide jacket
385 6035      pz    −5.7031     $ bottom of zircaloy ring, guide
    6040      pz    −0.0701     $ top of zircaloy ring
    6045      pz    −7.940      $ D2 level, 1.2 L
    6046      px     16.3985    $ Tangent to outside of D2
    6047      px    −0.4935     $ Tangent to outside of D2
390 c section 1 top is 4060
    6050      c/z   7.9525 −135.810 9.322 $ outside of volume
    6055      c/z   7.9525 −135.810 9.119 $ inside of volume
    6060      c/z   7.9525 −135.810 8.7   $ inside of lHe
    6065      c/z   7.9525 −135.810 8.446 $ inside of container
395 6070      c/z   7.9525 −135.810 8.2   $ outside of guide
    6075      c/z   7.9525 −135.810 8.0   $ inside of guide
    c section 2
    6080      gq    0.959585   0.694923   0.345492 &
                    −0.222078   0.893701   0.32528  &
400                 −52.647    170.672     103.44     10563.2  $ r=9.322
    6085      gq    0.959585   0.694923   0.345492 &
                    −0.222078   0.893701   0.32528  &
                    −52.647    170.672     103.44     10567 $ r=9.119
    6090      gq    0.959585   0.694923   0.345492 &
405                 −0.222078   0.893701   0.32528  &
                    −52.647    170.672     103.44     10582.9 $ r=8.2
    6095      gq    0.959585   0.694923   0.345492 &
                    −0.222078   0.893701   0.32528  &
                    −52.647    170.672     103.44     10586.1 $ r=8.0
410 c section 3
    6100      gq    0.902374   0.26306    0.834565 &
                    −0.536448  0.698328   0.25417  &
                    −94.6254   55.3317    44.0919    3403.02 $ r=9.322
    6105      gq    0.902374   0.26306    0.834565 &
415                 −0.536448  0.698328   0.25417  &
                    −94.6254   55.3317    44.0919    3406.76  $ r=9.119
    6110      gq    0.902374   0.26306    0.834565 &
                    −0.536448  0.698328   0.25417  &
                    −94.6254   55.3317    44.0919    3422.67 $ r=8.2
420 6115      gq    0.902374   0.26306    0.834565 &
                    −0.536448  0.698328   0.25417  &
                    −94.6254   55.3317    44.0919    3425.91 $ r=8.0
    c section 4
    6120      gq    0.883022   0.116978   1.0       &
425                 −0.642788  0.0        0.0       &
```

```
                        −101.341   36.8853   −75.5208   4246.6 $ r=9.322
       6125     gq    0.883022   0.116978   1.0        &
                      −0.642788  0.0        0.0        &
                      −101.341   36.8853   −75.5208   4250.35 $ r=9.119
430    6130     gq    0.883022   0.116978   1.0        &
                      −0.642788  0.0        0.0        &
                      −101.341   36.8853   −75.5208   4266.26  $ r=8.2
       6135     gq    0.883022   0.116978   1.0        &
                      −0.642788  0.0        0.0        &
435                   −101.341   36.8853   −75.5208   4269.5  $ r=8.0
    c   p6=(xo,yo,zo,asi,pol)=({−10.3137, −185.996, 37.7604, (90)1.5708, (250)
        ↪ 4.36332)
       6140     p    −0.34202  −0.939693  0          180.027 $ end of section 5
    c Cell detector surfaces
       9001      pz    5.0
440    9002      pz   −5.0
       9003      px    8.5298
       9004      px   −1.4702
       9010      py   −35.0
       9012      py   −45.0
445    9014      py   −55.0
       9016      py   −65.0
       9018      py   −75.0
       9020      py   −85.0
       9022      py   −95.0
450    9024      py   −105.0
       9026      py   −115.0
       9028      py   −125.0
       9030      py   −135.0
       9032      py   −145.0
455    9034      py   −155.0
       9036      py   −165.0
       9038      py   −175.0
       9040      py   −185.0
       9042      py   −195.0
460
    c ****************************************************************
    c ***                      Data Cards                         ***
    c ****************************************************************
    c
465 mode   n  p
    c
    [Reactor details omitted]
    c
    c ****************** Materials Specification ******************
470 c
```

```
c (+) Atomic  fraction  or  (−) Weight  fraction
c MTn = S(alpha,beta)  thermal  neutron  treatment  for  material  n
c
```
[Reactor details omitted]
```
475 c
    c ——— Helium Gas
    m2    2004          1.000000   gas=1.0      $
    c ——— Zr−2
    m3    40000        −0.982700   & $
480       50120        −0.014400   & $
          26000        −0.001400   & $
          24000        −0.000900   & $
          28000        −0.000600     $
    mt3   zr−h.20t
485 c ——— H2O (Coolant & Moderator)
    m6    1001          0.666670   & $ H
          8016          0.333330     $ O
    mt6   lwtr.20t
    c ——— Aluminum
490 m9   13027          1.000000     $
    mt9   al27.22t
    c ——— Graphite
    m11   6000          1.000000     $
    mt11  grph.20t
495 c ——— Heavy Water
    m13   1002          0.666670   & $
          8016          0.333330     $
    mt13  hwtr.20t
    c ——— Ortho−Deuterium
500 c m14   1002          1.000000     $
    c mt14 dortho.20t
    c ——— Methane
    m15   1001          0.800000   & $
          6000          0.200000     $
505 mt15 smeth.20t
    c ——— Lead
    m16  82204          0.014000   & $ Pb−204   1.4%
         82206          0.241000   & $ Pb−206  24.1%
         82207          0.221000   & $ Pb−207  22.1%
510      82208          0.524000     $ Pb−208  52.4%
    c ——— Air (Experimental geometry)
    m22   6000          0.020000   gas=0.02   & $
          7014          0.660000   gas=0.66   & $
          8016          0.320000   gas=0.32     $
515 c ——— Glass
    m26   14000         0.333300   & $
```

```
         8016          0.666700     $
  c ——— Acrylic
  m33   1001          0.534     $ H
520        6012          0.333     $ C
           8016          0.133     $ O
  c
  c ****************** Detectors  ******************
  c
525 c Virtual surface detectors
  c Fn:N S (or C)
  c FSn S1 ... Sk T (optional)
  c
  c default energy bins
530 c log bins, 16 per decade:
  e0   1.00E−09 1.15E−09 1.33E−09 1.54E−09 &
       1.78E−09 2.05E−09 2.37E−09 2.74E−09 &
       3.16E−09 3.65E−09 4.22E−09 4.87E−09 &
       5.62E−09 6.49E−09 7.50E−09 8.66E−09 &
535        1.00E−08 1.15E−08 1.33E−08 1.54E−08 &
       1.78E−08 2.05E−08 2.37E−08 2.74E−08 &
       3.16E−08 3.65E−08 4.22E−08 4.87E−08 &
       5.62E−08 6.49E−08 7.50E−08 8.66E−08 &
       1.00E−07 1.15E−07 1.33E−07 1.54E−07 &
540        1.78E−07 2.05E−07 2.37E−07 2.74E−07 &
       3.16E−07 3.65E−07 4.22E−07 4.87E−07 &
       5.62E−07 6.49E−07 7.50E−07 8.66E−07 &
       1.00E−06 1.15E−06 1.33E−06 1.54E−06 &
       1.78E−06 2.05E−06 2.37E−06 2.74E−06 &
545        3.16E−06 3.65E−06 4.22E−06 4.87E−06 &
       5.62E−06 6.49E−06 7.50E−06 8.66E−06 &
       1.00E−05 1.15E−05 1.33E−05 1.54E−05 &
       1.78E−05 2.05E−05 2.37E−05 2.74E−05 &
       3.16E−05 3.65E−05 4.22E−05 4.87E−05 &
550        5.62E−05 6.49E−05 7.50E−05 8.66E−05 &
       1.00E−04 1.15E−04 1.33E−04 1.54E−04 &
       1.78E−04 2.05E−04 2.37E−04 2.74E−04 &
       3.16E−04 3.65E−04 4.22E−04 4.87E−04 &
       5.62E−04 6.49E−04 7.50E−04 8.66E−04 &
555        1.00E−03 1.15E−03 1.33E−03 1.54E−03 &
       1.78E−03 2.05E−03 2.37E−03 2.74E−03 &
       3.16E−03 3.65E−03 4.22E−03 4.87E−03 &
       5.62E−03 6.49E−03 7.50E−03 8.66E−03 &
       1.00E−02 1.15E−02 1.33E−02 1.54E−02 &
560        1.78E−02 2.05E−02 2.37E−02 2.74E−02 &
       3.16E−02 3.65E−02 4.22E−02 4.87E−02 &
       5.62E−02 6.49E−02 7.50E−02 8.66E−02 &
```

```
           1.00E−01  1.15E−01  1.33E−01  1.54E−01  &
           1.78E−01  2.05E−01  2.37E−01  2.74E−01  &
565        3.16E−01  3.65E−01  4.22E−01  4.87E−01  &
           5.62E−01  6.49E−01  7.50E−01  8.66E−01  &
           1.00E+00  1.15E+00  1.33E+00  1.54E+00  &
           1.78E+00  2.05E+00  2.37E+00  2.74E+00  &
           3.16E+00  3.65E+00  4.22E+00  4.87E+00  &
570        5.62E+00  6.49E+00  7.50E+00  8.66E+00  &
           1.00E+01  1.15E+01  1.33E+01  1.54E+01  &
           1.78E+01  2.05E+01  2.37E+01  2.74E+01  &
           3.16E+01  3.65E+01  4.22E+01  4.87E+01  &
           5.62E+01  6.49E+01  7.50E+01  8.66E+01  &
575        1.00E+02
    c
    fC11 core side of lead plate, current
    f11:n 7733
    fS11 −6015 6045 6046 −6047 T
580 c
    fC22 end of web plate / front of tank, flux
    f22:n 2301
    fS22 −6015 6045 6046 −6047 T
    c
585 fC14 D2 Volume, flux
    f14:n 3055
    c
    c ****************** Source Specification ******************
    c
590 c ** Reactor Source Specification **
    c Form: KCODE NSRCK RKK IKZ KCT MSRK KNRM MRKP KC8
    c NSRCK = number of source histories per cycle
    c RKK = initial guess for keff
    c IKZ = number of cycles to be skipped before beginning tally accumulation
595 c KCT = number of cycles to be done
    c MSRK = number of source points to allocate storage for
    c KNRM = normalize tallies by 0=weight / 1=histories
    c MRKP = maximum number of cycle values on MCTAL or RUNTPE
    c KC8 = summary and tally information averaged over
600 c 0 = all cycles
    c 1 = active cycles only
    c
    kcode 50000 1.000000 20 5020
    c
605 [Reactor details omitted]
    c
    c Print and dump cycle
    c PRDMP NDP NDM MCT NDMP DMMP
```

211

```
    c    NDP = increment for printing tallies (in cycles)
610 c    NDM = increment for dumping to RUNTPE file (in cycles)
    c    MCT = flag to write MCTAL file and for OUTP comparisons
    c    NDMP = maximum number of dumps on RUNTPE file
    c prdmp    1000   1000  1   1000
    c nps      10000
615 c ctme     3600
    c Which tables to print
    print −160 −161 −162 $−175
```